



**RICARDO FARIA
MENDES**

METAL-ORGANIC FRAMEWORKS BASED ON FLEXIBLE BRIDGES

REDES METALO-ORGÂNICAS BASEADAS EM PONTES FLEXÍVEIS

Dissertação apresentada à Universidade de Aveiro, para cumprimento dos requisitos necessários à obtenção do grau de Doutor em Química, realizada sob a orientação científica do Doutor Filipe Alexandre Almeida Paz, investigador principal do Centro de Investigação CICECO – Aveiro Institute of Materials da Universidade de Aveiro

Apoio financeiro da FCT: SFRH/BD/84231/2012

FCT Fundação para a Ciência e a Tecnologia

MINISTÉRIO DA EDUCAÇÃO E CIÊNCIA



QUADRO
DE REFERÊNCIA
ESTRATÉGICA
NACIONAL
PORTUGAL 2007.2013



COMPETE

PROGRAMA OPERACIONAL FACTORES DE COMPETITIVIDADE

O júri

presidente

Doutor Joaquim Manuel Vieira

Professor Catedrático da Universidade de Aveiro

Doutora Maria Teresa Leal Duarte

Professora Catedrática da Universidade de Lisboa

Doutora Verónica Cortés de Zea Bermudez

Professora Catedrática da Universidade de Trás-os-Montes e Alto Douro

Doutor Luís Manuel Cunha Silva

Investigador de pós-doutoramento da Universidade do Porto

Doutor João Carlos Matias Celestino Gomes da Rocha

Professor Catedrático da Universidade de Aveiro

Doutor Filipe Alexandre Almeida Paz

Equiparado a Investigador Principal da Universidade de Aveiro (orientador)

Dedico este trabalho ao meus Pais e irmã, e em especial às minhas duas Princesas Sofia e Letícia.

agradecimentos

Em primeiro lugar, um agradecimento especial aos meus Pais, por tudo o que fizeram por mim, pois sem eles não me seria possível de todo chegar a este momento e ser a pessoa que sou hoje.

O meu agradecimento ao Departamento de Química, em especial o CICECO, por ter aceite me acolher na concretização deste trabalho.

Agradeço à Fundação para a Ciência e Tecnologia (FCT) pelo financiamento no âmbito da bolsa de doutoramento com referência SFRH/BD/84231/2012.

Um agradecimento ao Doutor Filipe Paz, por ter aceite me orientar durante estes últimos anos, e especialmente por me deixar ser autónomo durante todo o meu trabalho e pela ajuda prestada sempre que necessária. À Doutora Patrícia Silva, agradeço a ajuda fundamental que me prestou no início da minha estadia no CICECO, e principalmente pela companhia e amizade.

Ao Doutor Sérgio Vilela, agradeço a amizade de me ter feito sentir em casa desde o momento que aqui cheguei.

Ao Doutor José Fernandes um agradecimento especial por todo o tempo dispendido durante as nossas “aulas” de cristalografia (e não só). O que sei hoje é sem dúvida graças a toda a paciência e vontade de ensinar que sempre mostrou.

Às minhas colegas, Daniela Firmino e Jessica Barbosa, agradeço a ajuda e companhia sempre presente no laboratório.

Agradeço às Doutoradas Rosário e Paula Brandão por toda a disponibilidade e ajuda prestada nas análises de Raio-X, Agradeço também à Margaret pela amizade e disponibilidade e à Celeste por toda a ajuda que me prestou.

agradecimentos

Obrigado à Doutora Anabela Valente e ao seu grupo, em especial à Margarida Antunes pela colaboração prestada no trabalho de catalise. Igualmente agradeço ao Doutor Filipe Figueiredo e à Paula Barbosa pela disponibilidade e ajuda relativamente ao trabalho desenvolvido na parte de condução protónica.

Um obrigado ao Doutor Flávio Figueira pela constante disponibilidade para ajudar, bem como pela companhia nos momentos de relaxamento e “brainstorming”.

Obrigado aos companheiros de almoço do CICECO com quem tive o prazer da companhia.

Agradeço à Lisa por me ter aturado na “salinha” durante este tempo todo e pela companhia no café matinal.

Um agradecimento especial à “Doutora” Carla Pereira, por toda a companhia, amizade, cumplicidade (e as vivências, claro) durante estes longos anos. Tornou não só as viagens de comboio para Guimarães muito mais animadas, como iluminava o nosso trabalho sempre que estava presente.

Um agradecimento especial para os meus grandes amigos Carlos, Gonçalo, J. Ricardo, Sofia e Tânia pela companhia, amizade e apoio durante esta longa caminhada e por me aturarem há mais de uma década. Por fim agradeço à minha família, em especial aos meus Pais (novamente) e irmã, que me apoiaram e deram forças não só durante esta etapa mas também durante a minha vida.

palavras-chave

Polímero de Coordenação, Redes Metalo-Orgânicas, Dimensionalidade, Lantanídeos, Ligandos Orgânicos Flexíveis, Transformação Cristal-Cristal, Catalise, Condução Protónica

resumo

Esta tese pretende apresentar o trabalho desenvolvido na preparação de novos Polímeros de Coordenação ou Redes Metalo-Orgânicas de baixa dimensão (1D e 2D) pela auto-montagem de lantanídeos e ligandos orgânicos altamente flexíveis. Numa primeira etapa as condições ideais foram optimizadas utilizando abordagens sintéticas distintas: condições hidrotérmicas e de one-pot, o que permitiu o isolamento de cristais grandes; e a síntese por microondas, que foi a abordagem ideal para reduzir significativamente o tempo de reacção. Todos os materiais foram caracterizados utilizando a combinação de várias técnicas, como FTIR, análise elementar, RMN de estado sólido, microscopia electrónica (SEM e EDS) e termogravimetria. As estruturas cristalinas foram resolvidas utilizando análise de difracção de raios X de cristal único. Num segundo passo, os materiais de baixa dimensão foram utilizados como precursores para obter MOFs de dimensão superiores por transformação Cristal-Cristal, que foram seguidos de perto por análise de raios-X de cristal único. No último passo, as propriedades de alguns materiais foram investigadas, como o uso como potencial catalisadores heterogéneos e como condutores protónicos. Alguns materiais mostraram actividade catalítica notável em várias reacções orgânicas, enquanto um mostrou a maior condução protónica registada até agora para qualquer tipo de material.

keywords

Coordination Polymer, Metal-Organic Framework, Dimensionality, Lanthanides, Flexible Organic Linkers, Single-Crystal to Single-Crystal Transformation, Catalysis, Proton conductivity

abstract

This thesis aims to present the work developed in the preparation of new Coordination Polymers or Metal-Organic Frameworks with low dimensions (1D and 2D) by the self-assembly of lanthanides and highly flexible organic linkers. In a first step the ideal conditions were screened using distinct synthetic approaches: hydrothermal and one-pot conditions, which allowed the isolation of large crystals; and microwave-assisted synthesis, which was the ideal approach to reduce significantly the time of reaction. All materials were characterized using the combination of several techniques, such as FTIR, elemental analysis, solid-state NMR, electron microscopy (SEM and EDS) and thermogravimetry. The crystal structures were unveiled using single-crystal X-ray diffraction analysis. In a second step, the low dimensional materials were used as precursors to obtain higher dimensional MOFs by Single-Crystal to Single-Crystal transformation, which were followed closely by single-crystal X-ray analysis. In a final step, the properties of some materials were investigated, with potential use as heterogeneous catalysts and proton conductors. Some materials showed remarkable catalytic activity in several organic reactions, while one showed the highest proton conduction registered up to now for any kind of material.

Contents

Contents	i
Publications.....	v
List of Abbreviations.....	vii

Chapter 1 - Supramolecular Chemistry: The Case of Coordination Polymers and Metal-Organic Framework..... 1

1.1 – Coordination Polymers and Metal-Organic Frameworks: Origin and Terminology	1
1.2 – Building Blocks in CPs and MOFs Preparation	4
1.3 – Synthetic Methodologies in the preparation of CPs/MOFs.....	11
1.3.1 – <i>Scale-up in CPs and MOFs</i>	15
1.4 – Application of MOFs/CPs	16
1.5 – Structural Transformation in CPs/MOFs.....	17
1.5.1 – <i>Changing the Dimensionality of MOFs</i>	19
1.6 – Transforming MOF/CP: designing new functional materials	23
1.6.1 – <i>Gas Adsorption</i>	23
1.6.2 – <i>Luminescence</i>	27
1.6.3 – <i>Sensors</i>	29
1.6.4 – <i>Controlled release of molecules</i>	32
1.6.5 – <i>Water scavengers</i>	33
1.6.6 – <i>Magnetic materials</i>	36
1.7 –Main Objectives.....	37

Chapter 2 -One-Dimensional Lanthanide-Organic Coordination Polymer with Catalytic Activity..... 39

2.1 – Synthetic Strategy.....	40
2.2 – Crystal Structure Description: Single-Crystal and Synchrotron Powder X-Ray Diffraction studies	41
2.3 – Physicochemical Characterization.....	43
2.4 – Catalytic Application.....	47
2.5 - Transformation Studies	51
2.6 – Concluding Remarks	55

Chapter 3 -Lamellar Coordination Polymer with a Remarkable Catalytic Activity and Proton Conductivity..... 57

3.1 – Synthetic approach	58
3.2 – Crystal Structure Elucidation: $[\text{Gd}(\text{H}_4\text{nmp})(\text{H}_2\text{O})_2]\text{Cl}\cdot 2\text{H}_2\text{O}$ (2).....	59
3.3 – Physicochemical Characterization	64
3.4 – Heterogeneous catalysis	68
3.4.1 – <i>Styrene oxide alcoholysis</i>	68
3.4.2 – <i>Acetalisation of benzaldehyde</i>	72
3.4.3 – <i>Ketalisation of cyclohexanone</i>	73
3.4.4 – <i>Acetalisation of cyclohexanaldehyde</i>	74
3.4.5 – <i>General Catalytic considerations</i>	75
3.5 – Proton Conduction.....	77
3.5.1 – <i>Structural Transformation of 2 into 3</i>	77
3.5.2 – <i>Proton conductivity in 2 and 3</i>	79
3.6 – Concluding Remarks	82
Chapter 4 -Dynamic Breathing effect in Metal-Organic Frameworks: Reversible 2D-3D-2D-3D Single-Crystal to Single-Crystal Transformation	85
4.1 – Synthetic Strategy	85
4.2 – Crystal Structure Description: Single-Crystal X-Ray Diffraction studies	87
4.3 – Physicochemical Characterization	92
4.4 – Concluding Remarks	94
Chapter 5 -Large 3D Networks Based on Highly Flexible Tetraphosphonic acid Organic Linker	95
5.1 – Synthetic Strategy	96
5.2 – Microwave-assisted Synthesis of a 3D Europium-Organic Framework.....	97
5.2.1 – <i>Crystal Structure of $[\text{Eu}_2(\text{SO}_4)_2(\text{H}_6\text{htp})(\text{H}_2\text{O})_4]\cdot 10\text{H}_2\text{O}$ (8)</i>	97
5.2.2 – <i>Physicochemical Characterization</i>	101
5.3 – Microwave-assisted Synthesis of a 3D Lanthanum-Organic Framework.....	102
5.3.1 – <i>Crystal Structure of $[\text{La}_2(\text{SO}_4)_2(\text{H}_6\text{htp})(\text{H}_2\text{O})_6]\cdot 6\text{H}_2\text{O}$ (9)</i>	102
5.3.2 – <i>Physicochemical Characterization</i>	105
5.4 – Hydrothermal Synthesis of a 3D Lanthanum-Organic Framework	108
5.4.1 – <i>Crystal Structure of $[\text{La}_2(\text{SO}_4)_2(\text{H}_6\text{htp})(\text{H}_2\text{O})_4]\cdot 2\text{H}_2\text{O}$ (10)</i>	108
5.4.2 – <i>Physicochemical Characterization</i>	110
5.5 – Structural Transformations Studies	113
5.5.1 – <i>SC-SC of 9 into 10 by pH change</i>	113
5.5.2 – <i>SC-SC of 10 into 10_{dry} by dehydration</i>	113
5.6 – Concluding Remarks	116

Chapter 6 -Materials and Methods.....	117
6.1 – General Structural Characterization	117
6.2 – Reagents	117
6.3 – Routine Powder X-ray Diffraction	118
6.4 – Variable-Temperature Powder X-ray Diffraction	118
6.5 – Single-Crystal X-ray Diffraction Studies	118
6.6 – Catalysis	119
6.7 – Proton conduction.....	120
6.8 – One-Dimensional Lanthanide-organic Coordination Polymer with Catalytic Activity (Chapter 2).....	120
6.8.1 – Microwave-Assisted Synthesis (1mw)	120
6.8.2 – Hydrothermal Synthesis (1h).....	121
6.8.3 – One-pot synthesis (1op).....	121
6.8.4 – Transformation Tests.....	122
6.9 – Lamellar Coordination Polymer with a Remarkable Catalytic Activity and Proton Conductivity (Chapter 3)	122
6.9.1 – Hydrothermal synthesis of $[Gd(H_4nmp)(H_2O)_2]Cl \cdot 2H_2O$ (2ht)	122
6.9.2 – Microwave-assisted synthesis of $[Gd(H_4nmp)(H_2O)_2]Cl \cdot 2H_2O$ (2mw)	123
6.9.3 – One-Pot synthesis $[Gd(H_4nmp)(H_2O)_2]Cl \cdot 2H_2O$ (2op)	123
6.9.4 – Hydrothermal synthesis of $[Gd_2(H_3nmp)_2] \cdot xH_2O$ (3ht).....	123
6.9.5 – Microwave-assisted synthesis of $[Gd_2(H_3nmp)_2] \cdot xH_2O$ (3mw).....	124
6.9.6 – One-Pot synthesis of $[Gd_2(H_3nmp)_2] \cdot xH_2O$ (3op)	124
6.10 – Dynamic Breathing effect in Metal-Organic Frameworks: Reversible 2D-3D-2D-3D Single-Crystal to Single-Crystal Transformation (chapter 4).....	125
6.10.1 – Microwave-Assisted Synthesis of $[Ln_2(H_4nmp)_2(H_2O)_3(SO_4)] \cdot 8H_2O$ (4)	125
6.10.2 – Isolation of $[Ln_2(H_4nmp)_2(H_2O)_3(SO_4)] \cdot 6H_2O$ (5), $[Ln_2(H_4nmp)_2(H_2O)_3(SO_4)] \cdot 2H_2O$ (6) and $[Ln_2(H_4nmp)_2(H_2O)_2(SO_4)] \cdot H_2O$ (7)	125
6.11 – Large 3D Networks Based on Highly Flexible Tetraphosphonic acid Organic Linker (Chapter 5)	126
6.11.1 – Microwave-Assisted Synthesis of $[Eu_2(SO_4)_2(H_6htp)(H_2O)_4] \cdot 10H_2O$ (8)....	126
6.11.2 – Microwave-Assisted Synthesis of $[La_2(SO_4)_2(H_6htp)(H_2O)_6] \cdot 6H_2O$ (9)	126
6.11.3 – Hydrothermal Synthesis of $[La_2(SO_4)_2(H_6htp)(H_2O)_4] \cdot 2H_2O$ (10).....	127
Chapter 7 - Concluding Remarks	129
Bibliography.....	133

Publications

Within the scope of this doctoral thesis, the following articles were published in international journals with referees:

- **“Transforming metal–organic frameworks into functional materials” (Review)**

Ricardo F. Mendes and Filipe A. Almeida Paz

Inorganic Chemical Frontiers, 2015, Volume 2, pages 495-509

- **“Sustainable Synthesis of a Catalytic Active One-Dimensional Lanthanide–Organic Coordination Polymer”**

Ricardo F. Mendes, Patrícia Silva, Margarida M. Antunes, Anabela A. Valente and Filipe A. Almeida Paz

Chemical Communications, 2015, Volume 51, pages 10807-10810

- **Lamellar Coordination Polymer with a Remarkable Catalytic Activity**

Ricardo F. Mendes, Margarida M. Antunes, Patrícia Silva, Paula Barbosa, Filipe Figueiredo, Anthony Linden, João Rocha, Anabela A. Valente and Filipe A. Almeida Paz

Chemistry – A European Journal, 2016, Volume 22, 13136-13146

- **“Dynamic Breathing effect in Metal-Organic Frameworks: Reversible 2D-3D-2D-3D Single-Crystal to Single-Crystal Transformation”**

Ricardo F. Mendes and Filipe A. Almeida Paz

Inorganica Chimica Acta, 2016, Volume 460, 99-107

- **“Photoluminescent Metal-Organic Framework based on Highly Flexible Tetrapodal Organic Linker”**

Ricardo F. Mendes, Duarte Ananias, Luís D. Carlos, João Rocha and Filipe A. Almeida Paz

Crystal Growth and Design, 2017, Accepted

- **“Enhancing Proton Conductivity by Single-Crystal to Single-Crystal Transformation”**

Ricardo F. Mendes, Paula Barbosa, Patrícia Silva, Filipe Figueiredo and Filipe A. Almeida Paz

Advanced Functional Materials, 2017, Submitted

- **“Breathing effect in Lanthanide-Organic Frameworks based on a Highly Flexible Linker”**

Ricardo F. Mendes and Filipe A. Almeida Paz

Crystal Growth and Design, 2017, in Preparation

List of Abbreviations

bpy – bipyridine

BTC – 1,3,5 – benzenetricarboxylic acid

BTB – 1,3,5-tris(4-carboxylatophenyl)benzene

CN – Coordination Number

CP – Coordination Polymer

CPM – Crystalline Porous Materials

EDS – Energy-dispersive X-ray spectroscopy

Et – Etoxy

H₄pmd – 1,4-phenylenebis(methylene)diphosphonic acid

H₆bmt – (benzene-1,3,5-triyltri(methylene))triphosphonic acid

H₈htp – Hexamethylenediamine-*N,N,N',N'*-tetrakis(methylphosphonic acid)

Hex – Hexyloxy

HPDEC - Proton High-Power Decoupling

IRMOF – Isorecticular Metal-Organic Framework

Me – Metoxy

MIL – Materials Institute Lavoisier

MOF – Metal-Organic Framework

PBU – Primary Building Block

POM – Polyoxometalate

Pr – Propoxy

SBU – Secondary Building Block

SEM - Scanning Electron Microscopy

CHAPTER 1

Supramolecular Chemistry: The Case of Coordination

Polymers and Metal-Organic Framework

The area of materials science is an interdisciplinary field focused on the preparation and design of new materials. Understanding how the conditions used can influence the final product properties and performance from a chemical, physical and engineering point of view is of utmost importance. The field goes beyond the molecular synthesis, entering in the realm of the supermolecules. The term supramolecular chemistry is defined to be the study of these supermolecules, entities greater than the individual molecules. The term flourished after being introduced by Jean-Marie Lehn, who received the Nobel Prize in Chemistry together with Donald Cram and Charles Pedersen for their work in the synthesis of cryptands and crown ethers.[1, 2] Contrary to molecular chemistry, supramolecular chemistry aims to develop new complex and functional materials through the assembly of their component beyond the covalent bond, by using other intermolecular interactions, namely, hydrogen bonding, metal coordination, π - π interaction, among others.[3] The supramolecular chemistry can be divided into three categories: i) the chemistry of molecular recognition, being the most fundamental type of supramolecular chemistry; ii) chemistry of supermolecules composed of a small number of molecules built to specific shapes; and iii) the chemistry of molecular assembly by a large number of molecules. The work developed in my PhD and presented therein will be focused on the latter type of supramolecular chemistry, more specifically Coordination Polymers and Metal-Organic Frameworks.

1.1 – Coordination Polymers and Metal-Organic Frameworks: Origin and Terminology

Coordination Polymers (CP) and Metal-Organic Frameworks (MOF) are a class of materials with great importance in the area of material science, evident by the number of compounds and reports in the area. In fact, the Cambridge Crystallographic Data Center (CCDC) estimates that, up to May of 2015, the number of CP/MOF structures correspond to almost 7% of the Cambridge Structural Database, with a total of 54,341 structures reported.[4] CPs and MOFs are coordination networks constructed by the self-assembly of metal ions (from alkali to transition metals and lanthanides) with a myriad of organic linkers (with carboxylic, phosphonic or even sulfonic acid groups), through strong covalent bonds and intermolecular interactions. These coordination networks had initially attracted large attention as post-zeolite materials, mainly due to their greater advantages: i) while

zeolites need an organic or inorganic template to be prepared, CPs/MOFs only need a solvent; ii) the choice of metal center is far more diversified than in zeolites, which only a few cations, such as Si, Al and P can be used and iii) different materials can be synthesized using the same building blocks in case of CPs/MOFs, only by changing the experimental conditions.[5, 6] Although the initial investigations into these materials were based on the know-how obtained by the zeolite chemistry, their synthesis brought one more important advantage: the possibility of pore design. By selecting different organic linkers one could virtually construct materials with different shapes, sizes and chemical environment (*e.g.* by ligand functionalization). Not only that but their higher flexibility, when compared to zeolites, allowed structural modification by guest exchange or chemical reaction without loss of crystallinity. These processes could then be followed by X-ray diffraction analysis.[7]

For the last two decades various solids have been described that contained metal ions linked by molecular species. The terms for these materials are quite vast, from organic zeolite, organic-inorganic hybrid, coordination polymer (CP) to metal organic framework (MOF). Actually, the term “metal organic framework” is quite recent when compared to coordination polymers. It was first introduced in 1995 by Omar Yaghi and Hailian Li when they reported a 2D interpenetrated metal-organic open framework with large rectangular channels, $[\text{Cu}(\text{4,4'}\text{-bpy})_{1.5}]\cdot\text{NO}_3\cdot 1.25\text{H}_2\text{O}$, from the reaction of $\text{Cu}(\text{NO}_3)_2\cdot 2.5\text{H}_2\text{O}$, 4,4'-bipyridil and 1,3,5-triazine (Figure 1.1) at 140 °C.[8] For that reason, the number of articles reporting these types of materials may be greater, since some authors still use the coordination polymer terminology. As an example, in 1965 Tomic reported the synthesis of several materials by self-assembly of 1,5-dihydroxynaphtalene-2,6-dicarboxylic acid with different transition metals (Zn^{3+} , Ni^{3+} , Al^{3+} , and Fe^{3+}) which nowadays could be called as MOFs.[9] Nevertheless, the synthesis of these coordination materials (both MOFs and CPs) have become of greater interest, as evident by the increase of publication over the last decades (Figure 1.2), even surpassing their predecessors, the zeolites.

Although some authors did not differentiate these two terms,[10, 11] suggesting that coordination polymer and metal-organic framework are synonyms, others authors suggested definitions based on the chemical bonding.[12] Since there was no consensus in the scientific literature about the definitions of the terms, an IUPAC project was initiated in 2009 to address the terminology issues,[13] resulting in the following definitions:

i) Coordination Polymer: “A coordination compound with repeating coordination entities extending in 1, 2, or 3 dimensions”

ii) Coordination network: “A coordination compound extending, through repeating coordination entities, in 1 dimension, but with cross-links between two or more individual chains, loops, or spiro-links, or a coordination compound extending through repeating coordination entities in 2 or 3 dimensions”

iii) Metal-Organic Framework: “A metal–organic framework, abbreviated to MOF, is a coordination network with organic ligands containing potential voids”

These definitions can still be somehow ambiguous, especially due to the high number and variety of structures of these materials. For this reason, and for the sake of clarity, in this thesis Coordination Polymers will refer to compounds with 1 and 2 dimensions, while the term Metal-Organic Framework will be used for structures exhibiting a 3 dimensional network, without emphasis on the porosity.

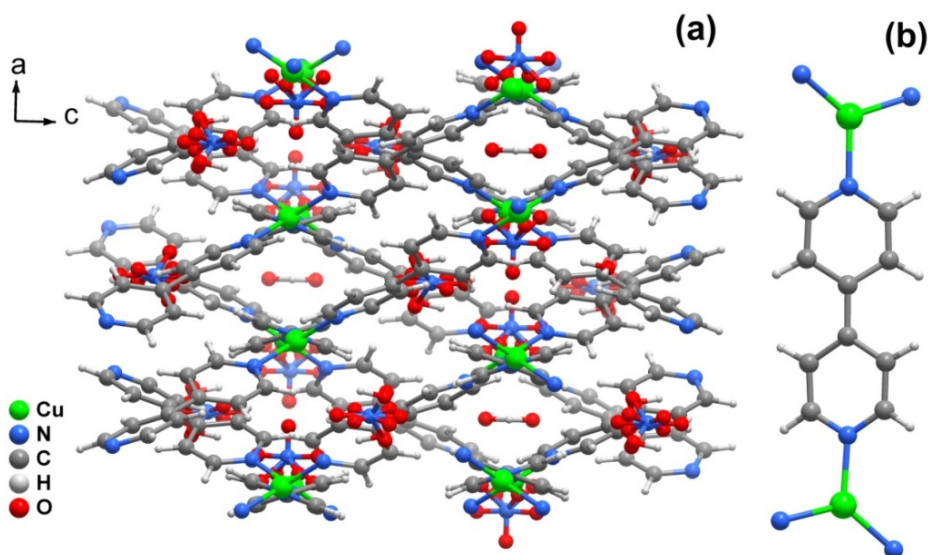


Figure 1.1 – (a) Crystal packing and (b) metal and organic linker coordination environment of the first material with the term MOF, [Cu(4,4'-bpy)_{1.5}](NO₃)(H₂O)_{1.25}, reported in 1995 by Yaghi and Li.[8]

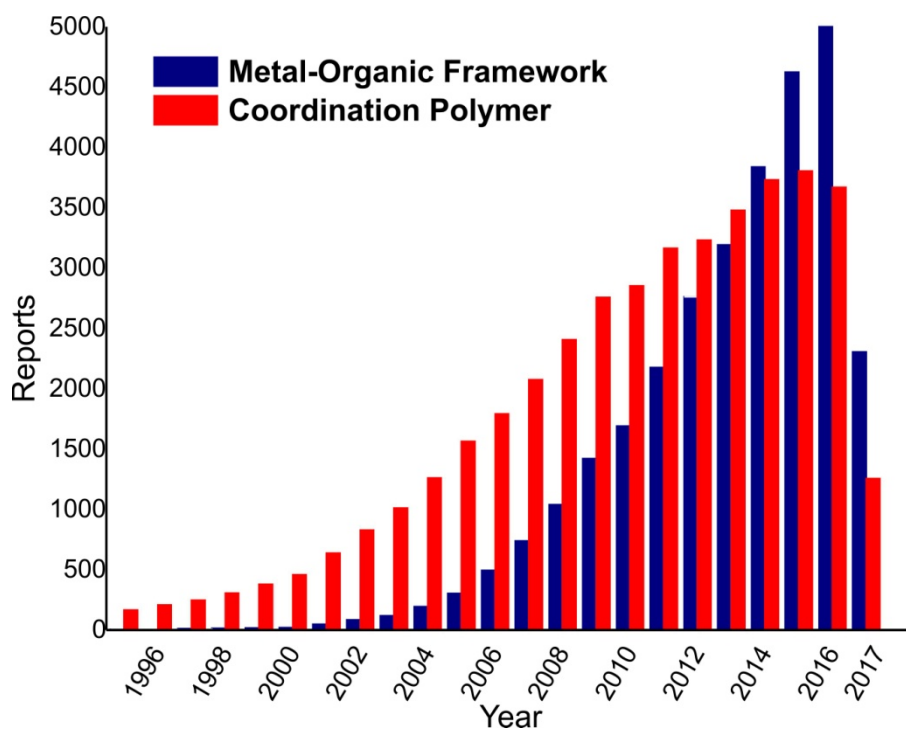


Figure 1.2 – Number of reports on Coordination Polymers (in red) and Metal-Organic Frameworks (in blue) by year of publication in the time between 1995 and 2016. Source: ISI Web of Knowledge [14]. Search Topics: Coordination Polymer and Metal-Organic Framework. Consulted on 30th May 2017.

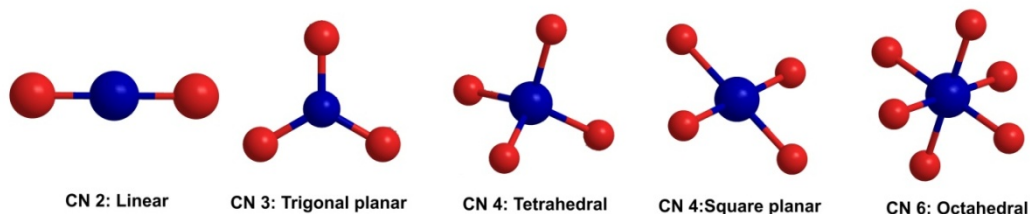
1.2 – Building Blocks in CPs and MOFs Preparation

CPs and MOFs have a wide interest in all quadrants of academic research and, in more recent years, with more direct applications in different industries.[15-17] They are a class of crystalline inorganic-organic hybrid materials comprised by an organic ligand (organic component) connected to a metal ion (inorganic component). These compounds are in general easy to prepare: starting from naked metal centers (often in solution), or clusters of metals, and appropriate organic molecules bearing coordinating groups in strategically located positions (the so-called Primary Building Units - PBUs), polymeric crystalline compounds can ultimately be isolated. The final morphology, dimensionality, shape and structure depend greatly on these PBUs. The worldwide remarkable interest in CPs/MOFs remains driven by a number of basic aspects: firstly, there are endless combinations of PBUs, with new compounds being reported on a daily basis; secondly, a close control and design of the employed PBUs (and even of the synthetic conditions), can lead to new remarkable topologies materials with the desired properties and architectures;[18] thirdly, the symbiotic presence in the same network of organic and inorganic components promotes the presence of unusual chemical or physical properties.[19] Therefore it is not much surprising that these materials can be targeted to a myriad of applications in different areas such as storage of gases,[20] catalysis,[21-23] photoluminescence[24-26] as drug delivery agents,[27, 28] thin films and membranes fabrication,[29] among many others.

Regarding the metal centers, their size, hardness/softness, and coordination geometry have an important role. Almost all types of metal can be introduced in CPs/MOFs, from alkali/alkaline-earth metals (Cs, K, Ba, or Sr^{2+})[30-33] to transition metals (Zn, Cd, Ni, Cu or Fe)[34-38] and even lanthanides (La, Pr, Ce, Sm, Tb, Eu).[39-45] Transition metals are the most commonly used. Depending on the metal, they can have different coordination numbers, varying from 2 to 6, originating different coordination geometries (Figure 1.3, *top*) and, therefore, different structures. Lanthanide ions are less used because of the unpredictability behavior of these metals with simple donor ligands due to the higher flexibility of their coordination environments. Their coordination numbers can vary from 7 to 11 (Figure 1.3, *bottom*), originating some original topologies with particular applications.[46] The high number of coordination of the lanthanides can affect the dimensionality of the final material, more specifically the type of coordination of the organic linker to the metal center. Our research group have reported the preparation of two new materials based on 1,4-phenylenebis(methylene)diphosphonic acid (H_4pmd) and lanthanum, $[\text{La}_2(\text{H}_2\text{pmd})_3(\text{H}_2\text{O})_{12}]$ and $[\text{La}_2(\text{H}_2\text{pmd})(\text{pmd})(\text{H}_2\text{O})_2]$, exhibiting a 1D and 3D dimensionality, respectively.[47] While in the first case the La^{3+} center is coordinated to three oxygen from three different phosphonic acid groups and six water molecules (total number of coordination of 9), in the second case the metal center is coordinated to seven oxygen from five phosphonic acid residues and a water molecule (total number of coordination of 8). In $[\text{La}_2(\text{H}_2\text{pmd})_3(\text{H}_2\text{O})_{12}]$ the phosphonic groups coordinate to the La^{3+} center by simple $\kappa^1\text{-O}$ mode of coordination, and only in one direction of the unit cell,

forming 1D chain material, while in $[\text{La}_2(\text{H}_2\text{pmd})(\text{pmd})(\text{H}_2\text{O})_2]$ the phosphonic acid groups coordinate to the metal center in a $\kappa^2\text{-O}$ and $\mu^2\text{-O,O}$ modes, that extends in every direction of the unit cell, forming a compact 3D network.

Transition Metal



Lanthanides

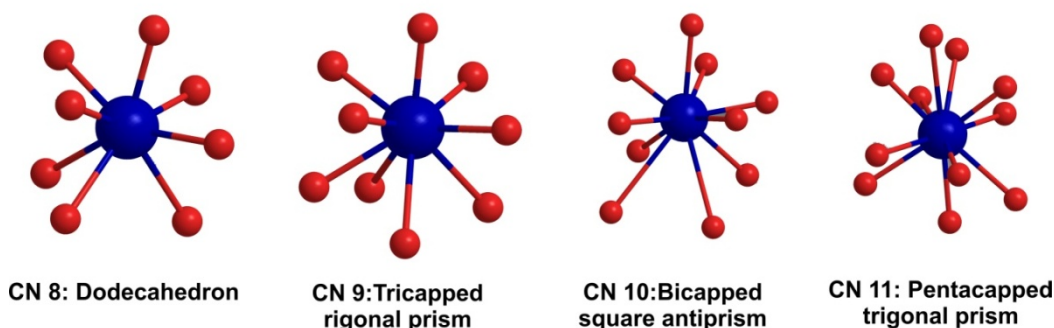


Figure 1.3 – Schematic representation of the possible coordination number (CN) and geometry of transition metals and lanthanides present in Metal-Organic Frameworks and Coordination Polymers.

Metal centers in CPs and MOFs seem to have also great influence in the morphology and crystallite size. Yamada and Yonekura synthesized a series of cyano bridged lanthanide MOFs by a simple one-pot reaction.[48] The resulting MOF nanoparticles showed decreasing size with decrease in metal radius and the crystal morphology was also different: hexagons with the larger metals (La to Nd) and stars for the smaller metals (Sm to Lu). We have also noted this trend in our research group when the hydrothermal reaction of (benzene-1,3,5-triyltris(methylene))triphosphonic acid with a series of lanthanides (Eu, Tb, Dy, Ho, Er, Tm, and Yb)[49] originated crystals with several micrometers for the metals with higher radius (Eu) and crystals in the nanometric scale for the smaller ones (Yb).

The other component in the preparation of CPs/MOFs, the organic ligand, plays also an important role, if not the most important, in the final structure and morphology of these materials. The organic ligands act as bridging linkers between metal ions. These ligands have to be multidentate with at least two donor atoms, mostly N-donor and O-donor, with the most common being ligands with functional groups as carboxylates and phosphonates, pyridyls and molecules with cyano groups. Since lanthanides usually coordinate poorly with molecules with cyano and amino groups and due to the higher number of reports in CPs/MOFs based on molecules with carboxylic and phosphonic acid

groups, a closer focus will be presented on the latter. The most common organic molecules used in these materials are presented in Figure 1.4 and 1.5..

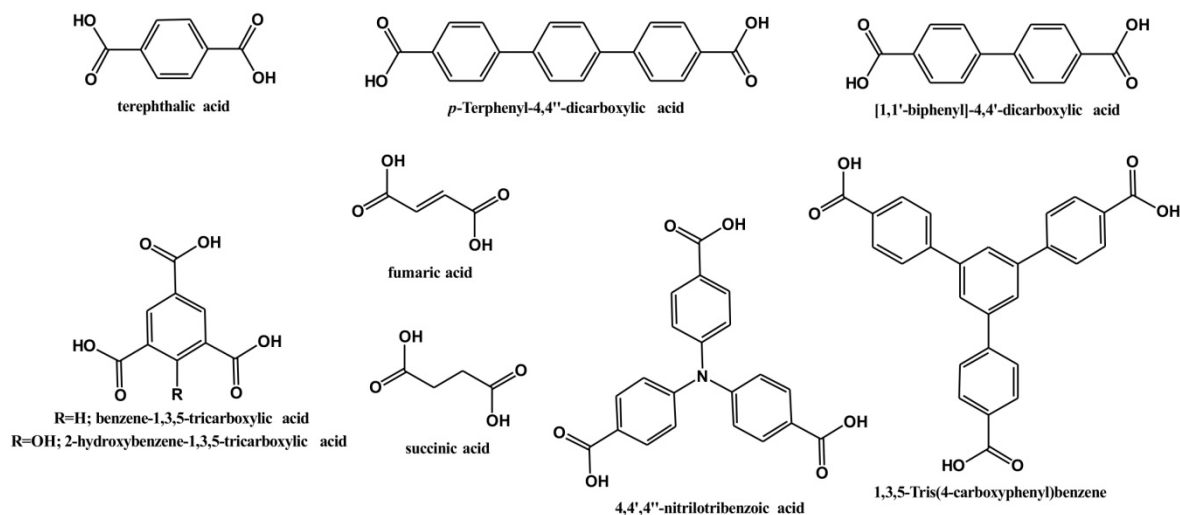


Figure 1.4 – Examples of carboxylic acids organic molecules used in the preparation of MOFs and CPs.[47, 50-58]

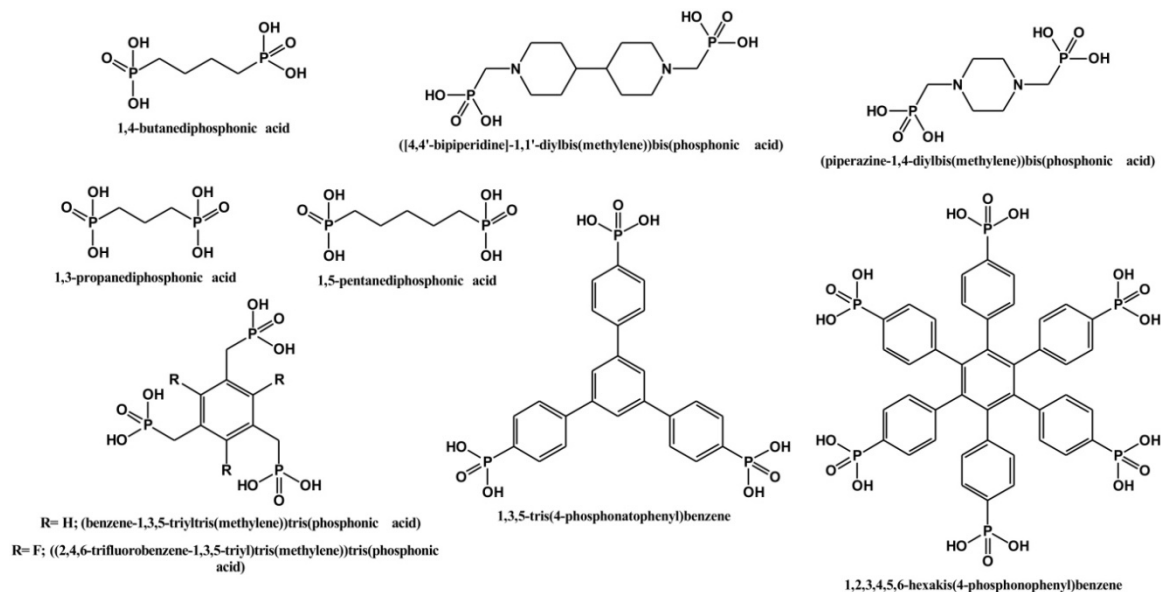


Figure 1.5 – Examples of phosphonic acids organic molecules used in the preparation of MOFs and CPs.[59-65]

The introduction of the organic component in these materials, in comparison to zeolites, gave the chemist the necessary tools to design them for specific applications. However, one of the drawbacks of CPs and MOFs when compared to the existing zeolites is the smaller thermal stability. The organic component in these materials is not stable at high temperatures, which is evident by their decomposition temperatures (in the range of

300-400 °C). This feature is very important, especially for porous materials, which need high stability at high temperatures for introduction and removal of guest molecules (*e.g.* gas sorption) while maintaining the structural crystallinity and integrity during this process.

The choice of the PBUs is thus crucial to obtain a material with the expected characteristic. CPs and MOFs were found to have higher thermal stability with organic linkers that have an aromatic part rather than aliphatic and with functional groups capable of forming chelates with the metal center, exhibiting higher thermodynamic stability.[9] The functionalization of the organic molecules can also improve their stability. Makal and co-workers have reported an increase in thermal and moisture stability by different functionalization of the organic linker.[66] In their work the [1,1':4',1'']Terphenyl-3,3'',5,5''-tetracarboxylic acid (H₄TPTC) was functionalized with either two methoxy, ethoxy, propoxy or hexyloxy groups (Figure 1.6) and reacted with copper nitrate, resulting in a series of isostructural (chemical compounds with similar chemical structures) MOFs. The thermal and moisture stability showed to increase with the increase of alkali chain number.

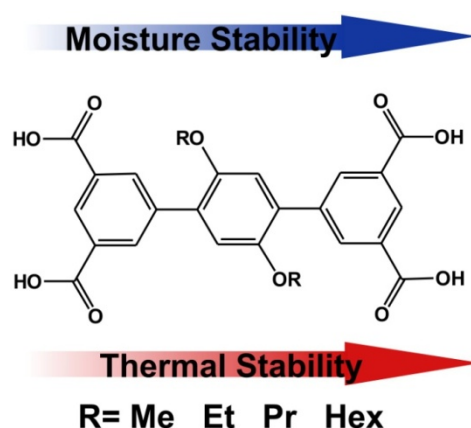


Figure 1.6 – Schematic representation of TPTC-OR (2',5'-di{alkyl}oxy-[1,1':4',1'']-terphenyl)-3,3'',5,5''-tetracarboxylate, R = Me, Et, Pr, Hex). The figure emphasizes the increase of moisture and thermal stability with the increase of alkali chain. Adapted from reference [66]

The ability to obtain this type of materials with virtually any organic linker gave birth to a series of MOFs exhibiting ultrahigh porosity by employing the isorecticular synthesis. The isorecticular principle allows the fine control of the pore size and nature in a structure without changing the underlying topology. In 1999 Yaghi and O'Keeffe's group synthesized the first highly porous MOF, MOF-5 [(Zn₄O(BDC)₃), where BDC = 1,4-benzenedicarboxylic acid, also known as IRMOF-1], leading to a major advance in the chemistry of porous MOFs.[67] MOF-5 comprises of Zn₄O(CO₂)₆ blocks (called secondary building blocks – SBU) connected to each other by six chelating BDC²⁻ units, giving rise to a cubic 3D framework (Figure 1.7). The framework was stable and remains its crystallinity even when fully desolvated and with temperatures up to 300 °C. The large cavity in MOF-5 (with 18.4 Å in sphere diameter) allowed for gas sorption measurements,

which showed a surface area of 2320 m²/g and vapor sorption of Ar, CH₂Cl₂, CHCl₃ and CCl₄, with values between 1.211 mg/g (for CH₂Cl₂) and 1.492 mg/g (for Ar).

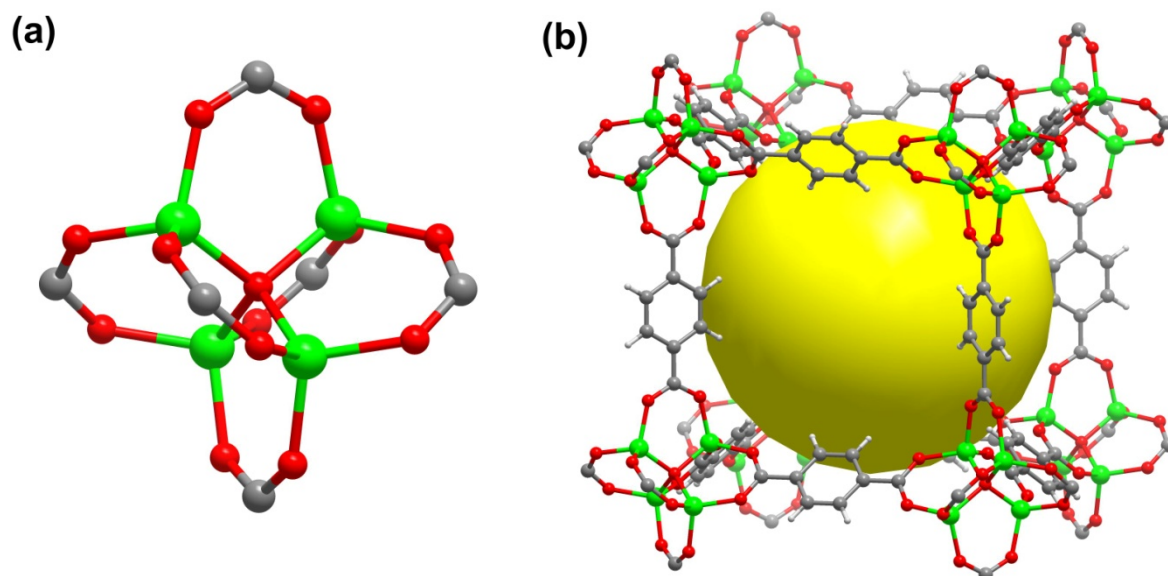


Figure 1.7 – Representation of the (a) Zn₄O(CO₂)₆ cluster SBU and (b) crystal packing of MOF-5. The large cavity present is indicated by the large yellow sphere with 18.4 Å of diameter. [67]

By maintaining the same SBU (Zn₄O(CO₂)₆) and by changing either the length or the chemical features of the ditopic organic linker Yaghi and co-workers were able to synthesize a series of 11 new materials, known as IRMOF-n (n= 1 to 16) with the same 3D cubic topology.[51] As expected, the free volume of these materials varies with the type and length of the organic linker, ranging from 55.8% for IRMOF-5 up to 91.1% for IRMOF-16. While the free volume is similar from IRMOF-1 to 7, due to the similarity in organic linker (Figure 1.8), the increase of the length in organic linker increases the free volume from 78.4% in IRMOF-1, 87% for IRMOF-10 to 91.1% for IRMOF-16. The most remarkable is that the lowest percentage of free volume for IRMOF-1 surpasses the ones found in some of the open zeolites.

Following the excellent results obtained with the IRMOF series, Yaghi obtained another series of porous materials using the same SBU but connecting to a tripodic linker instead.[68] MOF-177, MOF-180 and MOF-200 (Figure 1.9) have exceptional surface area, arising mainly by the presence of large pores, where the gas can be stored inside, rather than only at surface. In fact, MOF-200 detains the record for surface area of around 10400 m²/g.

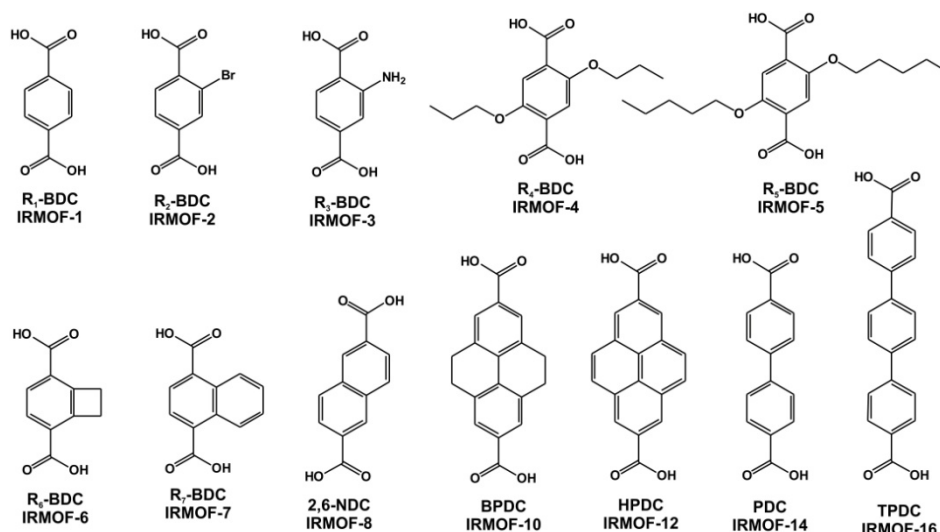


Figure 1.8 – Organic linkers used in the preparation of the isorecticular IRMOF-1 to 16. R₁-BDC: terephthalic acid; R₂-BDC: 2-bromoterephthalic acid; R₃-BDC: 2-aminoterephthalic acid; R₄-BDC: 2,5-dipropoxyterephthalic acid; R₅-BDC: 2,5-bis(pentyloxy)terephthalic acid; R₆-BDC: bicyclo[4.2.0]octa-1(6),2,4-triene-2,5-dicarboxylic acid; R₇-BDC: naphthalene-1,4-dicarboxylic acid; 2,6-NDC: naphthalene-2,6-dicarboxylic acid; BPDC: 4,5,9,10-tetrahydropyrene-2,7-dicarboxylic acid; HPDC: pyrene-2,7-dicarboxylic acid; PDC: [1,1'-biphenyl]-4,4'-dicarboxylic acid; TPDC: [1,1':4',1''-terphenyl]-4,4'-dicarboxylic acid. [51]

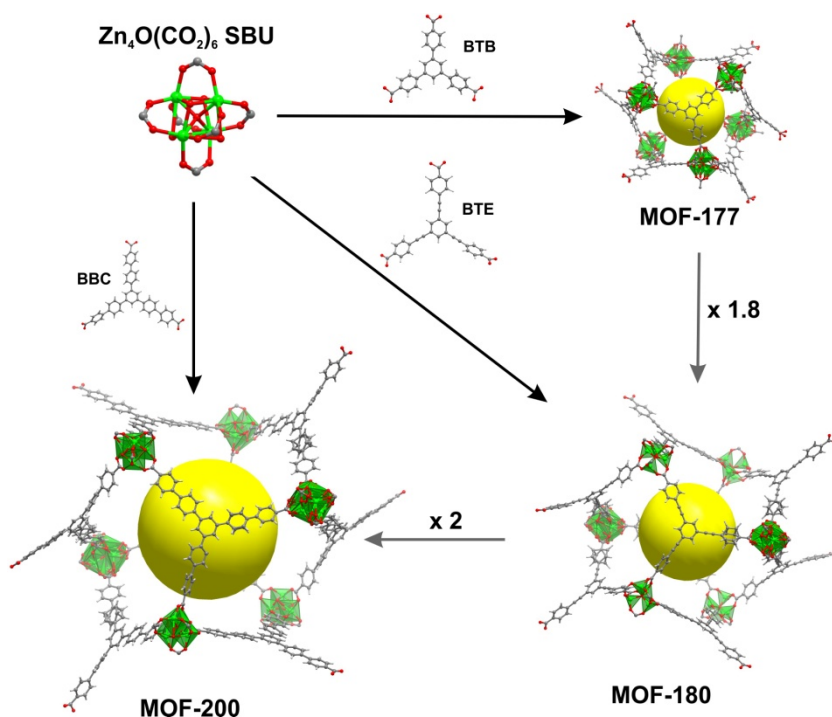


Figure 1.9 – Isorecticular expansion of a MOF exhibiting the same topology but with increase cavity size. The yellow sphere represents the largest sphere that would occupy the cavity. Legend: green-Zn; red-oxygen, dark gray-carbon; light gray-hydrogen. BTB stands for 4,4',4''-benzene-1,3,5-triyl-tribenzoate, BBC stands for 4,4',4''-(benzene-1,3,5-triyl-tris(benzene-4,1-diyl))tribenzoate and BTE stands for 4,4',4''-(benzene-1,3,5-triyl-tris(ethyne-2,1-diyl))tribenzoate. [68]

The pores of MOFs have sizes large enough to accommodate small molecules, but are rarely of sufficient sizes to incorporate larger molecules such as proteins. The isorecticular chemistry usually leads to the formation of interpenetrated structures by simple increase in organic linker length, with compact and smaller pore sizes. For this reason MOFs should be constructed exhibiting topologies that do not allow interpenetration.[69] This strategy was implemented by Hexiang Deng, working in Yaghi's group, by expanding the phenylene unit of IRMOF-74-II to 3, 4, 5, 6, 7, 9 and 11 phenylene rings (DH2PhDC to DH11PhDC, Figure 1.10).[70] This resulted in an increase of the tubular shaped sizes from 10x14 Å for IRMOF-74-II to 85x98 Å for IRMOF-74-XI. The pore size of the latter is of enough size to allow large molecules to pass into the pores without unfolding, as is for the case of the green fluorescent protein. The higher pore sizes are beneficial for surface modifications without sacrificing porosity. As an example, the oligoethylene glycol-functionalized IRMOF-74-VII allows the inclusion of myoglobin with no loss of crystallinity, while the original MOF shows negligible amount of inclusion.

The choice of both components in the preparation of MOFs and CPs is, therefore, of utmost importance. The type of connection between metal centers and organic linkers, all the way to the properties of the linker itself is vital to obtain materials for the desire application. However, these two components are not the sole variables in the equation: experimental conditions have also important influence in the final material, as presented in the next section.

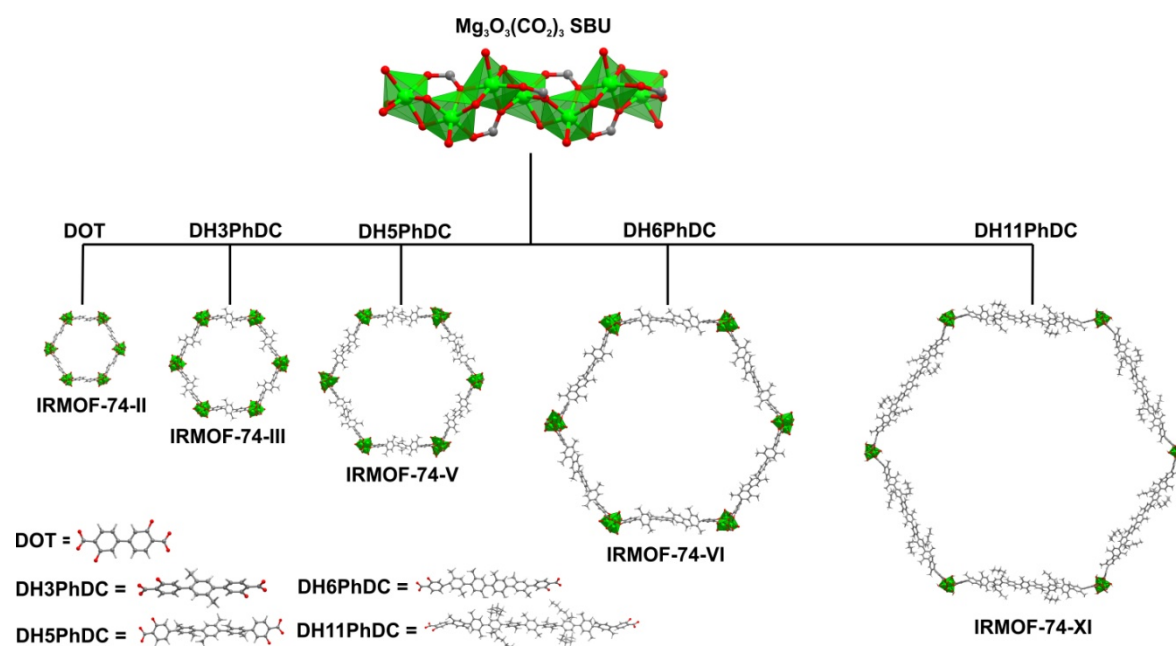


Figure 1.10 – Isorecticular expansion of a MOF exhibiting the same topology but with increase of ligand size, using the same SBU. Legend: green-Mg; red-oxygen; dark gray-carbon; light gray-hydrogen. [70]

1.3 – Synthetic Methodologies in the preparation of CPs/MOFs

CPs and MOFs have initially been synthesized from the self-assembly of metal ions and organic ligands under hydro(solvo)thermal conditions. This technique was adapted by the synthesis of zeolites and because the need to obtain crystals with considerable size was important due to the limitation of the single-crystal instruments of the time. With the improvement of technology, this limitation decreased over time and new synthetic techniques were implemented in their preparation. Depending on the final objective, MOF can be obtained by several different experimental apparatus, depending on the desired size of crystals, morphology, and time of reaction. While the experimentation and the trial-and-error approach are still in use in the preparation of these materials, many systematic and facile synthetic routes have been investigated and reported, such as microwave-assisted synthesis, electrochemical synthesis, and synthesis by ultrasound or microemulsion, or even by mechanochemical synthesis. In this section, the more used techniques in the preparation of MOF/CP will be discussed in more detail.

Solvent evaporation: in this method the starting reagents are dissolved in the solvent and the slow evaporation of the solvents or their diffusion over time creates large single crystals in small quantities over large periods of time, between weeks to months. The rate of crystal growth can be controlled by changing the temperature or by using thermal gradients, and by slow cooling, where the temperature is decreased at a rate ideal to the slow precipitation, favoring the crystal growth over the nucleation process. These techniques were used in most cases for the preparation of large crystal in a time where the limitations of the single-crystal diffractometer were higher.[67, 71-73]

Diffusion methods: this method is based on the contact between the two different species. It can be achieved by two approaches: solvent liquid diffusion and slow diffusion of reactants. In the first case the reaction products are dissolved in an adequate solvent and joined with a precipitant solvent, forming two layers with different densities. The precipitant solvent slowly diffuses into the separate layer and crystal growth occurs at the interface. In the other approach, the reactants are dissolved in different solvents, and are separated by physical barriers, such as two vials with different sizes or with the introduction of a gel. The reactants are then mixed through slow diffusion (Figure 1.11).[10, 74]

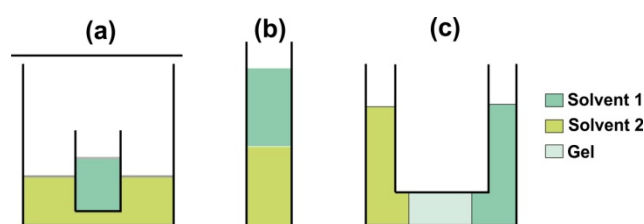


Figure 1.11 – Schematic representation of different diffusion methods: (a) vapor diffusion; (b) liquid diffusion and (c) growth from gels.

Hydro(solvo)thermal method: this method is adapted by the synthesis of zeolites and it the most commonly used methodology in the preparation of CPs and MOFs. It consists in the self-assembly of products from precursors, at temperatures comprised between 80-260 °C inside a pressurized closed vessel, normally designated autoclave (Figure 1.12). At these conditions the reduced viscosity of water or solvent enhances the diffusion process and thus favors the extraction and crystal growth from solution. Another advantage is the possibility to overcome the solubility problem of large organic molecules, while being able to produce and isolate single crystals at reduced reaction times (up to several days), when compared to the previous two techniques. However continues to be a highly time and energy consuming technique. Solvents most commonly used for CPs and MOFs preparation are water and dimethylformamide, but virtually any solvent can be used, as long as one takes in consideration their boiling point and the capacity to dissolve the starting reagents. The first reported MOF synthesized by Yaghi was obtained in hydrothermal conditions,[8, 67] as well as the well known HKUST-1.[75]



Figure 1.12 – Picture of one of the ovens used in the preparation of CPs and MOFs. (*inset*) picture of the Teflon reactor and autoclave.

Microwave-assisted method: this method provides an efficient way to synthesize purely inorganic porous materials with short crystallization time, narrow particle size distribution, facile morphology control, phase selectivity and efficient evaluation of process parameters, as well as being widely established in the synthesis of organic molecules.[76] The reagents are dissolved in the solvent inside a glass or Teflon vial and placed under a oscillating electric field, leading to a rapid heating of the reaction mixture (Figure 1.13). The main advantage of this method is its energy efficiency because power is only applied within the reactive mixture.[77] In the CP/MOF field microwave-assisted methodology was first used in the preparation of chromium trimesate, $[\text{Cr}_3(\text{F}(\text{H}_2\text{O})_3\text{O}(\text{BTC})_2] \cdot 28\text{H}_2\text{O}$ (MIL-100, where BTC stands for 1,3,5-benzene tricarboxylic acid).[78] The use of microwave allowed the preparation of MIL-100 after only 4 hour of reaction time, while the same reaction under hydrothermal conditions needed 96 hour to obtain the same material.[79] Because the reaction time is decrease

significantly, the main disadvantage is the reduced crystalline size. This limits the use of this technique to obtain crystals suitable for single-crystal X-ray diffraction analysis. On the other hand the CP/MOF properties might be enhanced, as showed by Sabouni et al.[80] While the preparation of CPM-5 (crystalline porous material based on indium and BTC) under hydrothermal conditions requires several days for crystallization, using microwave synthesis decreased the reaction time to only 10 minutes. Due to the decrease of the particle size, different surface areas were obtained: only 580 m²/g for the first case and 2187 m²/g for the second. The material obtained by microwave-assisted method showed also a high carbon dioxide uptake.

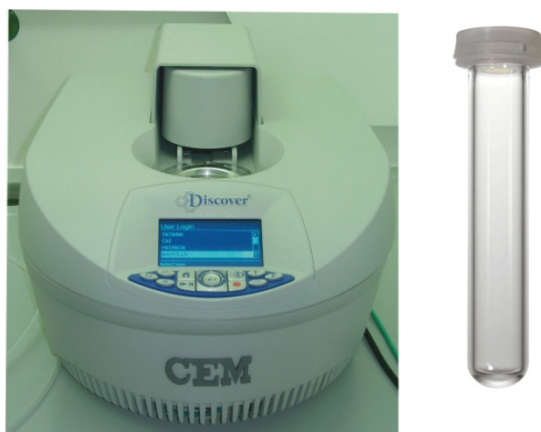


Figure 1.13 – Picture of the microwave instrument and the respective glass vial.

Ultrasound/sonochemical method: this method consists in the mixture and reaction of the reagents with the aid of ultrasonic irradiation (between 20 kHz and 10 MHz). The ultrasonic irradiation generates small bubbles in the solvent with high temperature (up to 5000 K) and pressure (up to 500 atm) in a span of a few microseconds. This method allows the preparation of small crystals with small reaction times. The same way as for microwave-assisted method, this technique can be used not only to decrease the reaction time, but also to improve properties and to obtain materials with different morphologies. [81] Although ultrasound techniques are not used very often, mainly because of the possibility to break some chemical species in the presence of ultrasonic waves, it is most commonly used for the preparation of nanosized MOFs and CPs.[82]

One-pot method: known as the “shake and bake” approach, the one-pot is a simple method based on the mixture of the starting reagents at ambient pressure. It has the possibility for scale up approach, since it has no limitation in terms of instrumentation. This method has gained some interest due to its simple preparation, low energy consumption and the possibility to obtain MOFs and CPs at room temperature and with reduced reaction times.[21, 23] On the other hand, when compared to other techniques, the one-pot approach lacks in terms or reproducibility. [47]

Electrochemical method: this synthesis provides a more precise control in the preparation of CP/MOF. The chemical reaction is performed by application of a current and involves the electron transfer between the electrode and the electrolyte. The main advantage of this method is the absence of counter ions, since the metal ion, rather than the metal salt, is used as an anode. This method has shown high efficiency with low temperature and high yields when compared to conventional synthesis. [83] The first MOF synthesized by this method was HKUST-1 by the BASF company, in an attempt to remove the anions for large-scale production. The electrochemical route is, nonetheless, not commonly used for the preparation of these materials, with more direct use in the preparation of thin films.[84]

The structure of the CP or MOF is in direct relation with the type of metal and organic linker used, as discussed previously. However, the experimental conditions used in the preparation of these materials also play an important role. The way that the organic ligand coordinates with the metal and the conformation it takes in the structure is affected by several factors: temperature, pH of the reaction medium, pressure, concentration of the building blocks, metal source and reaction time. Our research group has already reported the effect of temperature and concentration in the preparation of four lanthanide MOFs based on the ditopic phosphonic acid organic ligand 1,4-phenylenebis(methylene)diphosphonic acid (H_4pmd). [47] The one-pot reaction at room temperature originates the 1D $[La_2(H_2pmd)_3(H_2O)_{12}]$ CP while at 40 °C the 3D network $[La_2(H_2pmd)(pmd)(H_2O)_2]$ is obtained preferably. If the temperature is further increased to 80 °C $[La_2(H_2pmd)_3(H_2O)_2]$ or $[La_2(H_2pmd)(pmd)(H_2O)_4]$ are obtained as major components in a mixture with $[La_2(H_2pmd)(pmd)(H_2O)_2]$. Different materials can also be obtained by only changing the concentration of the building blocks. By reacting the metal ion with the ditopic phosphonic acid in a 1:1 ratio at 40 °C the 1D $[La_2(H_2pmd)_3(H_2O)_{12}]$ CP is obtained as pure phase. If the concentrations of both starting materials are cut in half, the 3D network $[La_2(H_2pmd)(pmd)(H_2O)_2]$ is formed instead. The same trend is observed in the reaction at 80 °C: $[La_2(H_2pmd)_3(H_2O)_2]$ is obtained when the reagents are in a 1:1 concentration ratio while $[La_2(H_2pmd)(pmd)(H_2O)_2]$ is formed by increasing the concentration of the organic ligand (to a 1:2 concentration ratio). The temperature dependence was also investigated by Dong and co-workers.[85] In their work a flexible ethylene glycol ether-bridging tetradentate ligand was used in the synthesis of two new materials with $AgSbF_6$. When the reaction was carried at 0 °C, the 3D network was obtained, while the 2D CP is formed at 30 °C. This change in dimensionality is attributed to the conformation adopted by the organic linker: in the 3D material the ligand adopts a *trans*-conformation while in the 2D it adopts a *cis*-conformation.

Besides temperature, the reaction time has one of the most important roles in the preparation of CPs/MOFs. As demonstrated by Ferey *et al.* the hydrothermal synthesis of chromium nitrate and terephthalic acid at 220 °C gives rise to MIL-101 after only 8 hours,[86] while if allowed to react for 3 days, MIL-58 is synthesized instead.[87] The difference in reaction time suggests that MIL-101 is more of a kinetic product, while MIL-58

is a thermodynamic product. The effect of reaction time can be better visualized in the microwave-assisted method, where higher condition screenings are performed. In the synthesis of $[\text{La}(\text{H}_4\text{bmt})(\text{H}_5\text{bmt})(\text{H}_2\text{O})_2] \cdot 3\text{H}_2\text{O}$ and $\text{La}_2(\text{H}_3\text{bmt})_2(\text{H}_2\text{O})_2 \cdot \text{H}_2\text{O}$ (where H_6bmt stands for (benzene-1,3,5-triyltris(methylene))triphosphonic acid), at moderate temperatures (90-100 °C) low reaction time favor the preparation of the first compound, while higher reaction times originates the latter instead.[88] This effect has been reported in other of our research works, in either microwave-assisted or one-pot conditions.[23, 47]

Temperature and reaction times are the two factors which most contribute to obtain different materials using the same starting building blocks. However the remaining factors, such as, pH or even metal source can, in some cases, affect the final product, as reported by Bauer and co-workers in the synthesis of analogues of MOF-5.[89] It is thus important when one is synthesizing a new MOF or CP to do a screening of a several conditions, in order to obtain the best results.

1.3.1 – Scale-up in CPs and MOFs

CPs and MOFs are manifestly of great importance in academic research, evident by the number of materials synthesized up to today and by the variety of potential applications. However, the synthesis of these materials in a larger scale (in industrial terms) is rather neglected. While there are *ca.* 1600 patents regarding MOFs (data from Espacenet database[90]) only some are for scale-up procedures,[91-95] despite the fact that several academic reports have shown the potential application of these materials in a more industrial view.[15, 17] The first successful scale-up was reported by Wang and co-workers. The scale-up was performed on the HKUST-1, allowing the synthesis of 80 g of compound in a single hydrothermal reaction for 18 hours.[96] The following reports of scale-up were performed by Muller's team, which reported the synthesis of MOF-2, MOF-5 and IRMOF-8 with 87, 91 and 92% of yield, respectively. [97]

The great challenge in the scale-up of CPs and MOFs for industrial applications is to obtain materials with: i) low cost and availability of the starting materials; ii) simple synthetic procedures, with low temperature and ambient pressure conditions; iii) high yields and iv) the use of small quantities of solvent. The presence of anions, due to the use of inorganic salts, also pose a challenge in the synthesis control, which led to the development of the electrochemical synthesis discussed in the previous section. Most reported scale-ups do not take these limitations into account, especially in terms of solvent use. Most synthesis use organic solvents, such as chlorobenzene and DMF, for the synthesis of MOF 2, ethanol for HKUST-1 and *N*-methyl-2-pyrrolidone for IRMOF-8. Not only that, but for the case of HKUST-1 scale-up the synthesis of 18 hours at 110 °C showed a product with a specific surface area of only 964 m²/g, a value bellow of the reported ones.

Despite the inherent problems of CP/MOF scale up, BASF company was able to scaled-up the synthesis without the use of organic solvents and has commercialized several MOF materials (Table 1.1), being one of the companies in the vanguard of CP/MOF

synthesis and industrial application. In 2007 they were involved in the project of the German Rainer Zietlow, who traveled for six months a total of 45000 km using a Volkswagen Caddy outfitted with 13 tanks of natural gas. Some of the tanks had natural gas loaded on the PCN-14 MOF, a system that according to the news report “provided with an overall driving range of more than 1500 miles (*ca.* 2400 km) between fill-ups”.[98]

Table 1.1 – List of comercial available MOF produced by the BASF company

Commercial Name	Compound Name	Components	
		Metal	Organic Linker
Basosiv™ M050	Magnesium formate	Mg	Formic acid
Basolite™ Z1200	ZIF-8	Zn	2-methylimidazole
Basolite™ C300	Cu-BTC MOF	Cu	Trimesic acid
Basolite™ A100	MIL-53	Al	Teraphtalic acid
Basolite™ F300	Fe-BTC	Fe	Trimesic acid

1.4 – Application of MOFs/CPs

The area of MOFs and CPs has gained ground, especially when compared to zeolites, due to the ease of preparation and more importantly, the possibility to fine tune their properties. The ability to use a myriad of organic linkers (with different lengths, bond angles or chirality) and metal ions, allow us to synthesized an infinite number of new materials, each one with a specific property. It is, therefore, not surprisingly the number of potential applications that MOFs/CPs can have. In this section some of the most used application will be highlighted:

Sorption/Separation of molecules: as presented in section 1.2, the size and properties of the pores in MOFs can be tailored by the so called isorecticular synthesis. Using the same SBU and by changing the length of the organic linker, one can obtain a series of MOFs which have affinity to different type of molecules. This ability of pore design, allied with the high surface area of MOFs makes them the ideal materials to adsorb different types of molecules. Due to energetic storage demands, hydrogen and methane storage by MOFs are the most studied.[99-102] Nonetheless, MOFs can also be used to remove harmful or toxic gases such as benzene, CO₂ and CO, H₂S, SO₂, NO and NH₃,[103-110] or even heavy metals ions from effluents, such as, As⁵⁺ and Hg²⁺. [6, 111, 112]

Catalysis: the channels in the MOFs or CPs can be tailored in order to design a material with characteristics for use in catalysis. Due to the extreme insolubility of MOFs/CPs in virtually every solvent, these materials are used as heterogeneous catalysts, a greater advantage when compared with the known homogeneous catalysts because of the ease separation and the possibility to recover them after reaction. The key in synthesis of MOFs/CPs for catalysis is the introduction of unsaturated metal centers and uncoordinated functional groups. However, the low chemical, hydrolytic and thermal stability of these

materials lack behind other catalyst used nowadays. Nonetheless, since the first reported catalysis in 1994 by the Cd-based MOF, $[\text{Cd}(\text{BPy})_2(\text{NO}_3)_2]$ (where BPy stands for 4,4'-bipyridine)[113] the reported MOFs and CPs have increased exponentially, being the second most tested application for these materials. Among the catalytic reaction using MOF/CP stands out the oxidation reaction, Knoevenagel and aldol condensation,[114-116] Suzuki coupling,[117, 118] ketalisation and ring opening reaction,[119-123] among many others.[22, 69, 124-126]

Biomedicine: the use of MOFs in medicine is mostly centered in either controlled release of drugs or as potential contrast agents. The first reported case of drug delivery in MOFs was presented in the Cr-based MIL-100 and MIL-101, incorporated with up to 1.4g of ibuprofen per gram of MOF. The drug was gradually release in a period of three days for MIL-100 and in a period of six days for MIL-101.[127] The Fe-based MIL-53 was also incorporate with ibuprofen with a slow kinetic release leading to a more precise concentration in blood.[128] Aspirin was another successfully incorporated drug in a Fe-based MIL-100, which showed 181% of loading efficiency and the gradual release in a period of eighteen days.[129] Due to the possibility to introduce paramagnetic metal ions into the network of the MOFs/CPs as, for instance, Gd^{3+} , Eu^{3+} and Tb^{3+} , the use of these materials as contrast agents have also attracted substantial interests.[130-134] These materials are used in the nanoscale, due to their size restriction to penetrate the cell walls. Although the results of MOFs/CPs in medicine are interesting the toxicity of these materials in the human body is not studied in depth, with only a few reports in the area.[135, 136]

Proton and Ionic conductors: in recent years, MOFs/CPs have been research with potential application to be efficient ion conductors. The ability to obtain crystalline materials which maintain their integrity when subject to external stimulus allows the researcher to better understand the dynamic of the material using X-ray diffraction techniques. With it was possible to better design new materials with enhanced conductivity. Nowadays, some MOFs/CPs show exceptional conductivities, surpassing the usual materials, such as Nafion® or polysulfone, operating at modest conditions (at temperatures below 100 °C and low humidity). It is not surprising the rise in number of publications regarding this application.[137-141]

1.5 – Structural Transformation in CPs/MOFs

As discussed previously, CPs and MOFs have one of the advantages of maintaining their crystallinity after external stimuli is applied, which is the main drive for using them as gas sorbents. Due to the aim of my PhD thesis, this next section will be focused on the structural changes obtained when different stimuli are applied, and how it affects on the final properties of the material.

As shown in Figure 1.14, and as widely reported in the literature, the polymerization of the PBUs can produce different types of coordination-based compounds. Following the IUPAC recommendations MOFs are solely those frameworks where the

self-assembly of the PBUs occurs in the three directions of space, leading to 3D networks (Figure 1.14); the compounds obtained when the polymerization is limited in one or two directions, promoting the formation of layered (2D) or chain-type (1D) compounds, are referred as CPs. Pursuing low-dimensional materials is not, however, a trivial task: for many combinations of PBUs, stopping the self-assembly process in one or more directions of space require the use of additional chemical species or the close control of the experimental conditions.

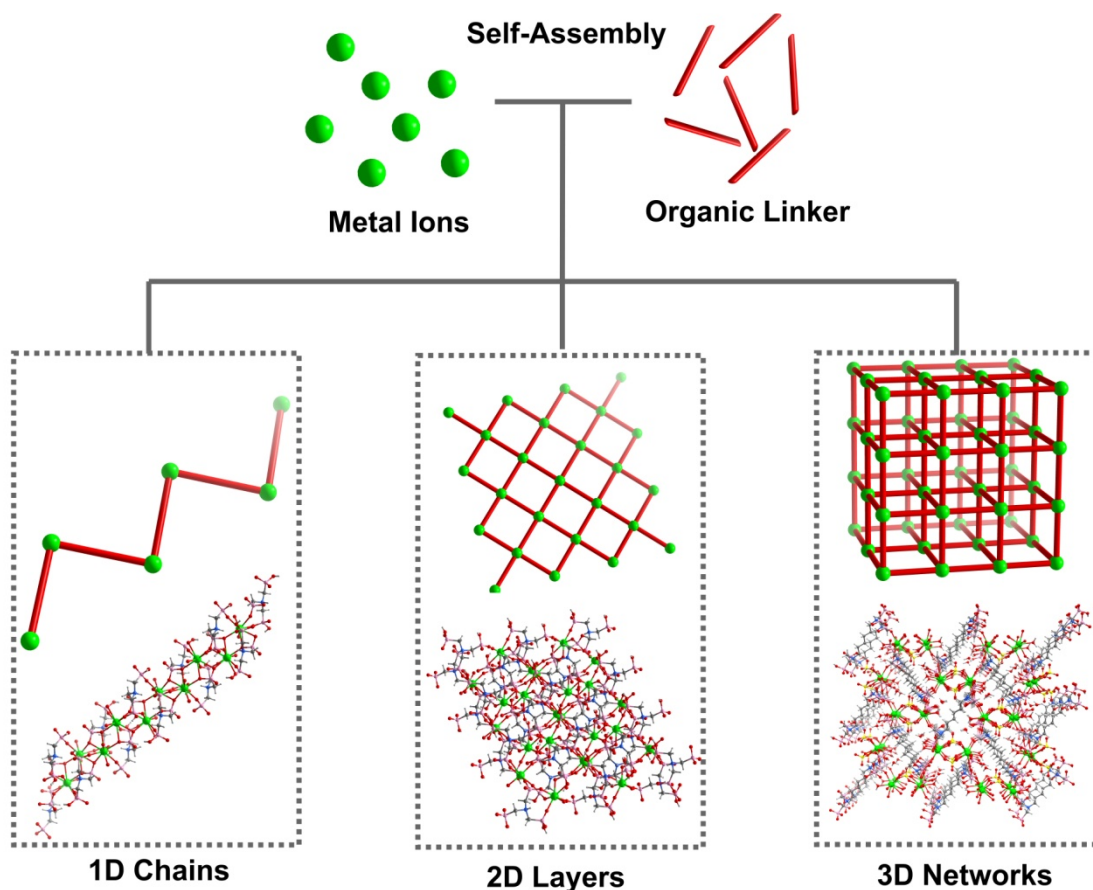


Figure 1.14 – Schematic representation of the formation of MOFs/CPs with different dimensionalities (1D, 2D and 3D).

For many chemical systems it is not clear why some experimental conditions lead preferentially to low dimension CPs while others to remarkable porous 3D networks. In a handful of cases scientists were able to exactly pinpoint the experimental conditions which control this self-assembly. For example, Liu *et al.*[142] discovered that for the mixed-metal Mo-Cu POM-based system with 1,10-(1,4-butanediyl)bis[2-(4-pyridyl)benzimidazole] (L^1), the pH plays a decisive role in the type and dimensionality of the isolated material: while a pH of *ca.* 3.5 promotes the formation of 1D hybrid chains $\text{Cu}(\text{HL}^1)_2(\beta\text{-Mo}_8\text{O}_{26})$, adjusting the pH to *ca.* 2.5 higher dimensional MOFs could be isolated, namely 2D $[\text{Cu}(\text{H}_2\text{L}^1)(\beta\text{-Mo}_8\text{O}_{26})(\text{H}_2\text{O})_2]\cdot 3\text{H}_2\text{O}$ and 3D $[\text{Cu}(\text{H}_2\text{L}^1)(\gamma\text{-Mo}_8\text{O}_{26})]\cdot 3\text{H}_2\text{O}$. However, in most experimental cases the reason for the systematic isolation of low-dimensional MOFs remains unknown. One interesting challenge posed to

researchers concerns the possibility of obtaining higher dimensional materials by means of transformations of low dimension CPs (for example, 1D-to-2D, 2D-to-3D or 1D-to-3D). A search in the literature reveals that these processes can indeed occur, sometimes with great improvement and fine-tuning of the properties of the materials.

1.5.1 – Changing the Dimensionality of MOFs

Chemical modifications on MOFs in order to change their dimensionality have been known for some years.[90, 143-153] Only in the last decade or so this process has, however, attracted the interest of scientists, with a handful of reviews on the subject being already available in the literature. [154, 155] These type of transformations occur through two general pathways: i) single-crystal-to-single-crystal (SC-SC) transformations, or ii) transformations via MOF dissociation, usually in solution. In the latter process, the MOF/CP partially or completely dissolves in the solvent employed with the PBUs reorganizing themselves into a new structure. The original MOF can, therefore, be considered as the starting chemical for the formation of a new material. In SC-SC processes the MOF/CP transformation is instead performed in the solid state, generally within the already available crystals, without the dissolution of the MOF/CP PBUs.

It is important to emphasize that post-synthetic modification of MOFs is not, usually, included in this group of transformations. Indeed, this relatively new, but highly important and widespread strategy to functionalize MOFs, almost exclusively requires the presence of 3D→3D' modifications taking advantage of the porous nature of the network and the maintenance of topological and porosity aspects. This subject has been already extensively reviewed in the literature [156, 157] and won't be discussed in most detail in this section.

Transformation of the dimensionality of MOFs can be performed using a wide variety of external stimuli such as:

Temperature: the most common external stimulus to change the dimensionality of MOF/CP is, by far, the variation of temperature.[158-161] Typically, the increase in temperature removes solvent molecules from the prepared materials allowing, in some cases, the replacement of the original solvent molecules by others. If the skeleton of the prepared frameworks is very rigid, it will not allow many important structural modifications on the PBUs connectivity, with only removal of solvent, leading to free channels or pores. But if the connectivity between the PBUs is more dynamic, new materials can indeed be prepared.

An interesting example comes from Mobin *et al.*[143] who reported the preparation of three isotypical 1D polymers formulated as $[(X)Hg(\mu-X)_2(L^2)]$ (where $X^- = Cl^-, Br^-$ or I^- ; $L^2 = 2-(2-hydroxyethyl)pyridine$). Even though the materials are 1D, interactions between the halogen and neighboring hydrogen atoms lead to the presence of close interactions forming supramolecular layers. Heating up the materials at 383 K for a short period of 90 minutes, the compounds with Br^- and I^- completely lose their crystallinity. The chloride-

based compound undergoes, however, a complete structural transformation as depicted in Figure 1.15. This transformation is fully reversible when the material is left at ambient conditions.

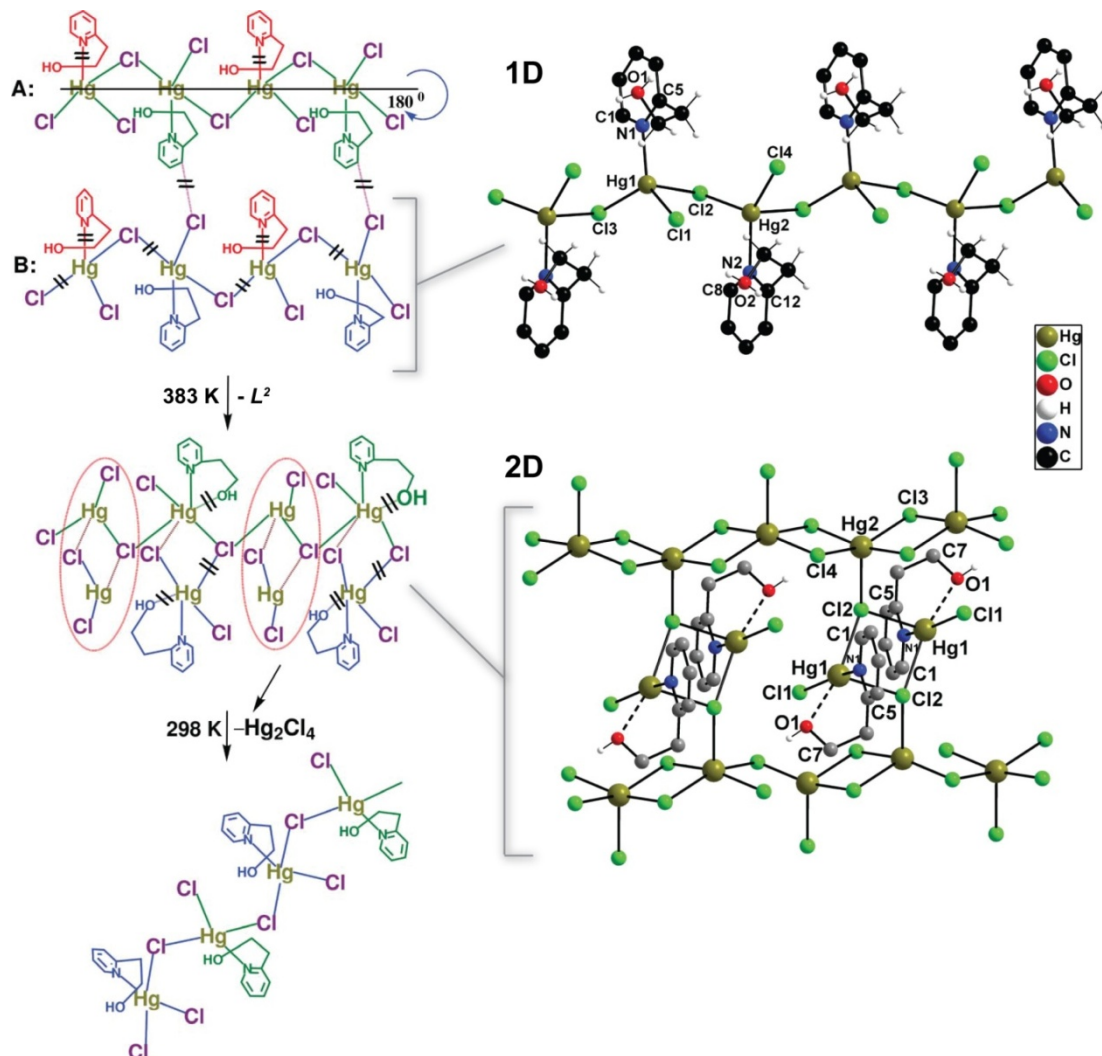


Figure 1.15 - Schematic representation showing the transformation of the 1D polymer $[(Cl)Hg(\mu-Cl)_2(L^2)]$ into a 2D network under the influence of temperature. The proposed pathways by the authors of the original paper are depicted on the left (= bond cleavage; - new bond formation). Reprinted with permission.[143] Copyright 2010 Royal Society of Chemistry.

A more extensive structural dynamics was reported by Kondo *et al.*[162] who showed the presence of remarkable stepwise transformations in a Co^{2+} system (Figure 1.16), which could even be accompanied visually by modification of the colour of the compounds. Discrete complexes forming the $[Co(bpy)_2(CH_3CN)_2(H_2O)_2] \cdot 2(OTf)$ compound convert spontaneously into 1D coordination polymers embedded in the $[Co(bpy)(OTf)_2(H_2O)_2] \cdot (bpy)$ crystal structure: acetonitrile solvent molecules and one bpy ligand are released from the coordination sphere of Co^{2+} being replaced by trifluoromethanesulfonate anions, promoting in this way the polymerization in one direction. Treating the 1D polymer at 423 K for a period of approximately 2 hours under

vacuum, a new transformation takes place promoting the formation of a 2D layered material formulated as $[\text{Co}(\text{bpy})_2(\text{OTf})_2]$ (Figure 1.16), which exhibited interesting adsorption capabilities. In addition, the discrete complex could even be directly transformed into the layered material by simple immersion in a dried solvent over a period of 10 days. This report by Kondo *et al.*[162] shows that the properties of one given system can be drastically modified by simply changing the dimensionality of the initially isolated compound.

Ganguly and co-workers have also reported a SC-SC transformation by heat of a 2D layered material, $[\text{Co}(\text{LP1})(\text{IPA})] \cdot 2\text{DMF} \cdot \text{H}_2\text{O}$ (where LP1 = 4,4'-oxybis(*N*-(pyridine-4-yl)benzamide) and IPA = isophthalate).[163] The transformation by heat was achieved by increasing the temperatures by 170 °C which allowed the removal of all solvent molecules. The resulting material displayed identical space group with one interesting change: the bis-pyridyl ligand changed its conformation. While in $[\text{Co}(\text{LP1})(\text{IPA})] \cdot 2\text{DMF} \cdot \text{H}_2\text{O}$ the ligand is in its *syn* conformation, in the dehydrated form the ligand changed to a *anti* conformation.

Change in pH: modification of the dimensionality can also be triggered by a change in the pH of medium where the MOF is placed or formed. A striking example comes from Fang *et al.*[164] who have self-assembled at ambient temperature Cd^{2+} cations with the Schiff base ligand 2-{[2-(dimethyl-amino)ethylimino]methyl}-6-methoxyphenol (H_5L^3), producing various complexes spanning from discrete complexes to 1D polymers. The authors relate the type and dimensionality of isolated compounds with the level of protonation of the organic ligand, which varies according to the pH: for values higher than 8 discrete (mononuclear and dinuclear) complexes are preferentially isolated; 1D polymers are prepared for pH values in the 5-7 range; decreasing the pH promotes again the isolation of discrete complexes.

Metal exchange: transformations based on exchanging of metals can be achieved through two distinct processes. The first, simpler and energetically favourable, concern the exchange of charge-balancing cations present in channels or pores. The second, more complex, involves the cleavage of coordination bonds and the formation/regeneration of new additional bonds, being, therefore, a more complex process. An exhaustive and detailed systematization of the results concerning these two processes was already published by Brozek and Dinca.[165] Even though this review is mainly based on structural aspects, the authors also compiled a series of improvements in direct applications as a consequence of the performed metal exchange.

As an example, Asha *et al.* reported a complete transmetalation of a 3D porous MOF, $[\text{H}_2\text{N}(\text{CH}_3)_2][\text{Ba}(\text{H}_2\text{O})(\text{BTB})]$ (where BTB stands for 1,3,5-tris(4-carboxylatophenyl)benzene)) in the presence of terbium anions.[166] Crystals were immersed in a solution of $\text{Tb}(\text{NO}_3)_3 \cdot 5\text{H}_2\text{O}$ for 24 h and the exchange was followed by fluorescence microscopy, showing the absence of dissolution of the crystal, proving to be a SC-SC transformation.

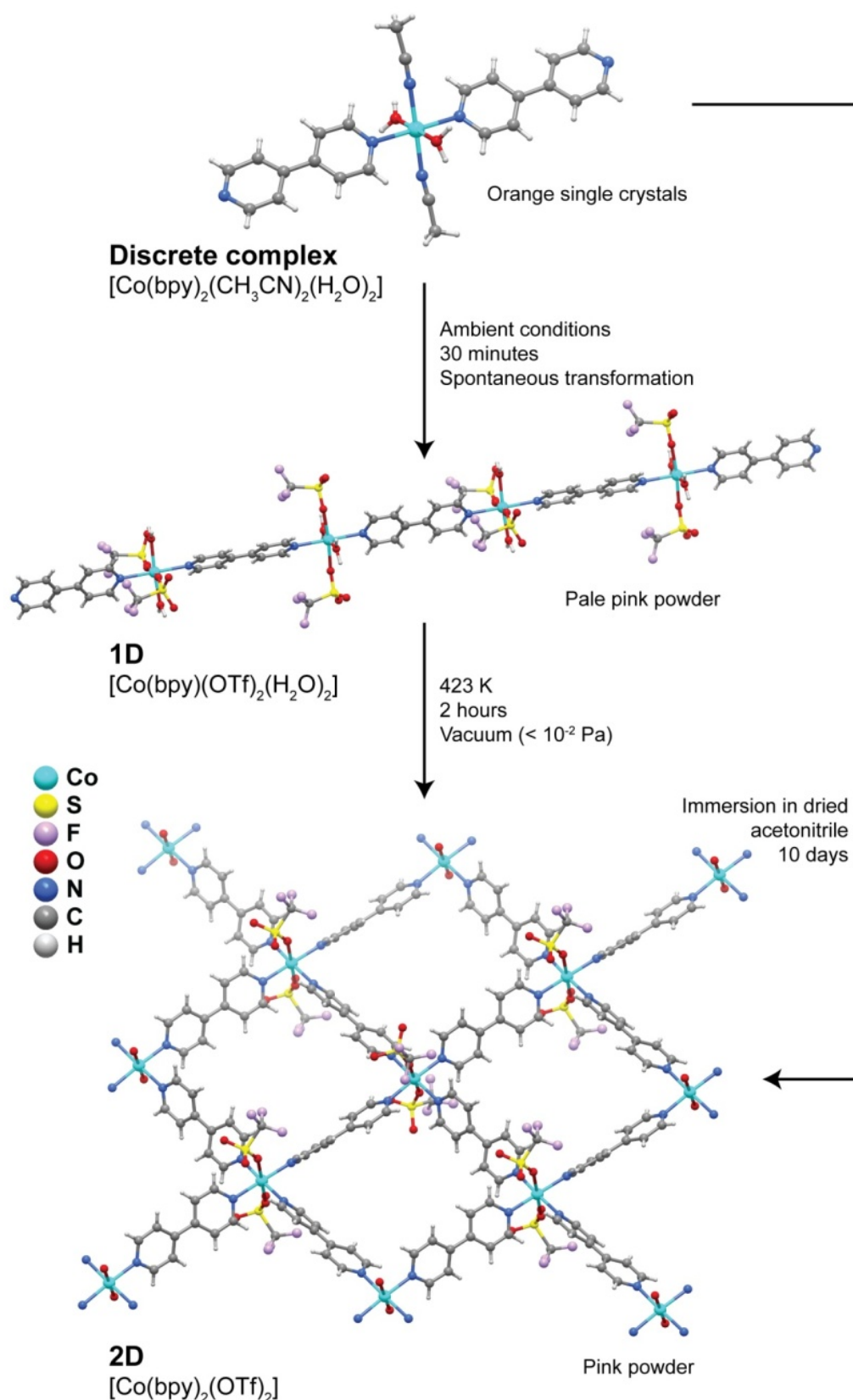


Figure 1.16 – Transformation pathways and experimental conditions for the discrete→1D, 1D→2D and discrete→2D conversions of the $[\text{Co}(\text{bpy})_2(\text{CH}_3\text{CN})_2(\text{H}_2\text{O})_2]$ (discrete), $[\text{Co}(\text{bpy})(\text{OTf})_2(\text{H}_2\text{O})_2]$ (1D) and $[\text{Co}(\text{bpy})_2(\text{OTf})_2]$ (2D) compounds. Adapted from the paper Kondo *et al.*[162]

1.6 – Transforming MOF/CP: designing new functional materials

As highlighted in the previous section the vast majority of research reports, and the known reviews on the subject, concerning the transformation of MOFs/CPs are mainly focused on purely structural aspects.[154, 155, 165] Taking advantage of these transformations to design new and clever functional materials is not a common aim of the authors, even though in some cases this was indeed achieved and very well explored. In this context, the next section will be focused on new MOF materials, typically of higher dimensionality, prepared from low dimension ones, with the transformation being concomitantly accompanied by a boost of the observed properties.

1.6.1 – Gas Adsorption

Transformation of MOFs through solvent removal or exchange is one of the most common processes reported in the literature, for which usually the dimensionality of the network remains unaltered.[167-169] Aiming potential applications the use of robust 3D networks is, thus, preferred so the channels can easily be evacuated while the network itself remains crystalline and able to interact with the guest gases or solvent molecules. If the solvent molecules are attached to the structuring metal centers (*i.e.*, the framework is formed by coordinatively unsaturated metal centers), their removal can in some cases induce an extensive structural modification through the reorganization of the metal coordination spheres. Even though many reports in the literature describe the release (sometimes reversible) of solvent molecules, only a handful of reports explore this to produce functional materials.

The manganese MOF $[\text{Mn}_3(\mu_5\text{-}L^4)(\mu_6\text{-}L^4)(\mu\text{-H}_2\text{O})(\text{H}_2\text{O})_4]\cdot 2\text{DMF}\cdot\text{H}_2\text{O}$ (where H_3L^4 = tris-(3-carboxylphenyl)phosphine oxide) reported by Jeong *et al.*[170] is a 3D MOF with the rare feature of possessing aqua bridges between metal centers. This highly unusual structural feature among crystalline MOFs was explored by the authors so to produce a novel functional material for the adsorption of gases. In a first step, the DMF molecules were exchanged by methanol through immersion at 40 °C over a period of 24 h (*please note*: the process is fully reversible if the compound is soaked in DMF and water – Figure 1.17). In a second step, heating the methanol-based compound at 50 °C under vacuum for 2.5 h leads to a fully desolvated material, $[\text{Mn}_3(\text{L}^4)_2]$, which besides retaining the main crystalline features of the methanol-based compound, also exhibits interesting adsorption properties. Indeed, the authors found that $[\text{Mn}_3(\text{L}^4)_2]$ adsorbs CO_2 with uptakes in the order of $31.9\text{ cm}^3\text{ g}^{-1}$, being approximately ten times more selective for this gas than for hydrogen (not adsorbed), nitrogen ($1.8\text{ cm}^3\text{ g}^{-1}$) and methane ($2.9\text{ cm}^3\text{ g}^{-1}$). This report of a 3D→3D' transformation through solvent displacement/replacement shows that simple treatments of as-prepared compounds can be used to “activate” the compounds to produce a functional material.

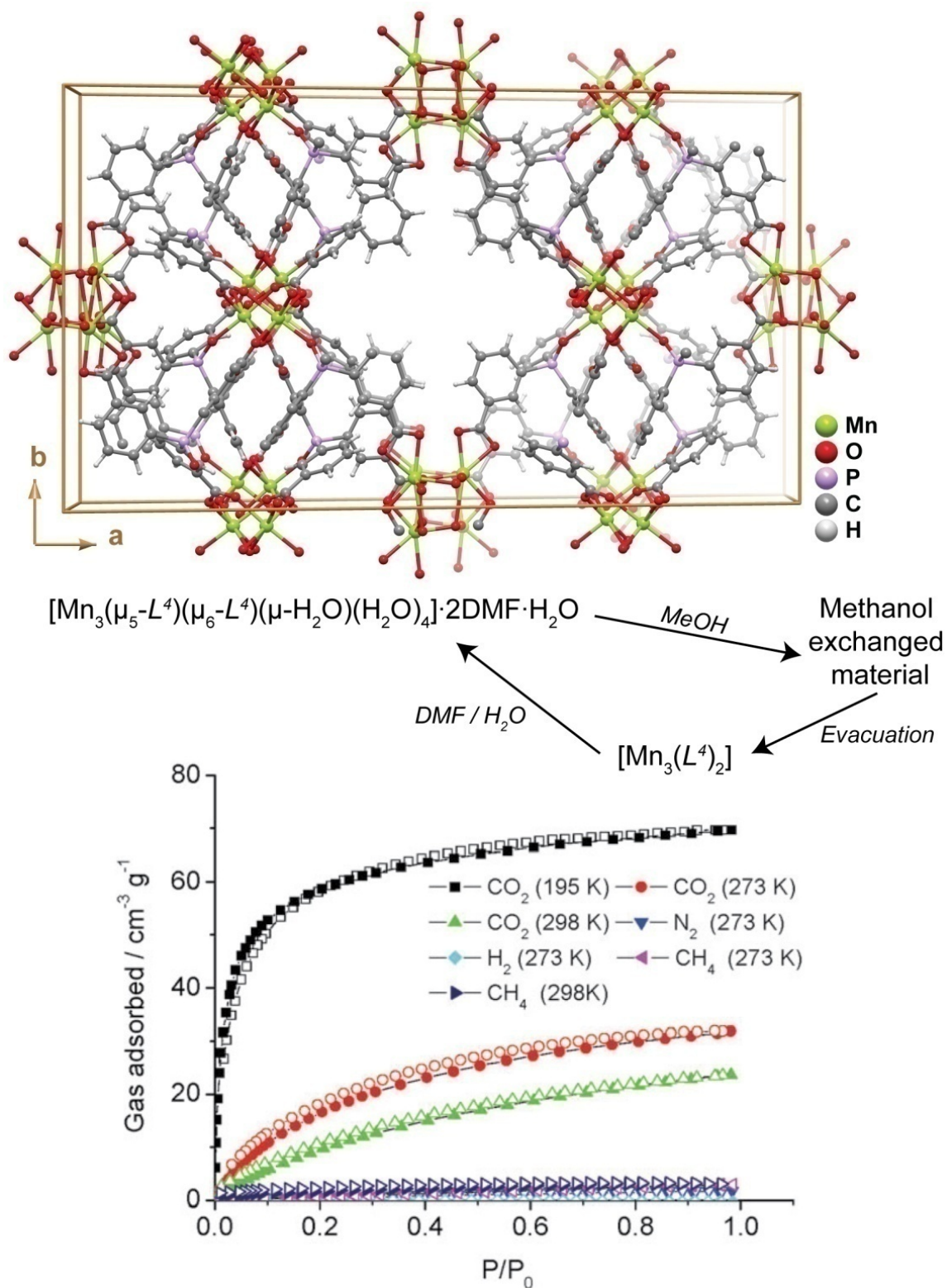


Figure 1.17 – (top) Crystal packing of $[\text{Mn}_3(\mu_5\text{-}L^4)(\mu_6\text{-}L^4)(\mu\text{-H}_2\text{O})(\text{H}_2\text{O})_4]\cdot 2\text{DMF}\cdot\text{H}_2\text{O}$ viewed along the [001] direction of the unit cell. (bottom) Gas uptake isotherms of $[\text{Mn}_3(L^4)_2]$. Adapted and reprinted with permission.[170] Copyright 2010 Royal Society of Chemistry.

A “0D”→2D transformation through solvent replacement and structure reorganization was reported by Zhai *et al.*[171] for Ni^{2+} -based compounds. From

hydrothermal synthesis the authors were able to isolate the $[\text{Ni}_3(\text{HL}^5)_6(\text{H}_2\text{O})_6]\cdot 9\text{H}_2\text{O}$ compound (where $\text{H}_2\text{L}^5 = 4\text{-(1,2,4-triazol-4-yl)phenylphosphonic acid}$) which is based on a discrete trinuclear Ni^{2+} complex. This compound was treated under hydrothermal conditions at 180 °C and low pH (*ca.* 3.0) for 7 hours to yield a new 2D layered MOF formulated as $[\text{Ni}(\text{HL}^5)_2]\cdot 7\text{H}_2\text{O}$. Indeed, this second step in the overall reaction permitted the displacement of the water molecules composing the Ni^{2+} coordination spheres, leading to the polymerization of the units into a novel layered material. Because the organic linker is based on phosphonate chelating groups, the resulting compound exhibited a remarkable thermal stability: it could endure refluxing benzene and ethanol for 7 days, acidic media and boiling water. The 2D MOF showed a remarkable performance in the adsorption of CO_2 , with an overall uptake of $80 \text{ cm}^3 \text{ g}^{-1}$, one of the highest reported to date to phosphonate-based MOFs. Moreover, the authors further showed that the material shows a very high selectivity towards CO_2 from a mixture with nitrogen, with a separation ratio of $\text{CO}_2 : \text{N}_2$ of *ca.* 114:1, much higher than those reported for a number of very stable ZIF materials.

The previous cases concern, basically, the removal of solvent molecules, sometimes with the modification of the dimensionality of the material, to produce functional materials. In other cases, the removal of solvent species could permit their replacement by other molecules. A remarkable example of the fabrication of a functional MOF comes from the research group of Lin who prepared a 2D layered MOF formulated as $[\text{Zn}_2(\text{L}^6)(\text{DMF})_4]\cdot 2\text{DMF}\cdot 4\text{H}_2\text{O}$ (where $\text{H}_4\text{L}^6 = \text{methanetetra(biphenyl-}p\text{-carboxylic acid)}$) using standard solvothermal synthetic conditions (reaction in DMF at 90 °C over a period of 2 days).[172] The same structure could also be isolated using Co^{2+} metal centers. Soaking this 2D MOF in dichloromethane at ambient temperature for approximately 8 hours, the authors were able to induce a 2D→3D SC-SC transformation (the colour and morphology of the crystals remained unaltered – Figure 1.18 a-c) producing a new crystalline compound formulated as $[\text{Zn}_2(\text{L}^6)(\text{H}_2\text{O})_2]\cdot x\text{solv}$. The 2D→3D occurs at the level of the metal centers: the departure of the coordinated DMF molecules induces a dimerization, producing a new SBU with water molecules in the first coordination sphere of the metal centers. This transformation was accompanied by a boost of the adsorption properties of the materials (Figure 1.18d): on the one hand, the BET surface area increases from 177 to $1170 \text{ m}^2 \text{ g}^{-1}$ (a seven-fold enhancement); on the other, the hydrogen uptake capacity (at 77 K and 1 atm) increases from 0.3 to 1.75 wt%, being comparable with the data reported for other well-known porous MOFs.

Another striking example of a new material was described by the research group of Oliver who have prepared a 3D Cd^{2+} -based MOF formulated as $[\text{Cd}(\text{HL}^7)(\text{L}^8)]\cdot n\text{DMF}$. [173] The authors showed that this material could undergo a SC-SC transformation to a fully desolvated phase by treating the as-prepared MOF at 300 °C under vacuum. The resulting framework, with empty pores, could accommodate new organic molecules, showing a high selectivity towards benzene, chloroform, 1,4-dioxane and THF (much more than for ethanol or methanol, for example). Besides this solvent

selectivity, the authors also showed that the dehydrated could also adsorb gases: for example, 2.5% N₂, 4.5% CO₂ and 3.4% N₂O (in mass).

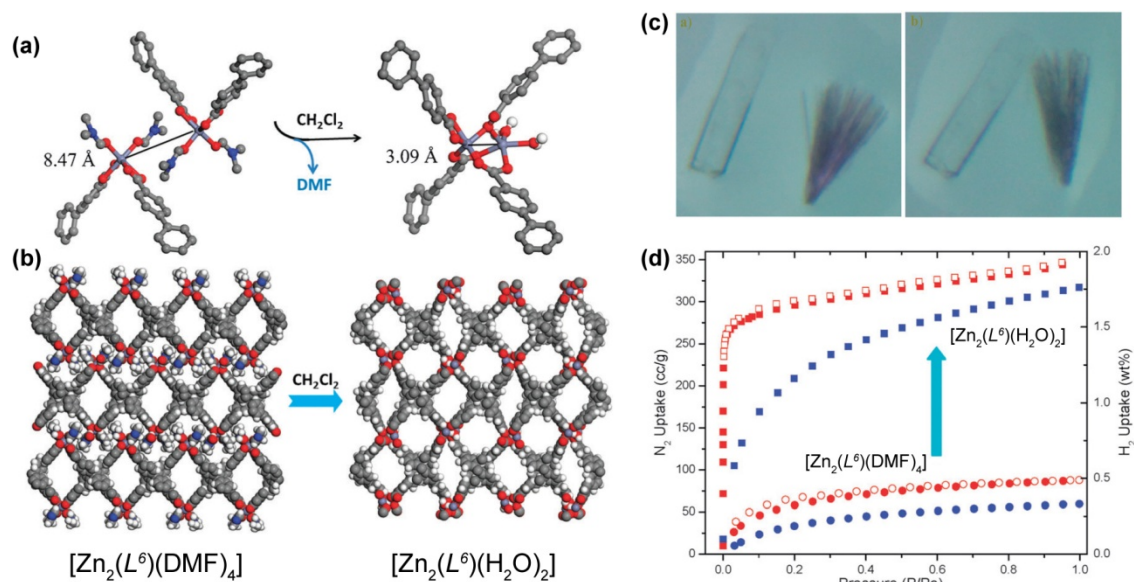


Figure 1.18 – (a) Dimerization of Zn²⁺ units promoted by the removal of the coordinated DMF molecules. (b) Crystal packing of (left) [Zn₂(L⁶)(DMF)₄]·2DMF·4H₂O and (right) [Zn₂(L⁶)(H₂O)₂]·xsolv. (c) Optical photographs of the (left) as-prepared [M₂(L⁶)(DMF)₄] (Zn²⁺ - colourless and Co²⁺ - purple) and compounds and (right) after exposure to dichloromethane for 3 hours. (d) Adsorption isotherms for N₂ (in red) and H₂ (in blue) at 77 K for [Zn₂(L⁶)(DMF)₄] and [Zn₂(L⁶)(H₂O)₂]. Adapted and reprinted with permission.[172] Copyright 2012 Royal Society of Chemistry.

Boosting gas adsorption on functional MOFs could also be achieved by acting directly on the chemical species present within the channels. Even though removing solvent can help to increase the available space for the adsorption of gas molecules, the presence of interacting sites to stabilize the gases is also of crucial importance. An example comes from the Long's research group who have chemically modified the charge-balancing ions present in the Mn₃[(Mn₄Cl)₃(L⁹)₈(CH₃OH)₁₀]₂ (where H₃L⁹ = 1,3,5-benzenetristetrazol) 3D network.[174] By immersing the 3D MOF in concentrated solutions of metal chlorides (in freshly distilled methanol) for approximately one month, the charge-balancing Mn³⁺ cations could be replaced by others such as Li⁺, Cu⁺, Fe²⁺, Co²⁺, Ni²⁺, Cu²⁺ or Zn²⁺. The authors discovered that even though the different metals in the channels do not lead to significant modifications in the overall H₂ adsorption, the adsorption enthalpies are however quite distinct. The most remarkable result concerns the Co²⁺-exchanged material which exhibits unprecedented initial adsorption enthalpies of 10.5 kJ mol⁻¹, being one of the higher enthalpies observed for H₂ adsorption in MOFs. Even though this is a rather straightforward 3D→3D SC-SC, this remarkable Co²⁺-based material can only be obtained using this alternative process.

1.6.2 – Luminescence

As exemplified in the previous sub-section, removing or exchanging solvent or guest species can induce important structural modifications that culminate with the improvement of the adsorption of gases or other molecules. The same process can, for example, be used to improve the photoluminescence behaviour of some materials. This is quite an important feature in, for example, lanthanide-based MOFs. For instance, the $[\text{Eu}_2(\text{L}^{10})_2(\text{OH})_2] \cdot 3\text{H}_2\text{O}$ (where H_2L^{10} = pyrimidine-4,6-dicarboxylic acid) 3D MOF reported by Sun *et al.*[175] can easily release the uncoordinated solvent molecules with the evacuated material being stable up to *ca.* 500 °C. In the absence of the quenchers from the crystallization water molecules the authors observed a small increase of the lifetime of the Eu^{3+} cations by *ca.* 10%. Lan *et al.*[176] prepared a porous $\text{Zn}_2(\text{L}^{11})_{0.5}(\text{DMSO})(\text{H}_2\text{O})$ (abbreviated herein as MOF·DMSO; where H_8L^{11} = 5,5'-(2,2-bis((3,5-dicarboxyphenoxy)methyl)propane-1,3-diyl)bis(oxy)diisophthalic acid) which could easily undergo solvent exchange and replacement (both coordinated and present in the channels) through hydrothermal treatment, leading to MOF·H₂O, MOF·DMF, MOF·EtOH and MOF·DMA. The various isolated networks retained the topological features of the parent DMSO-based compound (*i.e.*, a 3D→3D' transformation), but the authors observed the presence of small differences concerning the ligand coordination and conformation. Besides the 3D→3D' solvent exchange observed for MOF·DMSO, the authors also reported the same transformation concerning the encapsulation of the well-known Alq3 chromophore. The process could be accompanied visually with the colourless crystals of MOF·DMSO changing to yellow after 48 hours for the Alq3@MOF final compound (Figure 1.19). Moreover, the 3D→3D' transformation for the Alq3@MOF compound permitted a blue shift of the emission spectrum of the chromophore. In this way, the modified host MOF can be envisaged as an alternative way to modulate the luminescent properties of Alq3 and improve the performance of Alq3-based opto-electronic devices.

An unusual reversible 1D→2D transformation was reported by Wang *et al.*[177] who have prepared a 1D ladder-type compound isolated as $[\text{Zn}(\text{HL}^7)(\text{L}^8)_{0.5}(\text{H}_2\text{O})] \cdot n\text{H}_2\text{O}$ (where H_3L^7 = 1,3,5-benzenetricarboxylic acid and L^8 = 1,2-bis(4-pyridyl)ethane)(Figure 1.20). Noteworthy, the organic PBUs in this material are identical to those employed by Husain *et al.*[173] (see above) but in this case the resulting polymer has solvent molecules composing the first coordination sphere of the metallic center. Based on the location of these water molecules in relation to the crystal structure (pointing towards crystallographic interplanar spaces) the authors envisaged that if these molecules were removed a structural transformation could be triggered.

Moreover, because $[\text{Zn}(\text{HL}^7)(\text{L}^8)_{0.5}(\text{H}_2\text{O})] \cdot n\text{H}_2\text{O}$ exhibits a moderate blue emission band centred at *ca.* 410 nm (lifetime of *ca.* 1.8 ns), this transformation could also induce different luminescent properties. Based on a combination of various studies, the authors eventually were able to modify the crystal structure by heating the crystals from ambient temperature to *ca.* 180 °C, promoting the release of all solvent molecules and forming a new layered compound formulated as $[\text{Zn}(\text{HL}^7)(\text{L}^8)_{0.5}]$. Remarkably, the fluorescence peak

from the original material hypsochromically shifts to *ca.* 350 nm, with the intensity increasing by a two-fold factor and also being accompanied by an increment of the lifetime to *ca.* 2.3 ns. This process was shown to be completely reversible in the solid state, indicating a dynamic 1D \rightleftharpoons 2D conversion according to the experimental conditions.

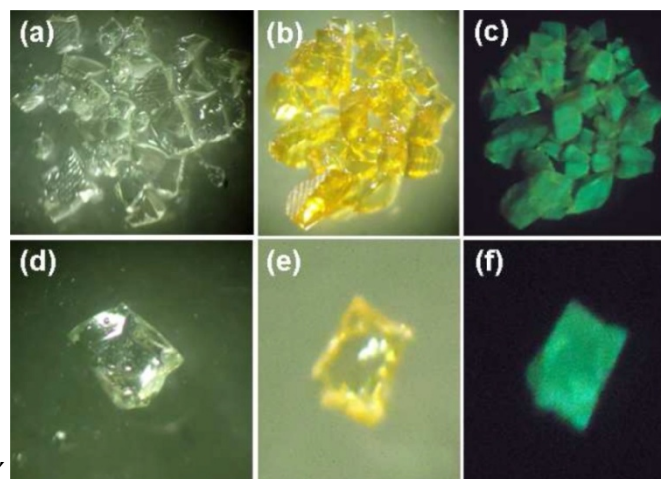


Figure 1.19 – Optical photographs of $\text{Zn}_2(\text{L}^{11})_{0.5}(\text{DMSO})(\text{H}_2\text{O})$ (**a, d**) before and (**b, e**) after encapsulating Alq3 molecules. (**c, f**) Optical photographs for Alq3 encapsulated in $\text{Zn}_2(\text{L}^{11})_{0.5}(\text{DMSO})(\text{H}_2\text{O})$ irradiated by UV light ($\lambda = 365$ nm). Reprinted with permission.[176] Copyright 2012 American Chemical Society.

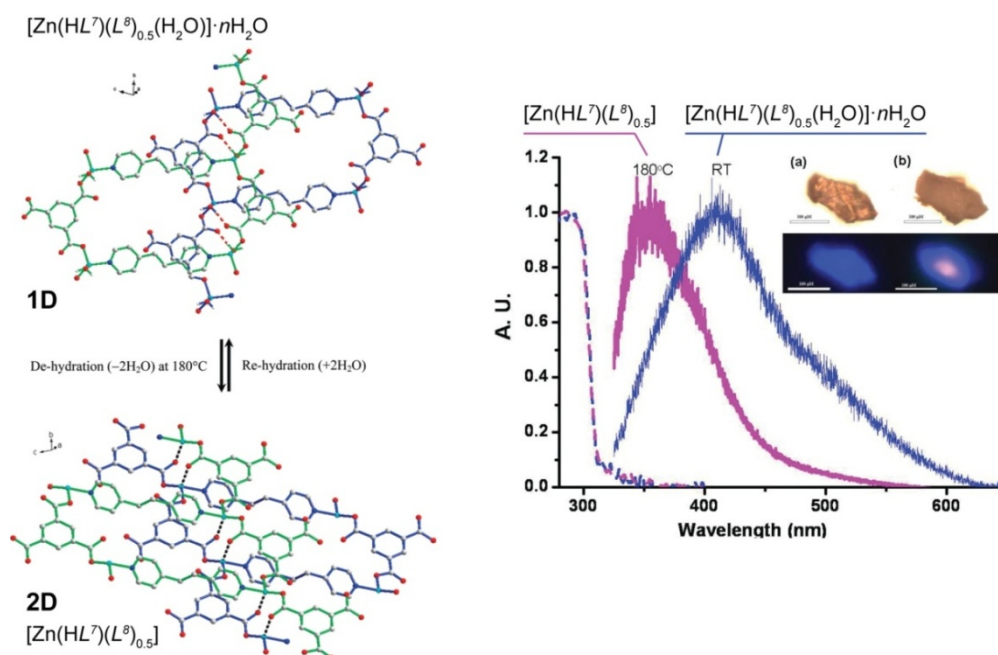


Figure 1.20 – (*left*) Schematic representation showing the reversible 1D \rightleftharpoons 2D conversion between the $[\text{Zn}(\text{HL}^7)(\text{L}^8)_{0.5}(\text{H}_2\text{O})] \cdot n\text{H}_2\text{O}$ phase containing the 1D polymer and the fully dehydrated $[\text{Zn}(\text{HL}^7)(\text{L}^8)_{0.5}]$ 2D phase. (*right*) Solid state absorption (dashed lines) and emission (solid lines) of $[\text{Zn}(\text{HL}^7)(\text{L}^8)_{0.5}(\text{H}_2\text{O})] \cdot n\text{H}_2\text{O}$ at ambient temperature (in blue) and $[\text{Zn}(\text{HL}^7)(\text{L}^8)_{0.5}]$ at 180°C (in magenta), $\lambda_{\text{ex}} = 325$ nm. Both the absorption and emission spectra have been normalized. *Inset*: Changes of color of (**a, upper**) $[\text{Zn}(\text{HL}^7)(\text{L}^8)_{0.5}(\text{H}_2\text{O})] \cdot n\text{H}_2\text{O}$ at ambient temperature and (**b, upper**) $[\text{Zn}(\text{HL}^7)(\text{L}^8)_{0.5}]$ at 180°C . Luminescence of $[\text{Zn}(\text{HL}^7)(\text{L}^8)_{0.5}(\text{H}_2\text{O})] \cdot n\text{H}_2\text{O}$ at ambient temperature (**a, lower**) and $[\text{Zn}(\text{HL}^7)(\text{L}^8)_{0.5}]$ (**b, lower**) at 180°C upon excitation at 325 nm. Scale bar is 100 μm . Reprinted and adapted with permission.[177] Copyright 2011 American Chemical Society.

1.6.3 – Sensors

If MOF transformation is triggered by the presence or absence of a specific chemical stimulus, the system could in principle be employed in the fabrication of a sensing device. The importance of these modifications could be boosted if the modification is, for example, accompanied by a change of a visible aspect of the materials such as colour. A striking example was described by Aslani and Morsali[178] who reported a SC-SC transformation of the 1D polymer $[\text{Pb}_2(L^{12})_2(\text{NO}_3)_2(\text{MeOH})]$ into the 2D layered material $[\text{Pb}(L^{12})(\text{NO}_3)]$ (where L^{12} = 8-hydroxyquinoline) (Figure 1.21). The authors achieved this transformation by simply heating the as-prepared material up to *ca.* 165 °C, with the process being accompanied by a modification of the crystal colour from light brown to yellow (Figure 1.21 – *right*). The transformation occurs due to the release of the coordinated methanol molecules. Remarkably, the process is fully reversible, being always of the SC-SC type: when the desolvated material is exposed to methanol it regenerates the original compound. More importantly, the process is also highly selective: in the presence of other common solvents such as ethanol, acetonitrile, dichloromethane, benzene and chloroform, transformation from the layered phase to the chain-type polymer does not occur. In summary, Aslani and Morsali[178] described a remarkable MOF system in which the reversible $1\text{D} \rightleftharpoons 2\text{D}$ transformation is solely and highly selectively triggered by the desorption / adsorption of methanol, being the process easily accompanied by a drastic change in colour.

Colour modification, associated with modifications in dimensionality, could also be triggered by the pH of the medium. Yamada *et al.*[179] investigated the transformation of a copper(II)-triazolate system known since the 60's to have both 1D and 3D networks. The authors prepared novel cubic 3D structures, formulated as $[\text{Cu}_3(L^{13})_3(\mu_3\text{-OH})]X_2 \cdot 6\text{H}_2\text{O}$ (where HL^{13} = 1,2,4-triazole and $X = \text{Cl}^-$ or Br^-), from relatively simple one-pot reactions at ambient temperature between copper(II) salts and the organic PBU. The resulting $[\text{Cu}_3(L^{13})_3(\mu_3\text{-OH})]X_2 \cdot 6\text{H}_2\text{O}$ 3D compounds were subjected to external pH stimuli in the solid state. Taking advantage of the insolubility of the 3D MOFs, the authors prepared suspensions of the compounds in water with a pH ranging from *ca.* 0.1 to 10 (by using $\text{HCl}/\text{Na}_2\text{CO}_3$ and $\text{HBr}/\text{Na}_2\text{CO}_3$ solutions): for the Cl^- -based compound, the colour of the MOF changed from blue to pale green (Figure 1.22 – *top left*); the same was observed for the Br^- -based compound but at even more acidic pH the colour changed to brown (Figure 1.22 – *top right*). The investigation was accompanied in detail using powder X-ray diffraction showing that the modification of the pH promoted a drastic structural modification: crystalline 3D $[\text{Cu}_3(L^{13})_3(\mu_3\text{-OH})]X_2 \cdot 6\text{H}_2\text{O}$ compounds were gradually converted into also crystalline 1D polymers formulated as $[\text{Cu}X_2(\text{HL}^{13})]$ (where $X = \text{Cl}^-$ or Br^-) (Figure 1.22 – *bottom*). The authors rationalized this remarkable $3\text{D} \rightarrow 1\text{D}$ transformation through the action of the acid on the bridges of the 3D MOF: basically, the process is triggered by the neutralization of the hydroxyl bridges and protonation of the organic linker, leading to a reorganization in the solid state of the MOF. The inverse

1D→3D process was attempted by employing NH₃ gas, but with no interesting results to be reported.

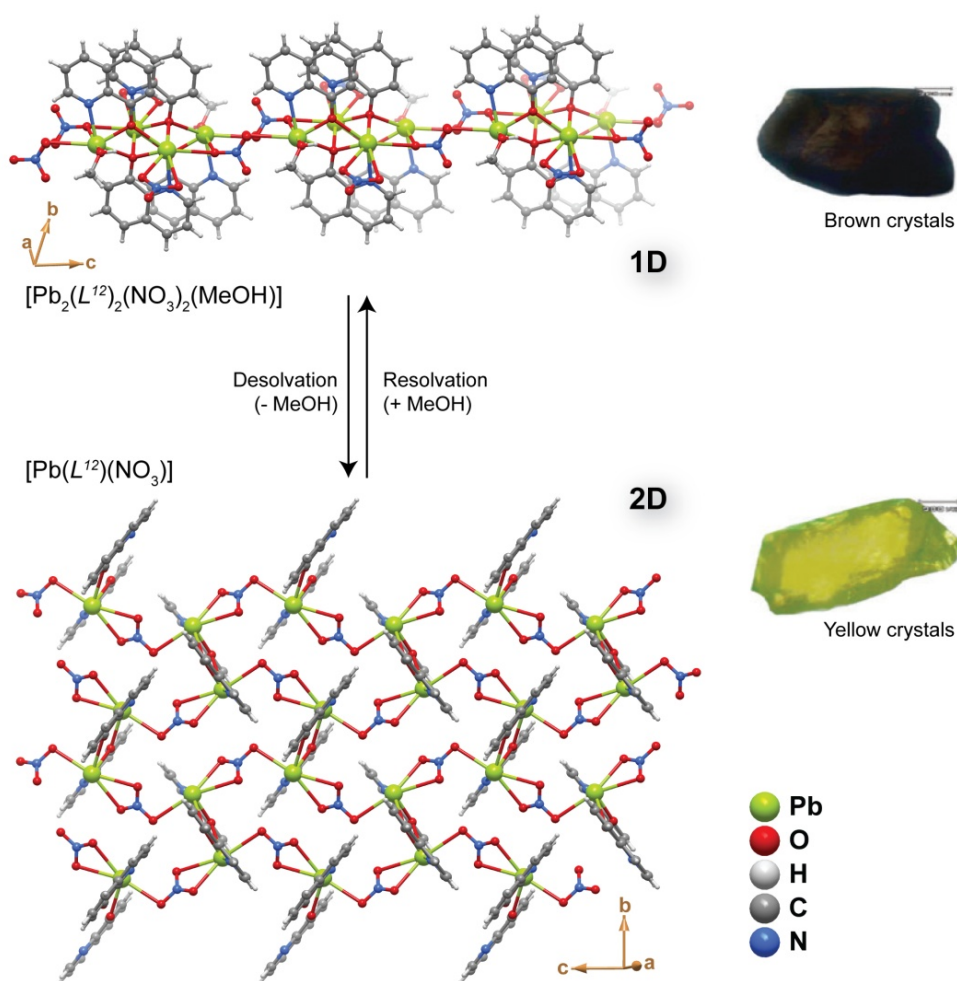


Figure 1.21 – Structural representation of the reversible conversion between the 1D $[\text{Pb}_2(L^{12})_2(\text{NO}_3)_2(\text{MeOH})]$ compound and the layered 2D $[\text{Pb}(L^{12})(\text{NO}_3)]$ CP through the removal or inclusion of methanol molecules. During the process the crystals of the materials change colour as depicted on the right. Reprinted and adapted with permission.[178] Copyright 2008 Royal Society of Chemistry.

A rarely encountered feature among crystalline structures, particularly MOFs, concerns the sensing of molecules based on drastic modifications of the resulting crystalline structures. The multidisciplinary research group headed by Lee Brammer presented a remarkable example of this feature in MOFs using a simple two-step process involving the removal, addition or replacement of structural framework organic linkers.[180] Vapour diffusion of pyridine (L^{14}) to an ethanolic solution of Zn^{2+} and (1*R*,3*S*)-(+)-camphoric acid (H_2L^{15}) produced the 2D MOF compound formulated as $[\text{Zn}_2(L^{15})_2(L^{14})_2] \cdot 2\text{EtOH}$. This layered material possesses the monodentate pyridine ligands and the uncoordinated ethanol solvent molecules pointing towards the interlayer space as shown in Figure 1.23. This structural feature facilitated the first step of the structural transformation: heating this parent compound at 150 °C for just 12 hours produces a new crystalline 3D material formulated as $[\text{Zn}(L^{15})]$. This process allowed the complete

removal of both the uncoordinated ethanol molecules and the axially-coordinated pyridine ligands from the paddlewheel SBUs, promoting a rearrangement of the coordination spheres and the interconnection into a 3D network. This was found to be, however, a highly dynamic process ($2D \rightleftharpoons 3D$): reversibility of the transformation was achieved by soaking $[Zn(L^{15})]$ in an ethanolic solution of pyridine. Because of this feature the authors envisaged that the structural reversibility of the material could permit the inclusion of other molecules. Indeed, soaking $[Zn(L^{15})]$ in solutions of pyrazine (L^{16}) or 3-bromopyridine (L^{17}) two completely different phases were isolated, also as crystalline networks (over a period of 7 days – see Figure 1.23): 3D $[Zn_2(L^{15})_2(L^{16})] \cdot 2DMF$ (*i.e.*, $3D \rightarrow 3D'$) and 2D $[Zn_2(L^{15})_2(L^{17})_2] \cdot DMF$ (*i.e.*, $3D \rightarrow 2D$). Even though the authors did not indicate the existence of any visual modification of the crystals (or powders), such as colour, this system constitutes a remarkable example of a two-step dimensionality modification through sensing / replacement of structural organic linkers. As shown in the report, the transformation can be easily followed using powder X-ray diffraction since the crystallinity of the compounds is retained throughout the processes.

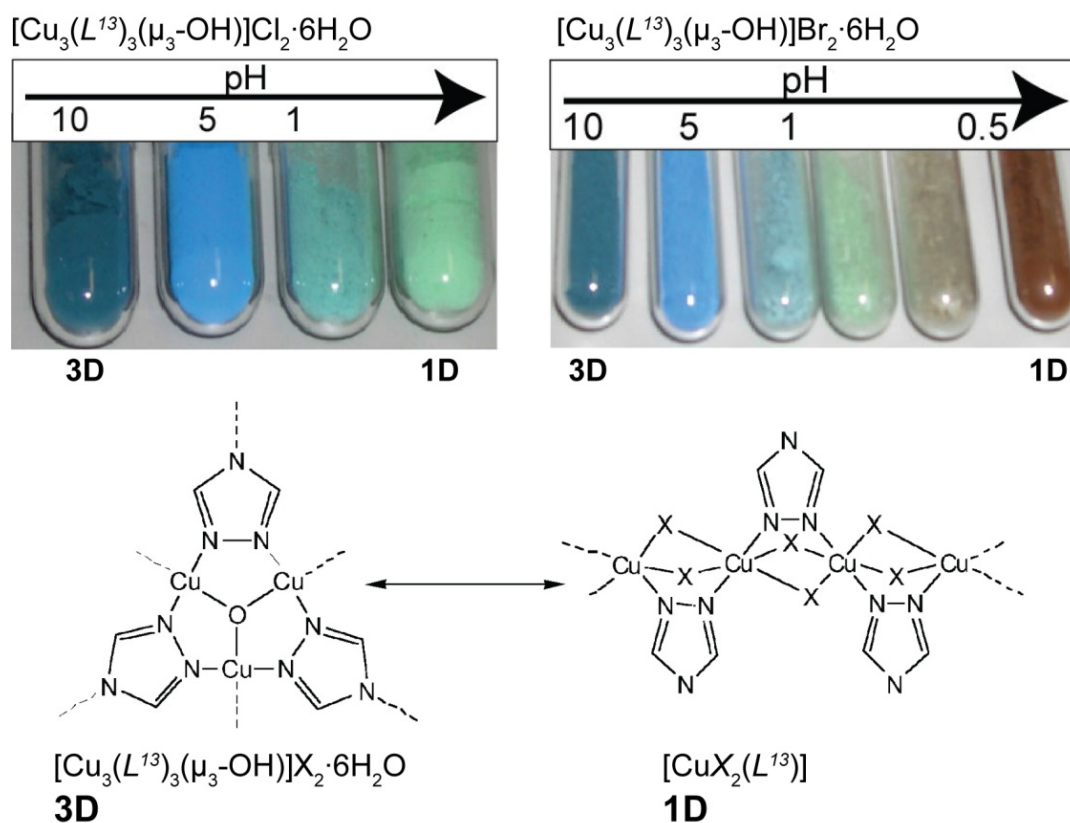


Figure 1.22 – (top) Colour modification of $[Cu_3(L^{13})_3(\mu_3-OH)]X_2 \cdot 6H_2O$ material (where $X = Cl^-$ or Br^-) according to the variation of the pH. (bottom) Structural conversion between fragments of the structures of 3D $[Cu_3(L^{13})_3(\mu_3-OH)]X_2 \cdot 6H_2O$ and 1D $[CuX_2(L^{13})]$ MOFs. Reprinted and adapted with permission.[179] Copyright 2011 Royal Society of Chemistry.

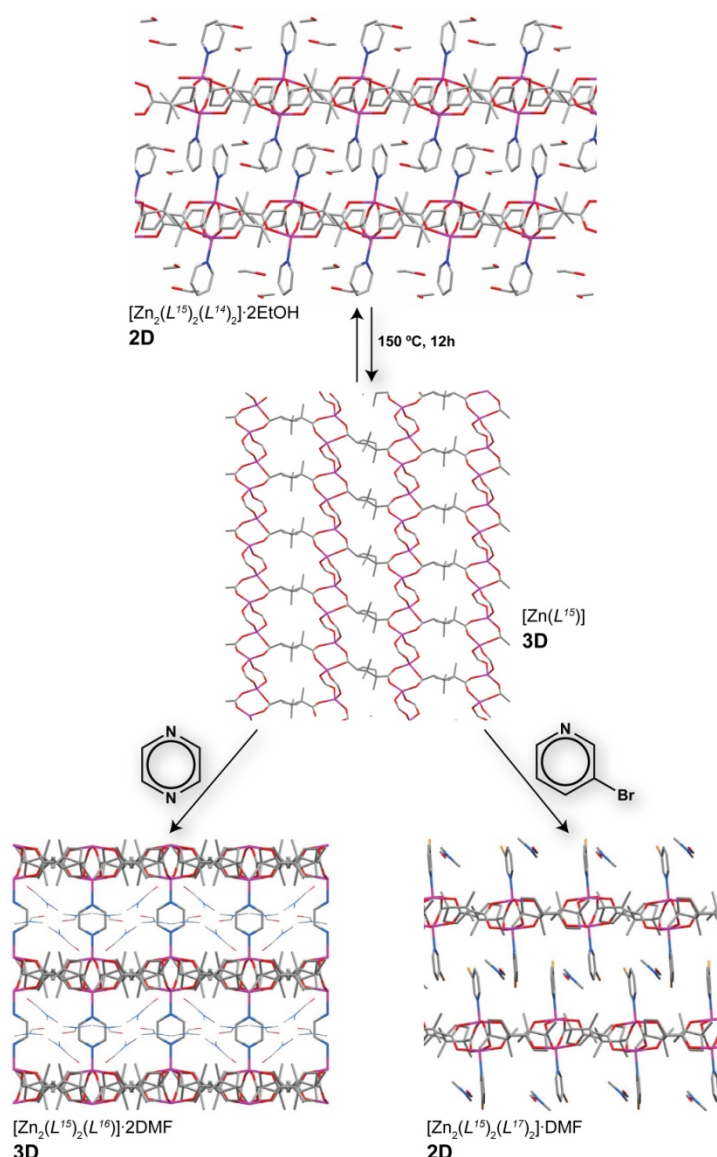


Figure 1.23 – Schematic representation of the various successive framework transformations of the materials based on (1*R*,3*S*)-(+)-camphoric acid: non-covalently pillared $[\text{Zn}_2(\text{L}^{15})_2(\text{L}^{14})_2] \cdot 2\text{EtOH}$ undergoes a reversible $2\text{D} \rightleftharpoons 3\text{D}$ transformation into the 3D non-porous $[\text{Zn}(\text{L}^{15})]$ compound, which when immersed in either pyrazine or 3-bromopyridine adsorbs these molecules producing 3D $[\text{Zn}_2(\text{L}^{15})_2(\text{L}^{16})_2] \cdot 2\text{DMF}$ (*i.e.*, $3\text{D} \rightarrow 3\text{D}^*$) and 2D $[\text{Zn}_2(\text{L}^{15})_2(\text{L}^{17})_2] \cdot \text{DMF}$ (*i.e.*, $3\text{D} \rightarrow 2\text{D}$). Reprinted and adapted with permission.[180] Copyright 2013 Wiley-VCH.

1.6.4 – Controlled release of molecules

Once incorporated into the structure of a MOF, active or structurally interesting molecules could be released into the surrounding medium, usually impelled by an external stimulus, leading to a modification of the overall crystalline structure of the compound. An outstanding example was very recently described by He *et al.*[181] based on the 2D Cu^{2+} MOF prepared using standard hydrothermal reaction procedures (130 °C, 3 days) between isonicotinic acid (HL^{18}), iodine and copper(II) nitrate: $[\text{Cu}(\text{L}^{18})_2] \cdot \text{I}_2$. The resulting layered MOF, (with (4,4) topology), has the striking feature of possessing molecular iodine

occupying the square pores (Figure 1.24 – *top*). The authors discovered that these molecules could be quickly released by heating the compound at 120 °C for just 8 hours under vacuum. During this SC-SC process, the 2D network undergoes a structural transformation into a 3D MOF formulated as $[\text{Cu}(L^{18})_2]$, motivated by the modification of the coordination modes of the organic ligand and an increase of the coordination number of Cu^{2+} (from 4 to 5). The molecular iodine could also be slowly released with time, as demonstrated by soaking $[\text{Cu}(L^{18})_2] \cdot \text{I}_2$ in dry methanol. Noteworthy, this process is also accompanied by a change in colour of the crystals (from black to green – Figure 1.24 – *bottom*), which could be used as a quick identification of the presence of a fully depleted material concerning iodine.

1.6.5 – Water scavengers

In many areas of industrial activity and scientific research, the presence of trace amounts of water hinders applications and activity of materials. Many solutions for this problem are known, such as the use of molecular sieves, heat, adsorption and the use of inorganic agents to promote dehydration. However, for real efficiency, in many systems the use of chemical reactions to remove all traces of water is absolutely necessary such as, for example, jet fuel. Even though MOFs are typically prepared in water, they can be used as water scavengers from a reaction medium based on structural conversion. The research group of Kitagawa described a series of this type of materials based on the highly flexible organic linker *tris*(2-carboxyethyl)isocyanuric acid (H_3L^{19}). From hydrothermal reactions, this flexible linker in the presence of solutions containing Ce^{3+} or Pr^{3+} nitrates and tetramethylammonium chloride (used as blocking agent) produces a 2D layered network formulated as $[\text{Ln}(L^{19})(\text{H}_2\text{O})_2] \cdot 2\text{H}_2\text{O}$. [182] Heating up the as-prepared compound (150 °C for 5 hours) leads to a new water-free 3D material, $[\text{Ln}(L^{19})]$ (Figure 1.25 – *top*). The authors rationalized such transformation based on the presence of coordinated water molecules in the coordination sphere of the lanthanide cations that, upon removal, lead to a rearrangement of the network. Both materials, $[\text{Ln}(L^{19})(\text{H}_2\text{O})_2] \cdot 2\text{H}_2\text{O}$ and $[\text{Ln}(L^{19})]$, are very stable in various solvents (*e.g.*, methanol, ethanol, THF, acetone) but once the 3D phase is placed in the presence of small amounts of water it reabsorbs this solvent regenerating the original 2D compound. This remarkable selectivity was even directed towards gases: besides the aforementioned solvent molecules, the 3D network also rejected gases such as nitrogen or CO_2 being extremely specific for water (Figure 1.25 – *bottom*). In the following year, the same research group reported a similar SC-SC behaviour for a transition metal-based MOF, [152] in which the 2D $[\text{Cu}_2(L^{19})(\text{OH})(\text{H}_2\text{O})_3] \cdot 1.5\text{H}_2\text{O}$ compound could be transformed, reversibly, into 3D $[\text{Cu}_2(L^{19})(\text{OH})]$ at an even lower temperature (*ca.* 80 °C for just 4 hours). This second water scavenger system even has the advantage of the reversible $2\text{D} \rightleftharpoons 3\text{D}$ transformation being accompanied by a change in colour: from greenish-blue (2D) to deep blue (3D).

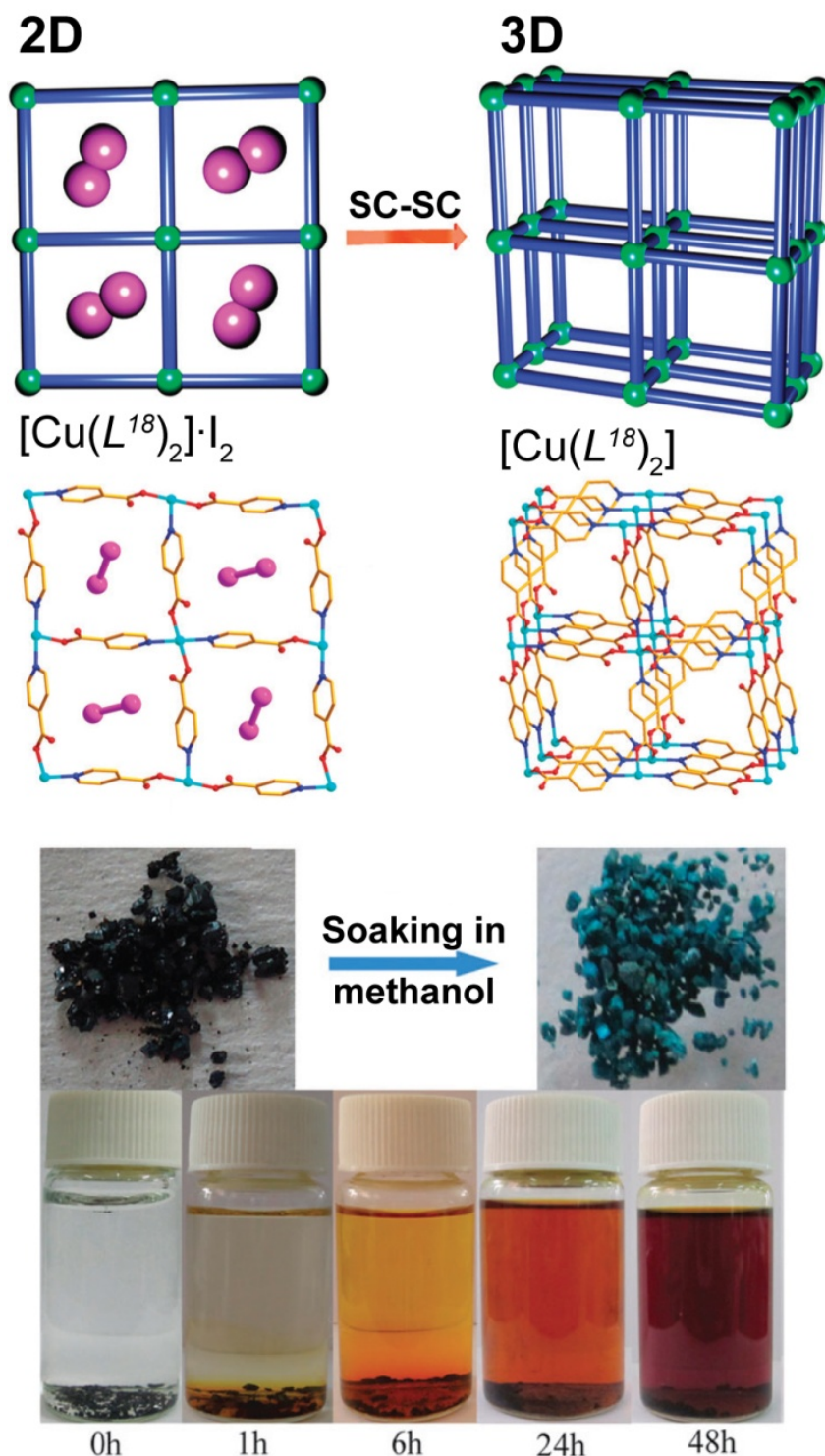


Figure 1.24 – (top) Schematic representation of the 2D→3D SC-SC transformation of $[\text{Cu}(\text{L}^{18})_2] \cdot \text{I}_2$ into $[\text{Cu}(\text{L}^{18})_2]$ by the release of the encapsulated iodine molecules. (bottom) Colour change from black to green during the release of iodine (also revealed in the methanol suspension at the bottom). Reprinted and adapted with permission.[181] Copyright 2012 Royal Society of Chemistry.

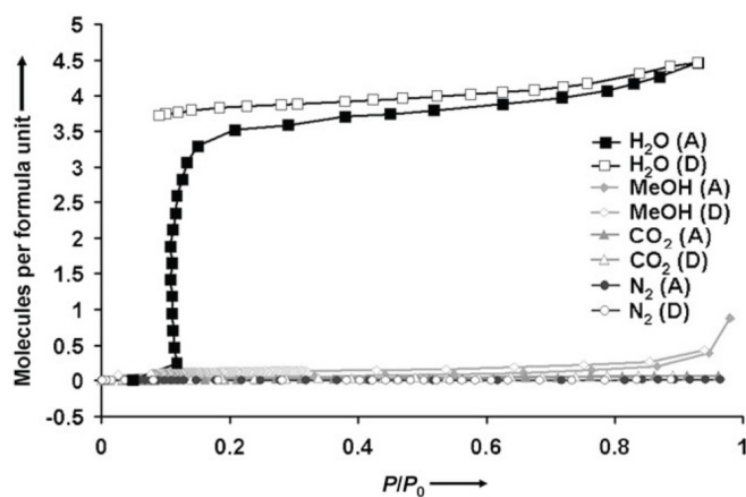
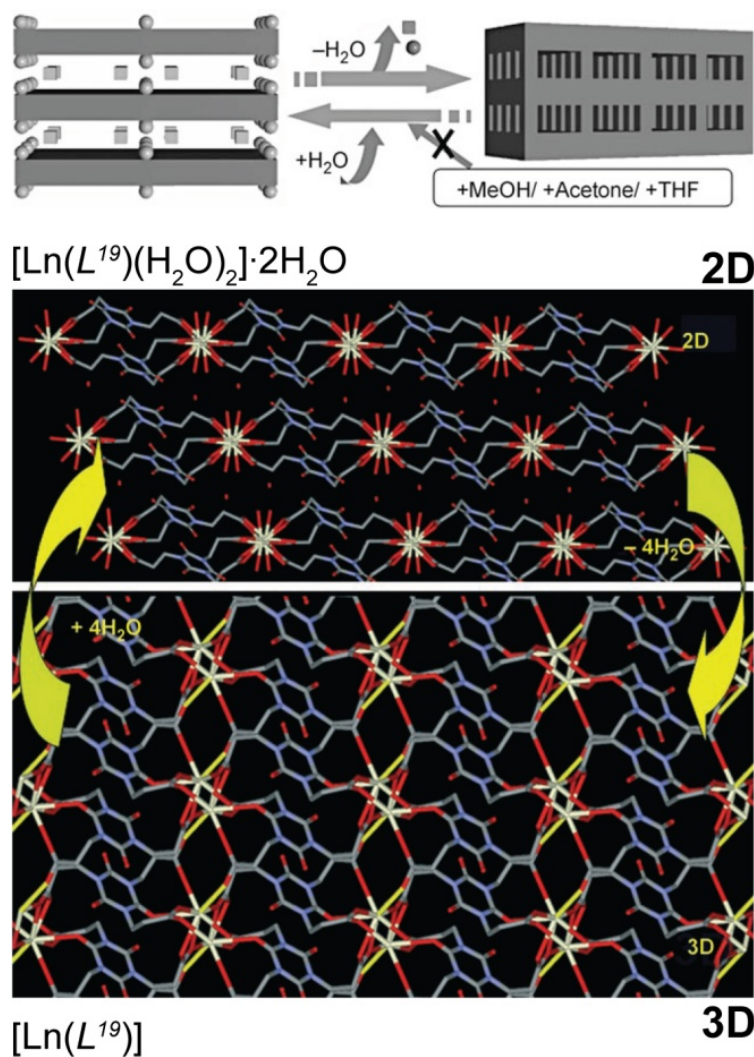


Figure 1.25 – (top) Schematic representation of the reversible 2D \rightleftharpoons 3D SC-SC transformation of $[\text{Ln}(\text{L}^{19})(\text{H}_2\text{O})_2] \cdot 2\text{H}_2\text{O}$ (where $\text{Ln}^{3+} = \text{Ce}^{3+}$ or Pr^{3+}) into $[\text{Ln}(\text{L}^{19})]$ by the release of the water molecules. Chemical diagrams prepared from the crystallographic determinations are also provided. (bottom) Adsorption (A) and desorption (D) isotherms of H_2O , MeOH, CO_2 and N_2 of the 3D $[\text{Ln}(\text{L}^{19})]$ MOF material. Reprinted and adapted with permission.[182] Copyright 2007 Wiley-VCH.

1.6.6 – Magnetic materials

It is feasible to assume that the structural rearrangements associated with the framework transformations described in the present review would also have significant impact of properties intimately associated with the metal centers such as, for example, magnetism. Surprisingly these features are not very much explored and reported. For example, in the study of the 2D $[\text{Cu}_2(L^{19})(\text{OH})(\text{H}_2\text{O})_3] \cdot 1.5\text{H}_2\text{O} \rightleftharpoons 3\text{D } [\text{Cu}_2(L^{19})(\text{OH})]$ system reported above,[152] the authors indicated that the dimensionality transformation was accompanied by a significant modification of the observed magnetic properties: the increased dimensionality of $[\text{Cu}_2(L^{19})(\text{OH})]$ fragmented the magnetic exchange pathways, which ultimately resulted in an overall weakening of the magnetic correlation.

Zhang *et al.*[183] described a remarkable system in which discrete (“0D”) complexes could be reversibly converted into 1D polymeric double zigzag chains with strikingly distinct magnetic properties (Figure 1.26). The achiral hexanuclear cluster $[\{\text{Fe}^{\text{III}}(L^{20})(\text{CN})_3\}_4\{\text{Fe}^{\text{II}}(\text{MeCN})(\text{H}_2\text{O})_2\}_2] \cdot 10\text{H}_2\text{O} \cdot 2\text{MeCN}$ (“0D”; where L^{20} = hydrotris(pyrazoly)borate) close packs in the solid state alongside with a tetrameric water cluster which imposes a physical separation between adjacent complexes. This cluster could be, however, removed from the material by heating the crystals at 150 °C under nitrogen atmosphere, promoting a SC-SC transformation leading to the formation of 1D $[\text{Fe}^{\text{III}}(L^{20})(\text{CN})_3]_4\text{Fe}^{\text{II}}(\text{H}_2\text{O})_2\text{Fe}^{\text{II}}$ chiral polymers. This “0D”→1D conversion was accompanied by a drastic modification of the magnetic properties: while the discrete cluster has a predominantly antiferromagnetic behaviour, the chiral 1D polymer is ferromagnetic. The authors also discovered that this structural transformation, and the observed properties, is fully reversible (“0D” \rightleftharpoons 1D): exposing the 1D $[\text{Fe}^{\text{III}}(L^{20})(\text{CN})_3]_4\text{Fe}^{\text{II}}(\text{H}_2\text{O})_2\text{Fe}^{\text{II}}$ polymer to vapours of water and acetonitrile regenerates quantitatively $[\{\text{Fe}^{\text{III}}(L^{20})(\text{CN})_3\}_4\{\text{Fe}^{\text{II}}(\text{MeCN})(\text{H}_2\text{O})_2\}_2] \cdot 10\text{H}_2\text{O} \cdot 2\text{MeCN}$.

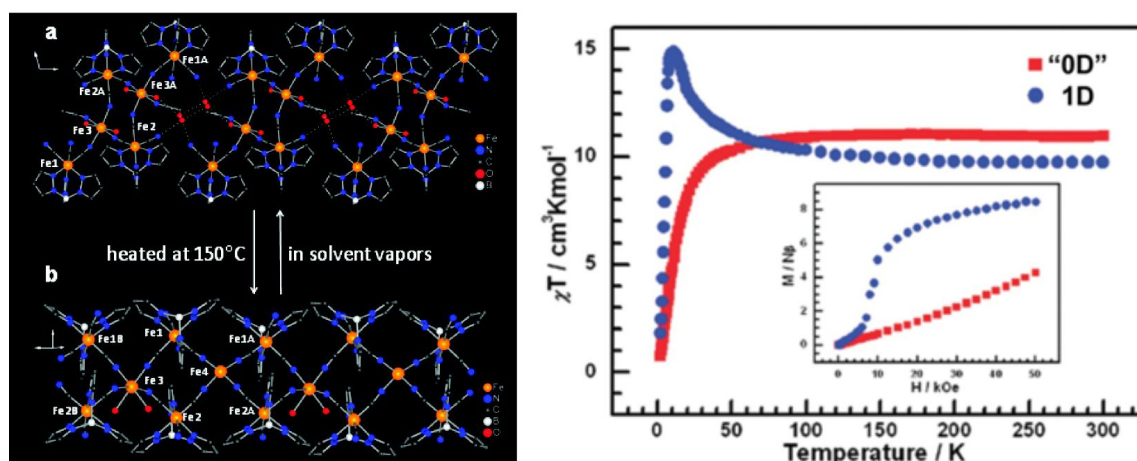


Figure 1.26 – (top) Schematic representation of portion of the crystal structures of $[\{\text{Fe}^{\text{III}}(L^{20})(\text{CN})_3\}_4\{\text{Fe}^{\text{II}}(\text{MeCN})(\text{H}_2\text{O})_2\}_2] \cdot 10\text{H}_2\text{O} \cdot 2\text{MeCN}$ (“0D”) and $[\text{Fe}^{\text{III}}(L^{20})(\text{CN})_3]_4\text{Fe}^{\text{II}}(\text{H}_2\text{O})_2\text{Fe}^{\text{II}}$ (1D) showing the presence of discrete complexes and 1D polymers, respectively. (bottom) χT vs. T plots (1 kOe field) and M vs. H plots at 2 K for the “0D” and 1 D compounds. Reprinted and adapted with permission.[183] Copyright 2009 American Chemical Society.

1.7 –Main Objectives

The work presented therein is focused on the preparation of new MOFs and CPs based on lanthanides and highly flexible phosphonic acids. The main purpose is directed to find the best conditions to obtain low-dimensional materials and use them as secondary building units to prepare large networks *via* single-crystal to single-crystal (SC-SC) transformations. Phosphonic acids were chosen over the conventional carboxylic acids due to their advantages. Phosphonic acids were initially hindered relatively to carboxylic acids because of three main problems: i) their preference to form dense metallic structures that, while having potential interesting function, it lacks in forming materials with high surface areas; ii) the fast precipitation when in contact with the metal solution gives rise to less crystalline materials; and iii) the presence of more coordination modes, allied to the different modes of coordination (not to mention the fact that protonated groups can also coordinated to the metal center) makes them even less predictable than materials with carboxylic acids. Nonetheless, the increase number of metal phosphonate frameworks is the evidence of their potential. Phosphonate groups are a strong anionic moiety, leading to the formation of stronger covalent bonds with metal ions. Not only that, but the C–PO₃ bond is considerably stronger than the C–CO₂ bond, allowing the formation of frameworks with higher thermal stability. Despite the low structural predictability, the higher number of coordination possible for the phosphonate results in a myriad of different arrangements and topologies. The greater advantage of phosphonates in MOFs is their increase biocompatibility, opening a new research area for these materials. Phosphonates have been extensively used as surface modifiers to improve the biocompatibility of bone replacements, among other biomedical applications.[184-188]

The work presented in this thesis is divided in two main parts, depending on the highly flexible phosphonic acid linker used:

i) Nitrilotris(methylphosphonic) acid (H₆nmp): one 1D and three 2D polymers will be presented, with emphasis on the 1D-2D and 2D-2D'/2D-3D SC-SC transformations (by change of pH, humidity and solvent removal), respectively. The remarkable catalytic and proton conductivity exhibited will also be discussed in Chapters 2 to 4.

ii) Hexamethylenediamine-*N,N,N',N'*-tetrakis(methylphosphonic acid) (H₈htp): three 3D materials will be discussed, with a detailed description of the 3D-3D' SC-SC transformation by solvent removal, in Chapter 5.

CHAPTER 2

One-Dimensional Lanthanide-Organic Coordination

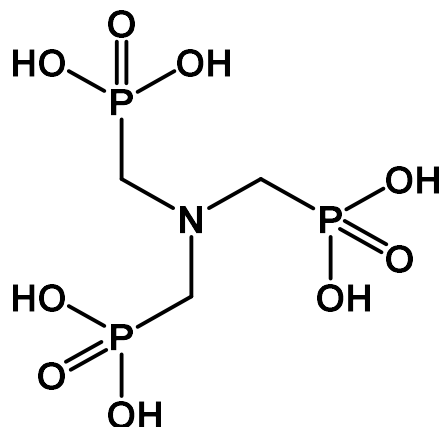
Polymer with Catalytic Activity

This chapter will be dedicated to the work developed in the preparation of a new 1D coordination polymer $[\text{La}_2(\text{H}_3\text{nmp})_2(\text{H}_2\text{O})_4] \cdot 4.5\text{H}_2\text{O}$ (**1**) [where H_6nmp stand for nitrilotris(methylphosphonic) acid, Scheme 2.1]. [23] The presence of the three $-\text{CH}_2$ groups in the H_6nmp organic linker allow for a higher freedom of the phosphonic acid groups which, ultimately, pose a challenge in the MOF/CP preparation due to its high flexibility. This high flexibility usual leads to the preparation of either complexes or amorphous materials. On the other hand, this particular characteristic is vital when one is looking for low dimensional materials. In the past decade the H_6nmp linker has already been used for the preparation of MOFs and CPs, with more interest in the preparation of these materials using transition metal. [43, 189-195]

In this chapter I will describe the synthesis of a 1D coordination polymer using three different methods: i) microwave-assisted synthesis, which allowed the rapid isolation of the pure compound at low reaction times and temperature; ii) hydrothermal and iii) one-pot, used with the sole purpose of obtaining large crystals for single-crystal X-ray diffraction studies. The structure of **1** was unveiled as $[\text{La}_2(\text{H}_3\text{nmp})_2(\text{H}_2\text{O})_4] \cdot 4.5\text{H}_2\text{O}$ by single-crystal X-ray diffraction of a crystal selected from the one-pot reaction and, due to the quality of the crystal, the structure was confirmed by two full Rietveld refinements performed on the microwave and hydrothermal powder samples. To avoid the isolation of layered materials using the H_6nmp organic linker and to promote the formation of the 1D polymer, reactions were performed at relatively low temperature (from 60 to 120 °C). Compound **1** was further characterized by a series of solid-state techniques, such as powder X-ray diffraction, thermogravimetry, FT-IR spectroscopy, elemental analysis, nuclear magnetic resonance and electron microscopy (SEM and EDS).

Building on our investigations on lanthanide-polyphosphonate networks, compound **1** was evaluated as a possible heterogeneous catalyst in the methanolysis of styrene oxide and in the acetalization of benzaldehyde. Our research group have already reported a one-dimensional (1D) polymer, $[\text{Ln}(\text{H}_4\text{bmt})(\text{H}_5\text{bmt})(\text{H}_2\text{O})_2] \cdot 3\text{H}_2\text{O}$ (H_6bmt = benzene-1,3,5-triyltris(methylene))triphosphonic acid), capable of acting as an excellent heterogeneous catalyst in the methanolysis of styrene oxide, even outperforming commercial MOFs such as the nano-sized HKUST-1. [88] Because this 1D MOF exhibited much better catalytic activity than, for example, the 3D zeolitic network $[\text{La}_2(\text{H}_3\text{bmt})_2(\text{H}_2\text{O})_2] \cdot \text{H}_2\text{O}$, [196] these

results prompted us investigate if low dimensional materials could also be isolated with the main objective to boost catalytic activity. The catalytic tests were performed in collaboration with Dra. Anabela Valente and Dra. Margarida Antunes.



Scheme 2.1 – Nitrilotris(methylphosphonic) acid (H_6nmp).

In the final part the structural transformation of compound **1** is also presented. By reacting **1** in water at 100 °C under typical one-pot conditions a complete conversion into $[La(H_3nmp)] \cdot 1.5H_2O$ (**2**) is observed,[197] while the same reaction in hydrothermal conditions lead to the formation of a mixture between $[La(H_3nmp)] \cdot 1.5H_2O$ and $[La(H_3nmp)]$. [198]

2.1 – Synthetic Strategy

One of the main challenges to prepare low dimensional CPs with polyphosphonic acid molecules is to control, in solution, the coordination step. In light to previous works,[197, 198] where H_6nmp has already been used in the preparation of different layered materials, we envisaged that to promote instead the formation of 1D polymers one should first act directly on this step. At first, the availability of the lanthanide cation should be diminished by changing the metal source to one much less soluble in water (the “green” solvent selected for the synthesis); second, the deprotonation of the phosphonate groups should also be considerably hindered to reduce the kinetics of crystal growth. Microwave irradiation was again used to promote a fast and uniform reaction between La_2O_3 and H_6nmp in the presence of sulphuric acid.

A new material, formulated as $[La_2(H_3nmp)_2(H_2O)_4] \cdot 4.5H_2O$ (**1**), was isolated and, as expected, X-ray diffraction studies show that it is composed by $\infty^1 [La_2(H_3nmp)_2(H_2O)_4]$ 1D CPs. For a relatively mild microwave irradiation of 50W, **1mw** could be isolated in just 1 min of irradiation at the low temperature of 60 °C. Increasing the reaction time and/or the temperature, the known layered phase $[La(H_3nmp)]$ is formed as a minor product.[197] At more extreme synthetic conditions amorphous compounds are, nevertheless, systematically and preferentially obtained (Figure 2.a).

An alternative synthetic, and still sustainable, approach we have also developed for this material is the use of one-pot synthesis (**1op**): in the absence of acid, the material could be isolated at 120 °C under stirring for 4 hours. Hydrothermal approaches also yield the same material (**1h**) and require a lower temperature (100 °C), but much longer reaction times (3 days) translating into considerable energy consumption.

The resulting materials obtained by these three methods show similar crystallinity (Figure 2.1b) exhibiting similar needle-like morphology, independent of the conditions used, with sizes ranging from 2 to 10 μm. The change in metal source for LaCl₃ proved to be ineffective since either [La(H₃nmp)]·1.5H₂O (**2**) or a mixture of phases was obtained.

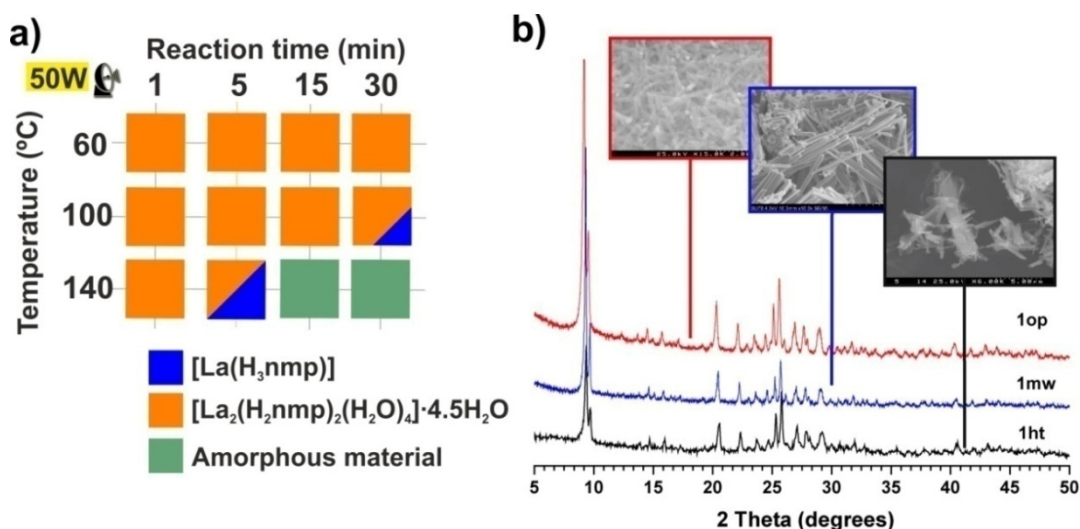


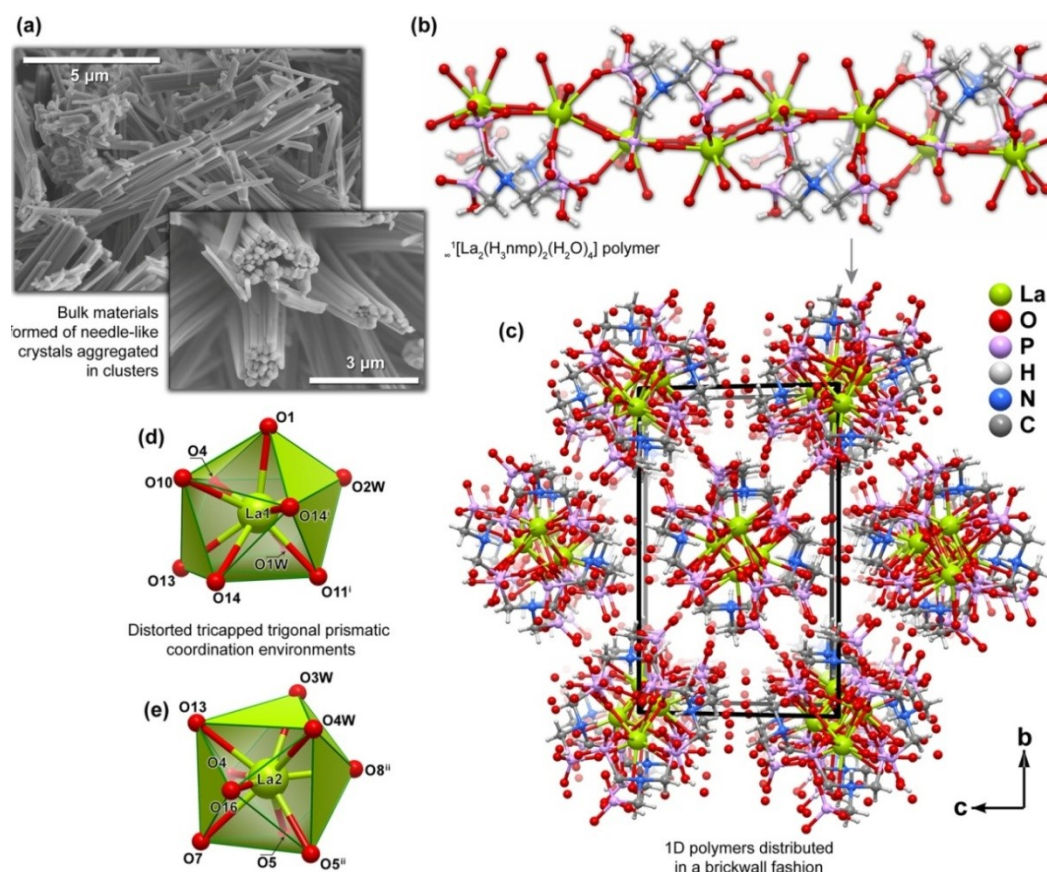
Figure 2.1 – (a) Optimization diagram for the microwave-assisted synthesis of [La₂(H₃nmp)₂(H₂O)₄]·4.5H₂O (**1mw**). (b) Comparison between the powder X-ray diffraction patterns and SEM images of the bulk [La₂(H₃nmp)₂(H₂O)₄]·4.5H₂O material obtained using the three methods described in the experimental section: **1mw**, **1op** and **1h**.

2.2 – Crystal Structure Description: Single-Crystal and Synchrotron Powder X-Ray Diffraction studies

The structural features of the material could only be unveiled by using a combination of high-resolution synchrotron powder X-ray diffraction with single-crystal X-ray diffraction, closely aided by various advanced bulk techniques such as solid-state NMR, FT-IR spectroscopy, thermoanalytical analyses and electron microscopy (Figure 2.2). The structure of **1** was unveiled as [La₂(H₃nmp)₂(H₂O)₄]·4.5H₂O by single-crystal X-ray diffraction of a crystal selected from the one-pot reaction and, due to the quality of the crystal, the structure was confirmed by two full Rietveld refinements performed on the microwave and hydrothermal powder samples. Independently of the preparation method, all materials exhibit the same structural features, particularly the ∞^1 [La₂(H₃nmp)₂(H₂O)₄] polymer with only small variations in average crystallite size being clearly noticeable (Figure 2.3).

Compound **1** crystallizes in the centrosymmetric *P2₁/c* space-group. The

$\infty^1[\text{La}_2(\text{H}_3\text{nmp})_2(\text{H}_2\text{O})_4]$ polymer (Figure 2.2b) is assembled by two crystallographically independent organic linkers and two La^{3+} metallic centers as depicted in Figure 2.2d and Figure 2.2e. Both metal centers are coordinated to two water molecules and seven oxygen atoms originating from neighbouring phosphonate groups, describing $\{\text{LaO}_9\}$ coordination environments whose geometries resemble distorted tricapped trigonal prisms. The bond distances and angles are in agreement with other lanthanide-based materials: in the range of 2.400(9) and 2.733(9) Å for the La-O bonds and between 63.2(3) and 150.2(3)° for the O-La-O angles. The connectivity between metal centres leads to the formation of a zigzag 1D chain with intermetallic $\text{La}\cdots\text{La}$ distances ranging between *ca.* 4.25 and 4.26 Å. Polymers grow along the [100] direction of the unit cell, packing in a typical brick-wall like fashion in the *bc* plane of the unit cell (Figure 2.2c). Uncoordinated water molecules occupy the interstitial spaces between adjacent polymers. As shown from the thermoanalytical studies, structural integrity of the $\infty^1[\text{La}_2(\text{H}_3\text{nmp})_2(\text{H}_2\text{O})_4]$ polymers is preserved while the coordinated water molecules remain attached to the metal centers. Once these are released (around *ca.* 100 °C) the material loses integrity and the crystal structure collapses (see next section for further detail).



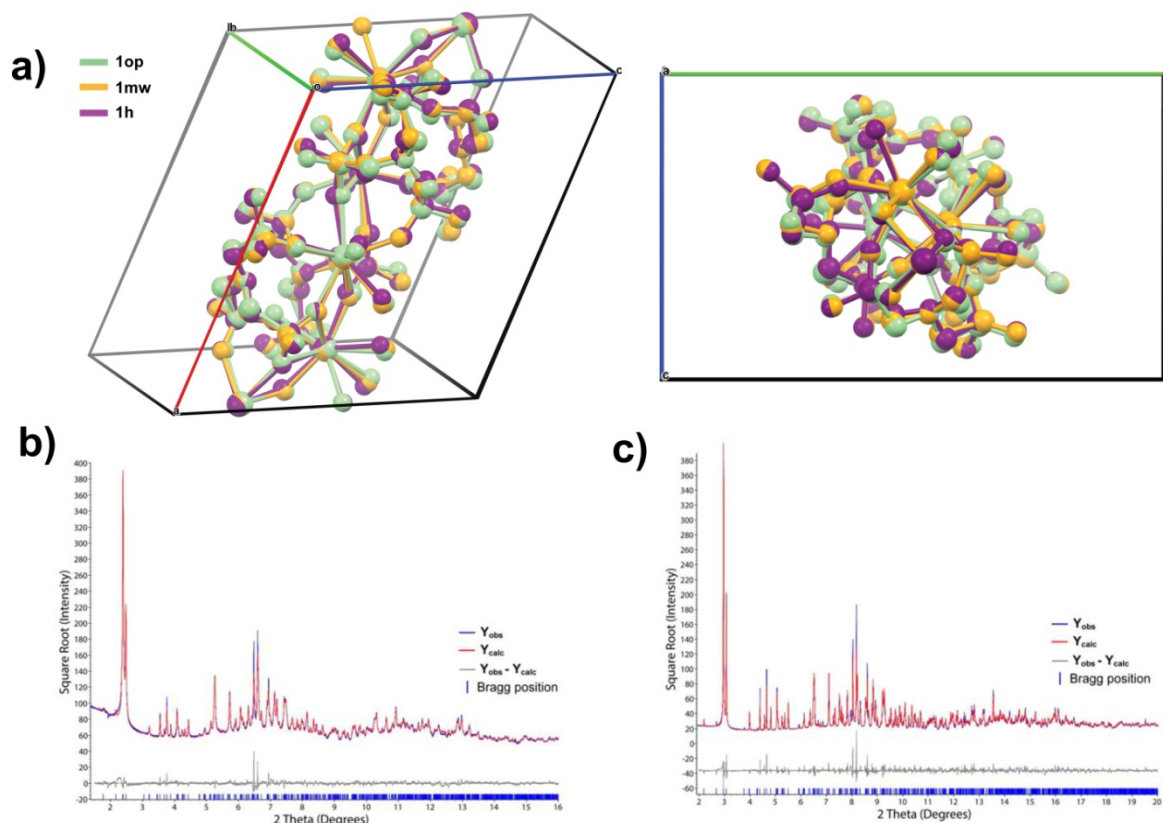


Figure 2.3 – (a) Unit cell and structure overlay of the ∞ [La₂(H₃nmp)₂(H₂O)₄] one-dimensional polymers present in the crystal structure determinations of **1mw**, **1h** and **1op** (images produced using the software package Mercury) and final Rietveld plot of (b) **1h** and (c) **1mw** (synchrotron X-ray diffraction data from ID31 and ID22 beam line at the ESRF – Grenoble, France). Observed data points are indicated as a blue line, the best fit profile (upper trace) and the difference pattern (lower trace) are drawn as solid red and grey lines, respectively. Blue vertical bars indicate the angular positions of the allowed Bragg reflections.

2.3 – Physicochemical Characterization

Thermogravimetry and Thermodiffractometry: thermogravimetric studies for the bulk [La₂(H₃nmp)₂(H₂O)₄]·4.5H₂O material prepared using the three employed synthetic approaches show that the thermal behaviour is very similar for all compounds. The small differences observed are attributed to the effect of the distinct crystallite size as shown in Figure 2.4, which has some influence in the kinetics of release of the various chemical components, particularly the water molecules (both of crystallization and coordinated).

The thermal stability of [La₂(H₃nmp)₂(H₂O)₄]·4.5H₂O was investigated between ambient temperature and *ca.* 800 °C as depicted in Figure 2.4. The presence of a large quantity and type of water molecules in the material prompted us to investigate the same behaviour in more detail between the ambient temperature and 160 °C by employing a much slower heating rate (Figure 2.4 *right*). In addition, for this latter temperature interval the overall crystallinity and phase identification of the bulk material was also evaluated by employing *in situ* variable-temperature powder X-ray diffraction studies (Figure 2.4 *right top*).

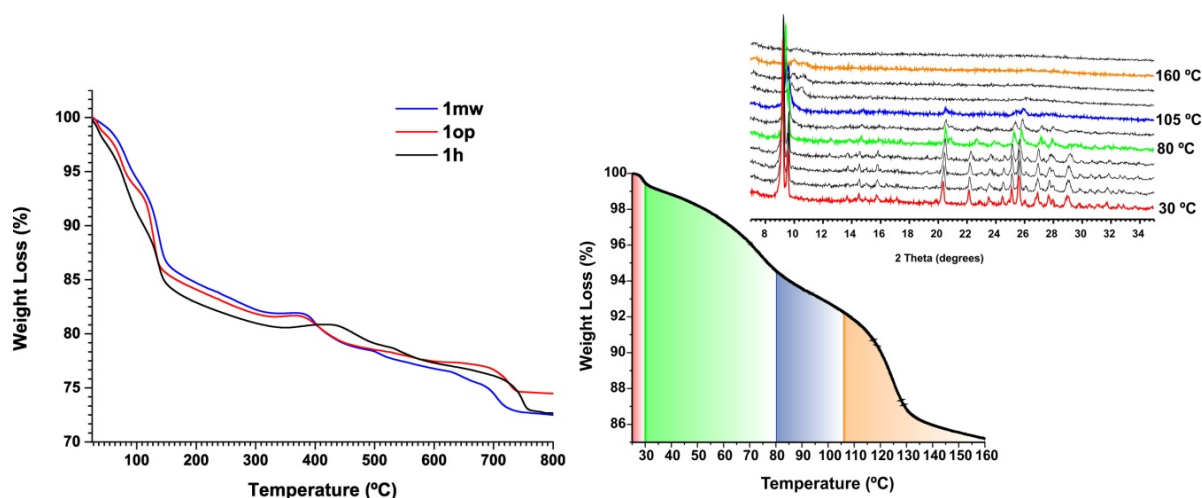


Figure 2.4- Comparison between the thermograms of the bulk $[\text{La}_2(\text{H}_3\text{nmp})_2(\text{H}_2\text{O})_4] \cdot 4.5\text{H}_2\text{O}$ materials obtained using the three methods described in the experimental section: **1mw**, **1op** and **1h** (*left*); and correspondence between the thermogram of $[\text{La}_2(\text{H}_3\text{nmp})_2(\text{H}_2\text{O})_4] \cdot 4.5\text{H}_2\text{O}$ (**1mw**), collected between ambient temperature and ca. 160 °C (heating rate of 1 °C/min), with variable temperature powder X-ray diffraction studies (*right*).

The material does not exhibit markedly visible and separated regions of thermal stability: transformations occur continuously between ambient temperature and *ca.* 800 °C. Nevertheless, it is clear that the thermal decomposition of the compound can be divided into two main stages: the first, corresponding to the release of all water molecules, occurs essentially at very low temperatures; the second, continuous over the overall temperature range, corresponds to the thermal decomposition of the organic component. For the first stage a second thermogravimetric study has been performed, with a much slower heating ramp in order to try to fully understand the process of release of the water molecules. Between ambient temperature and *ca.* 190 °C, **1mw** loses approximately 14.94% of mass which agrees well with the calculated value for the liberation of all water molecules, both of crystallization and coordinated (calculated value of *ca.* 14.91%). The release of these water molecules occurs in three-to-four consecutive steps without the presence of any plateau. Because of this it is difficult to assign each release step to a given family of water molecules. However, due to the very low temperature at which these moieties start to be liberated (as low as ambient temperature), it is feasible to assume that most of the uncoordinated molecules are released in a first stage. A similar behaviour was observed for the materials prepared using the alternative synthetic approaches: **1h** releases *ca.* 15.91% of mass up to *ca.* 160 °C, and **1op** *ca.* 15.44% up to a temperature of *ca.* 180 °C.

Variable-temperature powder X-ray diffraction studies on **1mw** corroborate the aforementioned assumption concerning the order of release of the water molecules up to a temperature of *ca.* 90 °C, the material retains some degree of crystallinity, strongly indicating that the released water molecules are not structurally very significant for the integrity of the 1D coordination polymer; when the coordinated water molecules start to be

released, the structure collapses and the material becomes amorphous, as clearly observed for the study performed at *ca.* 160 °C.

Upon release of all water molecules and after the compound becomes fully amorphous, the various weight losses observed are attributed to the slow decomposition of the organic component.

Vibration Spectroscopy: the FT-IR spectra of the bulk $[\text{La}_2(\text{H}_3\text{nmp})_2(\text{H}_2\text{O})_4] \cdot 4.5\text{H}_2\text{O}$ (**1**) materials is identical for the three employed synthetic methods as depicted in Figure 2.5, with the most striking bands being clearly associated with the chemical moieties composing the asymmetric unit.[199] The presence of a large number and diversity of water molecules is clearly observed in the spectra, with the existence of broad bands in the *ca.* 3500-3000 cm^{-1} and 1750-1650 cm^{-1} spectral ranges, attributed to the stretching and deformation vibrational modes of these chemical entities, respectively. The spectral region below *ca.* 1200 cm^{-1} is rich in various vibrational modes attributed to the coordinated phosphonate groups, particularly the symmetric and anti-symmetric $\nu(\text{P}=\text{O})$ modes. The presence of protonated POH groups from the organic linker is also markedly visible in the *ca.* 2850-2500 cm^{-1} spectral region, alongside with the $-\text{CH}_2-$ moieties which give rise to a number of stretching vibrational modes in the *ca.* 3050-2900 cm^{-1} spectral region.

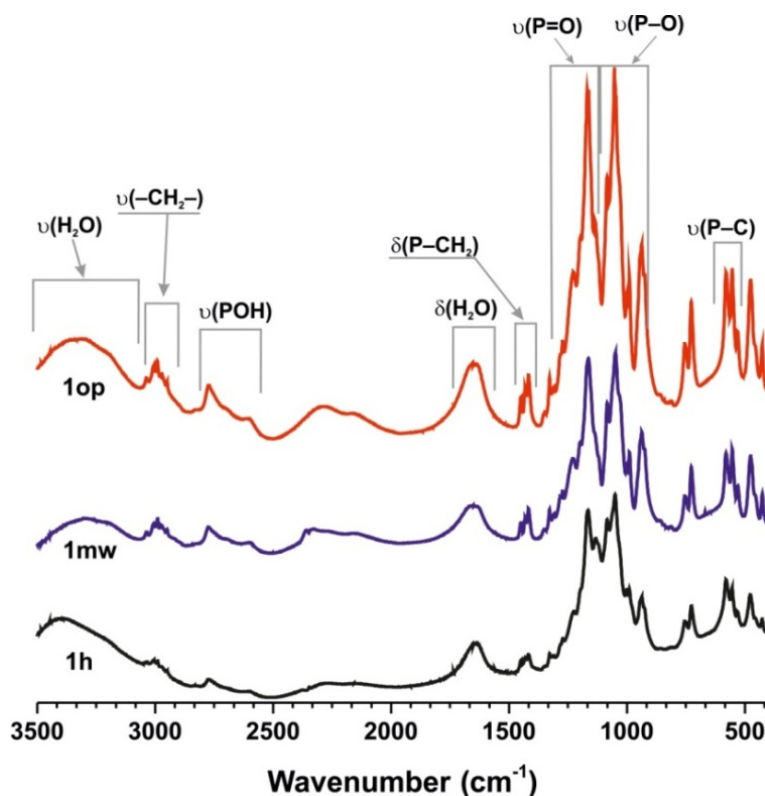


Figure 2.5 - Comparison between the FT-IR spectra of the bulk $[\text{La}_2(\text{H}_3\text{nmp})_2(\text{H}_2\text{O})_4] \cdot 4.5\text{H}_2\text{O}$ materials obtained using the three methods described in the experimental section: **1mw**, **1op** and **1h**.

Solid State Nuclear Magnetic Resonance: the presence of diamagnetic La^{3+} metallic centers in the structure of **1** permitted the use of solid-state NMR techniques to probe the composition of the asymmetric unit. Due to the overall poor crystal quality, as described in the technical section dedicated to X-ray diffraction, this solid-state NMR data was of crucial importance to unequivocally assess the number of crystallographically independent organic ligands in the asymmetric unit.

The HPDEC ^{31}P MAS spectrum of **1** shows, in the isotropic region, five well-resolved sharp peaks centered at *ca.* 2.6, 4.0, 5.3, 7.5 and 10.5 ppm (Figure 2.6). One of the resonances has a small visible shoulder, which is more noticeable in the spinning sidebands, referring to a 6th resonance centred at *ca.* 7.8 ppm. In short, the existence of six crystallographically independent phosphorus sites agrees well with the selected space group and the undertaken X-ray crystallographic studies.

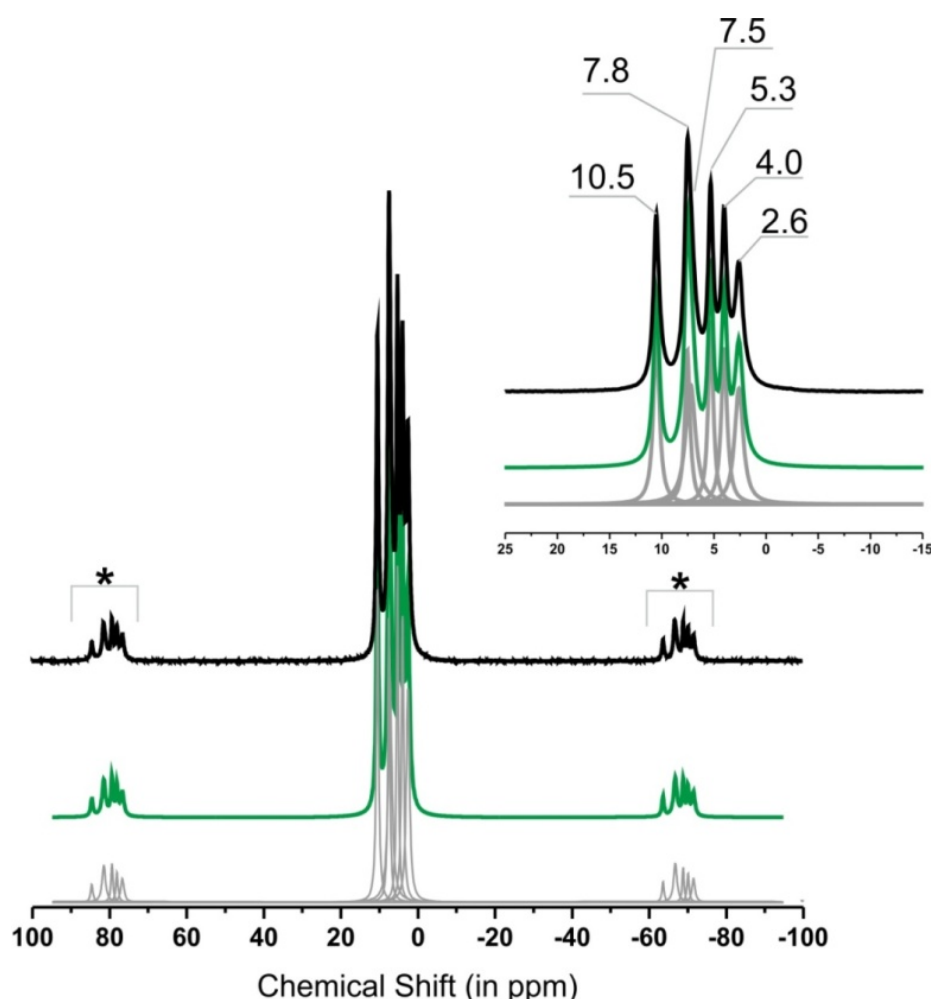
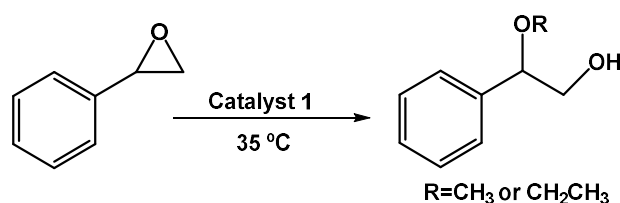


Figure 2.6- ^{31}P HPDEC MAS spectrum of $[\text{La}_2(\text{H}_3\text{nmp})_2(\text{H}_2\text{O})_4] \cdot 4.5\text{H}_2\text{O}$ (**1**). Spinning sidebands are denoted using an asterisk. Peak deconvolution and integration throughout the entire spectral range (*i.e.*, including the spinning sidebands) gives a ratio of *ca.* 0.89 : 1.16 : 1.25 : 0.88 : 0.86 : 0.96 for the isotropic resonances at *ca.* 10.5, 7.8, 7.5, 5.3, 4.0 and 2.6 ppm, respectively. The green line depicts the overall (*i.e.*, sum) data fit while the individual grey lines correspond to the fits of each single peaks.

2.4 – Catalytic Application

In terms of catalytic applications, and following the scope of our research group, compound **1** was tested as a heterogeneous catalyst in the alcoholysis of styrene oxide with methanol or ethanol, and in the acetalization of benzaldehyde with methanol. Epoxide ring opening reactions can afford β -alkoxy alcohols, which are functional, versatile intermediates used in (in)organic syntheses,[200] while, acetalisation reactions are important transformations in organic chemistry enabling the protection of carbonyl groups in the presence of other functional/reactive groups.[201-203] For the alcoholysis of styrene oxide (Scheme 2.2) **1** exhibits very high catalytic activity and excellent regioselectivity, giving the corresponding β -alkoxy alcohol products with 100% selectivity and 99% yield at 30 min (for 2-methoxy-2-phenylethanol) and 3 h (for 2-ethoxy-2-phenylethanol), respectively (Table 2.1). The alcoholysis of styrene oxide was faster with methanol than with ethanol (Figure 2.7), in line with that reported in the literature.[197, 204] This feature may be partly due to steric hindrance effects associated with the nucleophilic attack of the alcohol at the more hindered carbon atom of the oxirane ring. It is worth mentioning that the regio-chemical outcome of the epoxide ring opening reactions under acid or base conditions can be different: in the acid-catalysed reaction the nucleophile preferentially attacks the more substituted carbon of the oxirane ring, whereas in the base-catalysed reaction the less substituted carbon is preferred. Accordingly, the excellent regioselectivity towards the β -alkoxy alcohol product in the case of **1** is consistent with the acid nature of the active sites.



Scheme 2.2 – Reaction of styrene oxide with methanol or ethanol, catalyzed by **1**, to produce 2-methoxy-2-phenylethanol or 2-ethoxy-2-phenylethanol.

Table 2.1 – Ring opening of styrene oxide with methanol

Catalyst	Reaction time (h)	Conversion ^d (%)
1 ^b	0.25/0.5/1	86/98/99
1 ^c	0.25/1/2	45/87/97
La₂O₃	0.25/2/24	24/29/30
H₆nmp	0.25/0.5/1	59/97/99

^a Reaction conditions: styrene oxide (0.4M), methanol (1.5mL), catalyst [(b)20 g₁ L⁻¹ or (c) 3.3 g₁ L⁻¹ for **1** and 3.3 mM for La₂O₃ and H₆nmp]

^d Conversion of styrene oxide

A six-fold decrease in the amount of **1** from 20 to 3.3 g₁ L⁻¹ also led to similar outstanding catalytic results (Table 2.1). The role of the compound building blocks

(organic linker and metal center) in the catalysis process was investigated by performing catalytic tests in the polymer precursors (La_2O_3 and H_6nmp) and the heterogeneous nature of the reactions was investigated through leaching tests (see Chapter 6 for experimental details and Figure 2.8 and 2.9). Their catalytic performances (used in equivalent molar amounts to those corresponding to $3.3 \text{ g}_1 \text{ L}^{-1}$) indicated that the catalytic reaction is strongly promoted by Brönsted acidity: while H_6nmp led to 2-methoxy-2-phenylethanol as the sole product formed with 97% yield at 30 min, the reaction of styrene oxide in the presence of La_2O_3 was sluggish (a maximum conversion of 30% was reached at 30 min reaction; afterwards the catalyst was deactivated). The catalytic activity of **1** resembles more closely that of the ligand precursor than of the lanthanide one. Hence, the high catalytic activity of **1** is likely due to Brönsted acid sites associated with its organic component.

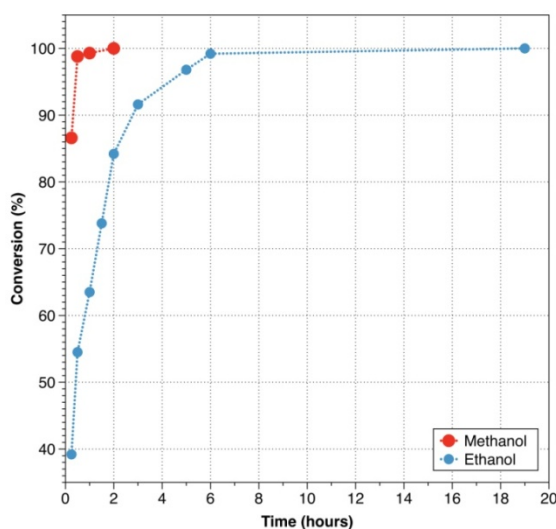


Figure 2.7 - Conversion of styrene oxide with methanol or ethanol in the presence of $[\text{La}_2(\text{H}_3\text{nmp})_2(\text{H}_2\text{O})_4] \cdot 4.5\text{H}_2\text{O}$ (**1**) at 35°C (catalyst load = $20 \text{ g}_1 \text{ L}^{-1}$). The corresponding β -alkoxy alcohol product was formed with 100% selectivity. *Please note:* dashed lines connected experimental points are only for illustrative purposes.

The catalyst was reused in consecutive batch runs of the methanolysis of styrene oxide (Figure 2.10), using simple centrifugation and filtration operations: a slight decrease of the initial reaction rate from the first to the second run was observed, but then it remained fairly similar. Conversion was, at least, 99% in consecutive 2 h batch runs, with 2-methoxy-2-phenylethanol selectivity being always 100%. While the structural integrity of **1** was always preserved, the average crystallite size decreased very slightly after the 1st run remaining relatively unchanged in subsequent runs (Figure 2.11).

Comparing the catalytic performance of **1** with that of the precursors we have inferred that it resembles more closely that of the ligand precursor, being thus associated with the Brönsted acid sites. The important role of Brönsted acidity of the catalyst for the target reaction has also been found for the 1D hybrid polymer $[\text{La}(\text{H}_4\text{bmt})(\text{H}_5\text{bmt})(\text{H}_2\text{O})_2] \cdot 3\text{H}_2\text{O}$ that exhibited outstanding catalytic performance in the

same reaction,[88] even outperforming the nano-sized commercial $[\text{Cu}_3(\text{BTC})_2]$ MOF (well known as HKUST-1).[205] **1** is more efficient than $[\text{La}(\text{H}_4\text{bmt})(\text{H}_5\text{bmt})(\text{H}_2\text{O})_2] \cdot 3\text{H}_2\text{O}$, with a total conversion of 97% reached at just 2 h of reaction, in opposition of 6 h for our previously reported material.

$[\text{La}_2(\text{H}_3\text{nmp})_2(\text{H}_2\text{O})_4] \cdot 4.5\text{H}_2\text{O}$ (**1mw**) was further studied as an heterogeneous acid catalyst in the acetalization of benzaldehyde with methanol (Scheme 2.3) at 35 °C. The material exhibited excellent selectivity towards benzaldehyde dimethyl acetal, which was formed as the sole product with 94% yield at 20 h reaction (Figure 2.12).

The catalytic performance of **1** compares favourably with that of other MOFs, namely $[\text{Al}_2(\text{BDC})_3]$, $[\text{Fe}(\text{BTC})]$ and $[\text{Cu}_3(\text{BTC})_2]$, as well as to other types of solid acid catalysts such as classical large-pore zeolites and mesoporous aluminosilicates. The registered differences in catalytic activities between the various materials may be partly due to distinct acidic properties.

For example, Timofeeva *et al.*[206] reported that the inclusion of electron-withdrawing NO_2 -groups into the UIO-66 framework enhanced its acidity and, ultimately, the catalytic activity in the acetalization of benzaldehyde with methanol. To the best of our knowledge this is the only material that could surpass **1** (at 4 h of reaction it converts 100 % of the substrate).[206] We note, however, that UIO-66- NO_2 is significantly more difficult to prepare than **1** (solvothelmal synthesis in a mixture of DMF / H_2O / HCl , for 2 days at 180 °C) and it has to be activated at 200 °C after each catalytic cycle. In short, we believe that based on purely practical and environmental reasons, **1** arises as one of the most efficient MOF material for the acetalization of benzaldehyde with methanol.

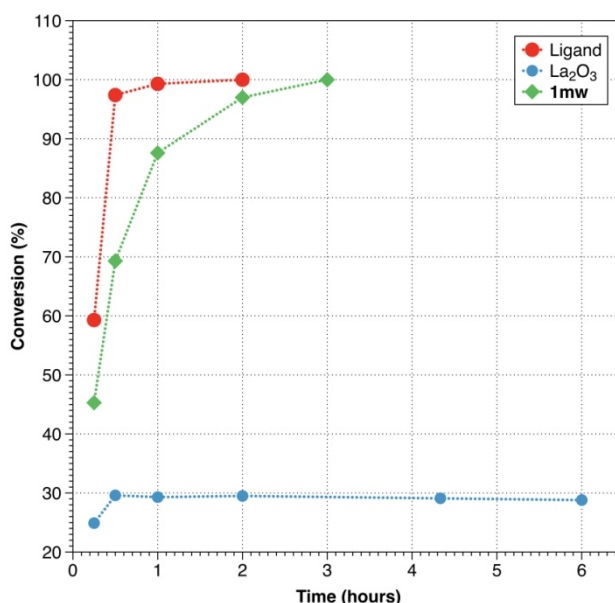


Figure 2.8 - Conversion of styrene oxide with methanol in the presence of **1**, the ligand precursor H_6nmp or the lanthanide precursor (La_2O_3), at 35 °C (catalyst load = $3.3 \text{ g}_\text{l} \text{ L}^{-1}$). The precursors were used in equivalent molar amounts to those corresponding to $3.3 \text{ g}_\text{l} \text{ L}^{-1}$. 2-Methoxy-2-phenylethanol was formed with 100% selectivity. Please note: dashed lines connected experimental points are only for illustrative purposes.

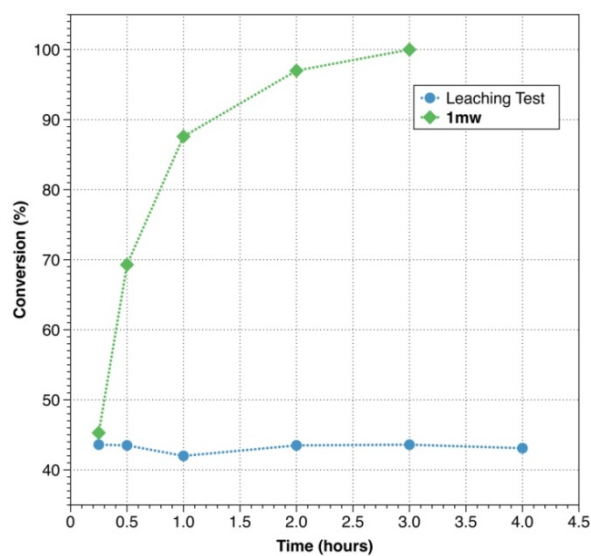


Figure 2.9 - Leaching test carried out for **1** in the methanolysis of styrene oxide at 35 °C, and comparison to the typical conditions without filtration of the catalyst (catalyst load = 3.3 g₁ L⁻¹). 2-Methoxy-2-phenylethanol was formed with 100% selectivity. *Please note*: dashed lines connected experimental points are only for illustrative purposes.

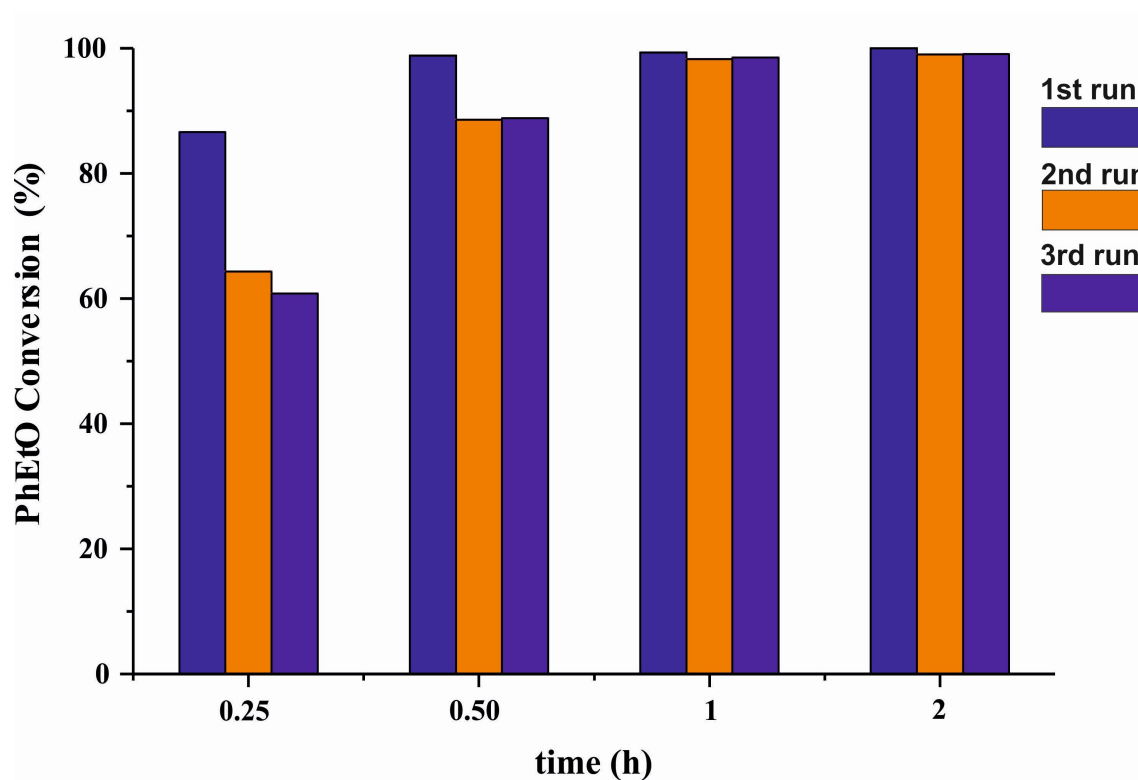


Figure 2.10 – Conversion of styrene oxide with methanol in the presence of **1** at 35 °C (catalyst load = 20 g₁ L⁻¹) for three consecutive batch runs.

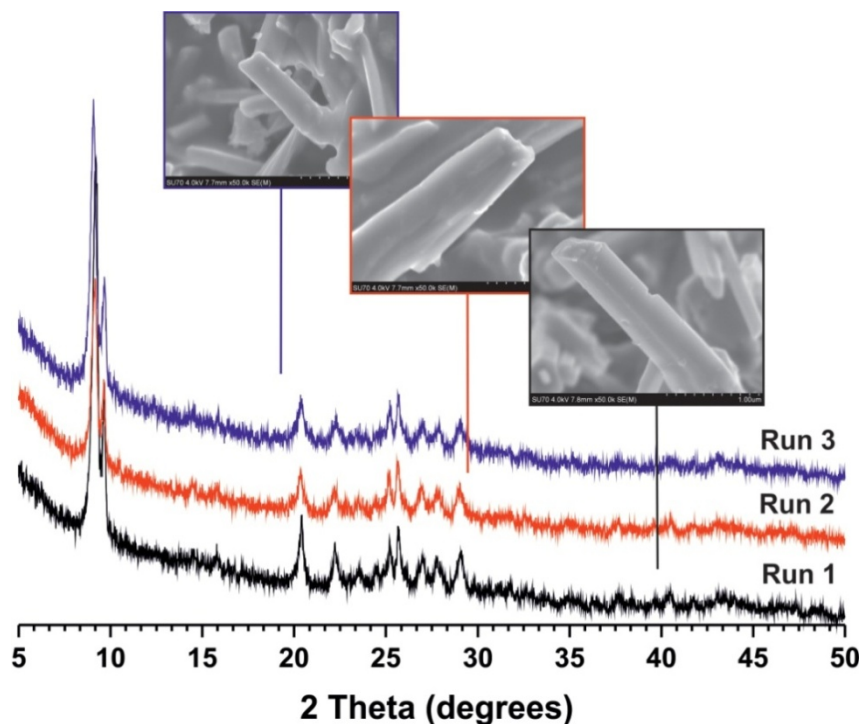
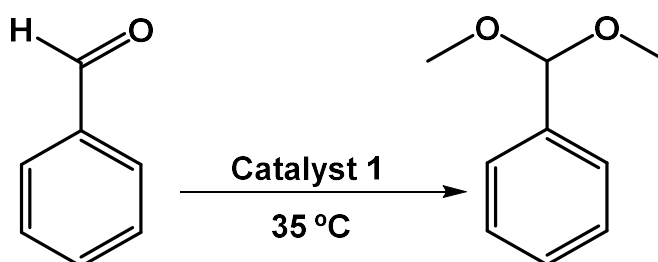


Figure 2.11 – Powder X-ray diffraction patterns and SEM images of the bulk 1 catalyst used in three consecutive batch runs of styrene oxide methanolysis.



Scheme 2.3 – Reaction of benzaldehyde with methanol catalyzed by 1, to produce benzaldehyde dimethyl acetal

2.5 - Transformation Studies

Motivated by the isolation of layered $[\text{La}(\text{H}_3\text{nmp})]$ [197] at more drastic synthetic conditions (Figure 2.1), and the observed structural robustness of the ${}^{\infty}[\text{La}_2(\text{H}_3\text{nmp})_2(\text{H}_2\text{O})_4]$ polymer, the possibility of transforming the phase herein reported into other functional materials has been investigated. $[\text{La}_2(\text{H}_3\text{nmp})_2(\text{H}_2\text{O})_4] \cdot 4.5\text{H}_2\text{O}$ (**1**) can be transformed at 100 °C into two different layered materials reported previously by our group $[\text{La}(\text{H}_3\text{nmp})] \cdot 1.5\text{H}_2\text{O}$ [198] and $[\text{La}(\text{H}_3\text{nmp})]$ [197]

Using one-pot conditions, $[\text{La}(\text{H}_3\text{nmp})] \cdot 1.5\text{H}_2\text{O}$ is always isolated as a pure phase after 24 h (Figure 2.13). The same occurs when a hydrothermal approach is employed in conjunction with a very slow cooling of the reaction vessels up to the ambient temperature

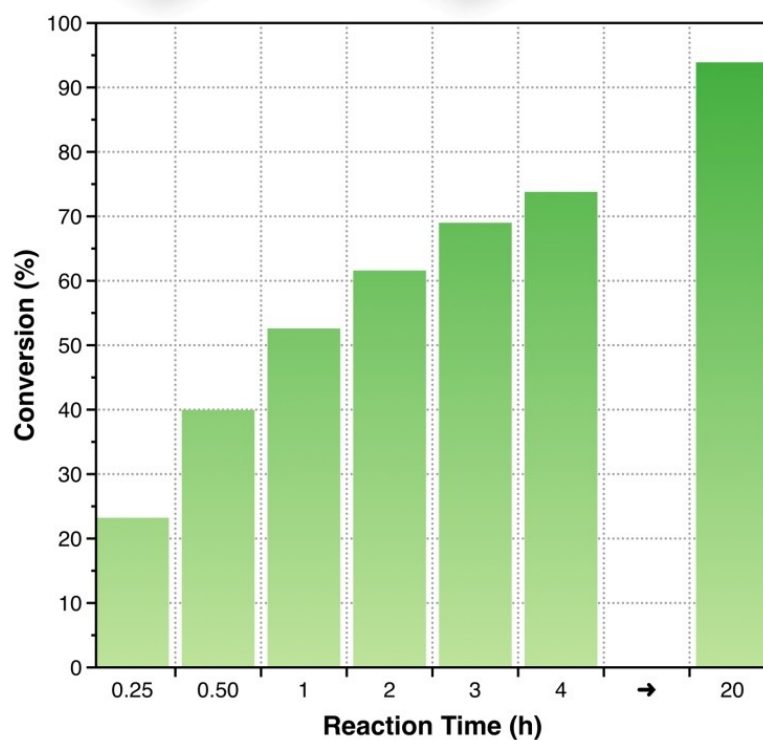


Figure 2.12– Conversion of benzaldehyde with methanol in the presence of **1** at 35 °C (catalyst load = 20 g₁ L⁻¹). The corresponding benzaldehyde dimethyl acetal product was formed with 100% selectivity.

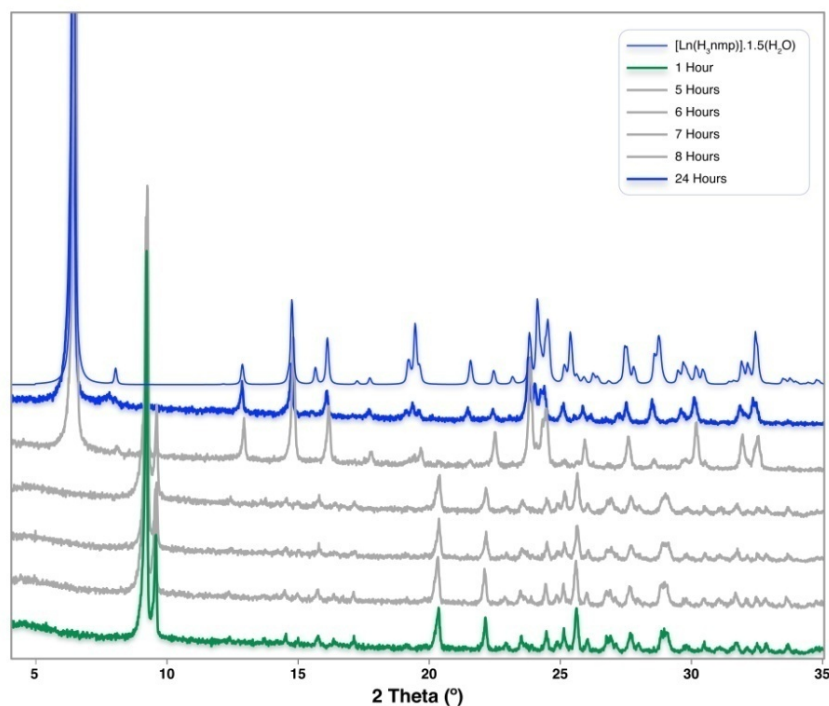


Figure 2.13 -Conversion of $[\text{La}_2(\text{H}_3\text{nmp})_2(\text{H}_2\text{O})_4] \cdot 4.5\text{H}_2\text{O}$ (**1**) into the layered $[\text{La}(\text{H}_3\text{nmp})] \cdot 1.5\text{H}_2\text{O}$ (**2**) material using one-pot conditions (100 °C over 24 h).

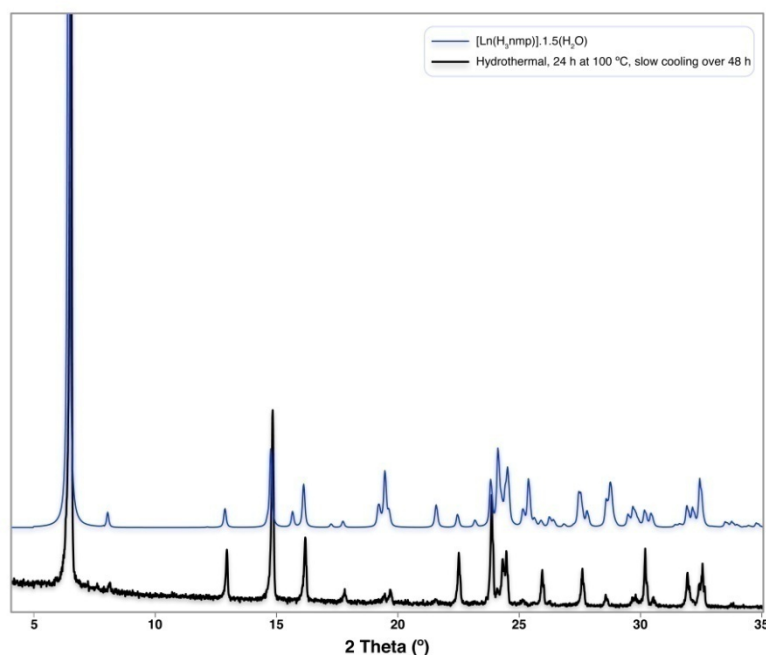


Figure 2.14 - Conversion of $[\text{La}_2(\text{H}_3\text{nmp})_2(\text{H}_2\text{O})_4] \cdot 4.5\text{H}_2\text{O}$ (**1**) into the layered $[\text{La}(\text{H}_3\text{nmp})] \cdot 1.5\text{H}_2\text{O}$ (**2**) material using hydrothermal conditions (100 °C over 24 h, with slow cooling to ambient temperature over a period of 48 h).

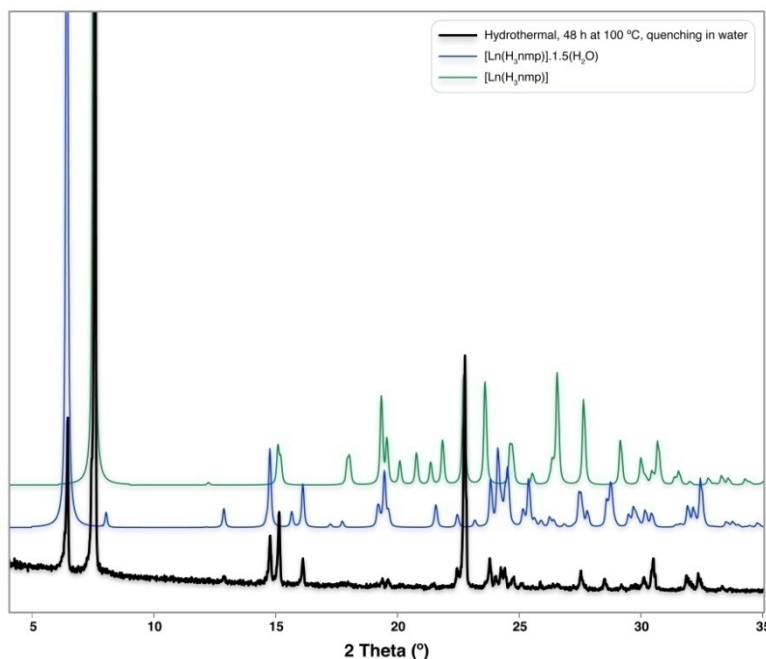


Figure 2.15 - Conversion of $[\text{La}_2(\text{H}_3\text{nmp})_2(\text{H}_2\text{O})_4] \cdot 4.5\text{H}_2\text{O}$ (**1**) into a mixture of layered $[\text{La}(\text{H}_3\text{nmp})] \cdot 1.5\text{H}_2\text{O}$ (**2**) and $[\text{La}(\text{H}_3\text{nmp})]$ (**3**) materials using hydrothermal conditions (100 °C over 48 h with a rapid quenching of the reaction vessels in cold water).

(Figure 2.14). If instead the vessels are quenched in cold water, a mixture of both $[\text{La}(\text{H}_3\text{nmp})] \cdot 1.5\text{H}_2\text{O}$ and $[\text{La}(\text{H}_3\text{nmp})]$ is isolated, with the latter material being the predominant phase (Figure 2.15). Figure 2.16 summarizes the reaction conditions

employed for the transformation tests and the phases that are obtained in each situation, while Figures 2.13 to 2.15 depict the powder X-ray diffraction patterns of the transformed phases compared with simulations for the two previously reported layered materials. No evidence for the real mechanism in which these transformations occur is evident. Even though during the one-pot synthesis no complete dissolution of **1** was observed, the need of addition of acid to all reactions might ultimately indicate that the primary building units may, indeed, undergo dissolution in a first stage and only then be used to produce compounds $[\text{La}(\text{H}_3\text{nmp})]\cdot 1.5\text{H}_2\text{O}$ and $[\text{La}(\text{H}_3\text{nmp})]$.

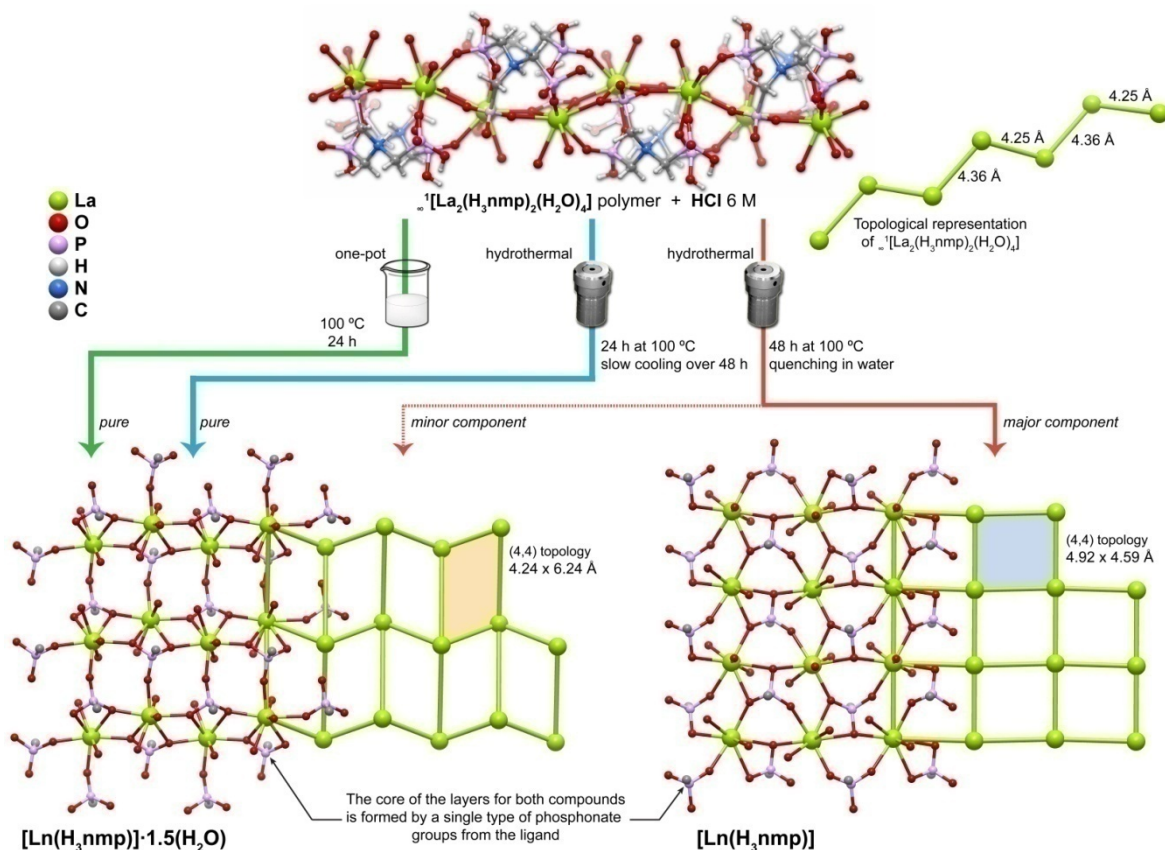


Figure 2.16 – Conversion of **1** into the layered $[\text{La}(\text{H}_3\text{nmp})]\cdot 1.5\text{H}_2\text{O}$ and $[\text{La}(\text{H}_3\text{nmp})]$ materials using hydrothermal and one-pot synthetic conditions

The two crystallographically independent La^{3+} coordination environments composing **1** share several similarities. Particularly, both environments comprise two coordinated water molecules that could easily be displaced in order to promote polymerization into $[\text{La}(\text{H}_3\text{nmp})]\cdot 1.5\text{H}_2\text{O}$ and $[\text{La}(\text{H}_3\text{nmp})]$. Indeed, as shown in Figure 2.16, the $\infty^1[\text{La}_2(\text{H}_3\text{nmp})_2(\text{H}_2\text{O})_4]$ polymer can be topologically envisaged as a zigzag chain of La^{3+} cations with intermetallic distances oscillating between 4.25 and 4.36 Å. A close inspection of the layers present in $[\text{La}(\text{H}_3\text{nmp})]\cdot 1.5\text{H}_2\text{O}$ and $[\text{La}(\text{H}_3\text{nmp})]$, both with a (4,4) topology, reveals that their core is simply assembled by the lanthanide cation and one phosphonate group, with small differences in the connectivity as shown in Figure 2.16. In

the case of compound $[\text{La}(\text{H}_3\text{nmp})]\cdot 1.5\text{H}_2\text{O}$, a clear zigzag chain with intermetallic distance of 4.24 Å strongly resembles the connectivity present in **1**. It is, thus, not surprising to observe that this material is easily obtained under all methods employed for the transformation tests, being readily isolated as a pure phase. The core layer of $[\text{La}(\text{H}_3\text{nmp})]$ is significantly more distinct implying a strong rearrangement of the connectivity of the phosphonate group (the intermetallic distances are, for example, significantly different from those present in **1**). In this context, one can easily understand how the transformation requires a longer reaction time (48 h) and a drastic quench of the temperature of the reaction vessel.

Due to these similarities in crystal structure we can go further and compare them in terms of applications, especially between **1** and $[\text{La}(\text{H}_3\text{nmp})]$. Both materials show activity in the methanolysis of styrene oxide. However **1** shows a surprising increase in conversion when compared to $[\text{La}(\text{H}_3\text{nmp})]$. While the latter converts 40, 77, and 100 % after 24, 48 and 72 hours, **1** can convert 99% after only 1 hour. The dimensionality seems to be therefore of great importance. This can be explained by the availability of the phosphonic acid groups in each material. As explained in Section 2.5 the catalytic activity of **1** resembles more closely that of the ligand precursor and its high catalytic activity is likely due to Brönsted acid sites associated with its organic component. The free phosphonic acid group in **1** (which in $[\text{La}(\text{H}_3\text{nmp})]$ is responsible to connect the zigzag chain of La^{3+}) might be the one responsible for this increase of catalytic activity.

2.6 – Concluding Remarks

In this chapter I presented the preparation of a new 1D coordination polymer, $[\text{La}_2(\text{H}_3\text{nmp})_2(\text{H}_2\text{O})_4]\cdot 4.5\text{H}_2\text{O}$ (**1**), by self-assembly of lanthanum and the highly flexible nitrilotris(methylphosphonic acid) (H_6nmp) organic linker. To avoid the systematic isolation of layered materials using this organic linker, and in order to promote the formation of 1D polymers, La_2O_3 was used as the metal source which was reacted with H_6nmp *via* three different methods: i) microwave irradiation, ii) conventional hydrothermal reaction and iii) one-pot synthesis. A novel 1D polymer, $^1[\text{La}_2(\text{H}_3\text{nmp})_2(\text{H}_2\text{O})_4]$, was isolated in just under 1 min and, as expected, exhibited a remarkable catalytic activity in both the alcoholysis of styrene oxide with methanol or ethanol and in the acetalization of benzaldehyde with methanol. Results clearly show that this new material surpasses all known compounds reported to date, including another 1D polymer previously reported by us, and that the reduction of the dimensionality boosted significantly the catalytic activity.. In addition, we have also demonstrated that the previously layered materials reported by our group could be obtained by chemical transformation of this low-dimensional MOF under appropriate conditions. We are currently exploring new ways to retain the low dimensionality of the MOFs while also reducing to the nano-range the crystallite size. We thus envisage that these materials can be processed into functional devices while the

properties herein described could further be improved toward meeting greater accessibility to the catalytic sites.

CHAPTER 3

Lamellar Coordination Polymer with a Remarkable Catalytic Activity and Proton Conductivity

In this section two 2D lamellar structures are presented, based on the same flexible triphosphonic acid linker reported in the previous chapter, nitrilotris(methylphosphonic) acid (Scheme 2.1). These materials appear as a continuation of the work developed in our research group based on this organic linker.[197, 198] In these previous works, due to the high flexibility of this organic linker, the resulting materials were isolated as microcrystalline powders. This limits the use of single-crystal X-ray diffraction to unveil their structural features, relying only on Rietveld refinement or synchrotron data. To overcome this problem we have introduced different acids in the reaction media.[23, 24] The acid acts as a retardant, protonating the organic linker, slowing the nucleation process and thus favoring the crystal growth.

In this work the introduction of hydrochloric acid in the synthesis forced the inclusion of additional acid sites and a new positively charged lamellar coordination polymer was synthesized. $[\text{Gd}(\text{H}_4\text{nmp})(\text{H}_2\text{O})_2]\text{Cl}\cdot 2\text{H}_2\text{O}$ (**2**) [where H_6nmp stands for nitrilotris(methylphosphonic acid)] is obtained in a typical one-pot approach using water as a “green” solvent. The hydrochloric acid plays an important role in the preparation of **2**. It not only allowed the formation of crystals suitable to unveil the structural features by single-crystal X-ray diffraction, but also is the source of chloride ions which are fundamental to maintain the integrity of the 2D layers, by forming strong hydrogen bonds. In this chapter I will describe the synthesis of **2**, as well as present the full characterization by thermogravimetry, FT-IR spectroscopy, elemental analysis and electron microscopy (SEM and EDS).

Following the studies presented in Chapter 2, $[\text{Gd}(\text{H}_4\text{nmp})(\text{H}_2\text{O})_2]\text{Cl}\cdot 2\text{H}_2\text{O}$ (**2**) was tested as a heterogeneous catalyst in the alcoholysis of styrene oxide and acetalisation of benzaldehyde. The surprising results in these reactions led us to test **2** in other catalytic reactions, such as acetalisation of cyclohexanaldehyde and ketalisation of cyclohexanone. For all reaction systems, very high conversions were reached (92-97%) in only 15-30 min, under mild conditions (35 °C, atmospheric pressure).

The high number of hydrogen interaction in between layers, as well as the presence of free phosphonic acid groups led us also to test **2** as a suitable proton conductor. The tests were performed in collaboration with Dr Filipe Figueiredo and Dra Paula Barbosa, at different temperatures and relative humidity. **2** also exhibit interesting protonic conductivity with values of $1.23 \times 10^{-5} \text{ Scm}^{-1}$ at 98% RH at 40 °C. At higher temperature

and humidity a single-crystal to single-crystal transformation is visible, accompanied with a great increase in conductivity values. At these conditions **2** is transformed into a previous material obtained in our group, $[\text{Gd}(\text{H}_3\text{nmp})]\cdot x\text{H}_2\text{O}$ (**3**). For this reason, I will also present in this chapter a structural comparison between the two structures (**2** and **3**) as well as the complete proton conductivity studies for the two materials.

3.1 – Synthetic approach

The main challenge in using flexible organic linkers is the difficult control in coordination and crystal growth. If not controlled properly, the assembly of this building blocks with different metals, especially lanthanides, can lead to the formation of amorphous materials. Even when crystalline materials are obtained, they normally lack in crystal quality. The use of acids helped considerably to obtain better crystals but in order to obtain pure-phase compounds, the experimental synthesis should first be fine tuned. In case of $[\text{Gd}(\text{H}_4\text{nmp})(\text{H}_2\text{O})_2]\text{Cl}\cdot 2\text{H}_2\text{O}$ (**2**) hydrochloric acid is fundamental in the synthesis because it is the source of chloride ions that charge-balance the 2D positively charged layers. **2** can be synthesized using three different methods:

i) Hydrothermal (**2ht**), at 100 °C for 18 h. The temperature does not influence the final product, as long as it stays above 100 °C and the $\text{HCl}:\text{H}_2\text{O}$ ratio is maintained in 1:1. The concentration of HCl is also important, with $[\text{Gd}(\text{H}_3\text{nmp})]\cdot x\text{H}_2\text{O}$ (**3**) being the sole product with lower concentrations.

ii) One-pot (**2op**), at 120 °C for 18 h. The temperature above 120 °C also does not affect the final product with $\text{HCl}:\text{H}_2\text{O}$ ratio of 1:1. The reaction time on the other hand plays an important role. At low reaction time (between 18-24h) **2** is obtained as a pure-phase compound, while as higher reaction times (between 24-48h) $[\text{Gd}(\text{H}_3\text{nmp})]\cdot x\text{H}_2\text{O}$ (**3**) is instead obtained as pure phase. The same applies for the concentration of HCl: lower concentrations favor the formation of **3**.

iii) Microwave (**2mw**), at 90 °C for 20 min. Microwave synthesis is ideal to prepare materials with low reaction times. However, at these conditions (between 5 and 10 min) **2** is obtained always in a mixture with $[\text{Gd}_2(\text{H}_3\text{nmp})_2(\text{H}_2\text{O})_4]\cdot 4.5\text{H}_2\text{O}$ (**1**) (presented in Chapter 2). **2** can however be obtained as a pure phase material at higher reaction times (between 20 and 30 min).

The other 2D lamellar structure based on the same building blocks, $[\text{Gd}(\text{H}_3\text{nmp})]\cdot x\text{H}_2\text{O}$ (**3**), was already studied in our research group and share some similarities with **2**. In fact, at higher temperatures and humidity the latter suffer a single-crystal to single-crystal transformation into **3**. Nevertheless **3** can also be obtained as pure-phase material using similar experimental conditions as for **2**:

i) Hydrothermal (**3ht**): poorly crystalline compound **3** could be isolated after just a few hours of reaction in water (*e.g.*, 2h at 140 °C or 1h at 190 °C). The crystallinity could be slightly improved using hydrochloric acid and longer reaction times (*e.g.* 12h at 120 °C with a $\text{HCl}:\text{H}_2\text{O}$ ratio of 1:2).

ii) Microwave (**3mw**): for temperatures lower than *ca.* 100 °C amorphous materials are isolated. Using the same conditions as for **2mw** without the presence of hydrochloric acid allow the preparation of pure-phase **3** but with low crystallinity.

iii) One-pot (**3op**): poorly crystalline material can be isolated at lower temperatures (*e.g.*, refluxing at 80 °C for 12h). The crystallinity can be improved by introducing hydrochloric acid in the reaction (HCl:H₂O ratio of about 1/1, with lower concentration than used for **2**) and refluxing at 120 °C for 48h.

One can see that despite the experimental method used the crystallinity for the two different materials is very similar (except for **3** under microwave radiation), as presented in Figure 3.1.

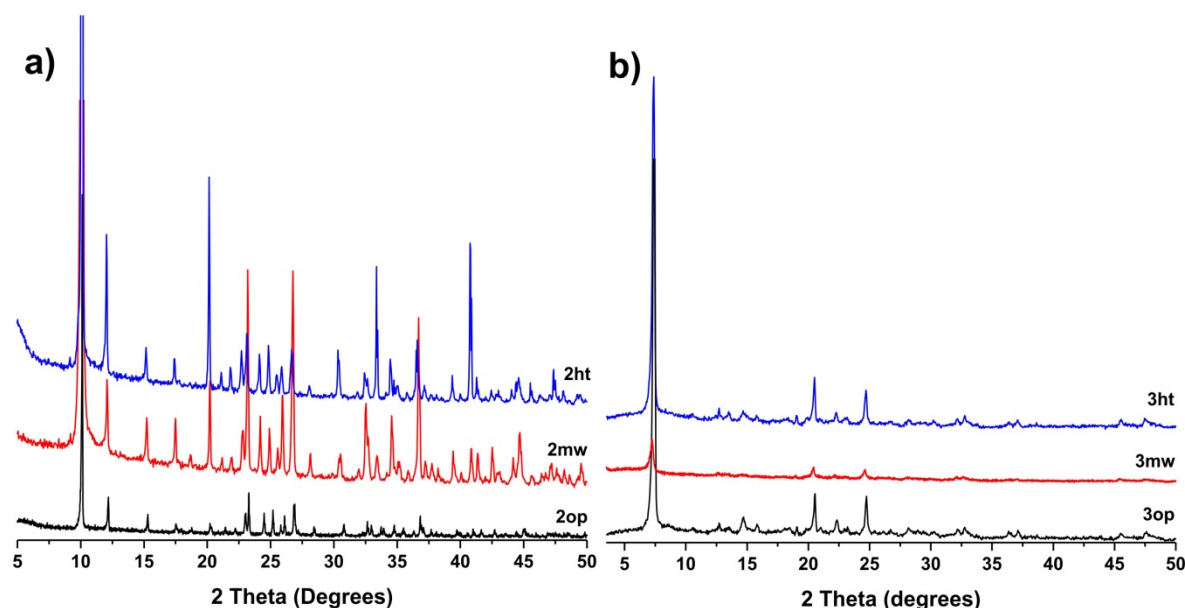


Figure 3.1 - Comparison between the powder X-ray diffraction patterns of the bulk (a) $[\text{Gd}_2(\text{H}_3\text{nmp})_2(\text{H}_2\text{O})_4] \cdot 4.5\text{H}_2\text{O}$ (**2**) and (b) $[\text{Gd}(\text{H}_3\text{nmp})] \cdot 3\text{H}_2\text{O}$ (**3**) materials obtained using the three methods described in the experimental section: one-pot (**op**), microwave (**mw**) and hydrothermal (**ht**).

3.2 – Crystal Structure Elucidation: $[\text{Gd}(\text{H}_4\text{nmp})(\text{H}_2\text{O})_2]\text{Cl} \cdot 2\text{H}_2\text{O}$ (**2**)

Compound **2**, formulated as $[\text{Gd}(\text{H}_4\text{nmp})(\text{H}_2\text{O})_2]\text{Cl} \cdot 2\text{H}_2\text{O}$, crystallizes in the non-centrosymmetric monoclinic *Ia* space group, being composed of infinite 2D positively charged layers, counter balanced by chloride ions which are located in the interlayer spaces.

The asymmetric unit consists of one eight-coordinated Gd^{3+} center, one bridging and chelating $\text{H}_4\text{nmp}^{2-}$ anionic organic linker, two coordinated and two uncoordinated water molecules plus the charge-balancing uncoordinated chloride anion (Figure 3.2). The crystallographic unique Gd^{3+} center is coordinated to a total of six phosphonate groups arising from four symmetry-related $\text{H}_4\text{nmp}^{2-}$ anionic organic linkers and two coordination water molecules, with the $\{\text{GdO}_8\}$ coordination polyhedron resembling a distorted dodecahedron (Figure 3.2). The Gd–O bond lengths were found in the 2.326(3)-2.564(3) Å

range, which is comparable to those reported for other Gd^{3+} -based phosphonate compounds. The internal O–Gd–O polyhedral angles were found in the $65.37(11)$ – $150.53(11)^\circ$ range. $\text{H}_4\text{nmp}^{2-}$ acts as a hexadentate organic linker connecting four symmetry-related metal centers. All phosphonate groups act μ_2 -O,O'-bridging moieties, with two of them being connected to the same pair of metal centers. As reported for the related $[\text{Pr}(\text{H}_3\text{nmp})]\cdot 1.5\text{H}_2\text{O}$ compound,[198] this high connectivity of the $\text{H}_4\text{nmp}^{2-}$ organic ligand is responsible for the trapping of Gd^{3+} centers inside a phosphonic-type inorganic matrix.

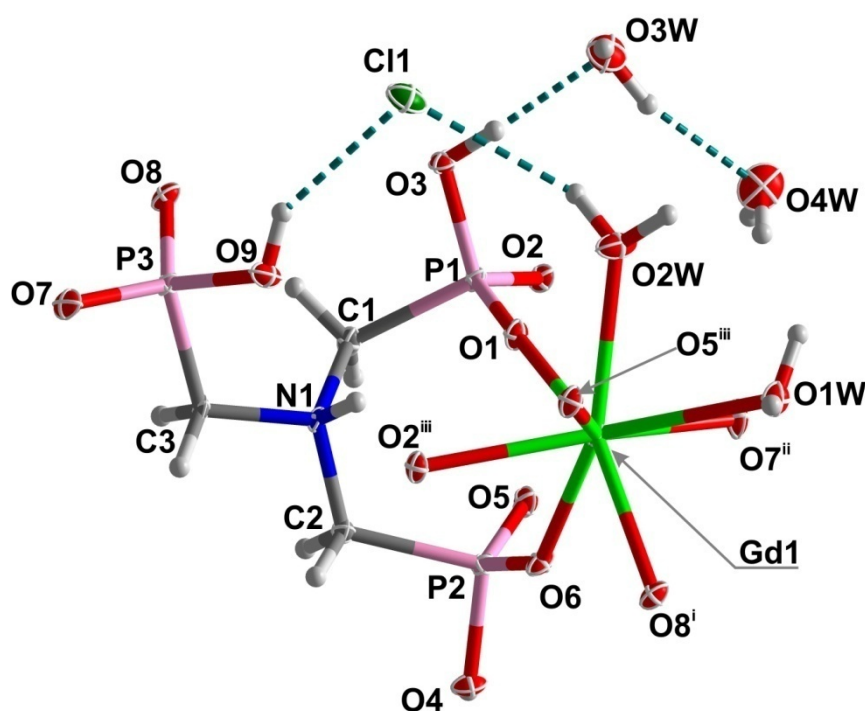


Figure 3.2 - The asymmetric unit of $[\text{Gd}(\text{H}_4\text{nmp})(\text{H}_2\text{O})_2]\text{Cl}\cdot 2\text{H}_2\text{O}$ (**2**) showing all non-hydrogen atoms represented as displacement ellipsoids drawn at the 50% probability level and hydrogen atoms as small spheres with arbitrary radius. The coordination sphere of the crystallographically independent metallic center was completed for the sake of clarity. Symmetry codes used to generate equivalent atoms: (i) $x+1, y, z$; (ii) $x+1, -y+1/2, z+1/2$; (iii) $x, -y+1/2, z-1/2$.

The layer arrangement is composed of one-dimensional inorganic zigzag chains running parallel to the c -axis of the unit cell, formed by Gd^{3+} polyhedra interconnected by three phosphonate groups from two different $\text{H}_4\text{nmp}^{2-}$ ligand residues [intermetallic $\text{Gd}\cdots\text{Gd}$ distance of $5.6081(3)$ Å]. The organic part of the ligand bridges these inorganic chains, forming a layer parallel to the ac plane with an additional intermetallic $\text{Gd}\cdots\text{Gd}$ distance of $8.4834(3)$ Å (Figure 3.3). The organic linker in **2** acts as a typical zwitterionic species, with the central nitrogen atom being protonated and the peripheral phosphonates groups being, each, singly negatively charged ($-\text{PO}_3\text{H}^-$). We note that this zwitterionic behavior has already been observed for other compounds based on aminophosphonate

residues.[198, 207] The protonated P–OH groups and coordinated water molecules of the $\infty^2[\text{Gd}(\text{H}_4\text{nmp})(\text{H}_2\text{O})_2]^+$ cationic layer donate their hydrogen atoms to neighbouring water molecules of crystallization and to the chloride anion (Figure 3.4).

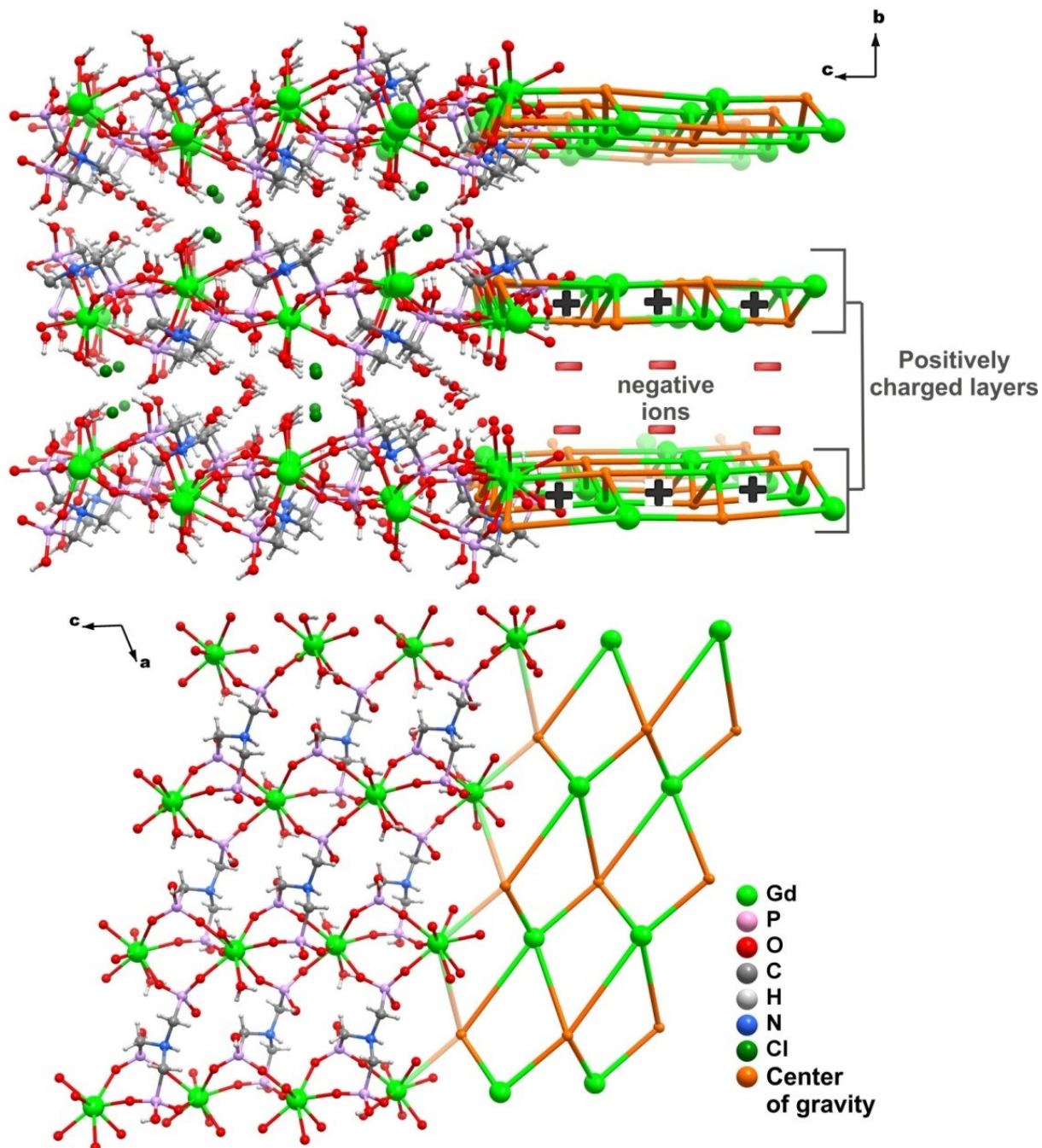


Figure 3.3 - Schematic representation of the (*top*) crystal packing of $[\text{Gd}(\text{H}_4\text{nmp})(\text{H}_2\text{O})_2]\text{Cl}\cdot 2\text{H}_2\text{O}$ (**2**) viewed in perspective along the [100] direction of the unit cell, and of the (*bottom*) $\infty^2[\text{Gd}(\text{H}_4\text{nmp})(\text{H}_2\text{O})_2]^+$ cationic layer. The 4-connected uninodal topology of the cationic layers is overlapped in both representations.

To the best of our knowledge **2** constitutes the first example of a phosphonate-based MOF having positively charged 2D layers, balanced in the interlamellar space by

uncoordinated chloride ions (Figure 3.3). This structural feature closely resembles those of the naturally-occurring layered double hydroxides (LDH), which are anionic clay materials with demonstrated usefulness in a wide range of applications, such as heterogeneous catalysts of a variety of organic reactions.[208] We note that for LDHs a variety of charge-balancing ions can be intercalated, ultimately improving catalytic activity. The presence of intercalated chloride anions in **2** has the same effect: two neutral layered materials based on the same organic linker and previously reported by our group, $[\text{La}(\text{H}_3\text{nmp})][197]$ (isolated from microwave-assisted synthesis) and $[\text{Pr}(\text{H}_3\text{nmp})]\cdot 1.5\text{H}_2\text{O}$ (prepared using hydrothermal synthesis), [198] performed comparatively poorly as heterogeneous acid catalysts with respect to the results therein described for **2**.

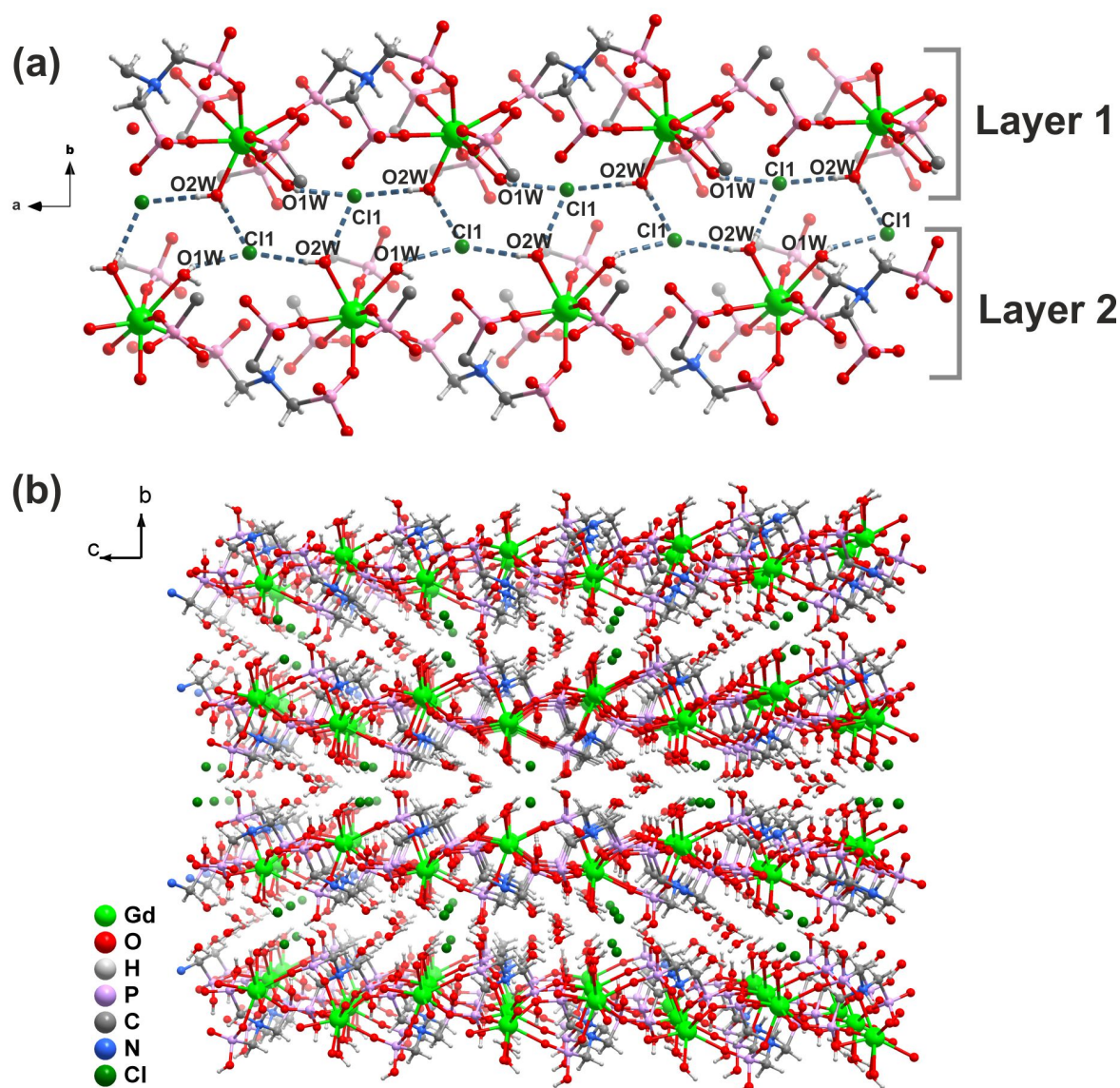


Figure 3.4 – (a) Schematic representation of the hydrogen bonding interactions located in the interlayer space of $[\text{Gd}(\text{H}_4\text{nmp})(\text{H}_2\text{O})_2]\text{Cl}\cdot 2\text{H}_2\text{O}$ (**2**) and involving the charge-balancing chloride anions. (b) Crystal packing of **1** viewed in perspective along the [100] direction of the unit cell.

All of these compounds have a 2D layered structure with the difference that **2** has positively charged sheets involved in strong hydrogen-bonding interactions. Looking at the structures from a topological perspective (*i.e.*, reducing each network to central nodes and connecting bridges), one can see that they are, nevertheless, very similar: on the one hand, the three layered networks are assembled by a single crystallographic independent Ln^{3+} center; on the other, the asymmetric unit is also composed of one $\text{H}_{6-x}\text{nmp}^{-x}$ ($x = 3$ or 4) residue. Structural differences occur, indeed, in the quantities of water molecules and the non-coordinating chloride ions for **2**. Thus, each organic residue is connected to four crystallographically independent Ln^{3+} centers, with all compounds being topologically uninodal networks with 4-connected nodes and a Schläfli point symbols of $\{4^4.6^2\}$ (Figure 3.3 and Figure 3.5).

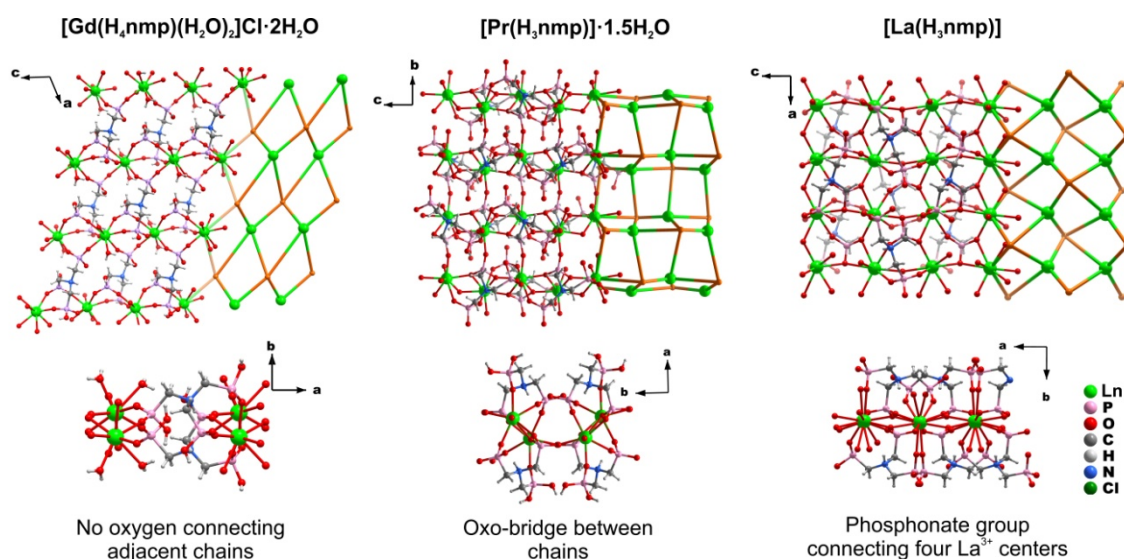


Figure 3.5 – Structural comparison between the crystal features and topologies of compounds $[\text{Gd}(\text{H}_4\text{nmp})(\text{H}_2\text{O})_2]\text{Cl}\cdot 2\text{H}_2\text{O}$ (**2**), $[\text{Pr}(\text{H}_3\text{nmp})]\cdot 1.5\text{H}_2\text{O}$ and $[\text{La}(\text{H}_3\text{nmp})]$. The orange node in the topological representations corresponds to the centre of gravity of the connecting organic ligand.

Structural differences between **2** and $[\text{La}(\text{H}_3\text{nmp})]$ or $[\text{Pr}(\text{H}_3\text{nmp})]\cdot 1.5\text{H}_2\text{O}$ arise, mainly, from the supramolecular interactions present between the layers. In **2**, coordinated water molecules and protonated P–OH groups interact with charge-balancing chloride anions and water molecules of crystallization, ultimately leading to a stronger close packing of cationic layers. In $[\text{Pr}(\text{H}_3\text{nmp})]\cdot 1.5\text{H}_2\text{O}$, which is also a hydrated material, the supramolecular interactions are limited to hydrogen bonds between P–OH groups and crystallization water molecules. These interactions are, thus, weaker than those found in **2**, resulting in a higher thermal stability for the latter: while in $[\text{Pr}(\text{H}_3\text{nmp})]\cdot 1.5\text{H}_2\text{O}$ the water molecules of crystallization are completely removed at *ca.* 75 °C immediately accompanied by a structural modification, **2** is stable up to *ca.* 150 °C. For $[\text{La}(\text{H}_3\text{nmp})]$ the interaction between layers is notably different: without solvent molecules the interaction between layers is achieved mainly by hydrogen bonding interactions associated with the protonated P–OH groups. Although the connectivity is the same for all three

compounds, in the case of [La(H₃nmp)] four metal centers are connected by a single phosphonate group forming a far more compact layer.

3.3 – Physicochemical Characterization

Thermal Behavior: The level of hydration level observed in the crystal structure was investigated by thermogravimetric analysis between ambient temperature and *ca.* 800 °C (Figure 3.6). The bulk [Gd(H₄nmp)(H₂O)₂]Cl·2H₂O (**2**) show a continuous weight loss with no visible plateaus. Nevertheless, as seen in Figure 3.6 one can divide the thermogram into three main regions, each corresponding to a combined weight loss. The first region, located between ambient temperature and *ca.* 195 °C, is attributed to the release of four water molecules (two of crystallization and two of coordination), corresponding to a total weight loss of 12.6% (calculated 12.8%). When the temperature is increased the material undergoes a crystalline phase transition, as clearly observed from the performed variable-temperature powder X-ray diffraction studies. There is some peak broadening (suggesting loss of crystallinity) and reflection dislocations, which is an indication of variation of the unit cell dimensions. We note that these structural modifications may suggest a closer proximity between the gadolinium oxide layers within the temperature-modified structure, a feature observed for [La(H₃nmp)].[197]

The next weight loss, in the range of about 195-355 °C (4.4%), can be attributed to the partial release of a hydrochloric acid residue (calculated 6.5%). The difference in calculated and observed weight loss might be due to the presence of agglomerates in the sample leading to an entrapment of the hydrochloric acid, which will be ultimately released at a higher temperature. To corroborate this assumption we have performed EDS analysis of the material calcined at different temperatures, clearly showing that up to *ca.* 350 °C all the chloride anions are released from the material (Figure 3.6 – inset; Figures 3.7, 3.8 and 3.9). Noteworthy, the release of HCl is accompanied by an overall loss of crystallinity.

Above *ca.* 350 °C additional weight losses (6.1% and 5.6% in the ranges of about 350-550 °C and 550-800 °C, respectively) are attributed to the full decomposition of the organic component.

Vibration Spectroscopy: The vibrational spectrum (Figure 3.10) contains a series of bands centered at about 3400 cm⁻¹ attributed to the $\nu(\text{O-H})$ stretching vibrational modes from both coordination and crystallization water molecules. The typical symmetric and asymmetric $\nu(\text{C-H})$ and $\nu(\text{N-H})$ stretching vibrational modes appear in the 3100-2750 cm⁻¹ region of the spectrum. The latter mode is found at about 3057 cm⁻¹, while the signals peaking at about 3027, 2982, 2954 and 2778 cm⁻¹ are attributed to the $\nu_{\text{sym+asym}}(\text{C-H})$ vibrational modes. In the central region of the spectrum, between 1500 and 1300 cm⁻¹, a number of very weak bands can be attributed to $\nu(\text{C-H})$ modes characteristic of P-CH₂ groups. The typical P-OH stretching modes were also observed between 2200

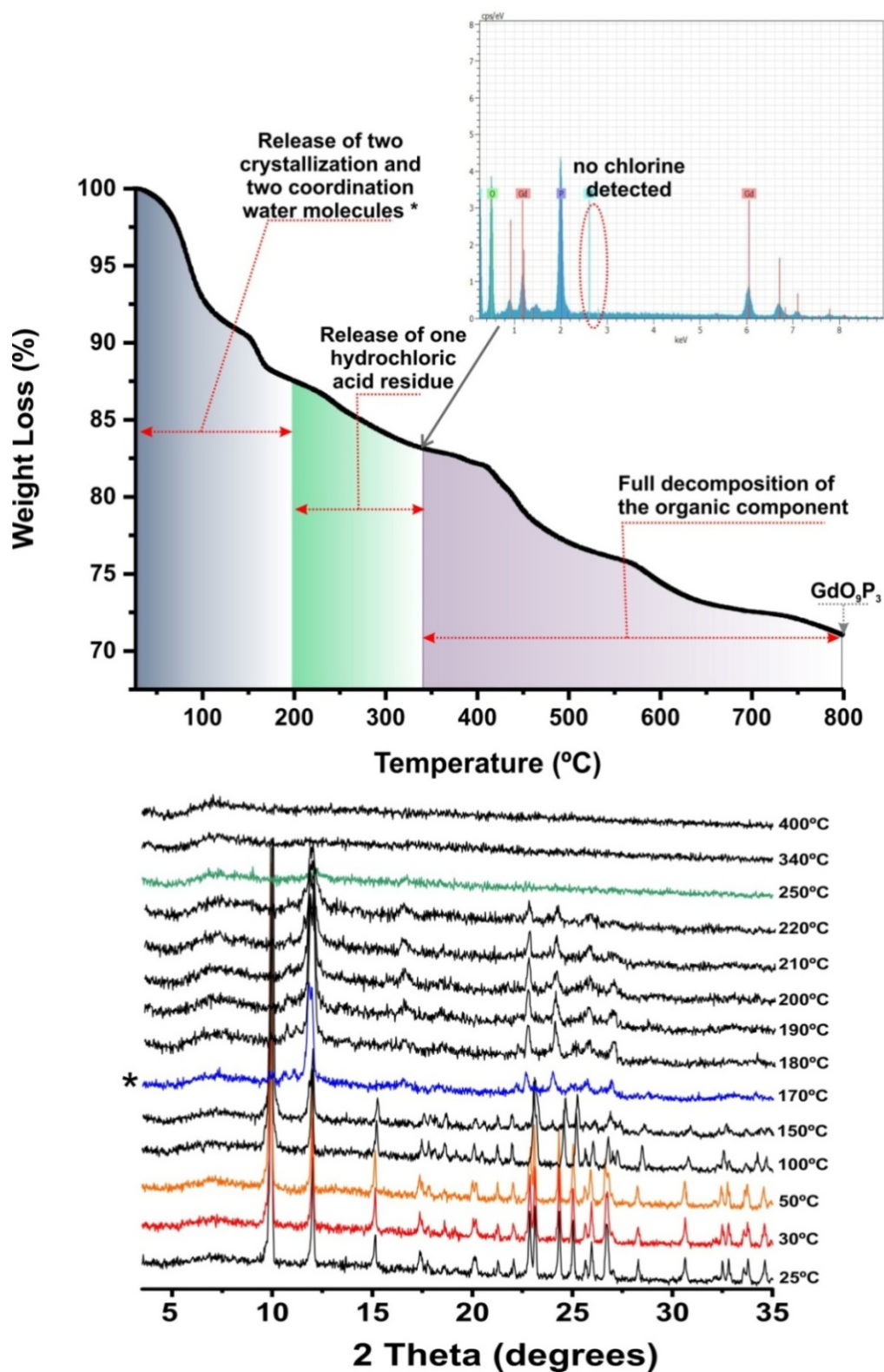


Figure 3.6 - Thermogram and thermodiffractometry studies of $[Gd(H_4nmp)(H_2O)_2]Cl \cdot 2H_2O$ (**2**) between ambient temperature and *ca.* 800 °C. EDS analyses show the absence of chlorine atoms in the sample calcined at 350 °C.

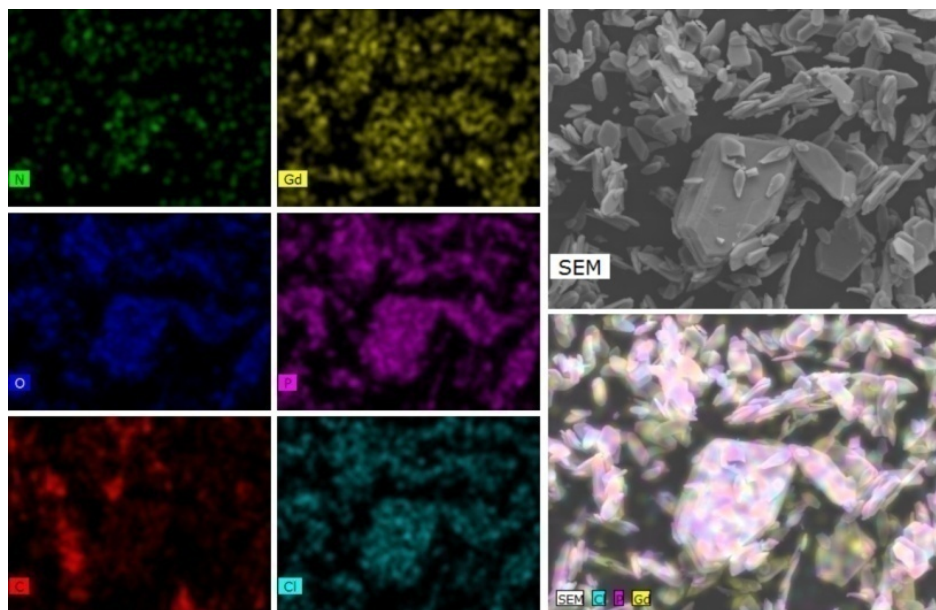


Figure 3.7 - Electron microscopy EDS mapping studies of a portion of the as-prepared $[\text{Gd}(\text{H}_4\text{nmp})(\text{H}_2\text{O})_2]\text{Cl}\cdot 2\text{H}_2\text{O}$ (**2**) material. The images show a uniform distribution of the heaviest elements present in **2**, thus confirming a homogeneous dispersion of both the Gd^{3+} cations and the organic ligand. Ratio of 1 : 2.8 and 1 : 1 for the Gd : P and Gd : Cl pairs, respectively.

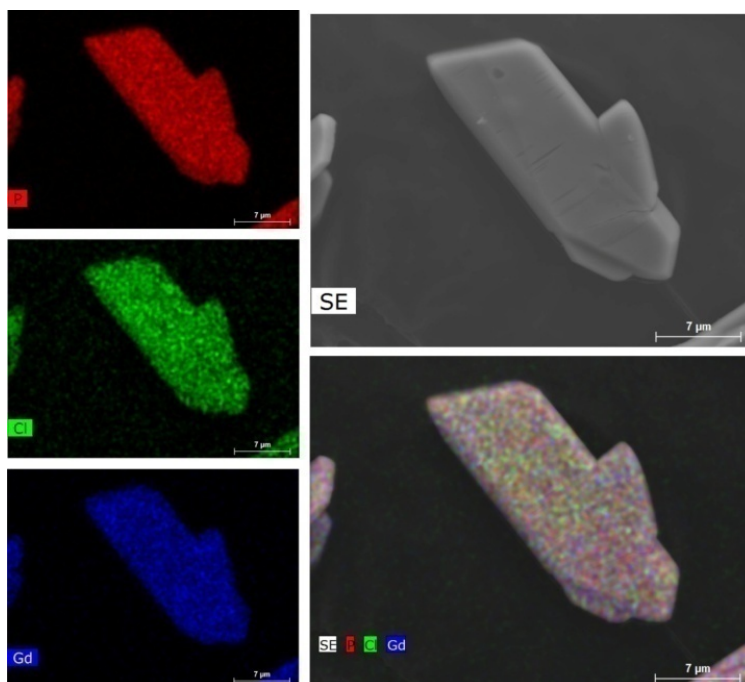


Figure 3.8 - Electron microscopy EDS mapping studies of a portion of the $[\text{Gd}(\text{H}_4\text{nmp})(\text{H}_2\text{O})_2]\text{Cl}\cdot 2\text{H}_2\text{O}$ (**2**) material calcined at *ca.* 250 °C for 24 hours. The images show a uniform distribution of the heaviest elements present in **2**, thus confirming a homogeneous dispersion of both the Gd^{3+} cations and the organic ligand. Ratio of 1 : 2.6 and 1 : 0.6 for Gd: P and Gd : Cl, respectively.

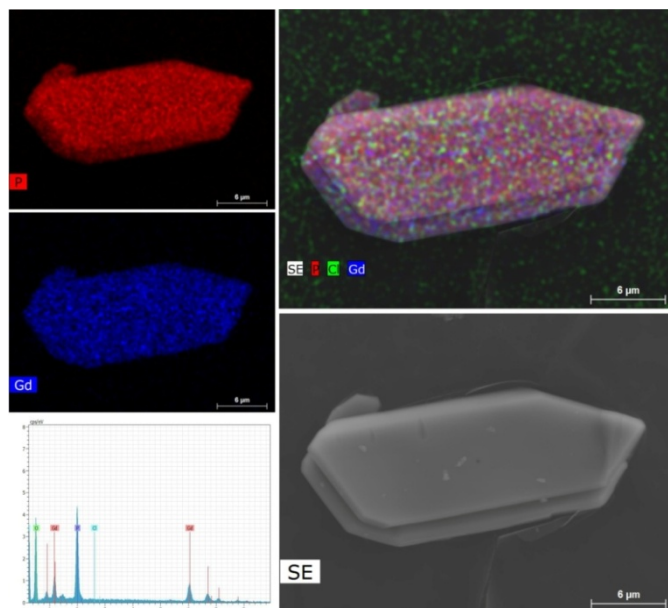


Figure 3.9 - Electron microscopy EDS mapping studies of a portion of the $[\text{Gd}(\text{H}_4\text{nmp})(\text{H}_2\text{O})_2]\text{Cl}\cdot 2\text{H}_2\text{O}$ (**2**) material calcined at 350 °C for 24 hours. The images show a uniform distribution of the heaviest elements present in **2** confirming a homogeneous dispersion of both the Gd^{3+} cations and the organic ligand. EDS analysis shows no presence of chlorine in the sample. Ratio of 1 : 2.5 for Gd : P.

and 2400 cm^{-1} as faint and broad bands. In the range of $1500\text{--}600\text{ cm}^{-1}$ it is possible to discern the typical $\nu(\text{C--N})$ stretching vibrational modes of tertiary amines assigned to the intense bands peaking at about 1133 , 1096 and 1075 cm^{-1} . The $\nu(\text{P--C})$ stretching vibrational modes are also observed, in particular between *ca.* $790\text{--}690\text{ cm}^{-1}$. Also in this region, the stretching vibrational modes of $\nu(\text{P=O})$ are clearly noticed between *ca.* 1340 and 1145 cm^{-1} , plus those of $\nu(\text{P--O})$ between *ca.* 1040 and 860 cm^{-1} .

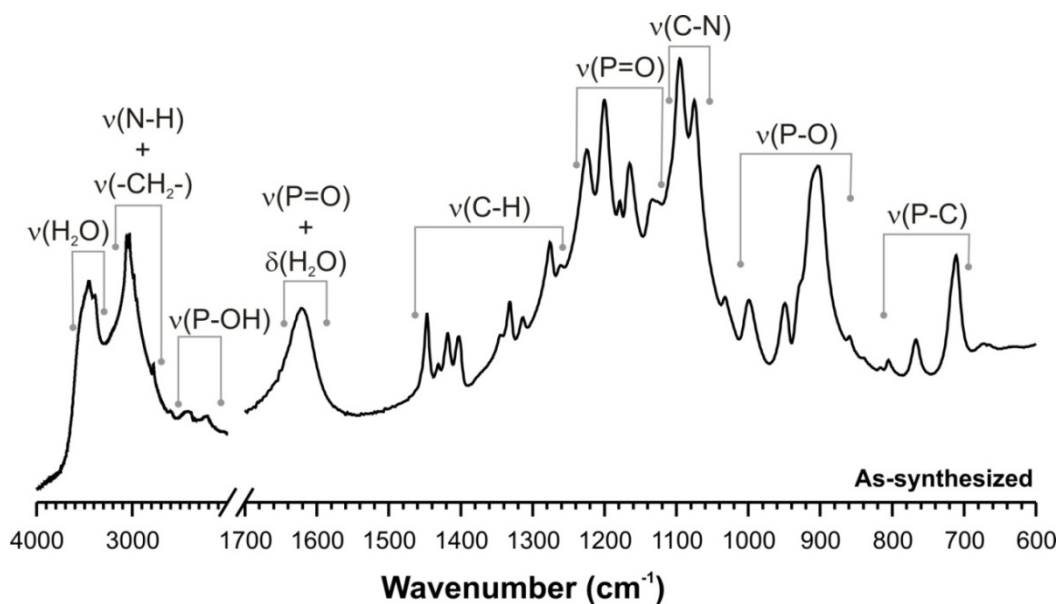


Figure 3.10 - FT-IR spectrum of $[\text{Gd}(\text{H}_4\text{nmp})(\text{H}_2\text{O})_2]\text{Cl}\cdot 2\text{H}_2\text{O}$ (**1**) in the $4000\text{--}600\text{ cm}^{-1}$ spectral region.

3.4 – Heterogeneous catalysis

[Gd(H₄nmp)(H₂O)₂]Cl·2H₂O (**2**) was tested as a heterogeneous catalyst for various important acid-catalysed reactions in both academia and chemical industry: epoxide alcoholysis, acetalisation of aromatic and aliphatic aldehydes, and ketalisation of ketones. As referred in Chapter 2, epoxide ring opening reactions can afford β -alkoxy alcohols, which are functional, versatile intermediates used in (in)organic syntheses.[200] On the other hand, acetalisation/ketalisation reactions are important transformations in organic chemistry enabling the protection of carbonyl groups in the presence of other functional/reactive groups.[201-203] Acetal and ketal chemicals can also advantageously possess high stability under basic conditions, and are stable to Grignard reagents, metal hydrides, oxidants, halogenation, and esterification reagents.[209] Ketals and acetals are used in the production of perfumes, fragrances and flavours,[210-212] cosmetics, in the food and beverage industries,[210-214] in pharmaceuticals,[210, 211, 215] plasticizers,[216] solvents and other intermediates.[210, 212, 217] Homogeneous mineral acids (HCl, H₃PO₄ and H₂SO₄) and metal triflates[218, 219] are generally used in these reactions.[220] Nevertheless, these chemical reactions can be more environmentally friendly and economically feasible if one uses more efficient heterogeneous catalysts. Compound **2** possesses a remarkable catalytic activity for these various chemical reactions, studied under atmospheric conditions while using relatively cheap alcohols as reacting solvents (methanol or ethanol). Whenever possible, the catalytic results for **2** in each reaction system are compared to literature data in the following discussion.

3.4.1 – Styrene oxide alcoholysis

These tests were performed with methanol and ethanol, always giving the corresponding β -alkoxy alcohol product with 100% selectivity, and excellent yields, under approximately atmospheric conditions (35 °C, atmospheric air). Methoxy-2-phenylethanol was obtained with 97% yield after only at 30 min reaction of styrene oxide with methanol, and 2-ethoxy-2-phenylethanol was obtained with 100% yield after 4h of reaction when ethanol was used instead (Figure 3.11).

In order to gain insights into the type of acidity, the catalytic performance of **2** was compared to that of the ligand (H₆nmp) and the lanthanide (Gd₂O₃) precursors. H₆nmp produced 2-methoxy-2-phenylethanol as the sole product formed with 97% yield after 30 min. The lanthanide precursor led, on the other hand, to a negligible styrene oxide conversion at 4 h (Figure 3.12).

The catalytic activity of **2** resembles more closely that of the ligand precursor than of the lanthanide one, suggesting that the high catalytic activity of **2** is due to Brønsted acid sites, which may be associated with its organic component.

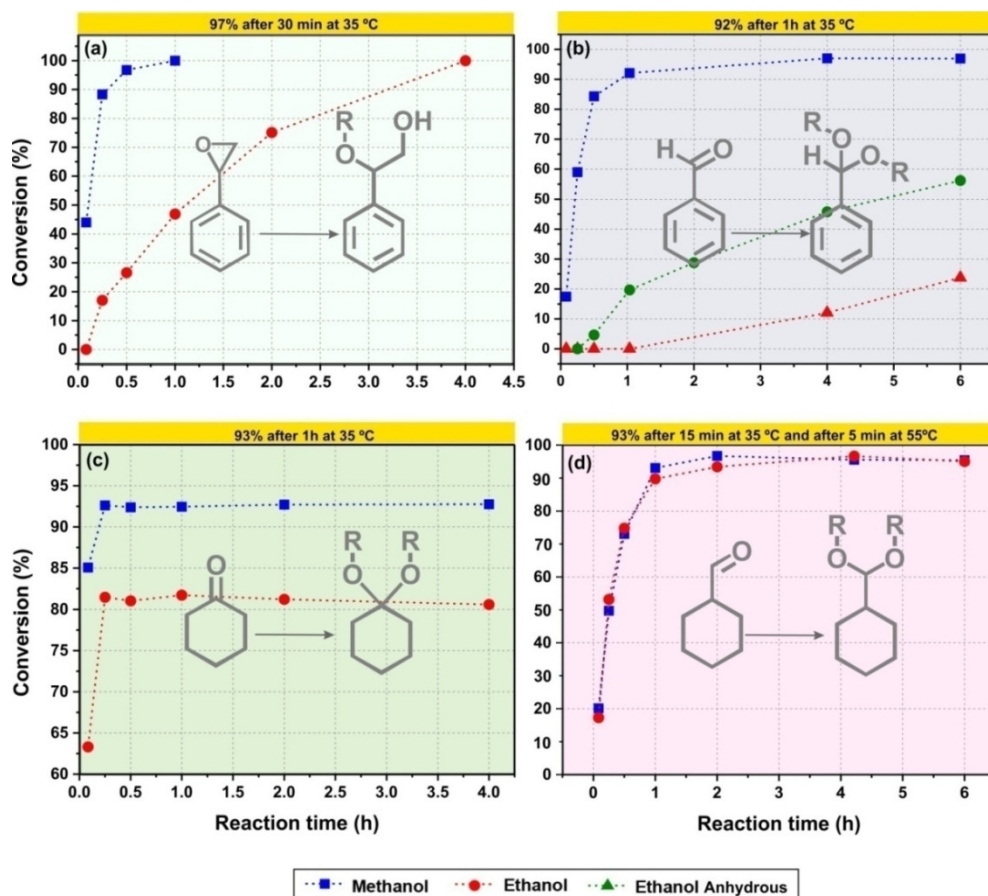


Figure 3.11 – Conversion of (a) styrene oxide, (b) benzaldehyde, (c) cyclohexanone and (d) cyclohexaldehyde with methanol or ethanol, in the presence of $[\text{Gd}(\text{H}_4\text{nmp})(\text{H}_2\text{O})_2]\text{Cl}\cdot 2\text{H}_2\text{O}$ (**2**) (catalyst load = $20\text{ g}_1\text{ L}^{-1}$). Please note: dashed lines connecting experimental points are only for illustrative purposes. R = CH_3 or CH_2CH_3 .

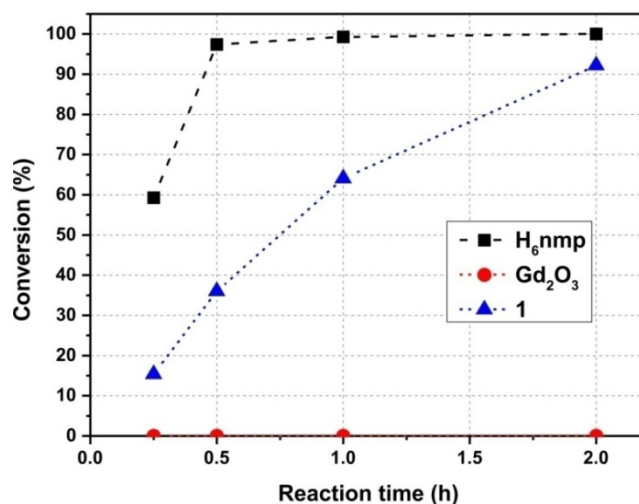


Figure 3.12. Conversion of styrene oxide with methanol in the presence of $[\text{Gd}(\text{H}_4\text{nmp})(\text{H}_2\text{O})_2]\text{Cl}\cdot 2\text{H}_2\text{O}$ (**2**), the ligand (H_6nmp) and the lanthanide precursor (Gd_2O_3), at 35 °C (catalyst load = $3.3\text{ g}_1\text{ L}^{-1}$). Precursors were used in equivalent molar amounts to those corresponding to $3.3\text{ g}_1\text{ L}^{-1}$. 2-Methoxy-2-phenylethanol was formed with 100% selectivity. Please note: dashed lines connecting experimental points are for illustrative purposes only

The Brönsted acidity associated with the P–OH groups in **2** can favour the protonation of the oxygen atom of the epoxide group. This leads to a favourable nucleophilic attack of the alcohol reagent at the more substituted carbon atom of the epoxide group, leading to the corresponding β -alkoxy alcohol product. A possible mechanism is depicted in Figure 3.13. Even though H₆nmp is an effective organocatalyst, the catalytic process is homogeneous in nature with implications in terms of demanding catalyst separation/regeneration.

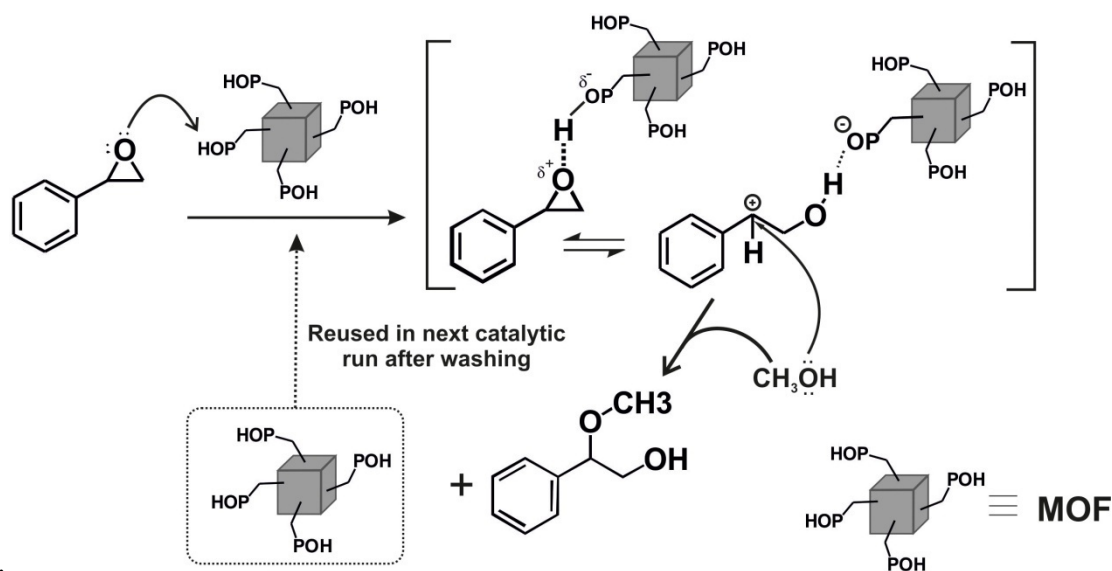


Figure 3.13 - Proposed mechanism for the alcoholysis of styrene oxide with methanol using $[\text{Gd}(\text{H}_4\text{nmp})(\text{H}_2\text{O})_2]\text{Cl}\cdot 2\text{H}_2\text{O}$ (**2**) as a heterogeneous catalyst.

Compound **2** was re-used in three consecutive reactions showing no considerable change in the conversion rate and maintaining its structural integrity (Figure 3.14). The heterogeneous nature of catalyst **2** was assessed by a leaching test at 35 °C. After separating the solid catalyst from the reaction mixture after 15 min the conversion of styrene oxide ceased to increase (remaining at *ca.* 15%), which is an indication of the absence of soluble active species (Figure 3.15). For comparison, the reaction of styrene oxide was carried out using HCl as a homogeneous catalyst (in an amount equivalent to that of Cl added with the MOF in a normal catalytic test), giving the β -alkoxy alcohol product with 97% yield at 15 min. As a consequence, if the solution of the leaching test for **2** contained any HCl, conversion should have increased, which was not observed.

The catalytic activity of **2** is comparable or superior to that of the 1D MOFs $[\text{La}_2(\text{H}_3\text{nmp})_2(\text{H}_2\text{O})_4]\cdot 4.5\text{H}_2\text{O}$ (compound **1**, chapter 2) [23] and $[\text{La}(\text{H}_4\text{bmt})(\text{H}_5\text{bmt})(\text{H}_2\text{O})_2]\cdot 3\text{H}_2\text{O}$ [88] previously reported by our groups (100% conversion after 3 and 6 h reaction, respectively). Although **2** is based on the same ligand as $[\text{La}_2(\text{H}_3\text{nmp})_2(\text{H}_2\text{O})_4]\cdot 4.5\text{H}_2\text{O}$ (**1**), it possesses instead a 2D layered structure with electron-withdrawing chloride ions located in the interlamellar space. Vermoortele *et al.* [221] reported that electron-withdrawing groups, such as nitro groups in UIO-66Zr-NO₂,

may influence the acid properties and induce (de)stabilizing effects on transition states, enhancing the catalytic activity.

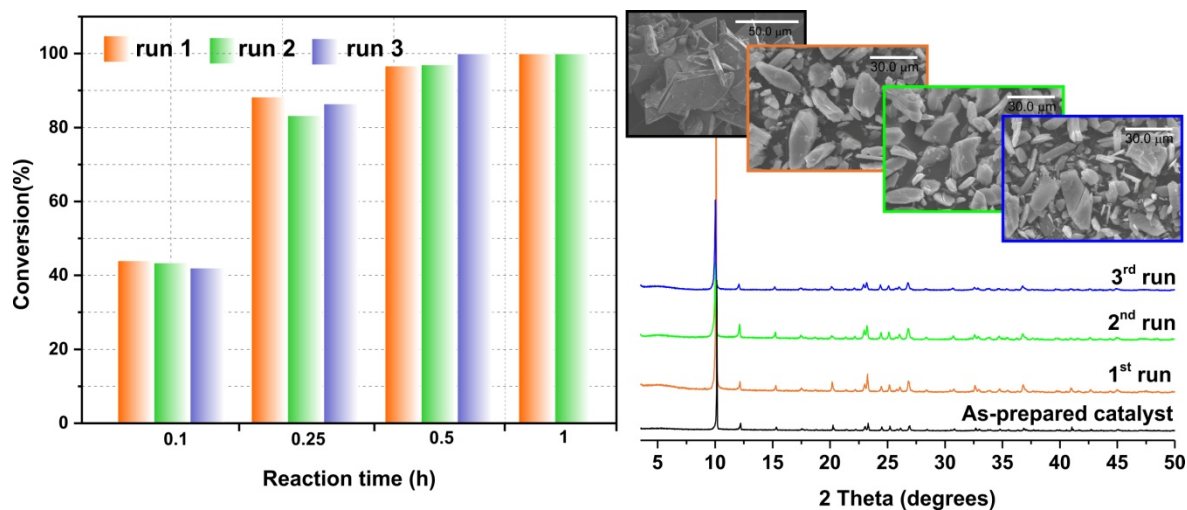


Figure 3.14 – (*left*) Conversion of styrene oxide in methanol in the presence of $[\text{Gd}(\text{H}_4\text{nmp})(\text{H}_2\text{O})_2]\text{Cl}\cdot 2\text{H}_2\text{O}$ (**2**) at 35 °C (catalyst load = $20 \text{ g}^1 \text{L}^{-1}$) and (*right*) Powder X-ray diffraction patterns and SEM images of the bulk $[\text{Gd}(\text{H}_4\text{nmp})(\text{H}_2\text{O})_2]\text{Cl}\cdot 2\text{H}_2\text{O}$ (**2**) catalyst used in three consecutive batch runs of the methanolysis of styrene oxide.

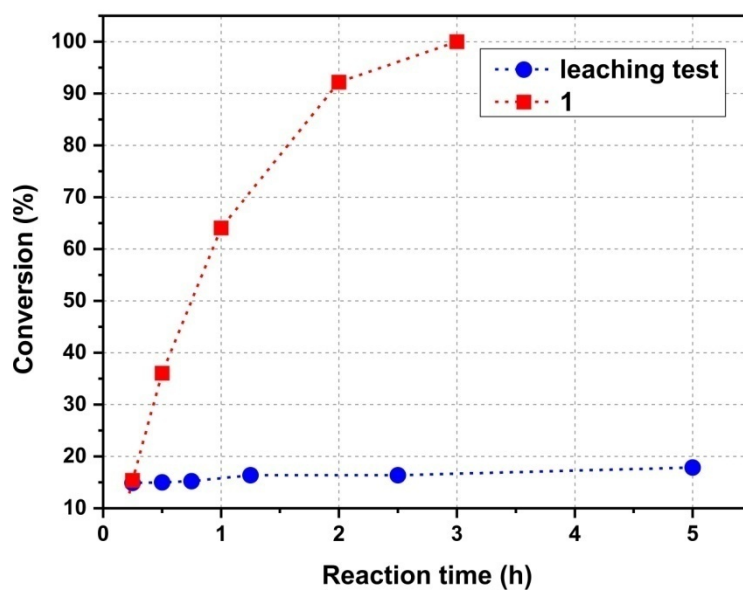


Figure 3.15. Leaching test carried out for $[\text{Gd}(\text{H}_4\text{nmp})(\text{H}_2\text{O})_2]\text{Cl}\cdot 2\text{H}_2\text{O}$ (**2**) in the methanolysis of styrene oxide at 35 °C, and comparison to the typical conditions without filtration of the catalyst (catalyst load = $3.3 \text{ g}^1 \text{L}^{-1}$). 2-Methoxy-2-phenylethanol was formed with 100% selectivity. *Please note:* dashed lines connecting experimental points are for illustrative purposes only.

The positive effect of NO_2 groups on catalytic activity when compared to the original MOF tested was found for various reactions, namely the cyclisation of (+)-citronellal, conversion of geraniol,[221] and reduction of 4-tert-butylcyclohexanone.[222]

In this way, we envisage that the electron-withdrawing chloride anions between the layers of **2** account for the enhanced catalytic activity. The activity of **2** is slightly surpassed by a MOF-supported heteropoly acid, namely MIL-101(HPW) (99% conversion and 99% selectivity at 0.33 h and 40 °C).[223] The synthetic procedure of this latter MOF is, however, much more complex, requiring higher temperatures, the need to synthesize the heteropoly acid, and activation under vacuum at 140 °C. In addition it suffered partial loss of catalytic activity over several cycles.

3.4.2 – Acetalisation of benzaldehyde

In this reaction 100% selectivity towards the benzaldehyde dialkylacetal product with excellent yields was observed: 92% benzaldehyde dimethyl acetal yield after 1h, and 56% benzaldehyde diethyl acetal yield after 6 h, for the reaction with methanol and ethanol, respectively (Figure 3.11). A possible mechanism of the Brönsted acid-catalysed alcoholysis of benzaldehyde is depicted in Figure 3.16. [224] The Brönsted acid site protonates the oxygen atom of the carbonyl group leading to the intermediate formation of a hemiacetal which, after water elimination, gives a carbocation. The latter undergoes a nucleophilic attack from another alcohol molecule giving the acetal product. The hemiacetal intermediate was not detected possibly due to its high reactivity under the catalytic conditions used.

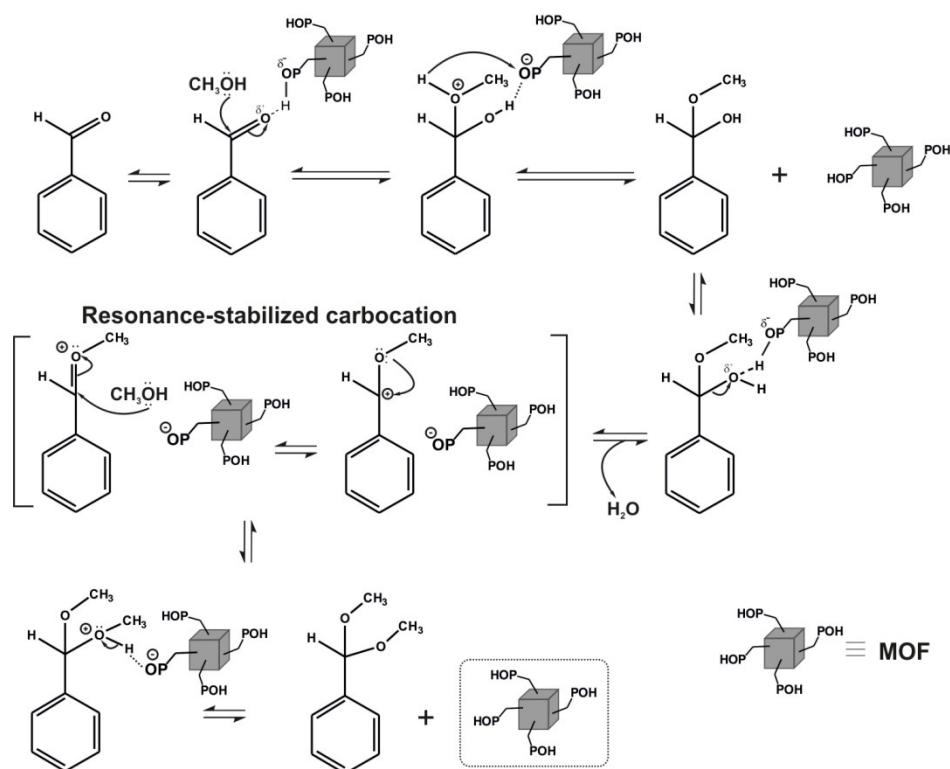


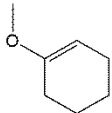
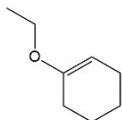
Figure 3.16 - Mechanistic proposal for the acetalisation of benzaldehyde with methanol in the presence of $[\text{Gd}(\text{H}_4\text{nmp})(\text{H}_2\text{O})_2]\text{Cl}\cdot 2\text{H}_2\text{O}$ (**2**) acting as a heterogeneous Brönsted acid catalyst. Mechanism adapted from reference [224].

The catalytic results for **2** are far superior to those previously reported for the 1D MOF $[\text{La}_2(\text{H}_3\text{nmp})_2(\text{H}_2\text{O})_4]\cdot 4.5\text{H}_2\text{O}$ (**1**) tested under identical reaction conditions (94% benzaldehyde dimethyl acetal yield after 20 h using a catalyst load of 20 g L^{-1}),[23] which may be partly related to the electron-withdrawing effects reported by Vermoortele *et al.* (and as discussed above).[221] The catalytic activity of **2** is, in this context, one of the best reported to date, surpassing those of $[\text{Al}_2(\text{BDC})_3]$, $[\text{Fe}(\text{BTC})]$, $[\text{Cu}_3(\text{BTC})_2]$, MIL-100(Fe) and UIO-66. [225-227] Compound **2** performed similarly to MIL-101(PTA),[228] MIL-101-NO₂d[224] and UIO-66-NO₂[206] which required, nevertheless, a thermal activation prior to use, whereas no pre-treatment was applied to **2**.

3.4.3 – Ketalisation of cyclohexanone

Reactions were performed with methanol or ethanol at 35 and 55 °C. With methanol, 93% cyclohexanone conversion was reached after 15 min (35 °C) (Figure 3.11) or after 5 min (55 °C), with the main reaction product being cyclohexanone dimethyl ketal (*ca.* 92-94% selectivity at *ca.* 93% conversion). Methoxycyclohexene was formed as a by-product (*ca.* 6-8% selectivity, Table 3.1). With ethanol, the corresponding ketal was formed with 94% selectivity at 81% conversion after 15 min (35 °C). Ethoxycyclohexene was also observed as a by-product (*ca.* 3% selectivity, Table 3.1). The mechanism of the Brønsted acid-catalysed ketalisation reaction in alcohol media may be similar to that of the acetalisation of benzaldehyde and is presented in Figure 3.17.

Table 3.1. By-products of the reaction of cyclohexanone with MeOH or EtOH as identified by GC-MS.

By-Product	Solvent	Chemical structure	% Yield
Methoxycyclohexene	MeOH		7
Ethoxycyclohexene	EtOH		5

Reaction conditions: 0.4 M CyOne, catalyst load of 20 g L^{-1} , 1 h, 35 °C.

Only two other previously investigated MOFs in the ketalisation of cyclohexanone are known, namely $[\text{Cu}_3(\text{BTC})_2]$ [225] and MIL-101-Cr-NO₂d.[224] $[\text{Cu}_3(\text{BTC})_2]$ was less active than **2** (80% conversion after 24 h), and the catalytic results for MIL-101-Cr-NO₂d are roughly comparable to those for **2** (90% conversion at 1.5 h using slightly less amounts of catalyst and substrate at 25 °C). The catalytic performance of **2** compares favourably to other solid acids, such as zeolites (H-Y,[229-231] H-ZSM5,[232-235] H-Mordenite,[235]

H-beta,[234, 235] mesoporous aluminosilicates Al-MCM-41[234, 236]) and heteropoly acid-based catalysts (e.g., $\text{H}_3\text{PW}_{12}\text{O}_{40}$)[234]. Sulfonated metal oxides led to 100% conversion of cyclohexanone after 30 min under similar reaction conditions (e.g., $\text{SO}_4^{2-}/\text{ZrO}_2$, $\text{SO}_4^{2-}/\text{TiO}_2$, $\text{SO}_4^{2-}/\text{SnO}_2$ [237]), albeit tetramethyloorthoformate was used as aketalisation agent and tetrachloromethane as the solvent, whereas in the present work, a relatively inexpensive alcohol with the dual function of reagent-solvent was used.

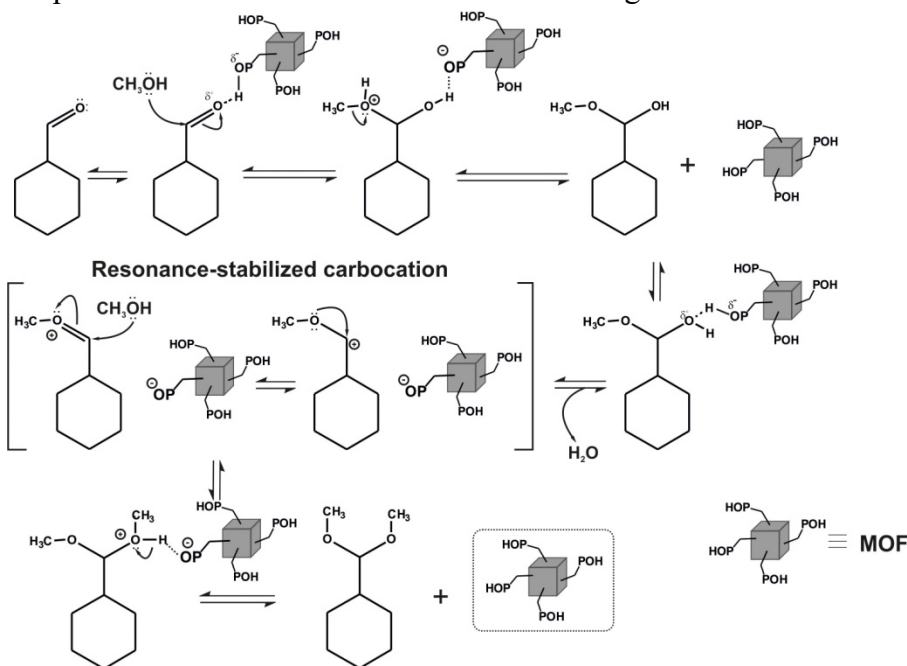


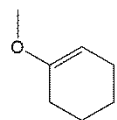
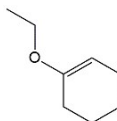
Figure 3.17 - Proposed mechanism for the acetalisation of cyclohexanaldehyde with methanol in the presence of $[\text{Gd}(\text{H}_4\text{nmp})(\text{H}_2\text{O})_2]\text{Cl}\cdot 2\text{H}_2\text{O}$ (**2**) acting as a heterogeneous Brønsted acid.

3.4.4 – Acetalisation of cyclohexanaldehyde

Cyclohexanaldehyde was reacted with methanol or ethanol at 35 °C or 55 °C. With methanol, **2** led to (dimethoxymethyl)cyclohexane in 88% yield at 93% conversion after 1 h (35 °C) (Figure 3.11). Identified by-products included cyclohexane carboxylic acid and methyl cyclohexanecarboxylate (Table 3.2). The reaction with ethanol led to 86% yield of (diethoxymethyl)cyclohexane at 90% conversion, 1 h (35 °C), with by-products including ethylcyclohexanecarboxylate (Table 3.2). The use of methanol and an increase of the reaction temperature to 55 °C under autogeneous pressure, led to methylcyclohexanecarboxylate as the sole observed product in 76% yield after 1 h. The mechanism for this reaction is also similar to the acetalisation of benzaldehyde (Figure 3.16). The hemiacetal was identified by GC-MS for the reaction with ethanol. To the best of our knowledge, catalyst **2** constitutes the first example of a MOF being investigated for the acetalisation of cyclohexanaldehyde in acidic medium. Clerici *et al.*[238] reported the acetalisation of cyclohexanaldehyde with MeOH in the presence of TiCl_4 in basic medium, which led to 94-98% acetal yield at 30 min and 0 °C. Although this constitutes a rather

interesting result, when compared to **2**, that reaction system was significantly more complex comprising the use of relatively toxic bases such as NH_3 or trimethylamine and the need for a refrigeration system to maintain low temperatures.

Table 3.2. By-products of the reaction of cyclohexanone with MeOH or EtOH as identified by GC-MS.

By-Product	Solvent	Chemical structure	% Yield
Methoxycyclohexene	MeOH		7
Ethoxycyclohexene	EtOH		5

Reaction conditions: 0.4 M CyOne, catalyst load of 20 g L^{-1} , 1 h, 35°C .

3.4.5 – General Catalytic considerations

The conversion versus times curves for the acetalisation and ketalisation reactions reached a plateau after *ca.* 2 h reaction due to thermodynamic limitations caused by the presence of water, formed as a co-product of the catalytic reaction. Similar kinetics effects were reported by Arrozi *et al.* for UiO-67 tested in benzaldehyde acetalisation.[227] Considerable differences in reaction rates were observed for **2** when ethanol of PA quality was used instead of anhydrous ethanol: with anhydrous ethanol, the yield of benzaldehyde diethylacetal after 6 h was 56%, whereas with ethanol PA, the yield was 23%. Ren *et al.*[239] also reported that the reaction of benzaldehyde with methanol in the presence of the 3D MOF $[\text{Tb}_2(\text{dpa})_3]$ (H_2dpa =1,4-phenylenediacetic acid) was considerably affected by water. When stoichiometric amounts of water were initially added to the reactor, conversion at 10 h and ambient temperature was 22%, compared to 78% conversion without the addition of water. On the other hand, Garcia *et al.*[240] reported for (2D) $[(\text{K}-18\text{-crown-6})_3][\text{M}_3^{\text{II}}(\text{H}_2\text{O})_4(\text{Ru}(\text{ox})_3)_3]$ ($\text{M}=\text{Cu}, \text{Co}, \text{Fe}, \text{Mn}$ and Zr ; $\text{ox}=\text{C}_2\text{O}_4^{2-}$) that the benzaldehyde dimethyl acetal yields could be slightly improved (from 50-83% to 56-98%, at $24 \text{ h}/70^\circ\text{C}$) after applying a thermal/vacuum pre-treatment to the MOF.

The reaction tended to be faster with methanol than with ethanol. These results agree with literature data for other MOFs tested as catalysts in the same reaction,[197, 204, 241] and may partly be due to steric hindrance effects. In all tested catalytic reactions a six-fold decrease in the amount of **2** from 20 to 3.3 g L^{-1} (and methanol as solvent) led to similar outstanding catalytic results. The catalyst could easily be recovered by washing/drying, and maintained its structural integrity after 3 runs for the styrene oxide alcoholysis (Figure 3.14) and after the acetalisation of benzaldehyde, the ketalisation of

cyclohexanone and acetalisation of cyclohexanaldehyde (Figure 3.18). The best results for the four reactions using compound **2** are presented in Table 3.3.

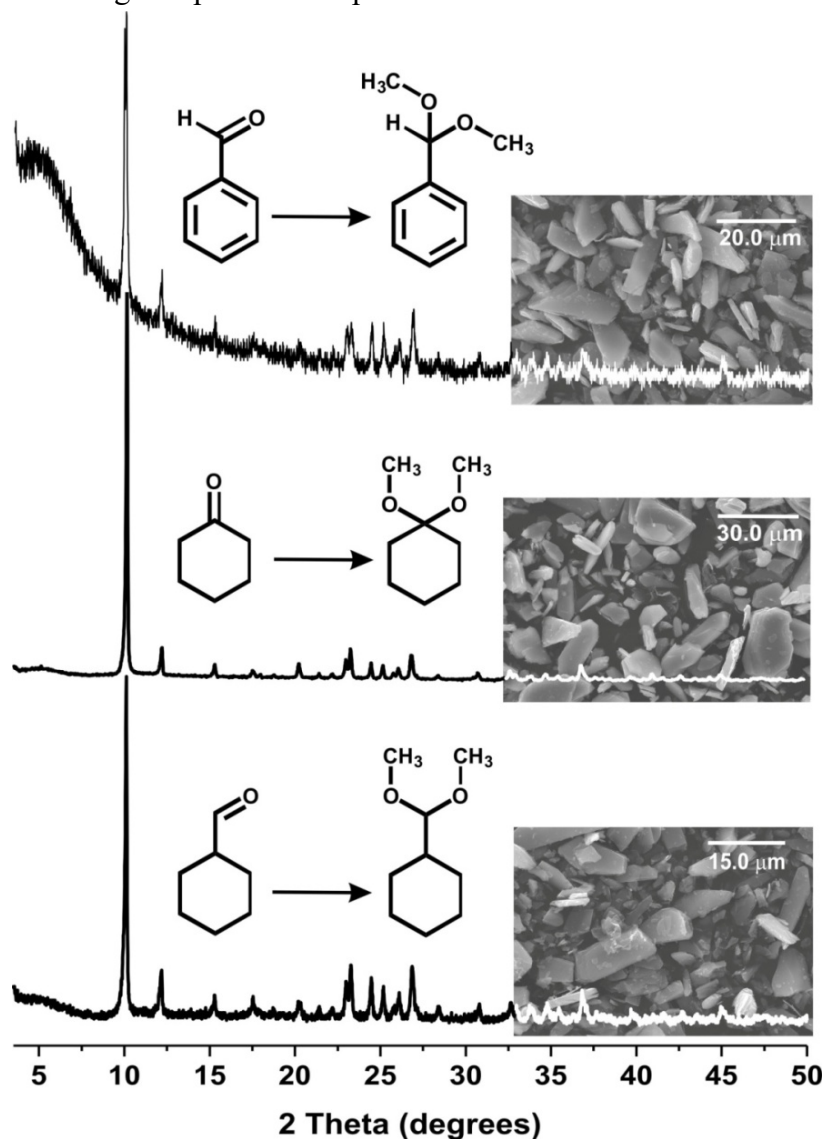


Figure 3.18 – Powder X-ray diffraction patterns and SEM images of the recovered $[\text{Gd}(\text{H}_4\text{nmp})(\text{H}_2\text{O})_2]\text{Cl}\cdot 2\text{H}_2\text{O}$ (**2**) catalyst used after the reactions of acetalisation of benzaldehyde, ketalisation of cyclohexanone and acetalisation of cyclohexanaldehyde.

Table 3.3 – Conversion of styrene oxide, benzaldehyde, cyclohexanone and cyclohexanaldehyde with methanol, in the presence of $[\text{Gd}(\text{H}_4\text{nmp})(\text{H}_2\text{O})_2]\text{Cl}\cdot 2\text{H}_2\text{O}$ (**2**)

Catalyst ^a	Reaction time (h)	Conversion ^d (%)
Styrene oxide alcoholysis	0.25/0.5/1	88/97/100
Acetalisation of benzaldehyde	0.25/1/4	59/92/96
Ketalisation of cyclohexanone	0.08/0.25/2	85/92/93
Acetalisation of cyclohexanaldehyde	0.5/1/4	73/93/95

^a Reaction conditions: substrate (0.4M), methanol (1.5mL), catalyst (20 g_l L⁻¹)

^d Conversion of substrate

3.5 – Proton Conduction

The ability to determine with precision the structures of CPs and MOFs by single-crystal X-Ray diffraction give us the opportunity to visualize their potential ion transfer pathways and possible application as proton conducting materials. As CPs and MOFs tend to form high-dimensional networks with 1D or 2D channels that are filled with solvent molecules and with non-coordinated –POH or –SOH groups suggests a good possibility to potential protonic conductivity behavior.

The presence of phosphonate-containing ligands with hydrogen-bonded chains in $[\text{Gd}(\text{H}_4\text{nmp})(\text{H}_2\text{O})_2]\text{Cl}\cdot 2\text{H}_2\text{O}$ (**2**) makes it suitable host structure to enable ionic transport along interlayer channels, where the adsorption of water molecules facilitated by the phosphonic acid groups provides paths for the structural diffusion of protons. However, at high temperatures **2** might release the chloride ion in the form of hydrochloric acid, leading to a phase transformation. In fact, we have observed that at high temperatures and humidity a single-crystal to single-crystal (SC-SC) transformation of **2** is induced. For this reason, and for the sake of clarity, in this section I will be presenting first the SC-SC transformation from $[\text{Gd}(\text{H}_4\text{nmp})(\text{H}_2\text{O})_2]\text{Cl}\cdot 2\text{H}_2\text{O}$ (**2**) to $[\text{Gd}(\text{H}_3\text{nmp})]\cdot x\text{H}_2\text{O}$ (**3**) following the results obtained in the proton conduction of these two materials.

3.5.1 – Structural Transformation of **2** into **3**

The SC-SC transformation of $[\text{Gd}(\text{H}_4\text{nmp})(\text{H}_2\text{O})_2]\text{Cl}\cdot 2\text{H}_2\text{O}$ (**2**) into $[\text{Gd}(\text{H}_3\text{nmp})]\cdot x\text{H}_2\text{O}$ (**3**) is observed when **2** is exposed to temperatures above 80 °C at a 98% relative humidity (RH). Compound **3**, formulated as $[\text{Gd}(\text{H}_3\text{nmp})]\cdot x\text{H}_2\text{O}$ and previously synthesized in our research group, crystallizes in the triclinic space group *P*-1. It is formed by infinite 2D layers maintained in a 3D conformation by hydrogen interactions between the phosphonate groups and crystallization water molecules. The asymmetric unit is composed of two heptacoordinated Gd^{3+} and two $\text{H}_3\text{nmp}^{3-}$ organic linkers (Figure 3.19).

The two Gd^{3+} centers are both coordinated to a total six phosphonate groups arising from five symmetry-related $\text{H}_3\text{nmp}^{3-}$ organic linkers, with the coordination polyhedron resembling a distorted pentagonal bipyramid. $\text{H}_3\text{nmp}^{3-}$ acts as a pentadentate linker in both cases, connecting to the two metal centers and other three symmetry equivalent. This high connectivity allow the formation of a compact layer and, as observed for other related compounds is responsible for the trapping of Gd^{3+} centers inside a phosphonic-type inorganic matrix.

The SC-SC transformation is only observed at high humidity (98% RH) and is believed to be induced, firstly, by the higher amount of water molecules in the interstitial space between the 2D layers present in **2**. This flow of water molecules will ultimately separate the layers further from each other (an increase of layer distance of *ca.* 2.3 Å) which are mainly responsible to weaken most of the hydrogen interactions. At this stage

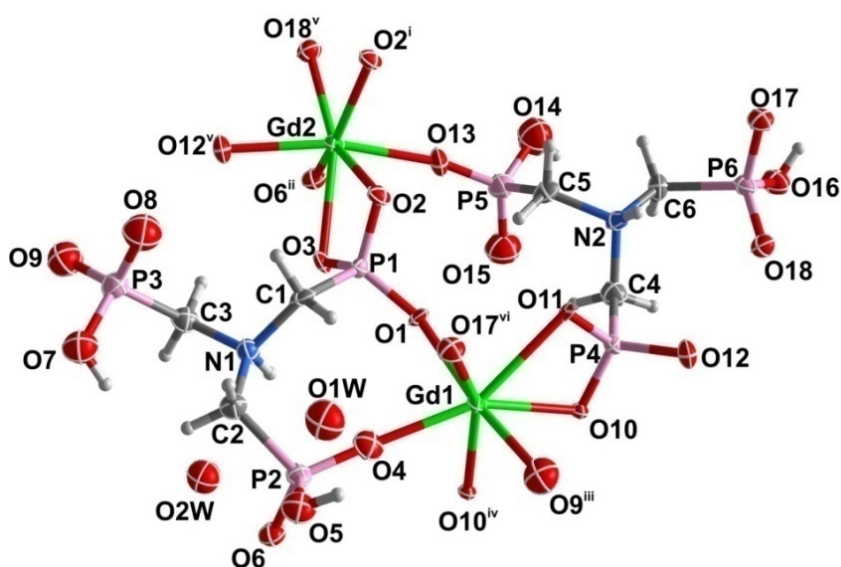


Figure 3.19 – The asymmetric unit of $[\text{Gd}(\text{H}_3\text{nmp})]\cdot x\text{H}_2\text{O}$ (**3**) showing all non-hydrogen atoms represented as displacement ellipsoids drawn at the 50% probability level and hydrogen atoms as small spheres with arbitrary radius. The coordination sphere of the crystallographically independent metallic center was completed for the sake of clarity. Symmetry codes used to generate equivalent atoms: (i) $-x, -y+1, -z+1$; (ii) $-x+1, -y+1, -z+1$; (iii) $x, y+1, z$; (iv) $-x+1, -y+2, -z+1$; (v) $x, y-1, -z+1$; (vi) $-x, -y+2, -z+1$.

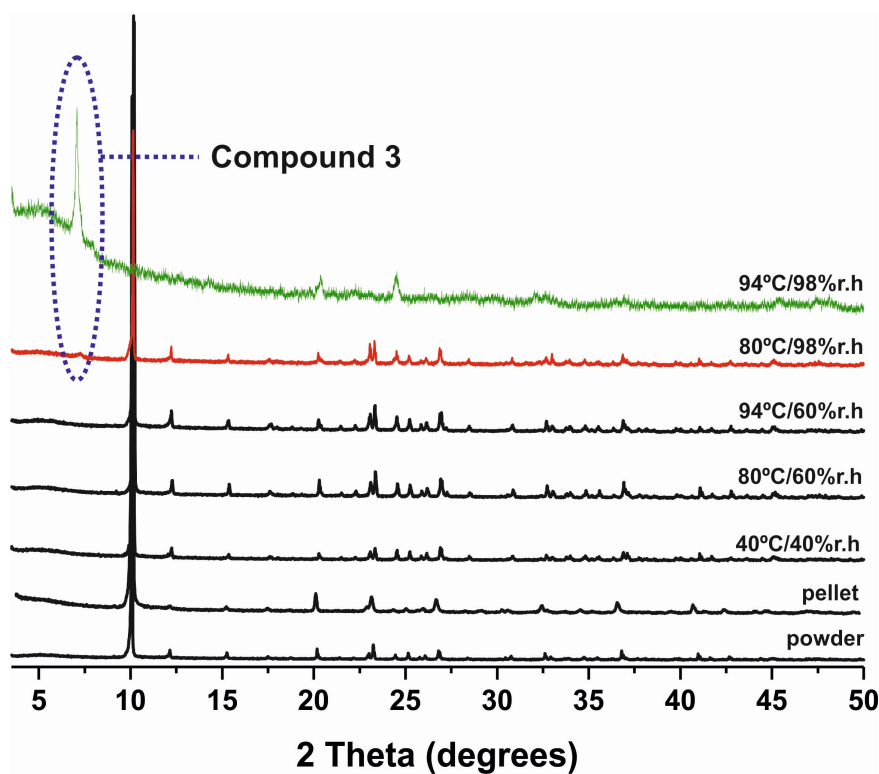


Figure 3.20 – Powder X-ray diffraction of $[\text{Gd}(\text{H}_4\text{nmp})(\text{H}_2\text{O})_2]\text{Cl}\cdot 2\text{H}_2\text{O}$ (**2**) when exposed to different humidity and temperature conditions. In the first two diffractograms is evident the SC-SC transformation of **2** to $[\text{Gd}(\text{H}_3\text{nmp})]\cdot x\text{H}_2\text{O}$ (**3**).

the chloride ion is released in the form of hydrochloric acid (evident by the oxidation of the metallic part of the proton conduction experimental apparatus). In the next stage, the temperature is of crucial importance. As depicted in Figure 3.20, the transformation is visible not only at high humidity but also at high temperatures (above 80 °C).

After the release of the chloride ion, several covalent O–La bonds (from the phosphonate groups) are destroyed (Figure 3.21) and all coordination water molecules are removed. The newly formed covalent bonds allow the formation of a more compact 2D layer observed in **3**, with a transformation similar to the folding of a sheet of paper. Figure 3.22 depicts this folding in a topological view. In there we can see that both organic linker and metal center displayed along the *a* axis (represented as orange and green colors in Figure 3.22) overlays the adjacent organic linker or metal center, forming a more compact, two layered 2D material. This folding is also evident by a decrease in unit cell from 17.46 to 12.84 Å (a reduction of *ca.* 26.5%).

When **3** is removed from the high humidity and temperature conditions its 2D layers stack on top of each other maintained by hydrogen interactions with the remaining crystallization water molecules.

3.5.2 – Proton conductivity in **2** and **3**

The mechanism of ion conduction in a solid material is mainly influenced by its structure, temperature and by the amount and mobility of charge carriers. The temperature dependence of the ionic conductivity at different RH conditions for compound **2** is shown in Figure 3.23. Conductivity measurements were firstly carried out with increasing temperature (1st run), at each RH and then during cooling down (2nd run). As observed for water-mediated proton conductors, conductivity increases with RH, although for temperatures higher than 60 °C at 98% RH this increase is especially marked. The conductivity at 94°C and 98% RH reaches 0.51 Scm⁻¹, which represents an increment of 5 orders of magnitude than that at 94 °C and 80% RH. As far as we know this is the highest conductivity value ever reported for a proton-conducting MOF material[138, 242, 243] and is comparable or higher than data typically found in literature for Nafion.[244, 245] To our knowledge the best MOF based materials up to this moment had conductivities at room temperature in the range of 4 x10⁻² Scm⁻¹, obtained for H₂SO₄@MIL-101 and {[(Me₂NH₂)₃(SO₄)]₂[Zn₂(ox)₃]}_n (ox = oxalate).[246, 247] With values ranging 0.5 Scm⁻¹ for our material, even at room temperature, we show an increase in conductivity in orders of magnitude of 10 to 1000 comparatively to most reported cases.[138]

With decreasing temperature (2nd run) the conductivity values at 98% RH are still in the range of 0.3-0.1 Scm⁻¹ and for lower RH and temperatures (40°C and 40% RH) the conductivity is 4 orders of magnitude higher than those of the 1st run. The large difference in conductivity as well as activation energies (*E_a*) between the 1st and 2nd run (Table 3.4) suggest different mechanisms in dynamic motion of the proton to explain the conducting process of compound **2**.

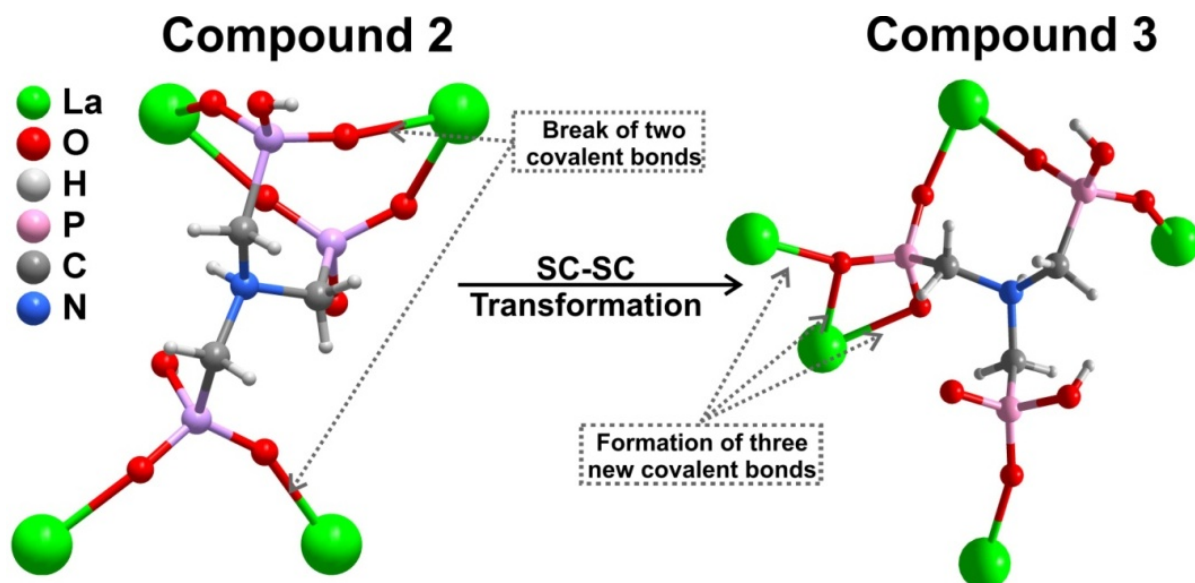


Figure 3.21 – Representation of the organic linker in $[\text{Gd}(\text{H}_4\text{nmp})(\text{H}_2\text{O})_2]\text{Cl}\cdot 2\text{H}_2\text{O}$ (**2**) and $[\text{Gd}(\text{H}_3\text{nmp})]\cdot x\text{H}_2\text{O}$ (**3**) and the coordination to the symmetry-related metal centers. It is emphasized the two broken and the three formed covalent O–La bonds during the SC-SC transformation.

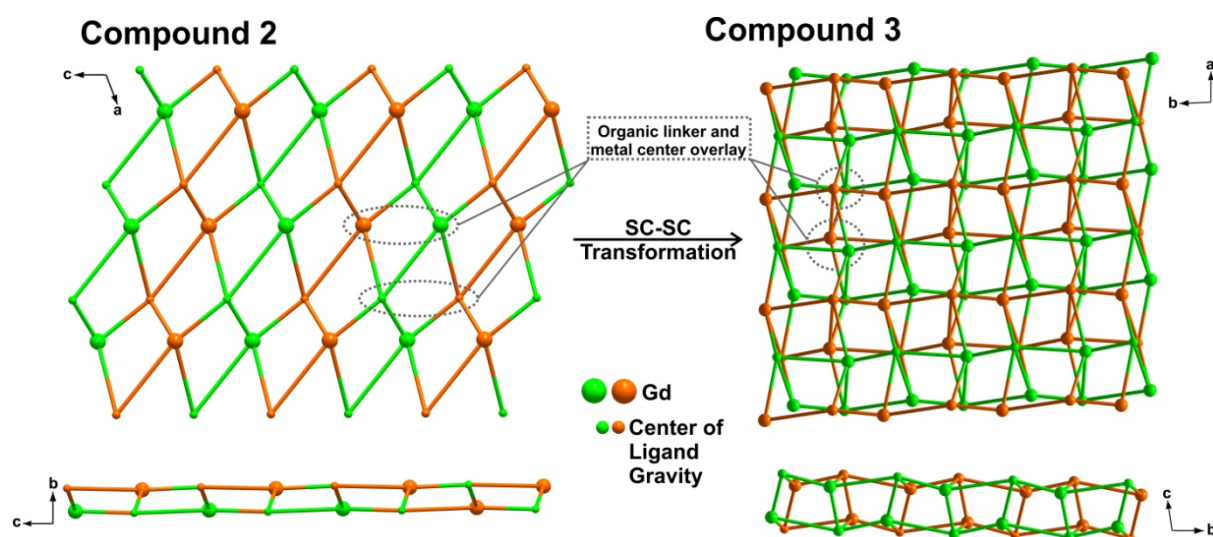


Figure 3.22 – Representation of the transformation in the 2D layer present in $[\text{Gd}(\text{H}_4\text{nmp})(\text{H}_2\text{O})_2]\text{Cl}\cdot 2\text{H}_2\text{O}$ (**2**) and $[\text{Gd}(\text{H}_3\text{nmp})]\cdot x\text{H}_2\text{O}$ (**3**) with the metal center and organic linker as nodes. It is emphasized the different parts folded in the SC-SC transformation (represented in orange and green).

In the 1st run, E_a was found to be much higher than typical hydrated proton conductors, such as Nafion ($E_a=0.22$ eV),^[248] increasing with RH, particularly near saturation. This suggests that the conduction process in **2** may be related to a non-efficient proton transfer pathway in the interlayer space. The water molecules may be trapped by hydrogen bonds in the channel or by electrostatic interactions with chloride ions, thus requiring higher energy to promote charge transport.

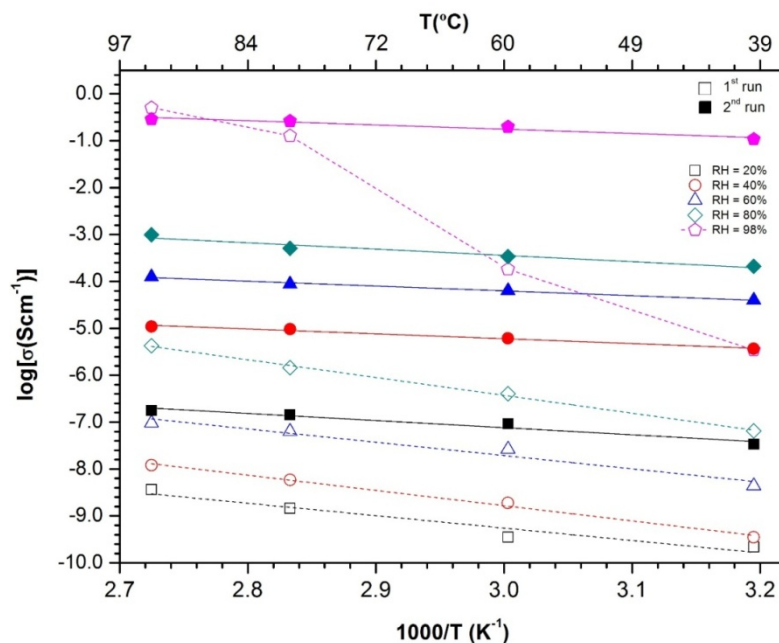


Figure 3.23 – Arrhenius plots for the protonic conductivity of $[\text{Gd}(\text{H}_4\text{nmp})(\text{H}_2\text{O})_2]\text{Cl}\cdot 2\text{H}_2\text{O}$ (**2**) measured under variable RH (■ – 98%, ◆ – 80%, ▲ – 60%, ● – 40%, ■ – 20%).

Other water-mediated proton-conducting MOFs reported in the literature [249-252] also presented high E_a values, usually in the range 0.6-1.32 eV, which were related with non efficient proton transfer pathways,[250] direct diffusion of additional protons with water molecules or the presence of other guest molecules [252] and small apertures between the micropores.[249, 251] The temperature dependence of the conductivity for the 2nd run displays the typical linear Arrhenius trend, with activation energy in the range 0.21-0.33 eV. The lower E_a values are indicative that charge transport mainly occurs through structural diffusion, where it seems to be the result of a more wide and hydrophilic proton-conducting pathway. In fact, XRD analysis (Figure 3.20) indicate a structural transformation of compound **2** above 80 °C at nearly saturated conditions, which explains the abrupt increase of conductivity in the 1st run and the hysteresis in conductivity after the 2nd run experiments. This structural transformation consists of a single-crystal to single-crystal (SC-SC) transformation of compound **2** to compound **3**, as described in the previous section. A pellet of compound **3** as-synthesized was also prepared and the results of ionic conductivity with increasing temperature and RH are presented in Figure 3.24. The results of conductivity at 98% RH of compound **2** are also represented for comparison. It is possible to observe that under nearly saturated conditions (98% RH) the conductivity behavior of **3** is very similar to that presented by **2**.

Table 3.4 – Activation energy in eV for the protonic conductivity of **2** measured under variable relative humidity.

RH (%)	20	40	60	80	98
1 st run	0.5	0.67	0.78	0.79	
2 nd run	0.33	0.24	0.23	0.30	0.21

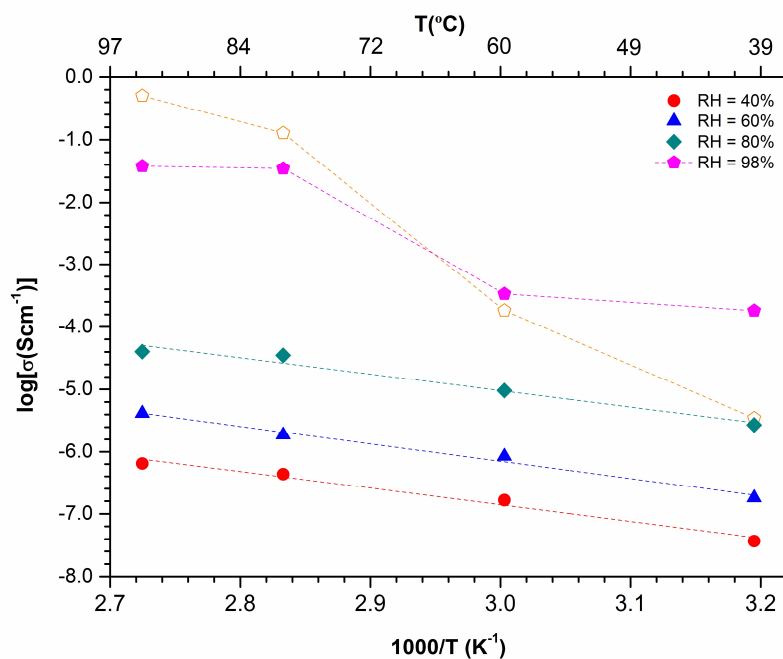


Figure 3.24– Conductivity measurements of $[\text{Gd}(\text{H}_3\text{nmp})] \cdot x\text{H}_2\text{O}$ (**3**).

3.6 – Concluding Remarks

In summary, the sustainable preparation of a cationic lamellar coordination polymer obtained by the self-assembly of Gd^{3+} and a polyphosphonic acid linker is presented. Though the structure shares similar features to previously reported layered materials obtained in our research group, the structural design of positively charged layers was managed using HCl in the synthesis. This led to the isolation of a new material which is a heterogeneous and versatile catalyst, exhibiting remarkable activity in four different reactions: alcoholysis of styrene oxide, acetalisation of benzaldehyde, ketalisation of cyclohexanone and, tested for the first time, in the acetalisation reaction of cyclohexanaldehyde. For all reactions, the reported material surpassed or, at least, equalled the catalytic results reported for other related materials studied in the literature (comprising a wide range of compounds from MOF structures to zeo-type materials).

Besides Brønsted acid properties, this new material possesses interesting proton conduction properties. At near ambient temperature and relative humidity, it also possesses interesting proton conduction properties, with the measured conductivities reaching $1.23 \times 10^{-5} \text{ Scm}^{-1}$, which compares favourably with other MOFs reported in the literature. Conductivity increases with RH, as expected for water-mediated proton conductors. However, this increase is especially marked between 80 and 98% RH, with an increment of 5 orders of magnitude, reaching values of conductivity of 0.51 Scm^{-1} , representing the highest conductivity value ever reported for a proton-conducting MOF. These values are also comparable or higher than data typically found in literature for the well known polymer Nafion. This significant increase in conductivity is attributed to the Single-Crystal

to Single-Crystal (SC-SC) transformation that **2** suffers at high temperatures and RH. The resulting material, $[\text{Gd}_2(\text{H}_3\text{nmp})_2] \cdot x\text{H}_2\text{O}$ (**3**) was characterized by single-crystal X-ray diffraction, and is formed by 2D layers maintained in a 3D conformation by hydrogen interactions between the phosphonate groups and crystallization water molecules. The increased distances between layers in **3** allows the transport of a higher amount of protons and because all coordination water molecules are removed, the 2D layers of **3** are maintained by weak hydrogen interactions with the remaining crystallization water molecules, which allows fast proton transfer between neighboring phosphonate groups and water molecules. The SC-SC transformation provided also an increase of free acidic protons from the partially protonated ligand observed due to a chemical modification of the framework. **3** can also be obtained as a pure-phase by conventional hydrothermal, microwave-assisted and one-pot conditions, showing conductivity behavior very similar to that presented by **2**.

This work is the perfect example of how small differences in structure can affect their properties. Although these two materials share some similarities in terms of structure, **2** show exceptional catalytic behavior in a series of organic reactions. If one compares the catalytic activity in the methanolysis of styrene oxide of the two materials, we can see that **2** has conversions around 97% after only 30 min, while for **3** the same value of conversion is only achieved after 72 h (unpublished data from our research group). On the other hand the protonic conductivity of **3** is increased considerably during the transformation process, showing conductivity values with 5 orders of increment.

CHAPTER 4

Dynamic Breathing effect in Metal-Organic Frameworks: Reversible 2D-3D-2D-3D Single-Crystal to Single-Crystal Transformation

The flexible organic linker nitrilotris(methyl phosphonic acid) (H_6nmp) was used to isolate a new family of CPs/MOFs by the self-assembly with La^{3+} cations using a fast and simple microwave synthetic approach. Sulfuric acid was included in the reaction media with two major functions: i) to slow down the deprotonation of the organic linker, thus favouring crystal growth over nucleation; ii) to block coordination sites usually occupied by phosphonic acids groups, with the aim to design more porous materials. The 2D layered material obtained, $[La_2(H_4nmp)_2(H_2O)_3(SO_4)] \cdot 8H_2O$ (**4**), undergoes spontaneous Single-Crystal to Single-Crystal (SC-SC) transformations at ambient temperature, which were followed by single-crystal and powder X-ray diffraction studies. The highly disordered water molecules in the channels are gradually removed originating in a consecutive fashion $[La_2(H_4nmp)_2(H_2O)_3(SO_4)] \cdot 6H_2O$ (**5**), $[La_2(H_4nmp)_2(H_2O)_3(SO_4)] \cdot 2H_2O$ (**6**) and $[La_2(H_4nmp)_2(H_2O)_2(SO_4)] \cdot H_2O$ (**7**). Materials are structurally very similar, being composed of “2D” layers formed by metallic centers in a zigzag conformation connected by the organic linker. While **4** and **6** are, in a topological perspective, identical (the sole difference being on the number of crystallization water molecules), being a 4-connected uninodal 2D networks with point symbol of $\{4^4.6^2\}$, **5** and **7** are in turn a 4,5-connected binodal (point symbol of $\{4^4.6^2\}\{4^4.6^4\}$) and 5-connected uninodal (point symbol of $\{4^6.6^4\}$) 3D networks, respectively. The main difference in these networks is the group that connects the “2D” layers: while in **5** the connection is achieved by the sulfate ion, in **7** the phosphonic acid residue is the main responsible by the formation of the 3D network, with the sulfate ion being coordinated to only one Ln^{3+} center. Because of the continuous transformation in ambient conditions of **4-6**, the full characterization description by elemental analysis, FTIR spectroscopy, thermogravimetry and electron microscopy (SEM and EDS) is presented only for the final and stable structure, **7**.

4.1 – Synthetic Strategy

Our research group has been focusing on the preparation of MOFs based on phosphonic acids by employing a set of different methodologies. Microwave-assisted synthesis proved to be a valuable tool to prepare MOFs with a considerable reduction of the reaction time with higher yields, particularly when compared to other methods (one-pot or hydro(solvo)thermal).[77] This methodology has, however, the drawback of obtaining,

in most cases, crystals with average size not suitable for single-crystal X-ray diffraction analysis. To overcome this limitation we have used hydrochloric acid in our reaction medium, as presented in Chapter 3.[23, 24] The acid acts as a retardant of the nucleation process by slowing down the deprotonation of the organic linker, therefore favouring crystal growth over nucleation. On the same time focus was directed also on understanding the effect that different acids have on the preparation of these materials. As a result, in this section the microwave methodology was employed in the preparation of four new MOFs synthesized solely in water with the addition of a small quantity of sulphuric acid: $[\text{La}_2(\text{H}_4\text{nmp})_2(\text{H}_2\text{O})_3(\text{SO}_4)] \cdot 8\text{H}_2\text{O}$ (**4**), obtained by slow crystallization after the microwave reaction; $[\text{La}_2(\text{H}_4\text{nmp})_2(\text{H}_2\text{O})_3(\text{SO}_4)] \cdot 6\text{H}_2\text{O}$ (**5**) $[\text{La}_2(\text{H}_4\text{nmp})_2(\text{H}_2\text{O})_3(\text{SO}_4)] \cdot 2\text{H}_2\text{O}$ (**6**) and $[\text{La}_2(\text{H}_4\text{nmp})_2(\text{H}_2\text{O})(\text{SO}_4)] \cdot \text{H}_2\text{O}$ (**7**), obtained by successive single-crystal to single-crystal (SC-SC) transformations of **4** (Figure 4.1, see next section for further details).

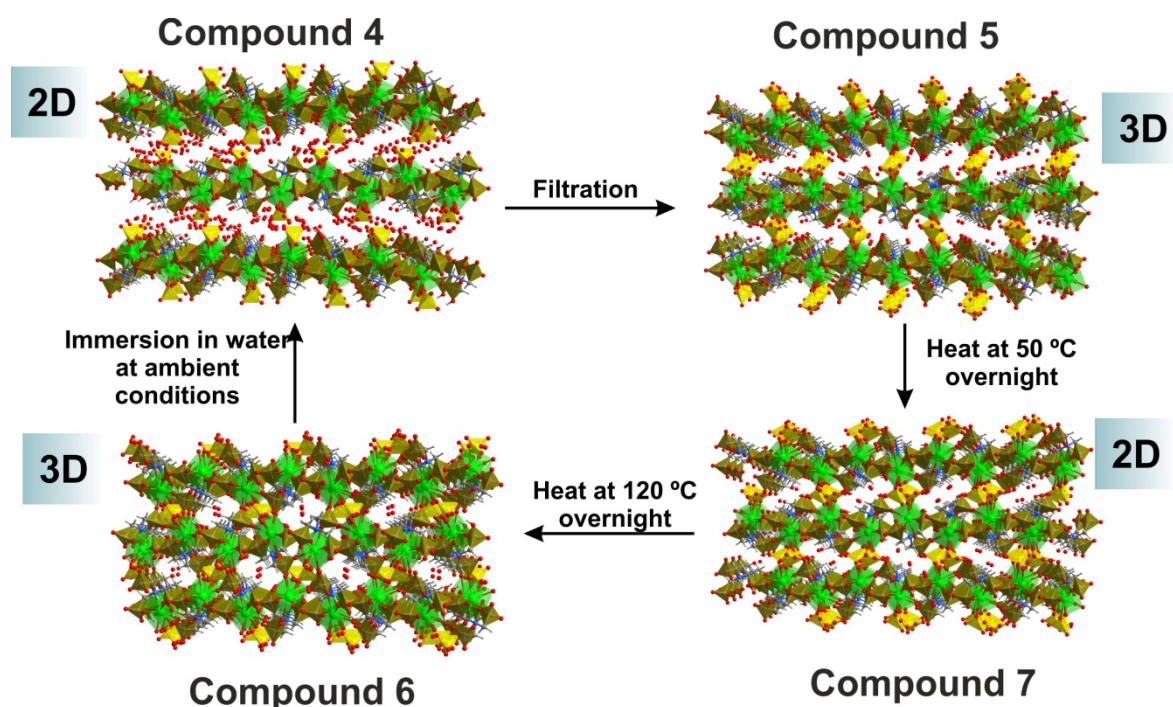


Figure 4.1 – Crystal packing (in the *bc* plane) and schematic representation of the single-crystal to single-crystal (SC-SC) transformation of $[\text{La}_2(\text{H}_4\text{nmp})_2(\text{H}_2\text{O})_3(\text{SO}_4)] \cdot 8\text{H}_2\text{O}$ (**4**). Into $[\text{La}_2(\text{H}_4\text{nmp})_2(\text{H}_2\text{O})_3(\text{SO}_4)] \cdot 6\text{H}_2\text{O}$ (**5**), $[\text{La}_2(\text{H}_4\text{nmp})_2(\text{H}_2\text{O})_3(\text{SO}_4)] \cdot \text{H}_2\text{O}$ (**6**) and $[\text{La}_2(\text{H}_4\text{nmp})_2(\text{H}_2\text{O})_2(\text{SO}_4)] \cdot \text{H}_2\text{O}$ (**7**). Legend: La-green, S-yellow, N-blue, O-red, P-brown, C-dark grey.

The SC-SC transformation described can be reversed by introducing **7** in a vial containing water (10 mg of **7** in 4 mL of deionized water) and left under vigorous stirring at ambient conditions for 24 h. After this time, **7** is reversed back into **4** and the transformation process can be set again in motion (for at least two cycles of dehydration/rehydration). The complete reversion from **7** to **4** was followed and proved by indexing in the single-crystal X-ray diffractometer a large number of crystals in solution after rehydration.

4.2 – Crystal Structure Description: Single-Crystal X-Ray Diffraction studies

To better understand the SC-SC transformation explained in the previous section, the four new MOFs were analyzed by single-crystal X-ray diffraction and formulated as $[\text{La}_2(\text{H}_4\text{nmp})_2(\text{H}_2\text{O})_3(\text{SO}_4)] \cdot 8\text{H}_2\text{O}$ (**4**), $[\text{La}_2(\text{H}_4\text{nmp})_2(\text{H}_2\text{O})_3(\text{SO}_4)] \cdot 6\text{H}_2\text{O}$ (**5**), $[\text{La}_2(\text{H}_4\text{nmp})_2(\text{H}_2\text{O})_3(\text{SO}_4)] \cdot 2\text{H}_2\text{O}$ (**6**) and $[\text{La}_2(\text{H}_4\text{nmp})_2(\text{H}_2\text{O})(\text{SO}_4)] \cdot \text{H}_2\text{O}$ (**7**). Aside from the fact that they crystallize in the same centrosymmetric monoclinic space group, $P2_1/c$, by comparing the empirical formulae and the crystal details we can see that all compounds share similarities: i) a single La^{3+} metal center in the asymmetric unit; ii) one $\text{H}_4\text{nmp}^{2-}$ residue with the same level of protonation, iii) half sulfate ion per Ln^{3+} center; iv) confined and coordinated water molecules as the sole solvent.

The coordination environment of La^{3+} is very similar for all materials (Figure 4.2). Even the bond lengths are very similar, and comparable to those reported for other La^{3+} -based materials, with the La–O distances ranging from 2.22(2) and 2.72(6) Å. If one considers the disordered molecules as one sole molecule, the coordination environments in compounds **4**, **5** and **7** are all octacoordinated, resembling a distorted dodecahedra. On the other hand, due to the bridge formed by the sulfate anion (see below for further detail), compound **6** is instead nonacoordinated, with the overall coordination environment resembling a highly distorted tricapped trigonal prism. While for **4** and **6** the La^{3+} center coordinates to six phosphonic acid residues, half sulfate anion and one coordinated water molecules (in two different positions), in **5** the metal center coordinates to an extra, symmetry-related sulfate anion. In **7**, on the other hand, the metal centers coordinate to seven phosphonic acid residues, and half sulfate ion and coordinated water molecule.

4 undergoes a reversible SC-SC transformation driven by water removal (mostly the crystallization ones), without a significant change in the backbone of the structure. For a simpler and more visual understanding of these transformations we have treated mathematically the networks to simple connecting rods and nodes. Based on the recommendations of Alexandrov *et al.*, [253] who suggested that any moiety (ligand, atom or clusters of atoms) connecting to three or more metallic centers (μ_n) should be considered as network nodes, we have considered the Ln^{3+} cation and the anionic $\text{H}_4\text{nmp}^{2-}$ ligand as nodes. As an exception, we have also included the sulfate ion as a non-topological connection (present in the figures as a sulfur atom). This moiety connects in most cases to a single node (metal center) so it is not a topological connection. However, due to its structural importance it is convenient to represent it (see below).

Taking this into account and using the software TOPOS [254] we observe that $[\text{La}_2(\text{H}_4\text{nmp})_2(\text{H}_2\text{O})_3(\text{SO}_4)] \cdot 8\text{H}_2\text{O}$ (**4**) is a 4-connected uninodal network with an overall Schläfli symbol of $\{4^4.6^2\}$ (Figure 4.3). **4** is composed by 2D layers, $\infty^2[\text{La}_2(\text{H}_4\text{nmp})_2(\text{H}_2\text{O})_3(\text{SO}_4)]$, separated by a total of four highly disordered crystallization water molecules per La^{3+} center. This high disorder, allied to the weak interaction with the P–OH groups is responsible for the rapid transformation, which upon filtration leads to the formation of $[\text{La}_2(\text{H}_4\text{nmp})_2(\text{H}_2\text{O})_3(\text{SO}_4)] \cdot 6\text{H}_2\text{O}$ (**5**).

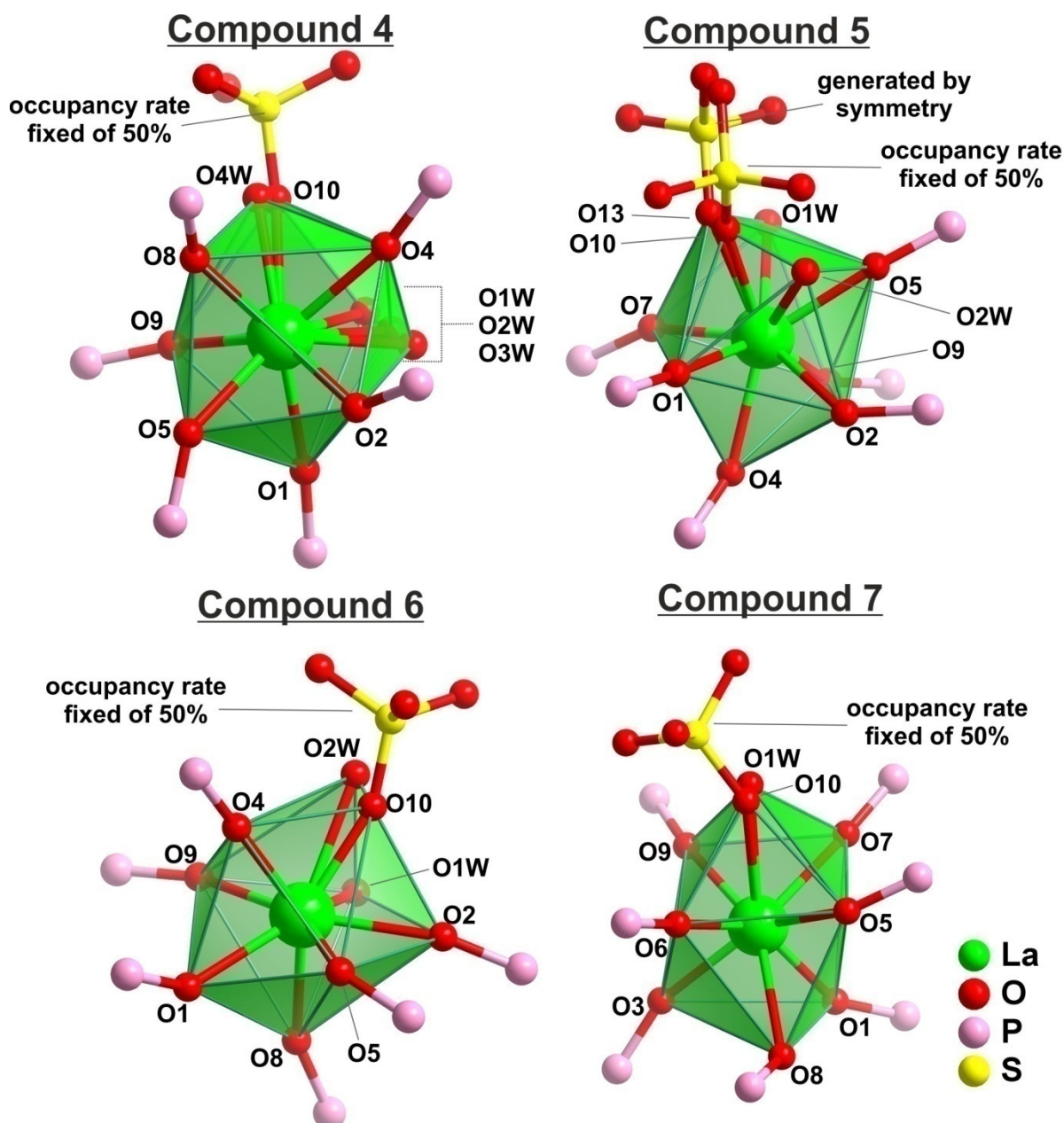


Figure 4.2 – Polyhedral representation of the distorted $\{\text{LaO}_8\}$ or $\{\text{LaO}_9\}$ coordination environments present in the crystal structure of $[\text{La}_2(\text{H}_4\text{nmp})_2(\text{H}_2\text{O})_3(\text{SO}_4)] \cdot 8\text{H}_2\text{O}$ (**4**), $[\text{La}_2(\text{H}_4\text{nmp})_2(\text{H}_2\text{O})_3(\text{SO}_4)] \cdot 6\text{H}_2\text{O}$ (**5**), $[\text{La}_2(\text{H}_4\text{nmp})_2(\text{H}_2\text{O})_3(\text{SO}_4)] \cdot 2\text{H}_2\text{O}$ (**6**) and $[\text{La}_2(\text{H}_4\text{nmp})_2(\text{H}_2\text{O})(\text{SO}_4)] \cdot \text{H}_2\text{O}$ (**7**).

The release of one crystallization water molecule per La^{3+} center and the rearrangement of the remaining two molecules in a more ordered fashion led to a decrease in distance between the $\infty^2[\text{La}_2(\text{H}_4\text{nmp})_2(\text{H}_2\text{O})_3(\text{SO}_4)]$ layers. This decrease is also markedly visible by the distances between metal centers of different layers: while in **4** the metallic centers of adjacent layers are separated by 9.715(7) Å, in **5** this distance is only of 7.292(3) Å. The difference of *ca.* 2.5 Å, and the small slide of the layers along the [001] direction, is enough to connect the sulfate ion to the La^{3+} center of the adjacent layer, forming a sulfate bridge between them, leading to the formation of a 3D network (Figure 4.4). **5** is therefore a 4,5-connected binodal network, with an overall Schäfli symbol of

$\{4^4.6^2\}\{4^4.6^6\}$ (Figure 4.3 and 4.4). Here we can see that while the organic linker maintains the same connection as in **4**, the metal center has an extra connection to the symmetry-related metal center of the adjacent layer via the sulfate anion.

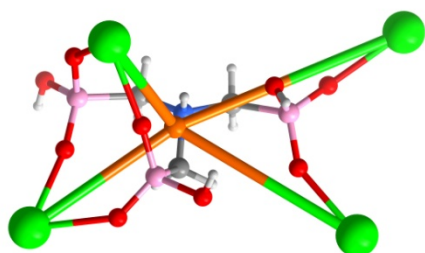
The next transformation, to $[\text{La}_2(\text{H}_4\text{nmp})_2(\text{H}_2\text{O})_3(\text{SO}_4)] \cdot 2\text{H}_2\text{O}$ (**6**), occurs over the period of one month after filtration of **4**, or by heating **5** at 50 °C overnight. One and half crystallization water molecules per La^{3+} center are removed, accompanied by an identical decrease in distance of the $\infty^2[\text{La}_2(\text{H}_4\text{nmp})_2(\text{H}_2\text{O})_3(\text{SO}_4)]$ layers. Interestingly, the metal centers seem to be farther away from each other [7.292(3) Å for **5** and 8.8362(13) Å for **6**]. In fact, although the layers are indeed closer they have also continued to slide along the [001] direction. The slide of the $\infty^2[\text{La}_2(\text{H}_4\text{nmp})_2(\text{H}_2\text{O})_3(\text{SO}_4)]$ layers is further responsible to break the bridge between metallic centers of adjacent layers formed by the sulfate ion which, ultimately, leads to the formation of the new 2D layered material. Because of this breakage, **6** is again a 4-connected uninodal network, with the same Schäfli symbol of **4** ($\{4^4.6^2\}$) (Figure 4.3 and 4.4). As we can see, **6** has as the same structural features as **4**, with the sole difference being the number of water molecules of crystallization.

Compound **6** can be further transformed into $[\text{La}_2(\text{H}_4\text{nmp})_2(\text{H}_2\text{O})(\text{SO}_4)] \cdot \text{H}_2\text{O}$ (**7**) at ambient conditions for a period of two more months or by heating **5** at 120 °C overnight. The transformation is accompanied by the release of half crystallization and one coordinated water molecule, following the usual decrease of distance between the newly formed $\infty^2[\text{La}_2(\text{H}_4\text{nmp})_2(\text{H}_2\text{O})(\text{SO}_4)]$ layers and the slide in the [001] direction. While in **5** this slide was partially responsible by the formation of a sulfate bridge between two metallic centers of adjacent layers, in **7** the connection between the $\infty^2[\text{La}_2(\text{H}_4\text{nmp})_2(\text{H}_2\text{O})(\text{SO}_4)]$ layers is otherwise achieved by the organic linker, forming a final 5-connected uninodal 3D network, with an overall Schäfli symbol of $\{4^6.6^4\}$ (Figure 4.3 and 4.4).

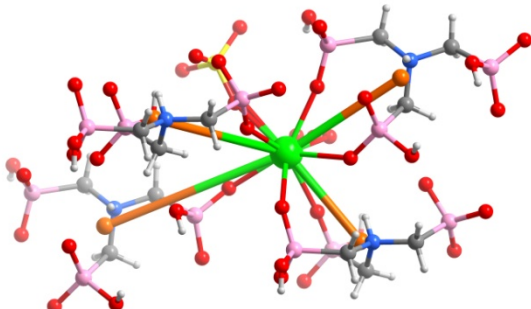
Although **7** is stable at ambient conditions and suffered no more transformations, it can be reversed back into compound **4** when immersed in water for a period of 24h at ambient conditions. Water molecules are reabsorbed into the pores of **7** leading to a swelling of the structure, strong enough to break the PO-Ln covalent bond that connects the $\infty^2[\text{La}_2(\text{H}_4\text{nmp})_2(\text{H}_2\text{O})(\text{SO}_4)]$ layers, and ultimately, leading back to the formation of the network of **4**.

These continuous, and reversible, SC-SC transformations are, at the end, driven mainly by the removal/adsorption of water molecules. This breathing motion can be described in three different ways: i) by changes in unit-cell dimensions, ii) by the interactions (or lack of them) between the solvent and the structure and iii) by an evident structural change within the framework of the material. During transformation from **4** to **7** there is a decrease in dimension of the unit cell in the *b* parameter of *ca.* 5 Å.

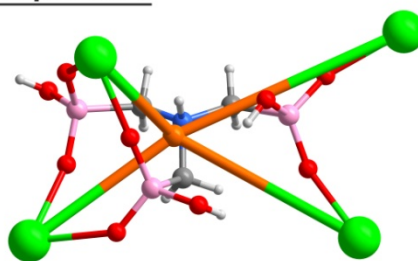
Compound 4



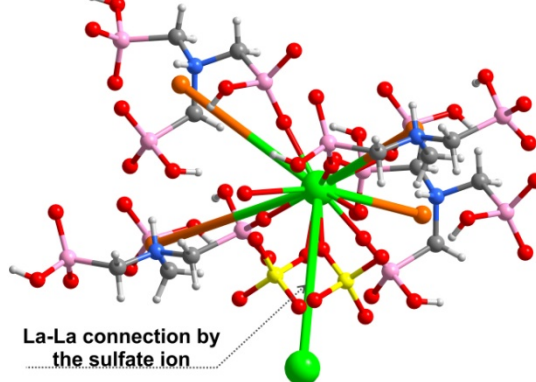
4-connected uninodal
2D network
Schäfli symbol of $\{4^4.6^2\}$



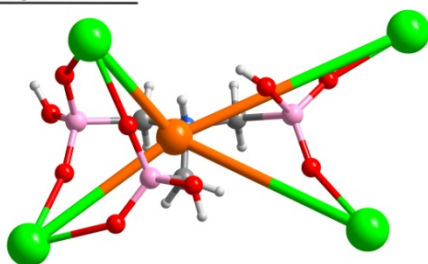
Compound 5



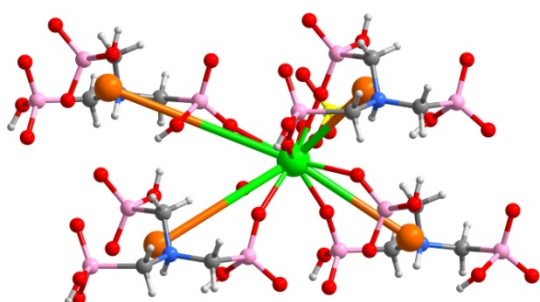
4,5-connected binodal 3D network
Schäfli symbol of $\{4^4.6^2\}\{4^4.6^6\}$



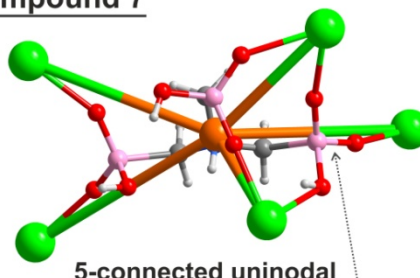
Compound 6



4-connected uninodal 2D network
Schäfli symbol $\{4^4.6^2\}$



Compound 7



5-connected uninodal
3D network
Schäfli symbol $\{4^6.6^4\}$

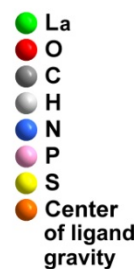
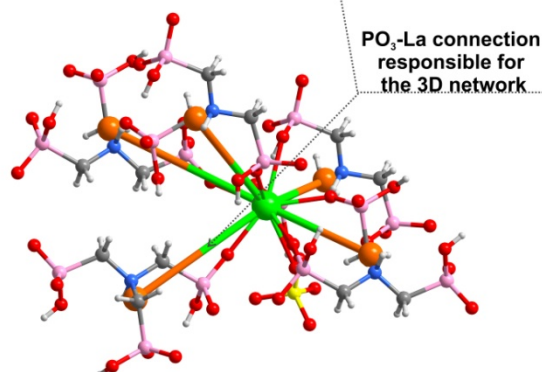


Figure 4.3 – Schematic representation of the connectivity of each individual node (*top* and *center*) and the “2D” layer (*bottom*) composing the different networks of $[\text{La}_2(\text{H}_4\text{nmp})_2(\text{H}_2\text{O})_3(\text{SO}_4)] \cdot 8\text{H}_2\text{O}$ (4), $[\text{La}_2(\text{H}_4\text{nmp})_2(\text{H}_2\text{O})_3(\text{SO}_4)] \cdot 6\text{H}_2\text{O}$ (5), $[\text{La}_2(\text{H}_4\text{nmp})_2(\text{H}_2\text{O})_3(\text{SO}_4)] \cdot 2\text{H}_2\text{O}$ (6) and $[\text{La}_2(\text{H}_4\text{nmp})_2(\text{H}_2\text{O})_2(\text{SO}_4)] \cdot \text{H}_2\text{O}$ (7).

Regarding the hydrogen bonding interactions it is evident a decrease in the number of these bonds with the removal of the water molecules in the interstitial space. While the

interactions with the solvent are reduced, new hydrogen bonds are formed, especially in the case of **7**. Six new hydrogen bonding interactions are formed between phosphonic acid groups of adjacent layers, once again indicative of their reduction in distance.

Topologically the four crystalline materials **4-7** remains practically unchanged. If one does not consider the connection between layers in **5** and **7** the “2D” layer remains exactly the same, as depicted in Figure 4.4. All have several chains composed of the metal centers in a zigzag conformation along the [001] direction, connected by the organic linker in an *ABAB...* fashion. The $\text{H}_4\text{nmp}^{2-}$ residue is the same for **4-6**, and acts as a hexadentate organic linker connecting four symmetry-related La^{3+} centers in a simple $\kappa^2\text{-O}$ mode. On the other hand, in **7** the $\text{H}_4\text{nmp}^{2-}$ residue acts as a heptadentate linker, connecting five La^{3+} centers in a $\kappa^2\text{-O}$ and $\kappa^3\text{-O}$ modes. The main difference between these structures is the bridge formed by the sulfate ion in **5** and the extra connectivity of the organic linker and the metal center in **7**.

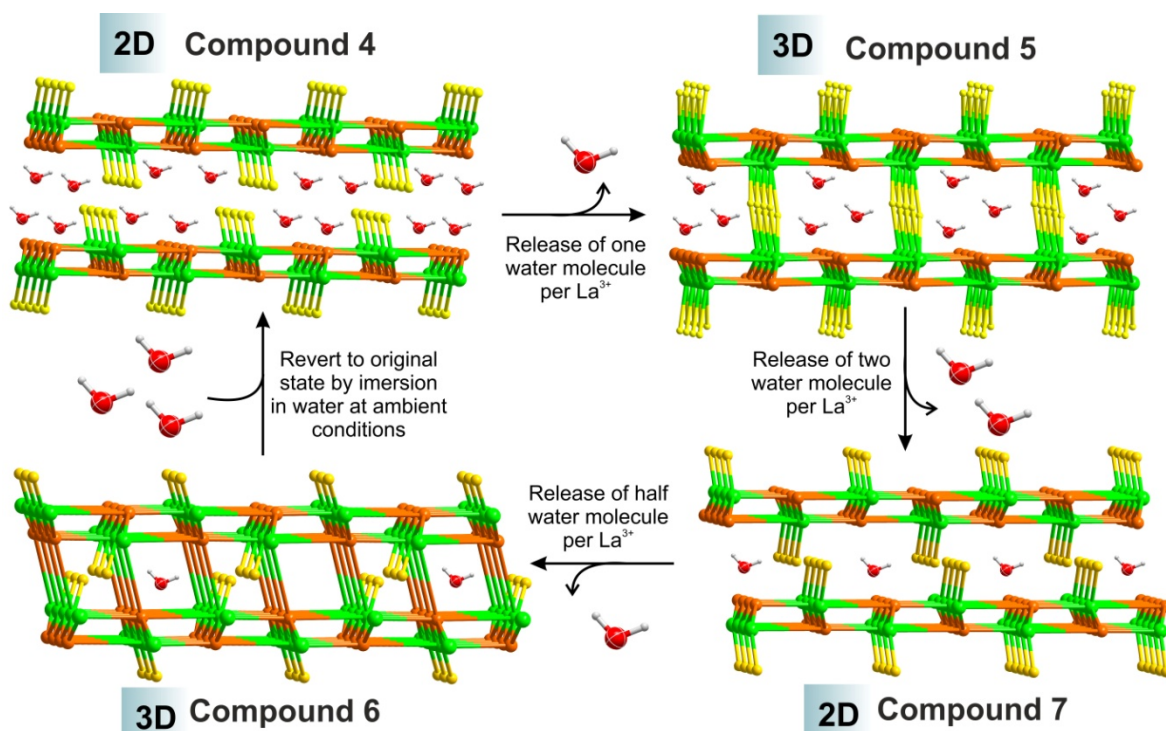


Figure 4.4 – Topological representation of the single-crystal to single-crystal (SC-SC) transformation of $[\text{La}_2(\text{H}_4\text{nmp})_2(\text{H}_2\text{O})_3(\text{SO}_4)] \cdot 8\text{H}_2\text{O}$ (**4**). Figure emphasizes the bridge formed between layers by the sulfate ion in the 2D-3D transformation of $[\text{La}_2(\text{H}_4\text{nmp})_2(\text{H}_2\text{O})_3(\text{SO}_4)] \cdot 8\text{H}_2\text{O}$ (**4**) into $[\text{La}_2(\text{H}_4\text{nmp})_2(\text{H}_2\text{O})_3(\text{SO}_4)] \cdot 6\text{H}_2\text{O}$ (**5**), as well as the formation of a new connection between layers by the organic linker in the 2D-3D transformation of $[\text{La}_2(\text{H}_4\text{nmp})_2(\text{H}_2\text{O})_3(\text{SO}_4)] \cdot \text{H}_2\text{O}$ (**6**) into $[\text{La}_2(\text{H}_4\text{nmp})_2(\text{H}_2\text{O})_2(\text{SO}_4)] \cdot \text{H}_2\text{O}$ (**7**). The water molecules are depicted only for representation and do not take into account their disorder. *Legend*: La-green, S-yellow, Center of ligand gravity- orange, O-red.

As presented in the previous chapters, acids have great importance in the preparation of MOFs and CPs. Hydrochloric acid allowed the preparation of the 1D polymer, $[\text{La}_2(\text{H}_3\text{nmp})_2(\text{H}_2\text{O})_4] \cdot 4.5\text{H}_2\text{O}$, based on the same organic linker, H_6nmp , in a rapid and simple microwave reaction (1 min at 60 °C, Chapter2).[23] In the same way, it

allowed also the preparation of another 2D polymer, $[\text{Gd}(\text{H}_4\text{nmp})(\text{H}_2\text{O})_2]\text{Cl}\cdot 2\text{H}_2\text{O}$, using the same building blocks, $[\text{Gd}(\text{H}_4\text{nmp})(\text{H}_2\text{O})_2]\text{Cl}\cdot 2\text{H}_2\text{O}$ (Chapter 3).[255] In this case the hydrochloric acid allowed the preparation of a highly crystalline material with enhanced acidic sites which improved its catalytic performance in a series of acid-base reactions. The main drawback of the organic linker H_4nmp is its high flexibility that makes it difficult to obtain 3D networks, especially with large pores. To date there is no reported materials using H_4nmp and lanthanides exhibiting a 3D network. This is where the sulfuric acid plays a crucial role in the present SC-SC transformation process. The sulfate ion is responsible not only for the connection of the “2D” layers in **5** but also is important to block coordination sites to the metal center, which ultimately leads to the formation of the final 3D network in **7**. As we can see, the use of acids can not only help us to improve the experimental procedure (by decreasing the reaction time) or improve the materials properties but also give us the tools to design different MOFs.

4.3 – Physicochemical Characterization

The low stability of $[\text{La}_2(\text{H}_4\text{nmp})_2(\text{H}_2\text{O})_3(\text{SO}_4)]\cdot 8\text{H}_2\text{O}$ (**4**) at ambient conditions, and the fact that one is not able to obtain pure-phase materials of the two intermediate phases ($[\text{La}_2(\text{H}_4\text{nmp})_2(\text{H}_2\text{O})_3(\text{SO}_4)]\cdot 6\text{H}_2\text{O}$ (**5**) and $[\text{La}_2(\text{H}_4\text{nmp})_2(\text{H}_2\text{O})_3(\text{SO}_4)]\cdot 2\text{H}_2\text{O}$ (**6**)), the following analyses were only performed to the final 3D material, $[\text{La}_2(\text{H}_4\text{nmp})_2(\text{H}_2\text{O})(\text{SO}_4)]\cdot \text{H}_2\text{O}$ (**7**).

Thermogravimetry: The thermogravimetric behavior of this material is simple (Figure 4.5), comprising of only four steps: the first, between ambient temperature and *ca.* 130 °C, is attributed to the release of half crystallization water molecules per asymmetric unit, corresponding to 1.8% of its total weight (calculated as *ca.* 1.8%); the second is attributed to the release of the remaining half coordinated water molecule, located between 205 and 275 °C, corresponding to a loss of 1.8% of its total weight (calculated as *ca.* 1.8%); the third step is assigned to the release of half sulfate ion as sulfuric acid between 310 and 405 corresponding to 9.7% of weight loss (calculated as *ca.* 9.8%); and finally the remaining weight loss is attributed to the decomposition of the organic component between 405 and 750 °C.

Vibrational Spectroscopy: The vibrational FT-IR spectra depicted in Figure 4.6 depicts the spectral regions containing the typical vibration modes present in $[\text{La}_2(\text{H}_4\text{nmp})_2(\text{H}_2\text{O})(\text{SO}_4)]\cdot \text{H}_2\text{O}$ (**7**) in the 3500-400 cm^{-1} region, including assignments for each main observed band. Compound **7** contains in the spectral region between 3500 and 3200 cm^{-1} a small broad band attributed to the $\nu(\text{O}-\text{H})$ stretching vibrational mode from both coordinated and crystallization water molecules. In the region between 3000 and 2100 cm^{-1} we find the typical $\nu(\text{O}-\text{H})$ and $\nu_{\text{sym}+\text{asym}}(\text{C}-\text{H})$ stretching vibration bands of $\text{PO}-\text{H}$ and $-\text{CH}_2-$ (between 3155 and 2905 cm^{-1} for $-\text{CH}_2-$ groups and at between 2810 and 2545 cm^{-1} for $\text{PO}-\text{H}$). The $\nu(\text{N}-\text{H})$ stretching vibrational mode is also found in this region, at

3022 cm^{-1} . Below 2000 cm^{-1} the spectra is composed of medium to very strong vibration bands, which are assigned to $\nu(\text{C-H})$ modes corresponding to the P-CH_2 groups between 1480 to 1380 cm^{-1} , to the $\nu(\text{P=O})$ and $\nu(\text{SO}_4^{2-})$ modes around 1315-1135 and to the $\nu(\text{P-O})$ at 1135-860 cm^{-1} respectively. The $\nu(\text{P-C})$ stretching vibrations are located at 709, 574 and 559 cm^{-1} .

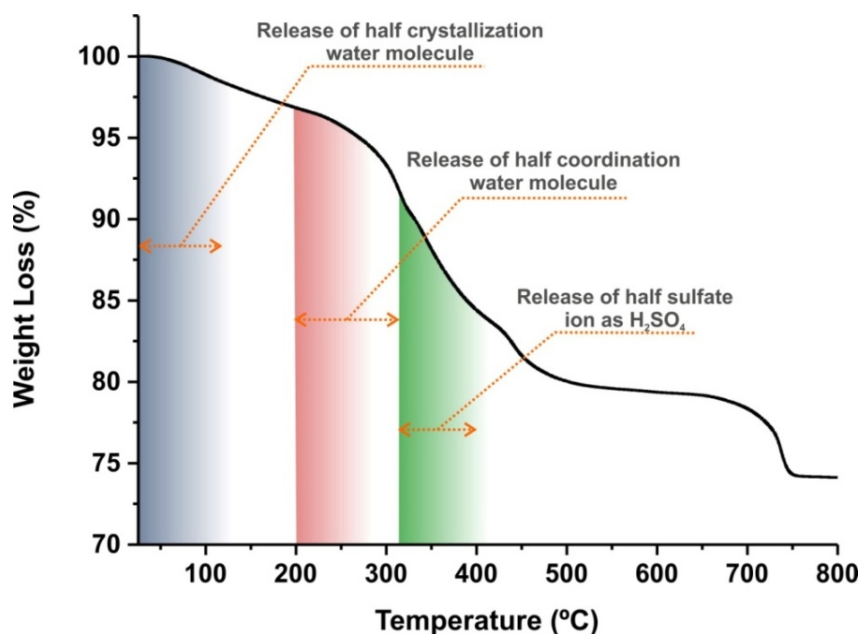


Figure 4.5 - Thermogram curve of $[\text{La}_2(\text{H}_4\text{nmp})_2(\text{H}_2\text{O})_2(\text{SO}_4)] \cdot \text{H}_2\text{O}$ (7) between ambient temperature and 800 °C.

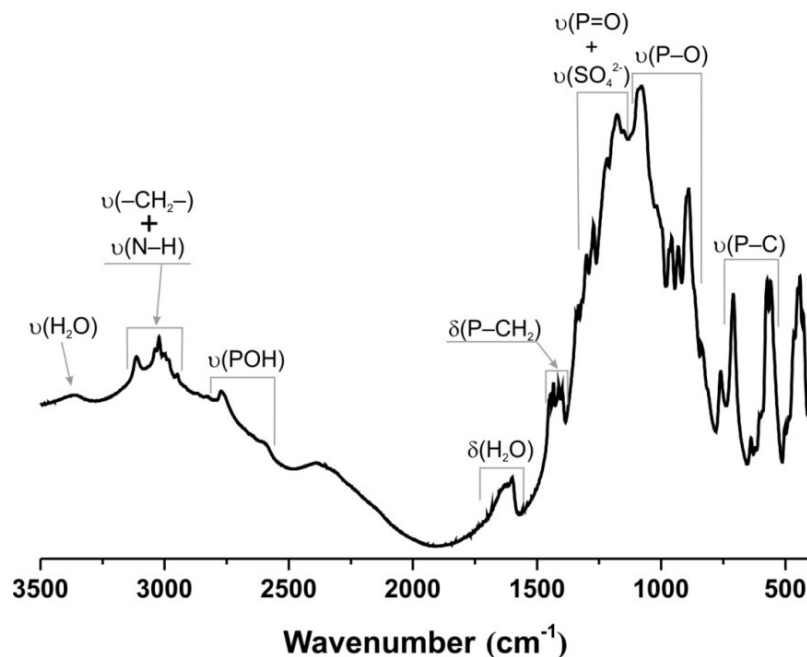


Figure 4.6 - FT-IR spectrum of $[\text{La}_2(\text{H}_4\text{nmp})_2(\text{H}_2\text{O})_2(\text{SO}_4)] \cdot \text{H}_2\text{O}$ (7) in the 3500-400 cm^{-1} spectral region and the corresponding assignments of the most significant bands.

4.4 – Concluding Remarks

The highly flexible nitrilotris(methylphosphonic acid) (H_6nmp) organic linker was assembled with rare-earth cations to produce a new family of MOFs under acidic conditions (by adding sulfuric acid to the reaction medium) *via* microwave irradiation. The crystalline 2D layered material obtained, $[La_2(H_4nmp)_2(H_2O)_3(SO_4)] \cdot 8H_2O$ (**4**), shows several dynamic and reversible Single-Crystal to Single-Crystal (SC-SC) transformations. Due to a high number of disordered water molecules present in the channels, **4** transforms with process starting immediately after filtration, originating a new material, $[La_2(H_4nmp)_2(H_2O)_3(SO_4)] \cdot 6H_2O$ (**5**). By allowing **5** to rest motionless at ambient conditions, two new structural transformations into other MOFs occurred: $[La_2(H_4nmp)_2(H_2O)_3(SO_4)] \cdot 2H_2O$ (**6**) and $[La_2(H_4nmp)_2(H_2O)(SO_4)] \cdot H_2O$ (**7**), obtained after one and three months, respectively. This process can, nonetheless, be faster by employing temperature overnight: 50 °C for **6** and 120 °C for **7**.

Despite the continuous transformations, and because it is caused mainly by removal of water molecules, all materials have very similar structural features. The asymmetric unit is composed in all cases by a single La^{3+} center and a H_4nmp^{2-} anionic organic residue, with the same level of protonation, and half sulfate ion coordinated to the metal center. In a topological view the 2D layers present in all materials are virtually the same for all materials, composed of metal centers forming a chain in a zigzag conformation along the [001] direction connected by the organic linker in an *ABAB...* fashion. Nevertheless, it is the few differences that are the basis of this dynamic 2D-3D-2D-3D transformation. The continuous removal of water molecules from the interstitial space allows the $\infty^2[La_2(H_4nmp)_2(H_2O)_x(SO_4)]$ ($x=3$ or 1) layers to be closer, and create new bonds. While in **5** it is responsible to the coordination of the sulfate ion to two La^{3+} centers of adjacent layers, forming a 3D structure, in **7** it allows a new connectivity of the organic linker to form the final 3D network. In the same way, this removal of water molecules are responsible for the slide of the $\infty^2[La_2(H_4nmp)_2(H_2O)_x(SO_4)]$ ($x=3$ or 1) layers in the [001] direction, which is responsible to break one of the La-O₄S bonds in **5**, leading to a 3D-2D transformation into **6**.

Further research concerning this new family of materials will be focused in a better control of the transformation process in order to obtain pure phases of the intermediate materials (**5-6**). We also aim to improve their stability by processing them into functional devices to study them as potential sensor or as heterogeneous catalysts.

CHAPTER 5

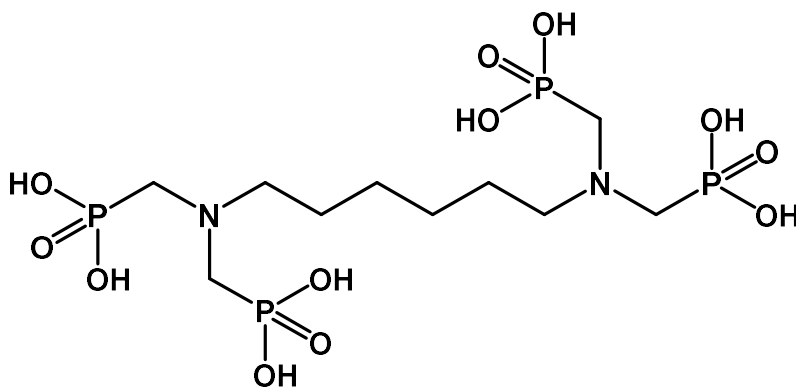
Large 3D Networks Based on Highly Flexible

Tetraphosphonic acid Organic Linker

In this chapter the highly flexible tetraphosphonic acid organic linker, Hexamethylenediamine-*N,N,N',N'*-tetrakis(methylphosphonic acid) (H_8htp , see Scheme 5.1) was used in the preparation of three new MOFs: $[Eu_2(SO_4)_2(H_6htp)(H_2O)_4] \cdot 10H_2O$ (**8**), $[La_2(SO_4)_2(H_6htp)(H_2O)_6] \cdot 6H_2O$ (**9**) and $[La_2(SO_4)_2(H_6htp)(H_2O)_4] \cdot 2H_2O$ (**10**). H_8htp pose similar challenge compared to the nitrilotris(methylphosphonic) acid (H_6nmp), presenting not only a higher freedom of the phosphonic acid groups but also an increased flexibility of the entire molecule due to the presence of six $-CH_2$ groups in the ligand backbone.

This chapter will be dedicated to the microwave-assisted (compound **8** and **9**) and hydrothermal (compound **10**) synthetic description and structural characterization of each material. All reaction allowed the isolation of single-crystals suitable for Single-crystal X-ray diffraction analysis. Despite the flexibility of the organic linker, these three compounds show similar 3D networks. All reactions were carried out in aqueous medium and because of the high flexibility of the organic linker sulfuric acid was added in small quantities. This acid is not only responsible to retard the coordination process, in the same way as for the hydrochloric acid presented in Chapters 2 and 3, but also to block the access of phosphonic acid groups by coordinating the sulfate anion to the metal center, leading to the formation of the compact 3D networks. The sulfuric acid proved to be crucial for the formation of these materials since the use of different acids originated either no precipitation or amorphous materials. When compared to the uniquely reported material based on the same building blocks, this synthetic approach allowed us to significantly reduce the reaction time considerably with an immediate crystal formation (compared to the 2 months reported).[256]

To each material a SC-SC transformation by solvent removal was tested. For compound **8** it is visible an irreversible structural transformation at 100 °C. Compounds **9** and **10** on the other hand show reversible SC-SC transformation at 100 °C. It was also possible to observe a structural transformation between compound **9** and **10** by means of pH change. In the final part of this chapter a structural elucidation will be presented of the SC-SC transformation of compound **10** by solvent removal (originating $[La_2(SO_4)_2(H_6htp)(H_2O)_3]$ (**10_dry**)) and the structural transformation of **9** into compound **10**. Due to the low quality of the dried crystals of compound **9**, no structural elucidation was achieved. It is presented, nevertheless, the transformation followed by powder X-ray diffraction.



Scheme 5.1 – Hexamethylenediamine-*N,N,N',N'*-tetrakis(methylphosphonic acid) (H_8htp)

5.1 – Synthetic Strategy

The main challenge in using the hexamethylenediamine-*N,N,N',N'*-tetrakis(methylphosphonic acid) (H_8htp) organic linkers lies in the difficult control in coordination and crystal growth. This linker poses a larger challenge when compared to the previous triphosphonic linker (H_6nmp) since an immediate precipitation is observed when H_8htp enters in contact with the metal solution. Most reports with this linker use alkaline earth or transition metals, such as calcium, barium or copper.[257-262] Due to a higher coordination number possible for lanthanides, the preparation of MOFs using these two building blocks is, thus, more demanding. There is only one reported MOF based on the H_8htp organic linker and lanthanides, synthesized by Colodrero and co-workers, $[La(H_5htp)] \cdot 7H_2O$. [256] This material was obtained by a close control of the reaction pH and a slow crystallization over a period of 2 months. The use of acids is, therefore, of utmost importance since it allows the protonation of the phosphonic acid groups, leading to a slower coordination rate. The synthesis with hydrochloric acid in similar conditions as for the previous materials (chapter 3) resulted in the formation of either amorphous material or no precipitation, using lower and higher concentrations of acid, respectively. To overcome this problem, sulfuric acid was used instead. Sulfuric acid will not only protonate the organic linker but, due to its geometrical similarity to the phosphonic acid groups, will “steal” coordination sites, leading to a more crystalline material. With this methodology it was possible to obtain three new 3D MOFs by:

i) Microwave-assisted synthesis, at 80 °C for 15 min, $[Eu_2(SO_4)_2(H_6htp)(H_2O)_4] \cdot 10H_2O$ and $[La_2(SO_4)_2(H_6htp)(H_2O)_6] \cdot 6H_2O$ (**9**) were obtained

ii) Hydrothermal, at 120 °C for three days, $[La_2(SO_4)_2(H_6htp)(H_2O)_4] \cdot 2H_2O$ (**10**) was obtained.

The sulfate ion is present in all material coordinated to the metal center, with the three materials exhibiting similar structural features.

5.2 – Microwave-assisted Synthesis of a 3D Europium–Organic Framework

5.2.1 – Crystal Structure of $[\text{Eu}_2(\text{SO}_4)_2(\text{H}_6\text{htp})(\text{H}_2\text{O})_4]\cdot 10\text{H}_2\text{O}$ (**8**)

Compound **8** was formulated as $[\text{Eu}_2(\text{SO}_4)_2(\text{H}_6\text{htp})(\text{H}_2\text{O})_4]\cdot 10\text{H}_2\text{O}$ by single crystal X-ray diffraction and crystallizes in the centrosymmetric space group $P2_1/c$. The structure has a 3D configuration, with large but compact pores occupied with disordered water molecules. The asymmetric unit is composed of one europium center, half $\text{H}_6\text{htp}^{2-}$ residue and seven water molecules (two coordinated and five of crystallization) (Figure 5.1). The Eu^{3+} is octacoordinated to one sulfate ion in a typical bidentate coordination fashion, two coordination water molecules and four different phosphonate residues, with the $\{\text{EuO}_8\}_x$ coordination polyhedron resembling a distorted dodecahedron. The Eu–O bond lengths were found to be 2.519(3) and 2.545(3) Å for the Eu– O_4S , between 2.427(3) and 2.457(3) Å for the Eu– $\text{O}(1,2)\text{W}$, and in the 2.292(2) and 2.381(3) Å range for the Eu– O_3P . These values are comparable to those reported for other Ln^{3+} -based phosphonate compounds [197, 263]. The internal O–Eu–O polyhedral angles were found as 55.70(8)° for O1–Eu–O2 (belonging to the sulfonate group), 70.22(9)° for O1W–Eu–O2W and between 70.52(9)° and 157.68(9)° for the remaining O–Eu–O angles. The $\text{H}_6\text{htp}^{2-}$ linker acts as an octodentate organic linker connecting eight symmetry-related metal centers. All phosphonate groups have a $\kappa^1\text{-O}$ mode of coordination, with all of them connecting to a different metal center.

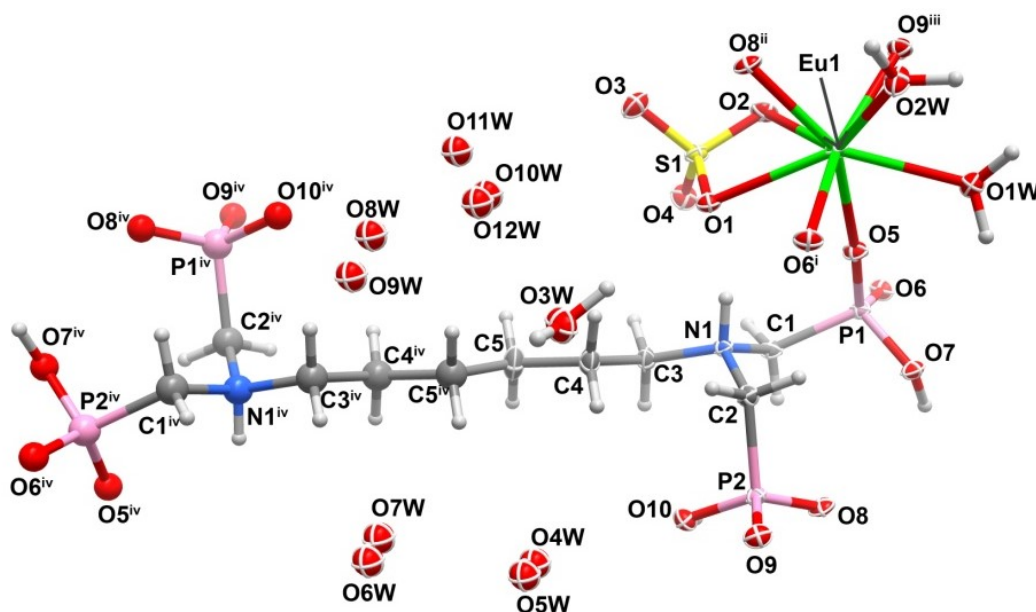


Figure 5.1 – The asymmetric unit of $[\text{Eu}_2(\text{SO}_4)_2(\text{H}_6\text{htp})(\text{H}_2\text{O})_4]\cdot 10\text{H}_2\text{O}$ (**8**) showing all non-hydrogen atoms represented as displacement ellipsoids drawn at the 50% probability level and hydrogen atoms as small spheres with arbitrary radius. The coordination sphere of the crystallographically independent metallic center, as well as the organic linker were completed for the sake of clarity. Symmetry codes used to generate equivalent atoms: (i) $-x+1, y-1/2, -z+1/2$; (ii) $x+1, y, z$; (iii) $-x+1, y+1/2, -z+1/2$; (iv) $-x+1, -y+1, -z+1$.

Each polyhedron has the two water molecules in opposite side of the sulfate ion, both directed to the pores of **8**. The remaining four phosphonates are in the same “plane” connecting to the adjacent metals, forming 2D metallic layers (Figure 5.2) with $\text{Eu}\cdots\text{Eu}$ distances of 6.2789(9) Å along the b axis and 12.4885(17) Å between each layer parallel to the ab plane. These 2D layers are connected by the outstretched organic linker, originating a compact 3D material (Figure 5.3).

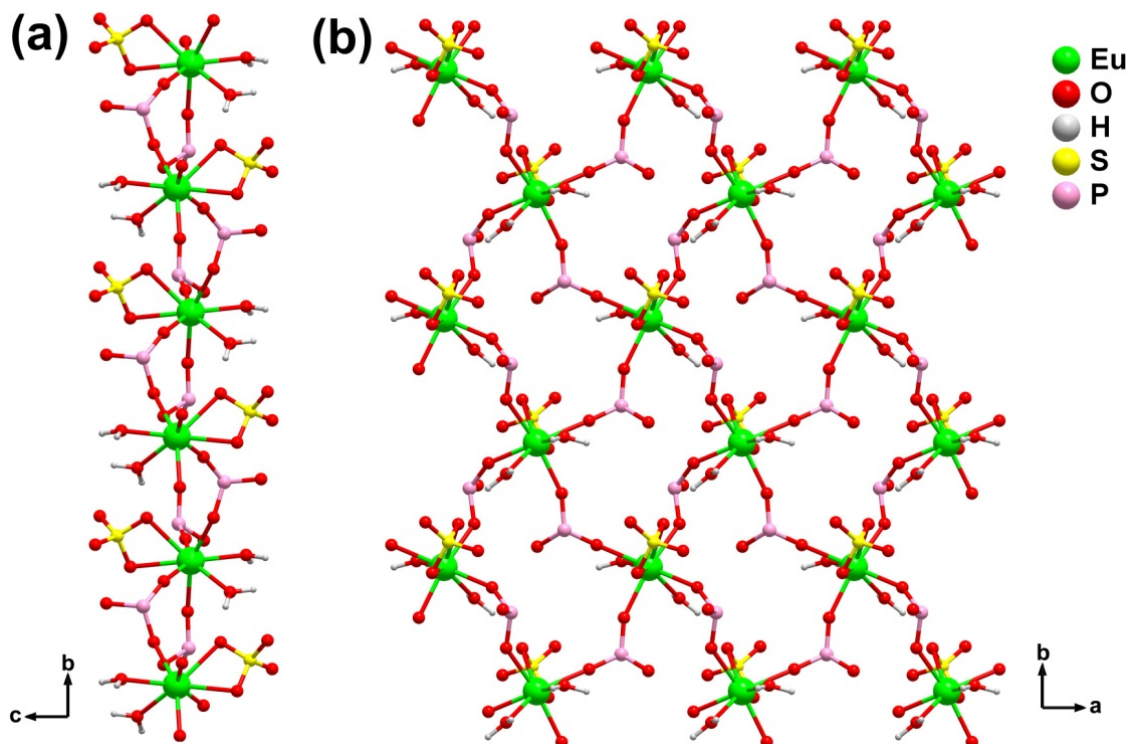


Figure 5.2 – Schematic representation of the 2D metallic layer in $[\text{Eu}_2(\text{SO}_4)_2(\text{H}_6\text{hpt})(\text{H}_2\text{O})_4]\cdot 10\text{H}_2\text{O}$ (**8**) formed by the Eu^{3+} centers along the b axis (**a**) and parallel to the ba plane (**b**). The organic linkers (except for the phosphonate groups) and solvent molecules were removed for clarity.

The disordered water molecules of crystallization occupy the pores of the structure. These molecules are engaged in several hydrogen bonding interactions between each other and with the phosphonate and sulfate groups (Figure 5.3, *inset*). We note that the removal of these solvent molecules leads to successive structural transformations. Moreover, the rehydration of the dry material leads to an amorphous material. Although the structure of the dried materials was unable to be unveiled by single-crystal x-ray diffraction, a possible explanation is presented: the increase in temperature of **8** should lead to the removal of the crystallization water molecules, which is accompanied by a shift in the [002] reflection to higher 2θ (see Figure 5.4). This is indicative of a decrease in the c axis length, resulting in an approximation of the 2D metallic layers. The rehydration of **8** introduces some water molecules but not in an order fashion, originating an amorphous material. This explanation is also supported by the FTIR study (see Figure 5.5).

In terms of topological view, and based on the recommendations of Alexandrov *et al.*,^[253] who have suggested that any moiety (ligand, atom or clusters of atoms)

connecting more than two metallic centers (μ_n) should be considered as a network node, **8** is a binodal network with a 4,8-connected nodes (four from the metal center and eight from the organic linker) and a Schäfli point symbol of $\{4^{12}\cdot6^{12}\cdot8^4\}\{4^6\}_2$. **8** shares the topology with the well known mineral fluorite. This type of topology is very interesting not only for the fact that most compounds with this topology have large cavities but, in the particular case of MOFs there is, to our knowledge, no self-interpenetrating structures.[264] This is a structural feature largely desired in the design of MOFs with large cavities.

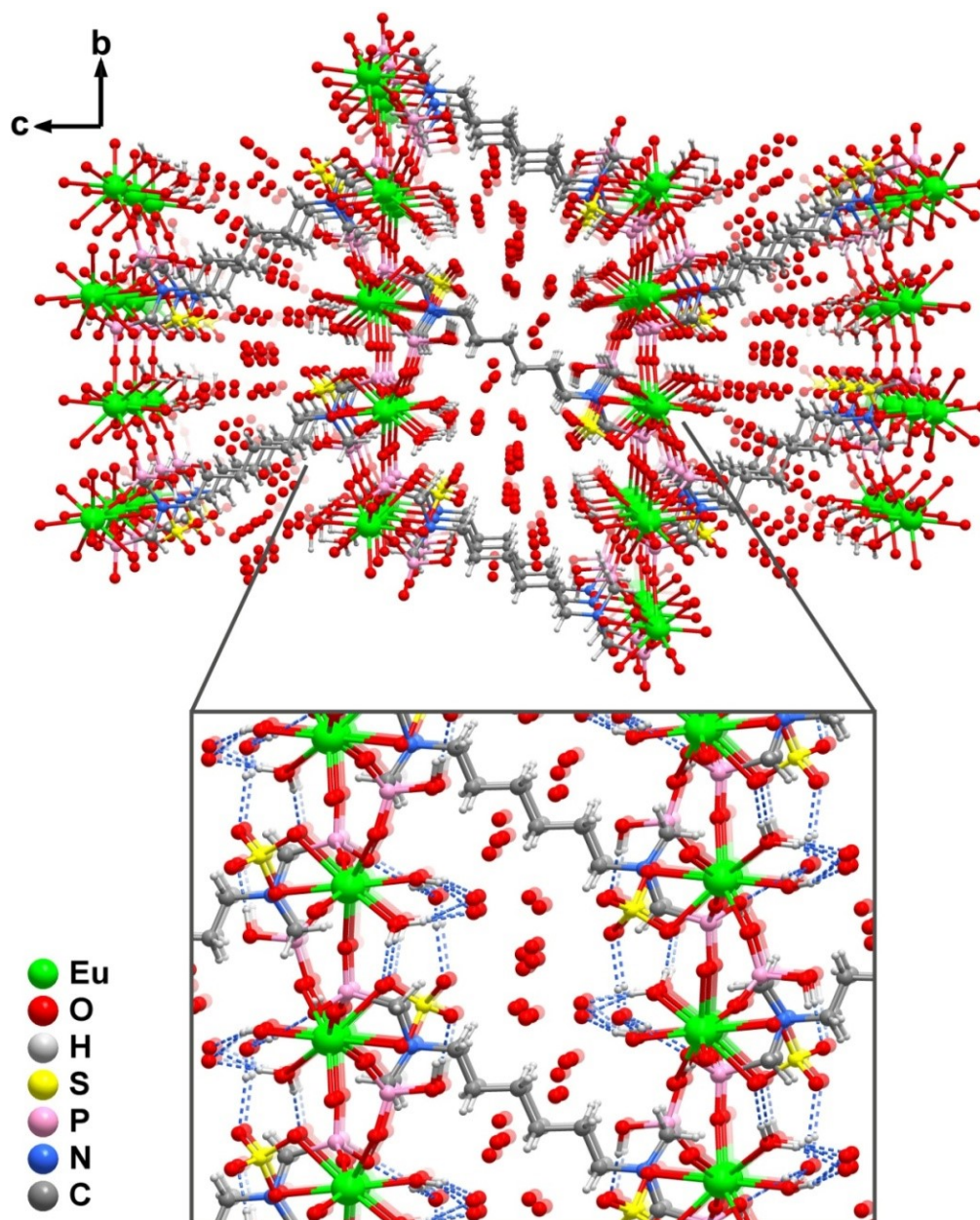


Figure 5.3 – 3D packing of $[\text{Eu}_2(\text{SO}_4)_2(\text{H}_6\text{htp})(\text{H}_2\text{O})_4]\cdot 10\text{H}_2\text{O}$ (**8**) along the $[100]$ direction, (*inset*) close up of the pore of **8** emphasizing the hydrogen interactions between water molecules and the phosphonate and sulfonate groups.

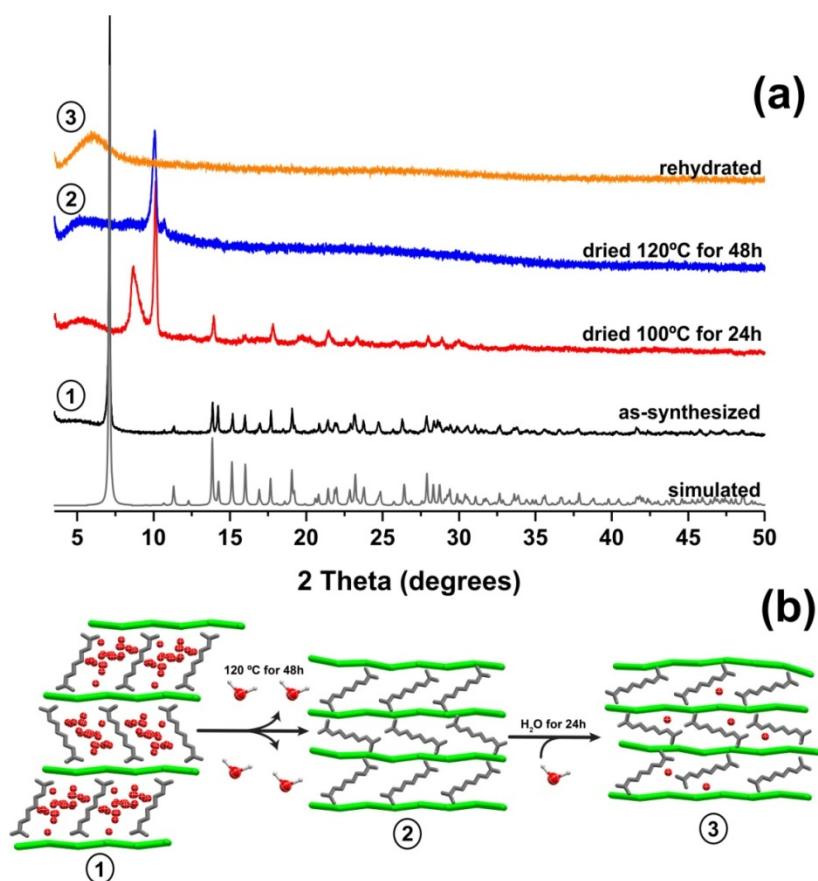


Figure 5.4 – (a) Powder X-ray diffraction patterns of the $[\text{Eu}_2(\text{SO}_4)_2(\text{H}_6\text{tp})(\text{H}_2\text{O})_4] \cdot 10\text{H}_2\text{O}$ (**8**) under different conditions. It is visible a structural transformation when the material is dried at different temperatures and its amorphization after rehydration. (b) Schematic representation of the possible transformation occurring in **8**. The numbers direct the readers to the corresponding Powder X-ray diffraction pattern.

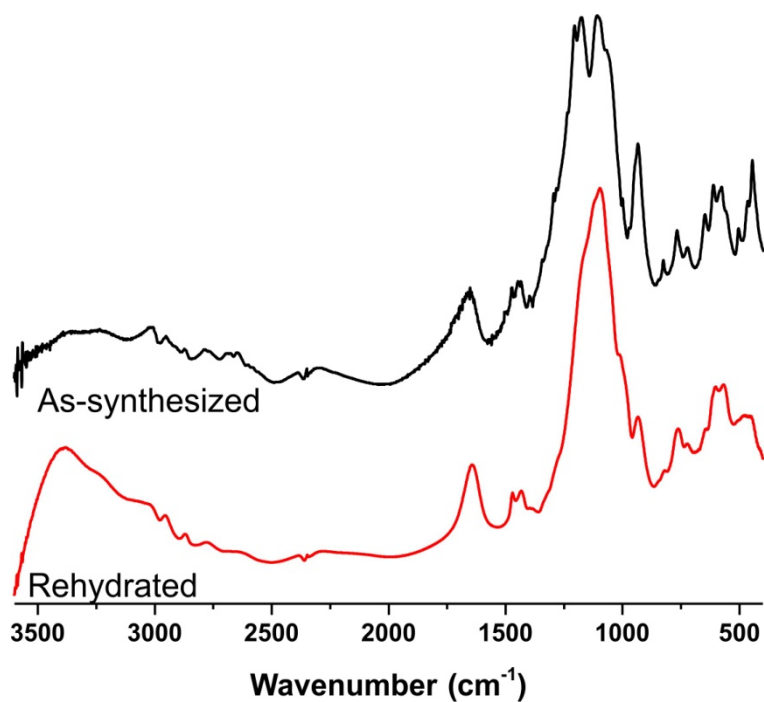


Figure 5.5 - FT-IR spectrum of the as-synthesized $[\text{Eu}_2(\text{SO}_4)_2(\text{H}_6\text{tp})(\text{H}_2\text{O})_4] \cdot 10\text{H}_2\text{O}$ (**8**) (black line) and the rehydrated material (red line) in the 4000-400 cm^{-1} spectral region. It is possible to observe the same bands for the rehydrated material as present in **8**.

5.2.2 – Physicochemical Characterization

Thermogravimetry Studies: The thermal stability of the bulk $[\text{Eu}_2(\text{SO}_4)_2(\text{H}_6\text{tp})(\text{H}_2\text{O})_4]\cdot 10\text{H}_2\text{O}$ (**8**) material was investigated between ambient temperature and *ca.* 800 °C (heating rate of 5 °C/min), to provide further information on the hydration level and stability of the material. As observed in Figure 5.6 the weight losses of **8** are continuous, being thus difficult to assign the temperature ranges to the expected residue release. For this reason a second analysis was performed from ambient temperature to 200 °C at a much slow heating rate (1 °C/min). With this analysis we were able to divide the thermogram into five well defined main regions. The first three weight loss are due to the release of water molecules, between ambient temperature and *ca.* 160 °C attributed to 5 crystallization and 2 coordination water molecules corresponding to a total weight loss of 21.1% (calculated 20.3%). The immediate weight loss, located between 215 and 435 °C is attributed to the release of the SO_4^{2-} ion in the form of one molecule of sulfuric acid, corresponding to a weight loss of 16.8% (calculated 15.8%). The last final weight loss is attributed to the complete calcinations of the material.

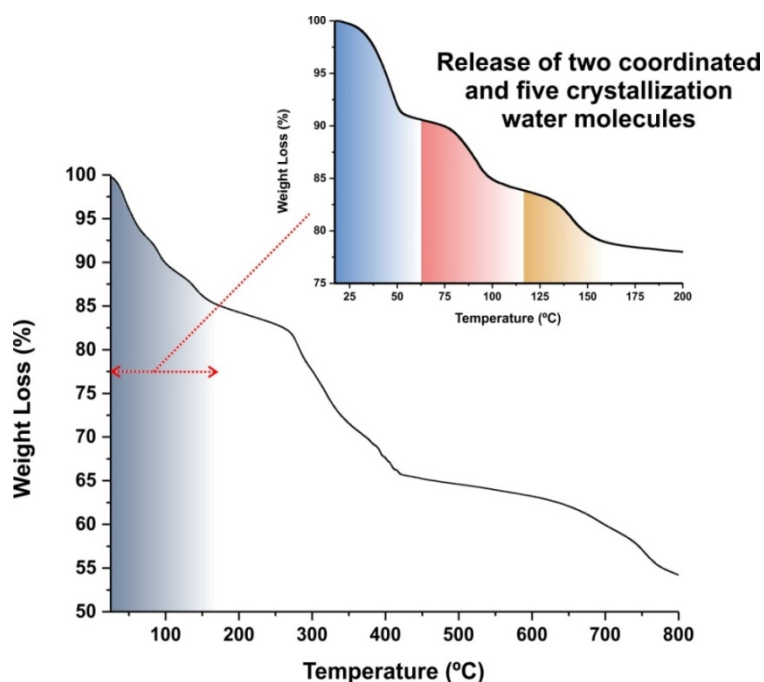


Figure 5.6 - Thermogram of $[\text{Eu}_2(\text{SO}_4)_2(\text{H}_6\text{tp})(\text{H}_2\text{O})_4]\cdot 10\text{H}_2\text{O}$ (**8**) registered between ambient temperature and *ca.* 800 °C at 5 °C/min and (*inset*) from ambient temperature and *ca.* 200 °C at 1 °C/min.

Vibrational spectroscopy: The vibrational FT-IR spectroscopy studies clearly support the structural features unveiled by the X-ray diffraction studies. Figure 5.7 depicts the FT-IR spectrum of $[\text{Eu}_2(\text{SO}_4)_2(\text{H}_6\text{tp})(\text{H}_2\text{O})_4]\cdot 10\text{H}_2\text{O}$ (**8**) in the 4000-350 cm^{-1} region, including assignments for each main observed band. Compound **8** contains a series of bands between 3640 and 3150 cm^{-1} attributed to the $\nu(\text{O-H})$ stretching vibrational modes from both coordination and crystallization water molecules. The

typical symmetric and asymmetric $\nu(\text{C-H})$ stretching vibrational modes appear in the $3100\text{--}2900\text{ cm}^{-1}$ spectral region. In the central spectral region, between 1650 and 1440 cm^{-1} , a number of very weak bands can be attributed to $\nu(\text{C-H})$ modes characteristic of P-CH_2 groups. The typical P-OH and $\nu(\text{N-H})$ stretching modes were also observed between 2825 and 2570 cm^{-1} as faint and broad bands. The $\nu(\text{P-C})$ stretching vibrational modes are also observed, in particular between *ca.* $800\text{--}690\text{ cm}^{-1}$. Also in this region, the stretching vibrational modes of $\nu(\text{P=O})$ are clearly noticed between *ca.* 1280 and 1140 cm^{-1} , plus those of $\nu(\text{P-O})$ between *ca.* 1040 and 990 cm^{-1} . The stretching vibrational modes of $\nu(\text{SO}_4^{2-})$ are also present but are superimposed by the vibrational modes of $\nu(\text{P=O})$ in the range between $1200\text{--}1140\text{ cm}^{-1}$.

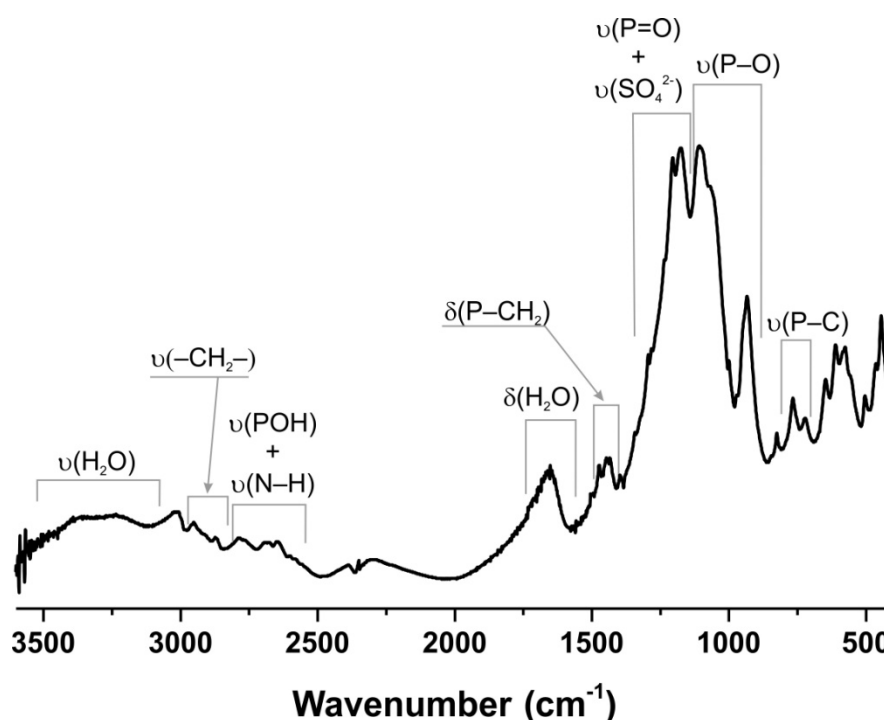


Figure 5.7 - FT-IR spectrum of the as-synthesized $[\text{Eu}_2(\text{SO}_4)_2(\text{H}_6\text{htp})(\text{H}_2\text{O})_4]\cdot 10\text{H}_2\text{O}$ (**8**) (black line) and the rehydrated material (red line) in the $4000\text{--}400\text{ cm}^{-1}$ spectral region. It is possible to observe the same bands for the rehydrated material as present in **8**.

5.3 – Microwave-assisted Synthesis of a 3D Lanthanum-Organic Framework

5.3.1 – Crystal Structure of $[\text{La}_2(\text{SO}_4)_2(\text{H}_6\text{htp})(\text{H}_2\text{O})_6]\cdot 6\text{H}_2\text{O}$ (**9**)

A similar microwave reaction as for compound **8** using lanthanum as the metal source allowed the preparation of a the new material **9** formulated by single-crystal X-ray diffraction as $[\text{La}_2(\text{SO}_4)_2(\text{H}_6\text{htp})(\text{H}_2\text{O})_6]\cdot 6\text{H}_2\text{O}$. **9** crystallizes in the centrosymmetric space group $P2_1/c$ with a 3D configuration, composed of 2D inorganic chains connected by the organic part of H_6htp , in a similar fashion as for **8**. The asymmetric unit (Figure 5.8) is composed of one lanthanum center, half $\text{H}_6\text{htp}^{2-}$ residue and six water molecules

(three coordinated and three of crystallization). The La^{3+} is octacoordinated to one sulfate ion in a simple $\kappa^1\text{-O}$ mode of coordination, three coordination water molecules and four different phosphonate residue with the $\{\text{EuO}_8\}_x$ coordination polyhedron resembling a distorted dodecahedron.

The La–O bond length was found to be 2.562(3) Å for the La–O₄S, between 2.581(3) and 2.590(3) Å for the La–O(1,2,3)W, and in the 2.427(3) and 2.497(2) Å range for the La–O₃P. The internal O–La–O polyhedral angles were found as 71.41(10)° for O1W–La–O2W, 134.41(9)° for O1W–La–O3W and 118.22(10)° for O2W–La–O3W and between 51.45(8)° and 147.10(9)° for the remaining O–La–O angles.

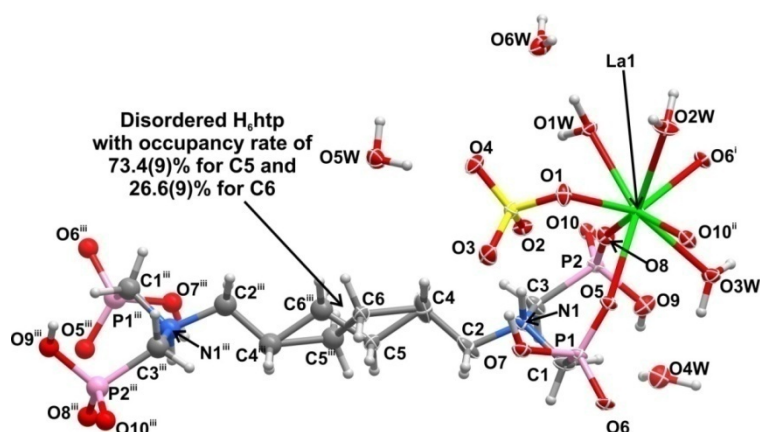


Figure 5.8 – The asymmetric unit of $[\text{La}_2(\text{SO}_4)_2(\text{H}_6\text{htp})(\text{H}_2\text{O})_6]\cdot 6\text{H}_2\text{O}$ (**9**) showing all non-hydrogen atoms represented as displacement ellipsoids drawn at the 50% probability level and hydrogen atoms as small spheres with arbitrary radius. The coordination sphere of the crystallographically independent metallic center as well as the organic linker were completed for the sake of clarity. Symmetry codes used to generate equivalent atoms: (i) $x, -y+3/2, z-1/2$; (ii) $x-1, y, z$; (iii) $-x+2, -y+1, -z+2$.

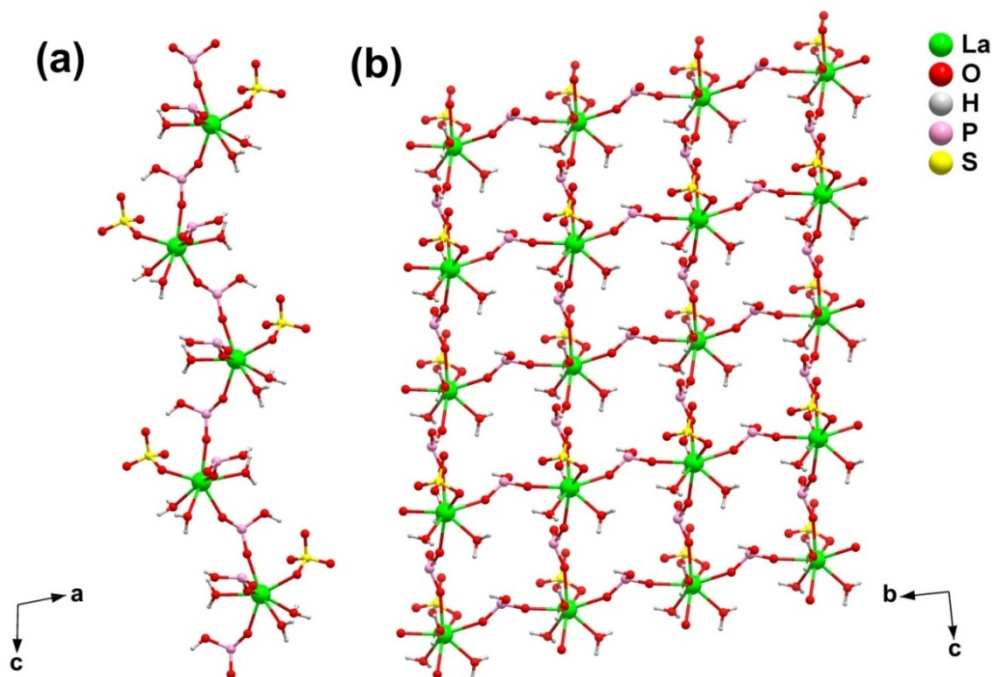


Figure 5.9 – Schematic representation of the 2D metallic layer in $[\text{La}_2(\text{SO}_4)_2(\text{H}_6\text{htp})(\text{H}_2\text{O})_6]\cdot 6\text{H}_2\text{O}$ (**9**) formed by the La^{3+} centers along the c axis (**a**) and parallel to the bc plane (**b**). The organic linkers (except for the phosphonate groups) and solvent molecules were removed for clarity.

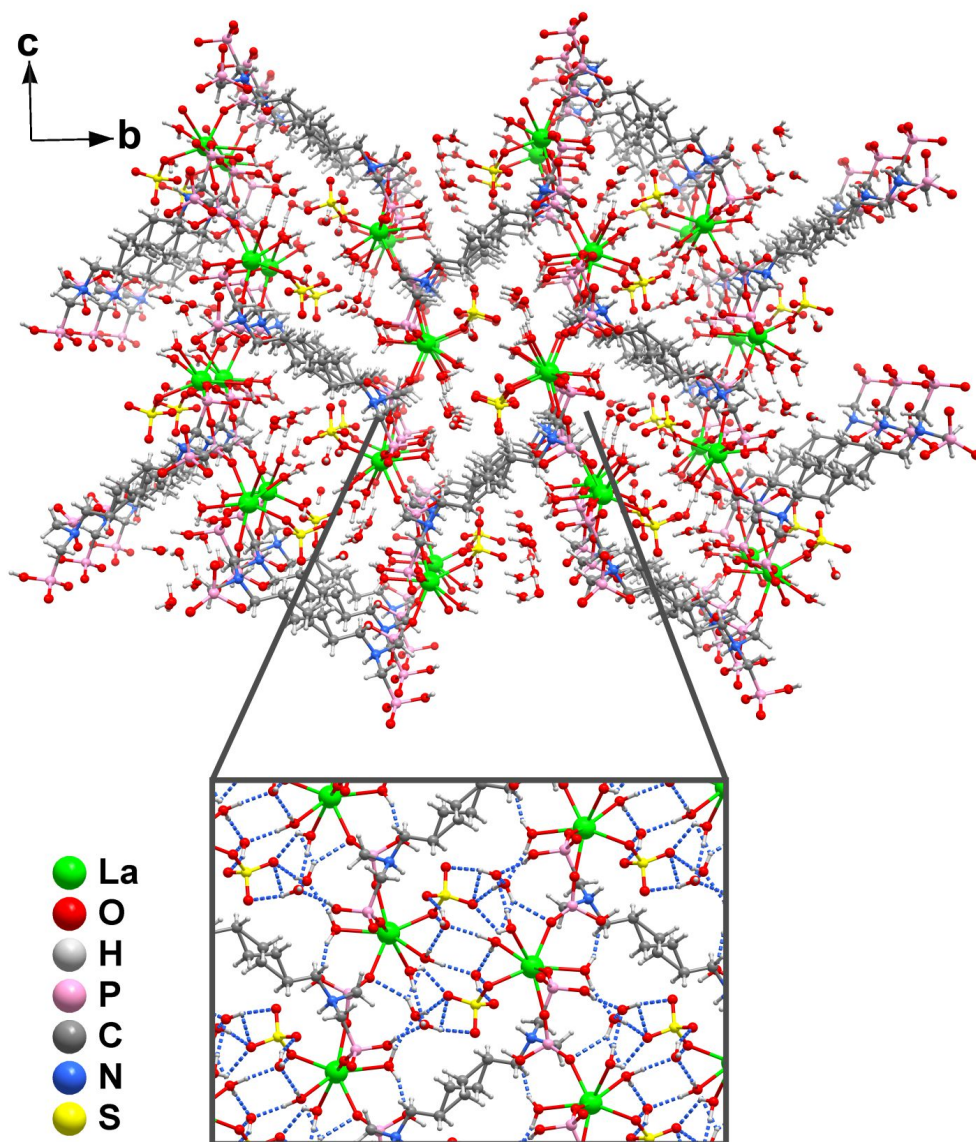


Figure 5.10 – 3D packing of $[\text{La}_2(\text{SO}_4)_2(\text{H}_6\text{htp})(\text{H}_2\text{O})_6] \cdot 6\text{H}_2\text{O}$ (**9**) along the $[100]$ direction, (*inset*) close up of the pore of **9** emphasizing the hydrogen interactions between water molecules and the phosphonate and sulfonate groups.

In terms of topological view, and based on the recommendations of Alexandrov *et al.*,^[253] **9** is a binodal network with a 3,6-connected nodes (3 from the metal center and six from the organic linker) and a Schäfli point symbol of $\{4.6^2\}_2\{4^2.6^{10}.8^3\}$. **9** shares the topology with another known mineral rutile. The coordinated water molecules and sulfate ions are directed to the center of the pores forming several hydrogen interactions with the crystallization n water molecules. These interactions are also responsible to maintain the 2D inorganic layer and, in turn, maintain the 3D network (Figure 5.10).

As for compound **8** the removal of these water molecules leads to a Single-crystal to Single-crystal transformation (**9_{dry}**). Although the crystals obtained were not suitable for single-crystal X-ray diffraction analysis, it is evident that the material maintains its crystallinity. In fact, contrary to **8**, this process is reversible, with **9_{dry}**

reverting to the initial state (**9**) at ambient conditions in a period of approximately two months or by immersing in water at 100 °C for 24h (Figure 5.11).

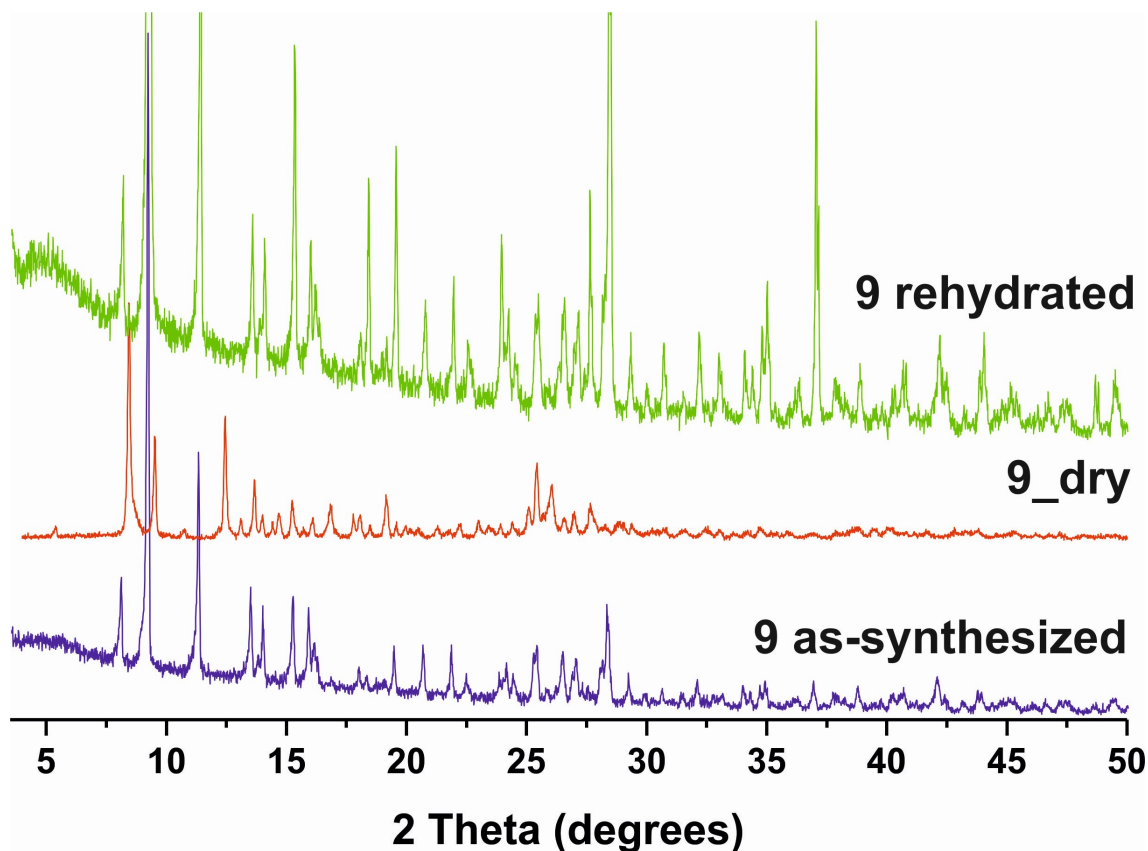


Figure 5.11 – Powder X-ray diffraction patterns of the $[\text{La}_2(\text{SO}_4)_2(\text{H}_6\text{htp})(\text{H}_2\text{O})_6]\cdot 6\text{H}_2\text{O}$ (**9**) under different conditions. It is visible a structural transformation when the material is dried and its reversibility after rehydration.

5.3.2 – Physicochemical Characterization

Thermogravimetry Studies: The level of hydration as well as the thermal stability of the bulk $[\text{La}_2(\text{SO}_4)_2(\text{H}_6\text{htp})(\text{H}_2\text{O})_6]\cdot 6\text{H}_2\text{O}$ (**9**) material was investigated between ambient temperature and *ca.* 800 °C (heating rate of 5 °C/min) as depicted in Figure 5.12. This analysis allowed the division of the thermogram into five well defined main regions. The release of the water molecules are confined in the first three steps: between room temperature and 85 °C the six crystallization water molecules are removed, with a total weight loss of 9.2% (calculated as 9.2%) while the remaining six coordination water molecules are removed in two steps, between 85-110 °C and between 110-220 °C, with a total weight loss of 9.3% (calculated as 9.2%). The sulfate ion is released in the form of one molecule of sulfuric acid in the following step, located between 220 and 485 °C, corresponding to a weight loss of 16.3% (calculated 16.7%). The last final weight loss is attributed to the complete calcination of the material.

Solid State NMR and Vibrational spectroscopy: The composition of the asymmetric unit, as well as a support of the structural features unveiled by the X-ray diffraction studies, $[\text{La}_2(\text{SO}_4)_2(\text{H}_6\text{htp})(\text{H}_2\text{O})_6]\cdot 6\text{H}_2\text{O}$ (**9**) was further investigated by

means of solid-state NMR and FTIR spectroscopy techniques. Figure 5.13 depicts the HPDEC ^{31}P MAS spectrum of **9**, which shows, in the isotropic region, the presence of two well-resolved sharp peaks centered at *ca.* -2.8 and 3.6 ppm. The peak deconvolution and integration throughout the entire spectral range (*i.e.*, including the spinning sidebands) gives a ratio of *ca.* 0.90 : 1.11, which are in agreement with the existence of only two crystallographic independent phosphorous sites in **9**. Figure 5.14, on the other hand, depicts the FT-IR spectrum of **9** in the 4000-400 cm^{-1} region, including assignments for each main observed band. The coordination and crystallization water molecules are observed by two medium bands between 3545 and 3245 cm^{-1} , attributed to the $\nu(\text{O-H})$ stretching vibrational modes. The organic component of **9** is contained in the remaining bands, namely the typical symmetric and asymmetric $\nu(\text{C-H})$ stretching vibrational modes, which appear in the 3100-2900 cm^{-1} spectral region, and the $\nu(\text{N-H})$ and the typical P-OH stretching modes are found between 2900 and 2635 cm^{-1} . In the central spectral region, between 1500 and 1370 cm^{-1} , a number of very weak bands can be attributed to $\nu(\text{C-H})$ modes characteristic of P-CH₂ groups. The $\nu(\text{P-C})$ stretching vibrational modes are also observed, in particular between *ca.* 875-710 cm^{-1} . Also in this region, the stretching vibrational modes of $\nu(\text{P=O})$ are noticed between *ca.* 1250 and 1140 cm^{-1} , plus those of $\nu(\text{P-O})$ between *ca.* 1140 and 1000 cm^{-1} . The stretching vibrational modes of $\nu(\text{SO}_4^{2-})$ are also present but are superimposed by the vibrational modes of $\nu(\text{P=O})$ in the range between 1250-1140 cm^{-1} .

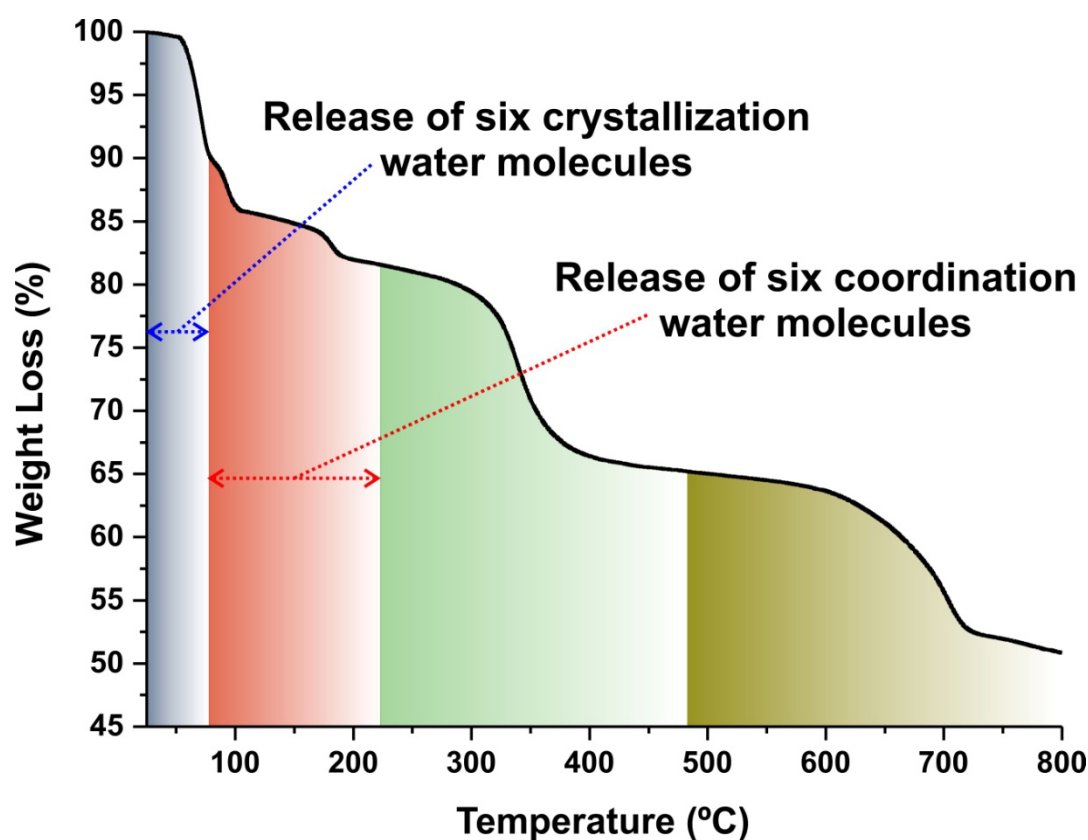


Figure 5.12 - Thermogram of $[\text{La}_2(\text{SO}_4)_2(\text{H}_6\text{tp})(\text{H}_2\text{O})_6] \cdot 6\text{H}_2\text{O}$ (**9**) registered between ambient temperature and *ca.* 800 °C at 5 °C/min.

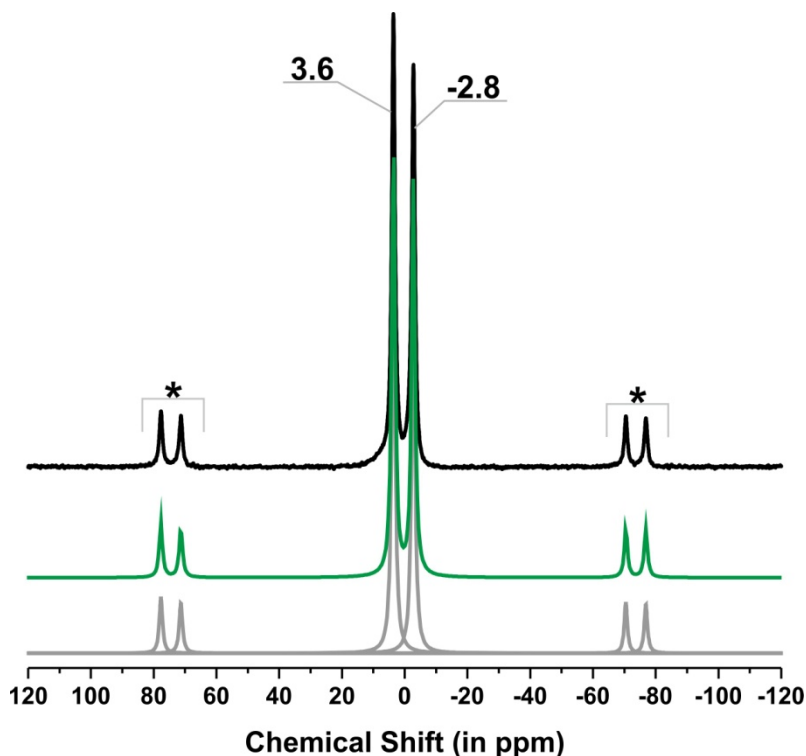


Figure 5.13 - ^{31}P HPDEC MAS spectrum of $[\text{La}_2(\text{SO}_4)_2(\text{H}_6\text{htp})(\text{H}_2\text{O})_6]\cdot 6\text{H}_2\text{O}$ (**9**). Spinning sidebands are denoted using an asterisk. Peak deconvolution and integration throughout the entire spectral range (*i.e.*, including the spinning sidebands) gives a ratio of *ca.* 0.90 : 1.11 for the isotropic resonances at *ca.* 3.6 and -2.8 ppm, respectively. The green line depicts the overall (*i.e.*, sum) data fit while the individual grey lines correspond to the fits of each single peak.

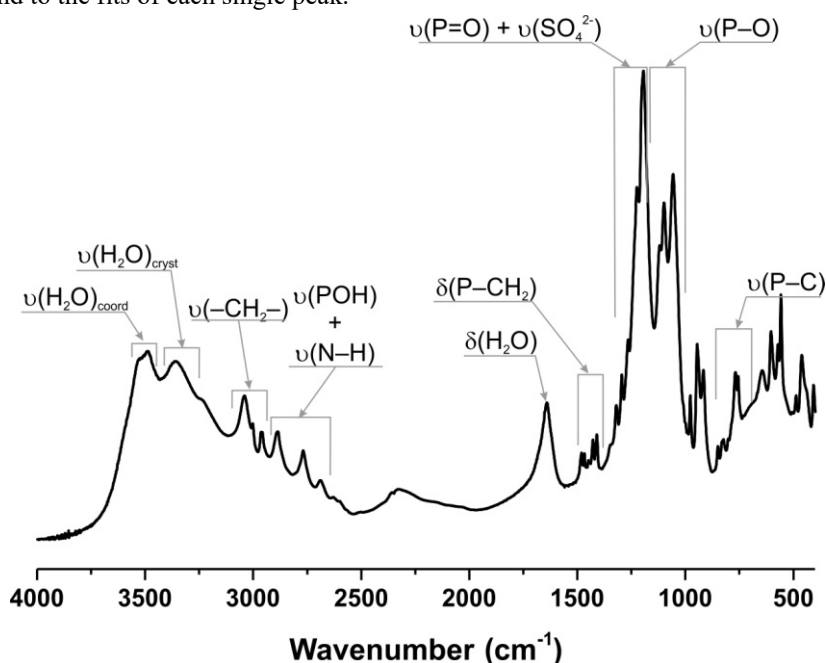


Figure 5.14 - FT-IR spectrum of the as-synthesized $[\text{La}_2(\text{SO}_4)_2(\text{H}_6\text{htp})(\text{H}_2\text{O})_6]\cdot 6\text{H}_2\text{O}$ (**9**) in the 4000-400 cm^{-1} spectral region.

5.4 – Hydrothermal Synthesis of a 3D Lanthanum-Organic Framework

5.4.1 – Crystal Structure of $[\text{La}_2(\text{SO}_4)_2(\text{H}_6\text{htp})(\text{H}_2\text{O})_4]\cdot 2\text{H}_2\text{O}$ (**10**)

Compound **10** obtained by hydrothermal conditions was formulated by single-crystal X-ray diffraction as $[\text{La}_2(\text{SO}_4)_2(\text{H}_6\text{htp})(\text{H}_2\text{O})_4]\cdot 2\text{H}_2\text{O}$ and crystallizes in the centrosymmetric space group $P2_1/c$. The structure has a 3D configuration, very similar to compound **8** and **9**, with very compact pores occupied with crystallization water molecules. The asymmetric unit (Figure 5.15) is composed of one lanthanum center, half $\text{H}_6\text{htp}^{2-}$ residue and three water molecules (two coordinated and one of crystallization). The La^{3+} is nonocoordinated to two sulfate ions (one in the same bidentate coordination fashion as in **8** and another in a $\kappa^1\text{-O}$ mode of coordination), two coordination water molecules and four different phosphonate residue with the $\{\text{EuO}_9\}_x$ coordination polyhedron resembling a slightly distorted monocapped square antiprism.

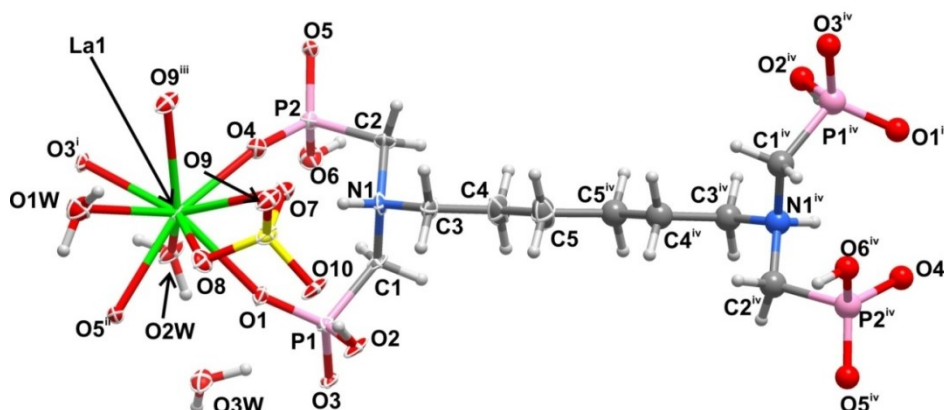


Figure 5.15 – The asymmetric unit of $[\text{La}_2(\text{SO}_4)_2(\text{H}_6\text{htp})(\text{H}_2\text{O})_4]\cdot 2\text{H}_2\text{O}$ (**10**) showing all non-hydrogen atoms represented as displacement ellipsoids drawn at the 50% probability level and hydrogen atoms as small spheres with arbitrary radius. The coordination sphere of the crystallographically independent metallic center as well as the organic linker were completed for the sake of clarity. Symmetry codes used to generate equivalent atoms: (i) $-x+1, y-1/2, -z+1/2$; (ii) $x-1, y, z$; (iii) $-x+1, -y, -z+1$; (iv) $-x+2, -y+1, -z+1$.

The La–O bond lengths were found to be 2.514(3) and 2.730(3) Å for the La–O₄S, 2.568(3) and 2.738(3) Å for the La–O(1,2)W, and in the 2.440(3) and 2.499(3) Å range for the La–O₃P. These values are comparable to those reported for other Ln^{3+} -based phosphonate compounds [197, 263]. The internal O–La–O polyhedral angles were found as 52.35(10)° for O8–La–O7 (belonging to the sulfonate group), 127.55(12)° for O1W–La–O2W and between 52.35(10)° and 145.11(10)° for the remaining O–La–O angles. The $\text{H}_6\text{htp}^{2-}$ linker acts as a hexadentate organic linker connecting six metal centers. All phosphonate groups have a $\kappa^1\text{-O}$ mode of coordination, with all of them connecting to a different metal center. The metal centers are connected with each other by these phosphonate groups and by the sulfate ions, forming a 2D inorganic layer parallel to the *bc* plane with La···La distances of 5.8285(11) and 11.8286(23) Å along

the c axis and in the range of 7.2318(17) Å between the 2D inorganic layers (Figure 5.16).

This high connectivity in every direction of the unit cell allows the formation of a compact 3D network. The metal centers are connected to each other not only by the phosphonate groups but also by the sulfate ions, forming a well organized 3D inorganic network (Figure 5.17). These metal centers form a hexagonal-like tube with La \cdots La distances ranging from 5.8286(14) and 7.4388(17) Å filled with crystallization water molecules and the stretched organic linker.

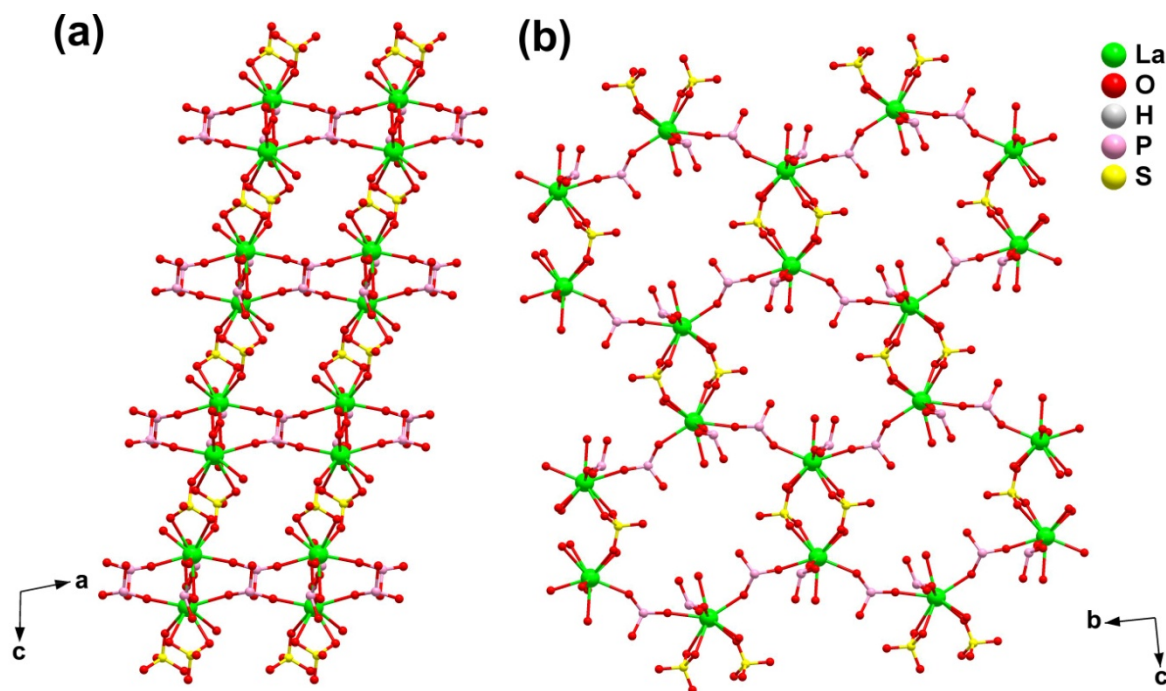


Figure 5.16 – Schematic representation of the 3D inorganic network in $[\text{La}_2(\text{SO}_4)_2(\text{H}_6\text{htp})(\text{H}_2\text{O})_4]\cdot 2\text{H}_2\text{O}$ (**10**) formed by the La^{3+} centers along the c axis (**a**) and parallel to the bc plane (**b**). The organic linkers (except for the phosphonate and groups) and solvent molecules were removed for clarity.

The small pores of **10** are well compacted with only a few crystallization water molecules. These molecules are maintained by several hydrogen interactions with the coordinated water molecules, phosphonate groups and sulfate ions. The coordinated water molecules also establish hydrogen interactions with the adjacent phosphonate and sulfonate groups, which allow a higher stability of the inorganic network. As for compound **9** the removal of these water molecules in **10** leads to a Single-crystal to Single-crystal transformation (**10_{dry}**). This process is also reversible, with **10_{dry}** reverting to the initial state (**10**) at ambient conditions in a period of approximately two months or by immersing in water at 100 °C for 24h (discussed in more detail in the next section).

In terms of topological view, and based on the recommendations of Alexandrov *et al.*,^[253] **10** is a binodal network with a 4,6-connected nodes (four from the metal center and six from the organic linker) and a Schäfli point symbol of $\{4.5^5\}_2\{4^2.5^8.6^2.8^3\}$.

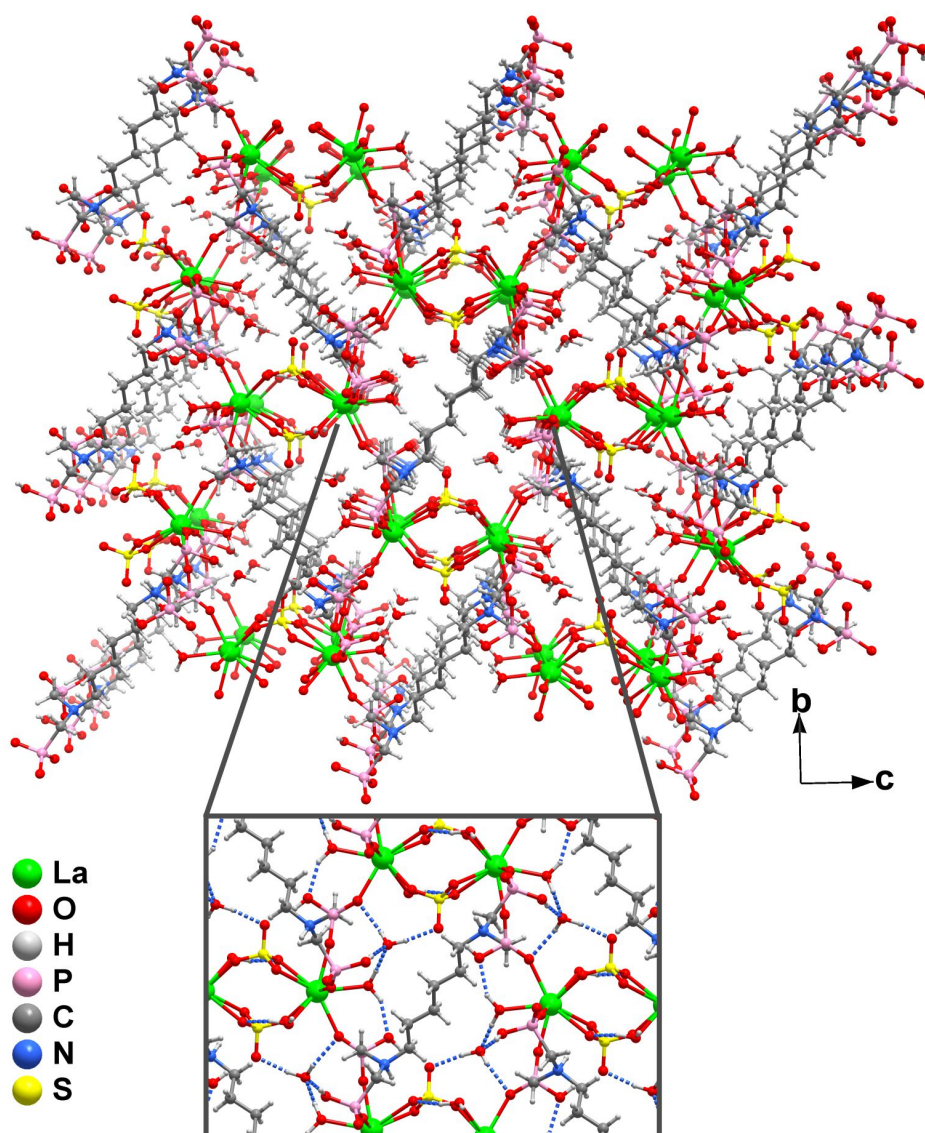


Figure 5.17 – 3D packing of $[\text{La}_2(\text{SO}_4)_2(\text{H}_6\text{htp})(\text{H}_2\text{O})_4]\cdot 2\text{H}_2\text{O}$ (**10**) along the $[100]$ direction, (*inset*) close up of the pore of **10** emphasizing the hydrogen interactions between water molecules and the phosphonate and sulfonate groups.

5.4.2 – Physicochemical Characterization

Thermogravimetry Studies: The thermal stability of the bulk $[\text{La}_2(\text{SO}_4)_2(\text{H}_6\text{htp})(\text{H}_2\text{O})_4]\cdot 2\text{H}_2\text{O}$ (**10**) material was investigated between ambient temperature and *ca.* 800 °C (heating rate of 5 °C/min) as depicted in Figure 5.18, to provide further information on the hydration level and stability of the material. With this analysis we were able to divide the thermogram into four well defined main regions with the first two weight losses are attributed to the release of the water molecules in **10**: the first located between room temperature and 175 °C due to the release of two water molecules of crystallization and two of coordination, with a total weight loss of 6.6% (calculated as 6.7%); and the second loss located between 175 and 240 °C attributed to the release of the final two coordinated water molecules, with a total

weight loss of 3.6% (calculated as 3.4%). The following weight loss, located between 240 and 580 °C is again attributed to the release of the SO_4^{2-} ion in the form of one molecule of sulfuric acid, corresponding to a weight loss of 17.4% (calculated 18.3%). The last final weight loss is attributed to the complete calcination of the material.

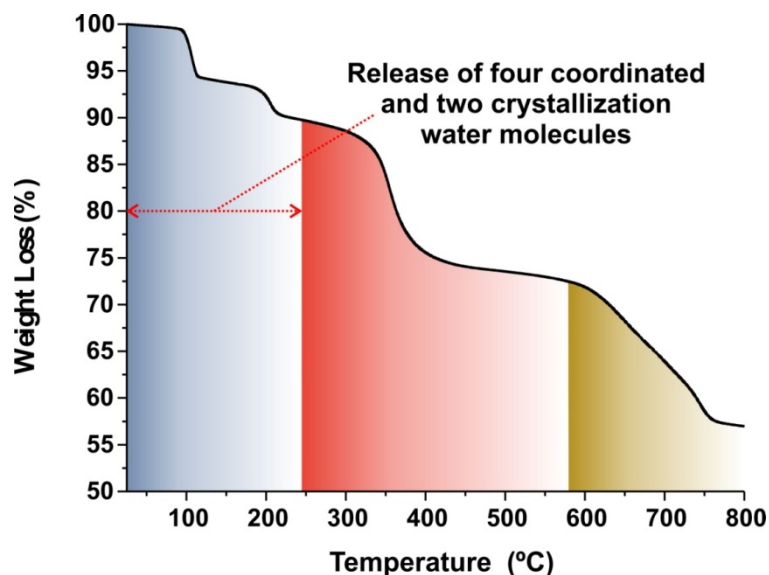


Figure 5.18 - Thermogram of $[\text{La}_2(\text{SO}_4)_2(\text{H}_6\text{hpt})(\text{H}_2\text{O})_4]\cdot 2\text{H}_2\text{O}$ (**10**) registered between ambient temperature and *ca.* 800 °C at 5 °C/min

Solid State NMR and Vibrational spectroscopy: The HPDEC ^{31}P MAS spectrum of $[\text{La}_2(\text{SO}_4)_2(\text{H}_6\text{hpt})(\text{H}_2\text{O})_4]\cdot 2\text{H}_2\text{O}$ (**10**) is presented in Figure 5.19. The isotropic region of the spectrum is composed of presence of two well-resolved sharp peaks centered at *ca.* -1.0 and 6.3 ppm. The peak deconvolution and integration throughout the entire spectral range (*i.e.*, including the spinning sidebands) gives a ratio of *ca.* 0.90 : 1.11, which are in agreement with the existence of only two crystallographic independent phosphorous sites in **10**. The vibrational spectroscopy also support the structural features unveiled by the X-ray diffraction studies. Figure 5.20 depicts the FT-IR spectrum of **10** in the 4000-400 cm^{-1} region, including assignments for each main observed band. The spectrum is very similar as for compound **9**. It is possible to distinct the coordination and crystallization water molecules in the range between 3630 and 3235 cm^{-1} , attributed to the $\nu(\text{O-H})$ stretching vibrational modes. The symmetric and asymmetric $\nu(\text{C-H})$ stretching vibrational modes, which appear in the 3100-2975 cm^{-1} spectral region, while the $\nu(\text{N-H})$ and the typical P-OH stretching modes are found between 2975 and 2795 cm^{-1} . In the central spectral region, the $\nu(\text{C-H})$ modes characteristic of P- CH_2 groups are located between 1500 and 1400 cm^{-1} . The $\nu(\text{P-C})$ stretching vibrational modes are also observed between *ca.* 790-690 cm^{-1} . The stretching vibrational modes of $\nu(\text{P=O})$ are observed between *ca.* 1300 and 1135 cm^{-1} , plus those of $\nu(\text{P-O})$ between *ca.* 1135 and 1000 cm^{-1} . The stretching vibrational modes of $\nu(\text{SO}_4^{2-})$ are also present but are superimposed by the vibrational modes of $\nu(\text{P=O})$ in the range between 1300-1135 cm^{-1} .

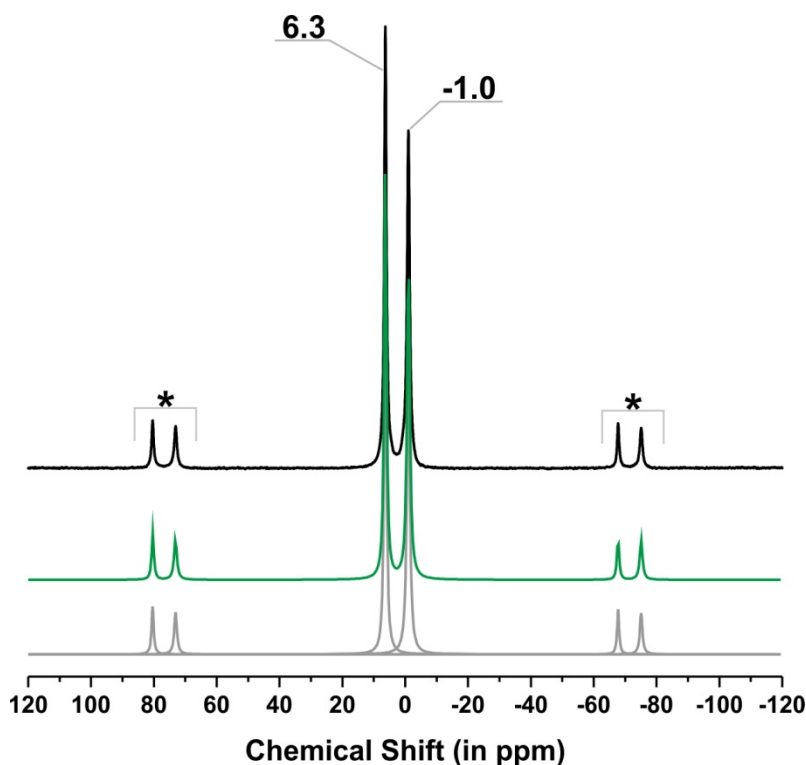


Figure 5.19 - ^{31}P HPDEC MAS spectrum of $[\text{La}_2(\text{SO}_4)_2(\text{H}_6\text{htp})(\text{H}_2\text{O})_4]\cdot 2\text{H}_2\text{O}$ (**10**). Spinning sidebands are denoted using an asterisk. Peak deconvolution and integration throughout the entire spectral range (*i.e.*, including the spinning sidebands) gives a ratio of *ca.* 1.01 : 0.99 for the isotropic resonances at *ca.* 6.3 and -1.0 ppm, respectively. The green line depicts the overall (*i.e.*, sum) data fit while the individual grey lines correspond to the fits of each single peaks.

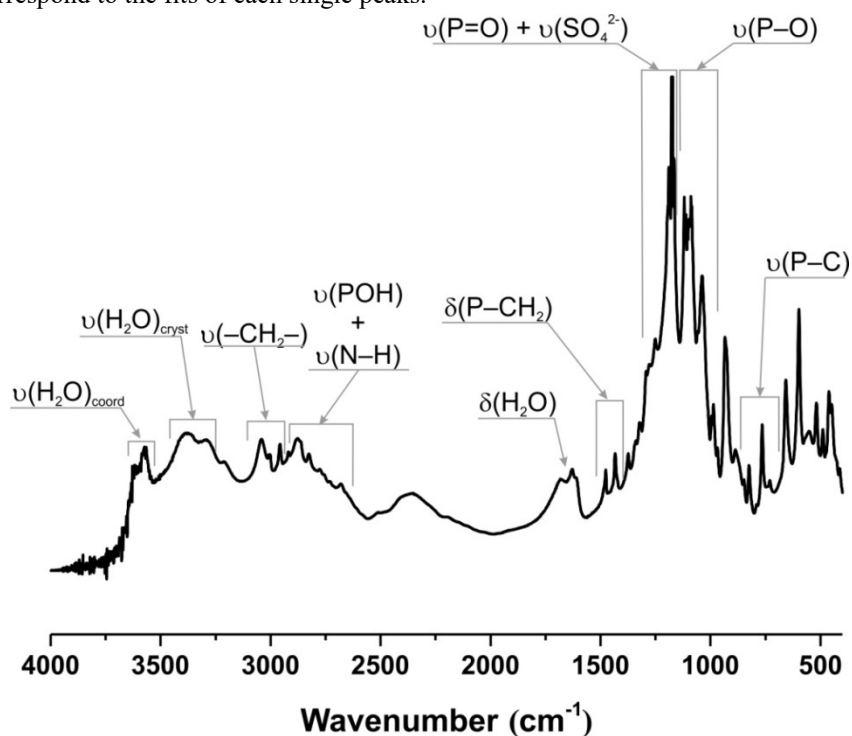


Figure 5.20 - FT-IR spectrum of the as-synthesized $[\text{La}_2(\text{SO}_4)_2(\text{H}_6\text{htp})(\text{H}_2\text{O})_4]\cdot 2\text{H}_2\text{O}$ (**10**) in the 4000-400 cm^{-1} spectral region.

5.5 – Structural Transformations Studies

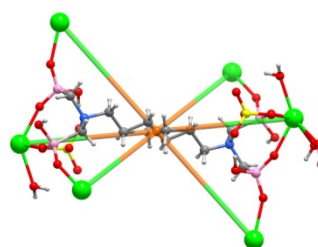
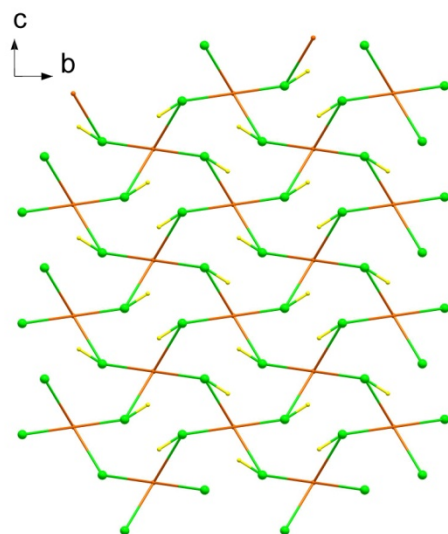
5.5.1 – SC-SC of **9** into **10** by pH change

The transformation of $[\text{La}_2(\text{SO}_4)_2(\text{H}_6\text{htp})(\text{H}_2\text{O})_6] \cdot 6\text{H}_2\text{O}$ (**9**) into $[\text{La}_2(\text{SO}_4)_2(\text{H}_6\text{htp})(\text{H}_2\text{O})_4] \cdot 2\text{H}_2\text{O}$ (**10**) occurs when **9** is introduced in a mildly alkaline aqueous solution of imidazole and left stirring at ambient temperature for a period of 24h. If one looks to the empirical formulae of the two compounds it is possible to observe that they share some similarities, being the main difference in the number of coordination and crystallization water molecules. In fact both materials have virtually the same asymmetric unit, composed of a lanthanum center connecting to a sulfonate ion, a $\text{H}_6\text{htp}^{2-}$ organic residue and coordinated water molecules. The main difference lies in the coordination environment of the La^{3+} center and the modes of coordination of the sulfate ion: while in **9** the La^{3+} center is octacoordinated, in **10** La^{3+} center is on the other hand nonocoordinated. This is due to the extra coordination of the sulfate ion which in **10**, besides the $\kappa^1\text{-O}$ connection we see in **9**, also connects to a symmetry-related metal center in a $\mu_2\text{-O, O}$ mode of coordination. During the transformation some crystallization and coordination water molecules are removed, followed by a decrease in distance of the inorganic layers formed by the metal centers (see section 5.4 for further detail) from 8.3758(5) to 5.7133(15) Å and from 13.2548(8) and 11.813(3) Å (distances between metal centers of adjacent layers). This decrease allowed the connection of the sulfate ion to the adjacent symmetry-related metal center, leading to the formation of the inorganic 3D network discussed in section 5.5. If one looks at these structures in a topological view, and based on the recommendations of Alexandrov *et al.*, [253] we have considered the Ln^{3+} cation and the anionic $\text{H}_4\text{nmp}^{2-}$ ligand as nodes. The same way as in Chapter 4, we have also included the sulfate ion as a non-topological connection (present in the Figures as a sulfur atom). Figure 5.20 depicts the topological representation of the two structures, where is evident the similar connection between the organic linker and the metal centers, with both being 6-connected, while the metal center in **10** share an extra connection to a symmetry related La^{3+} by sulfate bridge. This extra connection, alongside with the different number of water molecules are the main differences between **9** and **10**.

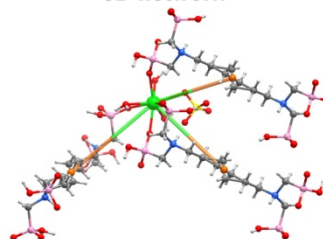
5.5.2 – SC-SC of **10** into **10_dry** by dehydration

The single-crystal to single-crystal transformation (SC-SC) of $[\text{La}_2(\text{SO}_4)_2(\text{H}_6\text{htp})(\text{H}_2\text{O})_4] \cdot 2\text{H}_2\text{O}$ (**10**) is induced by heating the material at 100 °C for 24h. The resulting material, $[\text{La}_2(\text{SO}_4)_2(\text{H}_6\text{htp})(\text{H}_2\text{O})_3]$ (**10_dry**) crystallizes in the $P2_1/n$ space group, with an asymmetric unit composed of a lanthanum center coordinated to half $\text{H}_6\text{htp}^{2-}$ residue, a sulfate ion (with the same connection as in **10**), and 1.5 coordinated water molecules. Due to the disorder in one of the coordinated water molecule, the La^{3+} metal center is either octa- or nonocoordinated. The transformation

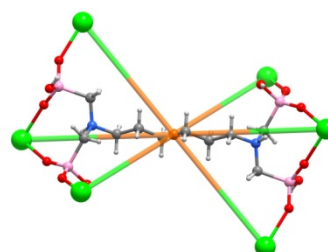
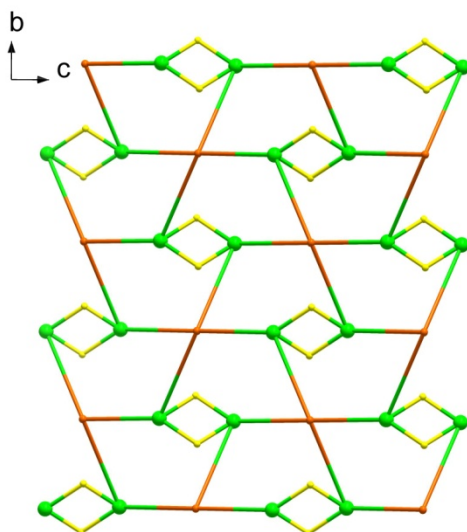
Compound 9



3,6-connected binodal
3D network



Compound 10



4,6-connected binodal
3D network

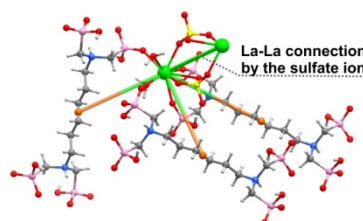


Figure 5.20 – Topological representation of $[\text{La}_2(\text{SO}_4)_2(\text{H}_6\text{tp})(\text{H}_2\text{O})_6] \cdot 6\text{H}_2\text{O}$ (**9**) and $[\text{La}_2(\text{SO}_4)_2(\text{H}_6\text{tp})(\text{H}_2\text{O})_4] \cdot 2\text{H}_2\text{O}$ (**10**) alongside with the schematic representation of the connectivity of each individual node.

of **10** into **10_{dry}**, is solely accompanied by removal of water molecules, with no break or formation of new bonds. If one looks at both structures in a topological view, as presented in Figure 5.21, we can see that they are virtually the same, with main difference being in the small distortion of the hexagonal-like tube formed by the metal centers (see section 5.4 for further detail), with no change in the distances between metal centers. The removal of the crystallization water molecules of the pores of the structures led to this distortion, as well as a disorder in the backbone of the organic linker and one of the phosphonate groups. It is not surprise that this transformation is reversible, with **10_{dry}** being completely reversed to the original phase after two months at ambient conditions or by immersing it in water at 100 °C for 24h (Figure 5.22).

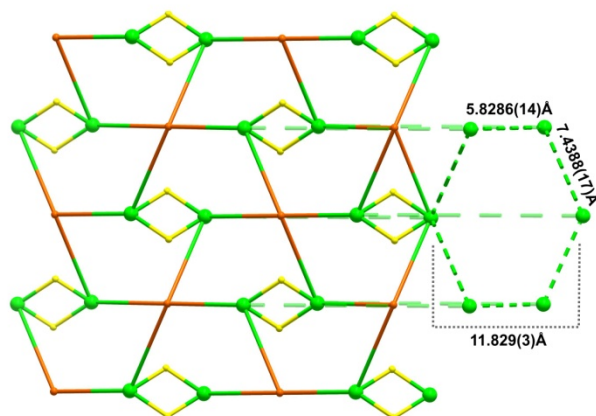
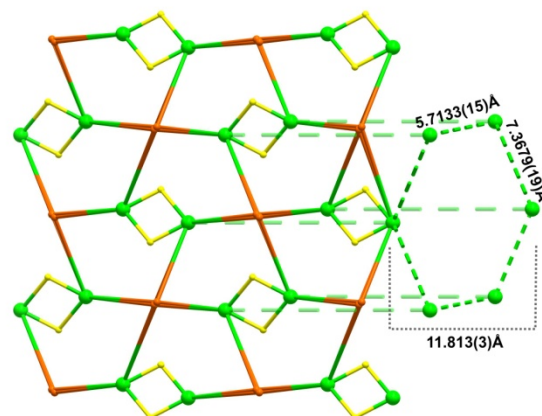
Compound 10**Compound 10_dry**

Figure 5.21 – Topological representation of $[\text{La}_2(\text{SO}_4)_2(\text{H}_6\text{tp})(\text{H}_2\text{O})_4] \cdot 2\text{H}_2\text{O}$ (**10**) and $[\text{La}_2(\text{SO}_4)_2(\text{H}_6\text{tp})(\text{H}_2\text{O})_3]$ (**10_dry**) along the $[100]$ direction. The figure emphasizes the distortion on the hexagon-like tube formed by the metal centers.

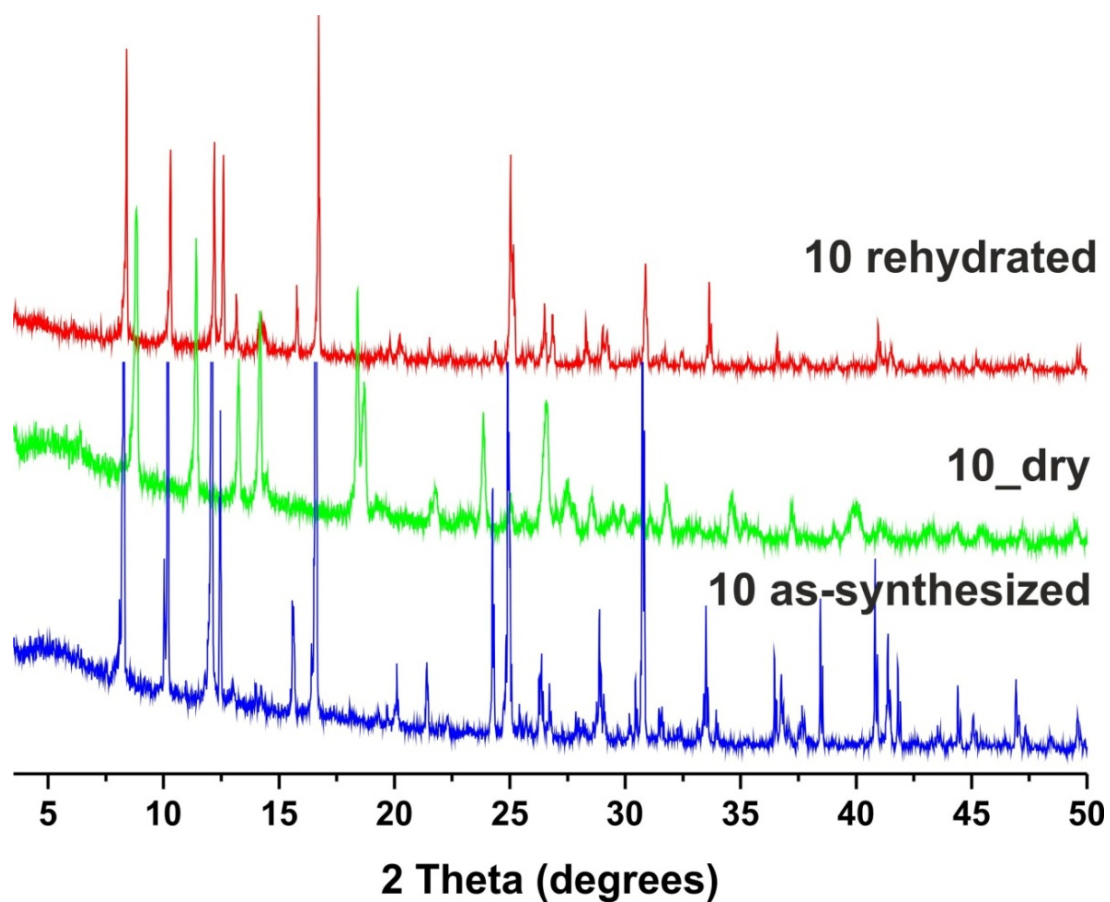


Figure 5.22 – Powder X-ray diffraction patterns of the $[\text{La}_2(\text{SO}_4)_2(\text{H}_6\text{tp})(\text{H}_2\text{O})_4] \cdot 2\text{H}_2\text{O}$ (**10**) under different conditions. It is visible a structural transformation when the material is dried and its reversibility after rehydration.

5.6 – Concluding Remarks

The highly flexible Hexamethylenediamine-*N,N,N',N'*-tetrakis(methylphosphonic acid) ($H_8\text{htp}$) organic linker was assembled with lanthanum and europium cations to produce a new family of 3D MOFs. Due to the flexibility of the organic linker synthesis were performed under acidic conditions. While hydrochloric acid (as well other types of acid) proved to be inefficient for the synthesis of these materials, with reactions originating either amorphous materials or no precipitation, sulfuric acid allowed us the preparation of highly crystalline materials, which were characterized by single-crystal X-ray diffraction studies. $[\text{Eu}_2(\text{SO}_4)_2(\text{H}_6\text{htp})(\text{H}_2\text{O})_4] \cdot 10\text{H}_2\text{O}$ (**8**) and $[\text{La}_2(\text{SO}_4)_2(\text{H}_6\text{htp})(\text{H}_2\text{O})_6] \cdot 6\text{H}_2\text{O}$ (**9**) were obtained by simple microwave synthesis, using water as the sole solvent, with the addition of small quantities of sulfuric acid. On the other hand $[\text{La}_2(\text{SO}_4)_2(\text{H}_6\text{htp})(\text{H}_2\text{O})_4] \cdot 2\text{H}_2\text{O}$ (**10**) was obtained by the conventional hydrothermal conditions, using similar reaction mixtures as for **8** and **9**, at 120 °C for a period of three days.

If one looks at the empirical formulae it is possible to see a similarity in all three compounds, composed of compact 3D networks with several cavities filled with crystallization water molecules embedded within, forming strong hydrogen interaction and maintaining their structural integrity. The removal of the crystallization water molecules of the pores of the structures leads to a reversible structural transformation in all compounds. Due to the poor crystal quality of the dried compounds **8** and **9**, it was only possible to follow the transformation by powder X-ray diffraction. The removal of the water molecules is accompanied by a shift in the reflections to higher 2θ , suggesting a decrease in pore size and the formation of a much more compact structure with a decrease in distance of the 2D metallic layers. This is evident by the similar SC-SC observed in compound **10**. In this case the dried material was studied by single-crystal X-ray diffraction, showing a material almost identical to the parent compound **10**, with the main difference in the slight distortion of the hexagonal-like tube formed by the metal centers.

The similarity in these materials is also corroborated by the structural transformation that **9** suffers when introduced in an aqueous basic solution, converting into compound **10**. The transformation is followed by the release of water molecules (both coordinated and of crystallization), following by a decrease in distance between the metallic layers. This allows the formation of a new connection between the sulfate ion and the adjacent symmetry-related metal center.

CHAPTER 6

Materials and Methods

6.1 – General Structural Characterization

SEM (Scanning Electron Microscopy) images were acquired using a high-resolution Hitachi SU-70 working at 4 kV. Samples were prepared by deposition on aluminum sample holders followed by carbon coating using an Emitech K950X carbon evaporator. EDS (Energy Dispersive X-ray Spectroscopy) data and SEM mapping images were recorded using the same microscope working at 15 kV while employing either a Bruker Quantax 400 or an ESprit 1.9 EDS microanalysis system.

Thermogravimetric analyses (TGA) were carried out using a Shimadzu TGA 50, from ambient temperature to *ca.* 800 °C (heating rate of 5 °C/min) or from ambient temperature to *ca.* 200 °C (heating rate of 1 °C/min) under a continuous stream of air at a flow rate of 20 mL min⁻¹.

Fourier Transform Infrared (FT-IR) spectra in the spectra range of 4000-350 cm⁻¹ were recorded as KBr pellets (2 mg of sample were mixed in a mortar with 200 mg of KBr) using a Bruker Tensor 27 spectrometer by averaging 256 scans at a maximum resolution of 2 cm⁻¹.

Elemental analyses for C, N and H were performed with a Truspec Micro CHNS 630-200-200 elemental analyzer at the Department of Chemistry, University of Aveiro. Analysis parameters: sample amount between 1 and 2 mg; combustion furnace temperature = 1075 °C; after burner temperature = 850 °C. Detection method: carbon - infrared absorption; hydrogen - infrared absorption; nitrogen – Thermal conductivity. Analysis time = 4 minutes. Gasses required: carrier – helium; combustion – oxygen; pneumatic – compressed air.

³¹P MAS spectra were recorded at 9.4 T on a Bruker Avance 400 wide-bore spectrometer (DSX model) on a 4 mm BL cross-polarization magic-angle spinning (CPMAS) VTN probe at 161.9 MHz. ³¹P HPDEC spectra a 90° single pulse excitation of 3.0 μs was employed; recycle delay: 60 s; ν_R = 8 or 12 kHz. Chemical shifts are quoted in parts per million (ppm) with respect to an 85% H₃PO₄ solution.

6.2 – Reagents

Chemicals were readily available from commercial sources and were used as received without further purification: gadolinium(III), europium(III) and lanthanum(III) oxide (at least 99.99%, Jinan Henghua Sci. & Tec. Co. Ltd);

nitrilotris(methylenephosphonic acid) [H_6nmp , $\text{N}(\text{CH}_2\text{PO}_3\text{H}_2)_3$, 97%, Fluka]; hexamethylenediamine-*N,N,N',N'*-tetrakis(methylphosphonic acid) solution (H_8htp , ~25% (T) in water, Fluka); hydrochloric acid (HCl , 37% Analytical Reagent Grade, Fisher Chemical); sulfuric acid (H_2SO_4 , 98% José Manuel Gomes dos Santos); ethanol absolute (Scharlau ACS, > 99.9%, analytical grade); ethanol absolute anhydrous (Carlo Erba, $\geq 99.9\%$); cyclohexanone (Aldrich, 99.8%); cyclohexanaldehyde (Aldrich, 98%); styrene oxide (Fluka, purum $\geq 97\%$); methanol (Sigma-Aldrich, chromasolv for HPLC, $\geq 99.9\%$); benzaldehyde (Sigma-Aldrich, 99%); potassium bromide (KBr for infra-red spectroscopy, > 99%, BDH SpectroSol).

6.3 – Routine Powder X-ray Diffraction

Routine Powder X-Ray Diffraction (PXRD) data for all prepared materials were collected at ambient temperature on a Empyrean PANalytical diffractometer ($\text{Cu K}_{\alpha 1,2}$ X-radiation, $\lambda_1 = 1.540598 \text{ \AA}$; $\lambda_2 = 1.544426 \text{ \AA}$), equipped with an PIXcel 1D detector and a flat-plate sample holder in a Bragg-Brentano para-focusing optics configuration (45 kV, 40 mA). Intensity data were collected by the step-counting method (step 0.01°), in continuous mode, in the $\text{ca. } 3.5 \leq 2\theta \leq 50^\circ$ range.

6.4 – Variable-Temperature Powder X-ray Diffraction

Variable-temperature powder X-ray diffraction data were collected on an PANalyticalX'Pert Powder diffractometer $\text{Cu K}_{\alpha 1,2}$ X-radiation ($\lambda_1 = 1.540598 \text{ \AA}$; $\lambda_2 = 1.544426 \text{ \AA}$), equipped with an PIXcel 1D detector, and a flat-plate sample holder in a Bragg-Brentano para-focusing optics configuration (40 kV, 50 mA), and a high-temperature Anton Paar HKL 16 chamber controlled by an Anton Paar 100 TCU unit. Intensity data were collected in the continuous mode (*ca.* 100 seconds data acquisition) in the angular range *ca.* $3.5 \leq 2\theta \leq 50$ (step 0.01°).

6.5 – Single-Crystal X-ray Diffraction Studies

All crystals were inspected and isolated using a Stemi 2000 stereomicroscope equipped with a Carl Zeiss lenses and were investigated using single-crystal X-ray diffraction. Crystal were selected manually and harvested from the batch powder and immersed in highly viscous FOMBLIN Y perfluoropolyether vacuum oil (LVAC 140/13, Sigma-Aldrich).[265] The crystals were then mounted on a Hampton Research CryoLoop and X-ray diffraction data were collected at 150(2) K on a Bruker D8 QUEST equipped with $\text{Mo K}\alpha$ sealed tube ($\lambda = 0.71073 \text{ \AA}$), a multilayer TRIUMPH X-ray mirror, a PHOTON 100 CMOS detector, and a Oxford Instruments Cryostrem 700+ Series low temperature device. The instrument was controlled with the APEX2 software package.[266] Crystal of $[\text{Gd}(\text{H}_4\text{nmp})(\text{H}_2\text{O})_2]\text{Cl}\cdot 2\text{H}_2\text{O}$ (**2**) was on the other hand mounted in a glass fiber. Preliminary X-ray diffraction data were collected at 160(2) K on an Oxford

Diffraction SuperNova, dual radiation diffractometer using a Mo K α microsource tube ($\lambda = 0.71073 \text{ \AA}$), an Atlas CCD detector, and an Oxford Instruments CryostremXL Series low temperature device.

The crystal structures were solved using the direct space algorithm implemented in SHELXT-2014,[267] which allowed the immediate location of almost all of the heaviest atoms composing the molecular unit. The remaining missing non-hydrogen atoms were located from difference Fourier maps calculated from successive full-matrix least-squares refinement cycles on F^2 using the latest SHELXL from the 2014 release.[268]

Crystallographic data collection and structure refinement details are summarized in references [23, 255, 269]

6.6 – Catalysis

A 5 mL borosilicate batch reactor, equipped with a magnetic stirrer (800 rpm) and a valve for sampling, was charged with 1.5 mL of methanol or ethanol, 0.4 M of substrate and the solid catalyst. Substrates studied were styrene oxide, benzaldehyde, cyclohexanone or cyclohexanaldehyde. The catalytic performance of compounds ($3.3\text{--}20 \text{ g}_1 \text{ L}^{-1}$) were compared to that of the ligand and the lanthanide precursor, $\text{H}_6\text{nmp}(\text{NC}_3(\text{PO}_3\text{H}_2)_3)$ and Ln_2O_3 , respectively (5.9mM, which corresponds to an equivalent molar amount of ligand or Ln^{3+} to that present in a CP load of $3.3 \text{ g}_1 \text{ L}^{-1}$). Reactions were carried out under atmospheric air, with the batch reactors immersed in an external thermostated oil bath (35 or 55 °C). Prior to reuse, the solid catalyst was separated from the reaction mixture by centrifugation (3500 rpm), washed with methanol or ethanol and dried under atmospheric conditions.

A leaching test was carried out by heating a stirred suspension of the CP ($3.3 \text{ g}_1 \text{ L}^{-1}$) in methanol and styrene oxide (0.4 M) for 15 min at 35 °C, and subsequently separating the solid by centrifugation and passing the solution through a $0.20 \mu\text{m}$ PVDF w/ GMF Whatman membrane. The obtained filtrate was transferred to a pre-heated (35 °C) batch reactor, and left to react at the same temperature under stirring.

The progress of the catalytic reactions of styrene oxide and benzaldehyde were monitored using a Varian 3800 GC equipped with a capillary column (Chrompack, CP-SIL 5 CB, $50 \text{ m} \times 0.32 \text{ mm} \times 0.5 \text{ mm}$) and a flame ionization detector. H_2 was used as the carrier gas. The progress of the catalytic reactions of cyclohexanaldehyde and cyclohexanone was monitored using a GC-MS [Trace GC 2000 Series (Thermo Quest CE Instruments) - DSQ II (Thermo Scientific)] using He gas as the carrier gas. The same instrument was used for the identification of the reaction products for all substrates using the commercial databases Wiley 6 and US National Institute of Science and Technology (NIST)-Mainlib and Replib. The MS data for cyclohexanaldehyde and cyclohexanone and the corresponding acetal and ketal, respectively, are as follows:

Cyclohexanaldehyde GC-MS m/z (relative intensity): 112 (M^+ , 18), 97 (7), 94 (57), 84 (9), 83 (95), 81 (14), 79 (30), 77 (5), 71 (8), 70 (30), 69 (6), 68 (46), 67 (12), 66 (5), 57 (9), 56 (10), 55 (100), 53 (7), 41 (22), 39 (9).

DimethoxymethylcyclohexaneGC-MS m/z (relative intensity): 127 (30), 95 (40), 76 (7), 75 (100), 67 (6), 47 (8), 45 (6).

DiethoxymethylcyclohexaneGC-MS m/z (relative intensity): 141 (30), 104 (6), 103 (100), 95 (29), 75 (26), 55 (5), 47 (15).

CyclohexanoneGC-MS m/z (relative intensity): 99 (M^+ , 6), 98 (100), 83 (18), 80 (9), 70 (32), 69 (52), 56 (10), 55 (95), 43 (6), 42 (33), 41 (17), 39 (11).

Cyclohexanone dimethyl ketalGC-MS m/z (relative intensity): 144 (M^+ , 11), 113 (62), 111 (6), 102 (7), 101 (100), 97 (5), 88, (7), 81 (28), 79 (6), 55 (8).

Cyclohexanone diethyl ketal GC-MS (m/z): 172 (M^+ , 17), 130 (6), 129 (90), 127 (100), 101 (32), 99 (46), 98 (11), 97 (9), 83 (7), 81 (38), 73 (29), 70 (8), 69 (5), 55 (11).

6.7 – Proton conduction

Proton conductivity (σ) of pelletized samples was studied by electrochemical impedance spectroscopy. Disc shaped samples were obtained after pressing the powders in a uniaxial press at 6.25 MPa, and then isostatically at 200 MPa. The apparent density of these pellets was obtained from measurements of their weight and the geometric dimensions. Silver electrodes were applied on both sides of the pellets by painting with a commercial paste (Agar Scientific). Samples were placed in ceramic tubular sample holders inside a climatic chamber (ACS DY110) in order to carry out the measurements under variable temperature (25-94 °C) and relative humidity (RH, 20-98%). Before the measurements, one of the pellets was pre-treated overnight at 120 °C. Impedance spectra were collected between 20 Hz and 2 MHz with a test signal amplitude of 100 mV using an Agilent E4980A LCR meter. Spectra were analyzed with ZView (Version 2.6b, 1990–2002, Scribner Associates) to assess the ohmic resistance (R), which was normalized to the geometry of the samples to calculate the conductivity using the formula $\sigma = L(RA)^{-1}$, where L is the thickness of the pellets and A is the surface area of the electrodes.

6.8 – One-Dimensional Lanthanide-organic Coordination Polymer with Catalytic Activity (Chapter 2)

6.8.1 – Microwave-Assisted Synthesis (1mw)

A reactive mixture composed of 0.1422 g (0.477 mmol) of nitrilotri(methylphosphonic) acid (H_6nmp) and 0.0808 g (0.247 mmol) of La_2O_3 in *ca.* 5 mL of distilled water and 100 μ L of concentrated sulphuric acid, was prepared at ambient temperature inside a 10 mL IntelliVent microwave reactor. Reaction took place inside a CEM Focused Microwave Synthesis System Discover S-Class equipment, under constant magnetic stirring (controlled by the microwave equipment) using, typically, an irradiation power of 50 W. A constant flow of air (*ca.* 20-30 psi of pressure) ensured a close control of the temperature inside the reactor. The resulting product, $[La_2(H_3nmp)_2(H_2O)_4] \cdot 4.5H_2O$

(**1mw**), was isolated as a white microcrystalline powder and it was recovered by vacuum filtration, washed with copious amounts of distilled water and then air-dried at ambient temperature.

The optimal synthetic conditions were found by systematically varying the microwave-assisted experimental parameters such as: temperature (60, 100, and 140 °C) and irradiation time (1, 5, 15 and 30 min). The irradiation power was maintained constant at 50 W.

6.8.2 – Hydrothermal Synthesis (**1h**)

The hydrothermal approach towards **1h** is similar to that describe above for **1mw** with very small modifications: a reactive mixture containing H₆nmp (0.2600 g, 0.869 mmol) and La₂O₃ (0.1400 g, 0.430 mmol) in *ca.* 6 mL of distilled water, but without the addition of acid, was placed inside an adapted Teflon-lined Parr Instruments reaction vessel (autoclave with internal volume of *ca.* 10 mL). The vessel was then placed inside a pre-heated oven at 100 °C for a period of 72 hours. After this period, the vessel was quenched to ambient temperature by immersing under cool water. The resulting white powder, identified as **1h**, was recovered by vacuum filtration, washed with copious amounts of distilled water and then air-dried at ambient temperature.

6.8.3 – One-pot synthesis (**1op**)

This approach was developed and optimized with two main objectives: i) to isolate crystals suitable for single-crystal X-ray diffraction studies; ii) to develop an alternative sustainable synthetic approach to that described above where microwave irradiation was used. A reactive mixture composed of 0.0845 g (0.283 mmol) of nitrilotri(methylphosphonic) acid (H₆nmp) and 0.1588 g (0.487 mmol) of La₂O₃ in *ca.* 10 mL of distilled water, with an overall molar ratio of *ca.* 0.5:1:2000 (La³⁺:H₆nmp:H₂O), was prepared at ambient temperature inside a 25 mL round glass flask and kept under vigorous magnetic stirring for 4 hours at 120 °C. The resulting white powder was recovered by vacuum filtration, washed with copious amounts of distilled water and then air-dried at ambient temperature.

Elemental CHN composition (%). *Calcd:* C 6.65; H 3.31, N 2.67. *Found:* C 6.62; H 3.47, N 2.70.

Thermogravimetric analysis (TGA) data (weight losses in %) and derivative thermogravimetric peaks (DTG; in italics inside the parentheses): 22-45 °C -1.62% (34 °C); 45-96 °C -4.65% (75 °C); 96-180 -9.17% (128 °C); 180 -458 °C -5.53% (402 °C); 458-771 °C -4.46% (724 °C). Total loss: 25.4%.

Selected FT-IR data (in cm⁻¹; from KBr pellets): $\nu(\text{H}_2\text{O}) = 3500\text{-}3125$; $\nu(-\text{CH}_2-)$ = 3055-2915_{w-m}; $\nu(\text{POH}) = 2844\text{-}2530\text{w-m}$; $\delta(\text{H}_2\text{O}) = 1664\text{m}$; $\delta(\text{P-CH}_2) = 1450\text{m}, 1431\text{m}$

and 1417m; $\nu(\text{P}=\text{O}) = 1255\text{-}1109\text{m-vs}$; $\nu(\text{P}-\text{O}) = 1109\text{-}888\text{vs}$; $\nu(\text{P}-\text{C}) = 755\text{m}$ and 727m.

6.8.4 – Transformation Tests

Hydrothermal conditions: In a Teflon-lined Parr Instruments reaction vessel *ca.* 30 mg of $[\text{La}_2(\text{H}_3\text{nmp})_2(\text{H}_2\text{O})_4]\cdot 4.5\text{H}_2\text{O}$ (**1mw**) were mixed with 4 mL of distilled water and 1 mL of hydrochloric acid 6 M. The vessel was allowed to heat up to *ca.* 100 °C and the reaction took place over a period of 24 h, followed by a slow cooling of the vessel up to ambient temperature (over a period of 48 h). The remaining solid was recovered by vacuum filtration, washed with distilled water and dried in open air. The resulting product was identified as a pure phase identical to $[\text{La}(\text{H}_3\text{nmp})]\cdot 1.5\text{H}_2\text{O}$, previously reported by our group by Cunha-Silva *et al.*[198]

Using a similar experimental procedure to that described in the previous paragraph but using instead 48 h of reaction followed by a quenching of the reaction vessel in cool water, **1mw** was found to be converted into a mixture of $[\text{La}(\text{H}_3\text{nmp})]\cdot 1.5\text{H}_2\text{O}$ [198] and $[\text{La}(\text{H}_3\text{nmp})]$,[197] with the latter material being the predominant phase.

One-pot: In this experiment *ca.* 30 mg of **1mw** was mixed with 4.5 mL of distilled water and 0.5 mL of hydrochloric acid 6 M in a round flask under vigorous magnetic stirring at 100 °C. Samples were removed at different reaction times (1, 5, 6, 7, 8 and 24 hours), filtered and washed with copious amounts of water. Phase identification was performed using powder X-ray diffraction studies, showing that **1mw** was fully converted into pure $[\text{La}(\text{H}_3\text{nmp})]\cdot 1.5\text{H}_2\text{O}$. [198]

6.9 – Lamellar Coordination Polymer with a Remarkable Catalytic Activity and Proton Conductivity (Chapter 3)

6.9.1 – Hydrothermal synthesis of $[\text{Gd}(\text{H}_4\text{nmp})(\text{H}_2\text{O})_2]\text{Cl}\cdot 2\text{H}_2\text{O}$ (**2ht**)

A reactive mixture containing H_6nmp (0.1671 g, 0.558 mmol) and La_2O_3 (0.0888 g, 0.272 mmol) in *ca.* 3 mL of distilled water and 3 mL of hydrochloric acid 6M, was placed inside an adapted Teflon-lined Parr Instruments reaction vessel (autoclave with internal volume of *ca.* 10 mL). The vessel was then placed inside a pre-heated oven at 100 °C for a period of 18 hours. After this period, the vessel was allowed to cool to ambient temperature. The resulting white powder, identified as $[\text{Gd}(\text{H}_4\text{nmp})(\text{H}_2\text{O})_2]\text{Cl}\cdot 2\text{H}_2\text{O}$ (**2h**), was recovered by vacuum filtration, washed with copious amounts of distilled water and then air-dried at ambient temperature.

6.9.2 – Microwave-assisted synthesis of $[\text{Gd}(\text{H}_4\text{nmp})(\text{H}_2\text{O})_2]\text{Cl}\cdot 2\text{H}_2\text{O}$ (**2mw**)

A reactive mixture composed of 0.1545 g (0.518 mmol) of H_6nmp and 0.1622 g (0.495 mmol) of La_2O_3 in *ca.* 3 mL of distilled water and 3 mL of hydrochloric acid 6M was prepared at ambient temperature inside a 10 mL IntelliVent microwave reactor. Reaction took place inside a CEM Focused Microwave Synthesis System Discover S-Class equipment, under constant magnetic stirring (controlled by the microwave equipment) using an irradiation power of 50 W at 90 °C for a 20 minutes. A constant flow of air (*ca.* 20-30 psi of pressure) ensured a close control of the temperature inside the reactor. The resulting product, $[\text{Gd}(\text{H}_4\text{nmp})(\text{H}_2\text{O})_2]\text{Cl}\cdot 2\text{H}_2\text{O}$ (**2mw**), was isolated as a white microcrystalline powder and it was recovered by vacuum filtration, washed with copious amounts of distilled water and then air-dried at ambient temperature.

6.9.3 – One-Pot synthesis $[\text{Gd}(\text{H}_4\text{nmp})(\text{H}_2\text{O})_2]\text{Cl}\cdot 2\text{H}_2\text{O}$ (**2op**)

A mixture containing H_6nmp (0.1425 g, 0.477 mmol) and Gd_2O_3 (0.1587 g, 0.438 mmol) in *ca.* 10.0 mL of distilled water and 10.0 mL of HCl 6 M was stirred thoroughly in a round bottom flask. The resulting solution was kept immersed at 120°C for 18h in an oil bath, after which time the vessel was allowed to cool slowly to ambient temperature. Crystals of $[\text{Gd}(\text{H}_4\text{nmp})(\text{H}_2\text{O})_2]\text{Cl}\cdot 2\text{H}_2\text{O}$ (**2op**) were readily obtained after *ca.* 15 min, and a few days later individual crystals could be harvested manually from the vessels and their structure investigated using single-crystal X-ray diffraction

Elemental composition (in %): C 6.41, H 3.23, N 2.49. Found: C 6.40, H 3.22, N 2.34.

Thermogravimetric analysis (TGA) data (weight losses in %) and derivative thermogravimetric peaks (DTG; in italics inside the parentheses): 22-140°C -9.2% (81°C), 140-195°C -3.1% (164°C), 195-355°C -4.7% (245°C), 355-510°C -6.2% (418°C), 510-700°C -4.2% (585°C) and 700-800°C -1.5%.

Selected FT-IR data (in cm^{-1}): $\nu(\text{H}_2\text{O})_{\text{coord}} = 3529\text{w}$; $\nu(\text{H}_2\text{O})_{\text{cryst}} = 3447\text{w}$ and 3376w ; $\nu(\text{N-H})$ and $\nu_{\text{sym+asym}}(\text{C-H}) = 3052\text{-}2981\text{w}$; $\nu(\text{POH}) = 2359\text{-}2341\text{w}$; $\delta(\text{H}_2\text{O}) = 1615\text{w}$; $\delta(\text{P-CH}_2) = 1446\text{-}1401\text{m}$; $\nu(\text{P=O}) = 1345\text{-}1163\text{m-vs}$; $\nu[(\text{CH}_2)_3\text{-N}] = 1130\text{-}1000\text{vs}$; $\nu(\text{P-C}) = 767\text{m}$ and 710m .

6.9.4 – Hydrothermal synthesis of $[\text{Gd}_2(\text{H}_3\text{nmp})_2]\cdot x\text{H}_2\text{O}$ (**3ht**)

A suspension containing H_6nmp (0.153 g, 0.512 mmol) and $\text{GdCl}_3\cdot 6\text{H}_2\text{O}$ (0.190 g, 0.512 mmol) in *ca.* 15.0 mL of distilled water (molar ratios of about 1 : 1 : 650) was stirred thoroughly in open air (at ambient temperature) for five minutes. The resulting homogeneous suspension was transferred to an adapted Teflon-lined Parr Instruments reaction vessel (autoclave with internal volume of *ca.* 24 mL), which was then placed

inside a custom preheated oven. Typically, reactions took place in a static configuration. After reacting, the vessels were allowed to cool: (i) slowly to ambient temperature or (ii) drastically under cold water (*i.e.*, autoclave quenching). *Please note*: regardless of the procedure, the isolated product was later shown to be the same. The optimal conditions were 140 °C for 18h. The contents of the autoclaves were formed by a white suspension, with the final product being recovered by vacuum filtration, washed with copious amounts of distilled water, air-dried and its crystal structure investigated using standard powder X-ray diffraction.

6.9.5 – Microwave-assisted synthesis of $[\text{Gd}_2(\text{H}_3\text{nmp})_2]\cdot x\text{H}_2\text{O}$ (**3mw**)

A reactive mixture with identical chemical composition to that described for the typical hydrothermal synthesis using convection heating was stirred thoroughly in open air for five minutes. The resulting homogeneous suspension was transferred to a 10 mL IntelliVent reactor that was placed inside a CEM Focused Microwave™ Synthesis System Discover S-Class equipment. Reactions took place with constant magnetic stirring (controlled by the microwave equipment) and by monitoring the temperature and pressure inside the vessels. A constant flow of air (*ca.* 10 bar of pressure) ensured a close control of the temperature inside the vessel. After reacting for 10 min at 100 °C, a white suspension was obtained, and the final product was recovered by vacuum filtration, followed by washing with copious amounts of distilled water, and then air-dried overnight.

6.9.6 – One-Pot synthesis of $[\text{Gd}_2(\text{H}_3\text{nmp})_2]\cdot x\text{H}_2\text{O}$ (**3op**)

A mixture containing H_6nmp (0.1505 g, 0.503 mmol) and Gd_2O_3 (0.1506 g, 0.195 mmol) in *ca.* 10.0 mL of HCl 6M/ H_2O was prepared in a round bottom flask and heated to reflux. The synthetic conditions used to prepare $[\text{Gd}_2(\text{H}_3\text{nmp})_2]\cdot x\text{H}_2\text{O}$ (**3op**) were investigated by systematically varying the temperature (between 100 and 120°C), the reaction time (between 12 and 48 hours) and the HCl/ H_2O volume ratio (between 1/9 and 1/1). After reacting, the vessels were allowed to cool slowly to ambient temperature and crystals of the final product were readily formed after *ca.* 15 min. Crystalline material of **3op** was manually harvested from the vessels and used for single crystal X-ray diffraction studies.

Elemental composition (in %): C 7.79, H 2.18, N 3.03. Found C 7.76, H 2.17, N 2.78.

Thermogravimetric analysis (TGA) data (weight losses in %) and derivative thermogravimetric peaks (DTG; in italics inside the parentheses): 15–140°C -4.7% (59°C), 350°C–425°C -1.6% (408°C), 425–620°C -4.4% (460°C), 620–800°C -3.3%. For MWAS: 30–140°C -3.9% (61°C), 320°C–427°C -2.2% (411°C), 430–620°C -4.2% (455°C), 620–800°C -3.9%.

Selected FT-IR data (in cm^{-1}): $\nu(\text{H}_2\text{O})_{\text{coord}} = 3500 \text{ w}$; $\nu(\text{N-H}) = 3005 \text{ w}$, $\nu_{\text{sym+asym}}(\text{C-H}) = 2845, 2777, 2747, 2660 \text{ w}$; $\nu(\text{P-OH}) = 2325 \text{ w}$; $\delta(\text{H}_2\text{O}) = 1630 \text{ w}$; $\delta(\text{P-CH}_2) = 1482,$

1428, 1402, 1328 m ; $\nu(P=O) = 1208, 1172\ m\text{-vs}$; $\nu((CH_2)_3-N) = 1120$ (shoulder), 1099, 1070, 1047 vs ; $\nu(P-O) = 1005, 988, 945, 913\ m$; $\nu(P-C) = 808, 753, 723\ m$.

6.10 – Dynamic Breathing effect in Metal-Organic Frameworks: Reversible 2D-3D-2D-3D Single-Crystal to Single-Crystal Transformation (chapter 4)

6.10.1 – Microwave-Assisted Synthesis of $[Ln_2(H_4nmp)_2(H_2O)_3(SO_4)] \cdot 8H_2O$ (4)

A reactive mixture composed of 0.1471 g (0.047 mmol) of nitrilotri(methylphosphonic) acid (H_6nmp) and 0.0844 g (0.025 mmol) of Ln_2O_3 ($Ln^{3+} = La^{3+}$ or Eu^{3+}) in *ca.* 5 mL of distilled water and 500 μL of concentrated sulfuric acid, with an overall molar ratio of *ca.* 0.5 : 1 : 6000 : 200 ($La^{3+} : H_6nmp : H_2O : H_2SO_4$) was prepared at ambient temperature inside a 10 mL IntelliVent microwave reactor. Reaction occurred inside a CEM Focused Microwave Synthesis System Discover S-Class equipment, under constant magnetic stirring (controlled by the microwave equipment) using an irradiation power of 50 W at 90 $^{\circ}\text{C}$ for 20 minutes. A constant flow of air (*ca.* 20-30 psi of pressure) ensured a close control of the temperature inside the reactor. After reacting, the solution was transparent and was allowed to rest motionless for three days, after which time small crystals started to appear. The resulting white crystals of $[Ln_2(H_4nmp)_2(H_2O)_3(SO_4)] \cdot 8H_2O$ (4) (where $Ln^{3+} = La^{3+}$ and Eu^{3+}), were filtered and washed with copious amounts of water to remove the excess of sulfuric acid. Crystals were left in open air.

6.10.2 – Isolation of $[Ln_2(H_4nmp)_2(H_2O)_3(SO_4)] \cdot 6H_2O$ (5), $[Ln_2(H_4nmp)_2(H_2O)_3(SO_4)] \cdot 2H_2O$ (6) and $[Ln_2(H_4nmp)_2(H_2O)_2(SO_4)] \cdot H_2O$ (7)

After filtration, **4** suffered several Single-Crystal to Single-Crystal transformations: $[Ln_2(H_4nmp)_2(H_2O)_3(SO_4)] \cdot 6H_2O$ (**5**) was obtained one day after filtration; $[Ln_2(H_4nmp)_2(H_2O)_3(SO_4)] \cdot 2H_2O$ (**6**) after one month; and $[Ln_2(H_4nmp)_2(H_2O)_2(SO_4)] \cdot H_2O$ (**7**) after three months. This transformation could be forced by using thermal treatment: **6** and **7** can be obtained when **5** is heated in an oven overnight at 50 and 120 $^{\circ}\text{C}$, respectively.

Elemental CH composition (%): Calcd: C 7.2; H 2.3; N 2.8. Found: C 6.8; H 2.3; N 2.8.
Thermogravimetric analysis (TGA) data (weight losses in %) and derivative thermogravimetric peaks (DTG, in italics inside the parentheses: 25-130 $^{\circ}\text{C}$ -1.81% (83 $^{\circ}\text{C}$); 205-275 $^{\circ}\text{C}$ -1.79% (250 $^{\circ}\text{C}$); 310-405 $^{\circ}\text{C}$ -9.71% (340 $^{\circ}\text{C}$). Total loss: 13.3%.

Selected FT-IR data (in cm^{-1} ; from KBr pellets): $\nu(\text{H}_2\text{O}_{\text{cryst}}) = 3500\text{-}3250\text{br}$; $\nu(-\text{CH}_2- + \text{N}-\text{H}) = 3155\text{-}2905\text{m-br}$; $\nu(\text{POH}) = 2810\text{-}2545\text{br}$; $\delta(\text{H}_2\text{O}) = 1705\text{-}1560\text{m}$; $\delta(\text{P}-\text{CH}_2) = 1480\text{-}1380\text{m}$; $\nu(\text{P}=\text{O} + \text{SO}_4^{2-}) = 1315\text{-}1135\text{vs}$; $\nu(\text{P}-\text{O}) = 1135\text{-}860\text{vs}$; $\nu(\text{P}-\text{C}) = 740\text{-}520\text{m}$.

6.11 – Large 3D Networks Based on Highly Flexible Tetraphosphonic acid Organic Linker (Chapter 5)

6.11.1 – Microwave-Assisted Synthesis of $[\text{Eu}_2(\text{SO}_4)_2(\text{H}_6\text{htp})(\text{H}_2\text{O})_4]\cdot 10\text{H}_2\text{O}$ (8)

A reactive mixture containing Eu_2O_3 (0.0426 g, 0.124 mmol), 125 μL of concentrated sulfuric acid in *ca.* 4 mL of distilled water and 125 μL of the hexamethylenediamine-*N,N,N',N'*-tetrakis(methylphosphonic acid) solution (H_8htp) was prepared at ambient temperature inside a 10 mL IntelliVent microwave reactor under vigorous stirring. The resulting white solution was placed inside a CEM Focused Microwave Synthesis System Discover S-Class equipment, under constant magnetic stirring (controlled by the microwave equipment) for 15 minutes at 80 $^\circ\text{C}$ using an irradiation power of 50 W. A constant flow of air (*ca.* 20-30 psi of pressure) ensured a close control of the temperature inside the reactor. The resulting product, $[\text{Eu}_2(\text{SO}_4)_2(\text{H}_6\text{htp})(\text{H}_2\text{O})_4]\cdot 10\text{H}_2\text{O}$ was isolated as white crystals, recovered by vacuum filtration and washed with copious amounts of water.

Elemental composition (in %): C 9.69, H 4.39, N 2.26. Found: C 10.94, H 4.25, N 2.35.

Thermogravimetric analysis (TGA) data (weight losses in %) and derivative thermogravimetric peaks (DTG; in italics inside the parentheses): 17-65 $^\circ\text{C}$ -9.5% (45 $^\circ\text{C}$), 65-120 $^\circ\text{C}$ -6.8% (90 $^\circ\text{C}$), 112-160 $^\circ\text{C}$ -4.8% (138 $^\circ\text{C}$), 160-800 $^\circ\text{C}$ -24.6% (281 $^\circ\text{C}$).

Selected FT-IR data (in cm^{-1}): $\nu(\text{H}_2\text{O}) = 3640\text{-}3150\text{w}$; $\nu(\text{N}-\text{H})$ and $\nu_{\text{sym}+\text{asym}}(\text{C}-\text{H}) = 3000\text{-}2800\text{w}$; $\nu(\text{POH}) = 2825\text{-}2570\text{w}$; $\delta(\text{H}_2\text{O}) = 1645\text{w}$; $\delta(\text{P}-\text{CH}_2) = 1520\text{-}1380\text{m}$; $\nu(\text{P}=\text{O}) = 1280\text{-}1140\text{m-vs}$; $\nu[\text{P}-\text{O}] = 1040\text{-}990\text{vs}$; $\nu(\text{P}-\text{C}) = 800\text{-}690\text{m}$.

6.11.2 – Microwave-Assisted Synthesis of $[\text{La}_2(\text{SO}_4)_2(\text{H}_6\text{htp})(\text{H}_2\text{O})_6]\cdot 6\text{H}_2\text{O}$ (9)

A reactive mixture containing La_2O_3 (0.0479 g, 0.124 mmol), 200 μL of concentrated sulfuric acid in *ca.* 5 mL of distilled water and 200 μL of the hexamethylenediamine-*N,N,N',N'*-tetrakis(methylphosphonic acid) solution (H_8htp) was prepared at ambient temperature inside a 10 mL IntelliVent microwave reactor under vigorous stirring. The resulting white solution was placed inside a CEM Focused

Microwave Synthesis System Discover S-Class equipment, under constant magnetic stirring (controlled by the microwave equipment) for 15 minutes at 80 °C using an irradiation power of 50 W. A constant flow of air (*ca.* 20-30 psi of pressure) ensured a close control of the temperature inside the reactor. The resulting product, $[\text{La}_2(\text{SO}_4)_2(\text{H}_6\text{htp})(\text{H}_2\text{O})_6]\cdot 6\text{H}_2\text{O}$ was isolated as white crystals, recovered by vacuum filtration and washed with copious amounts of water.

Elemental composition (in %): C 10.21, H 4.28, N 2.38. Found: C 11.01, H 4.23, N 2.30.

Thermogravimetric analysis (TGA) data (weight losses in %) and derivative thermogravimetric peaks (DTG; in italics inside the parentheses): 25-85 °C -10.4% (71 °C), 85-105 °C -3.8% (93 °C), 105-220 °C -16.7% (182 °C), 220-485°C -16.3% (340 °C), 485-800 – 14.3% (703 °C).

6.11.3 – Hydrothermal Synthesis of $[\text{La}_2(\text{SO}_4)_2(\text{H}_6\text{htp})(\text{H}_2\text{O})_4]\cdot 2\text{H}_2\text{O}$ (10)

A suspension containing 200 µL of hexamethylenediamine-*N,N,N',N'*-tetrakis(methylphosphonic acid) solution (H_8htp), La_2O_3 (0.0449 g, 0.121 mmol) and 12.5 µL of sulphuric acid in *ca.* 4 mL of distilled water was stirred thoroughly in open air (at ambient temperature). The resulting homogeneous suspension was transferred to an adapted Teflon-lined Parr Instruments reaction vessel, which was then placed inside an oven with the following program: 24h controlled heating from ambient temperature to 120 °C; 24h reacting at 120 °C and another 24h of controlled cooling to room temperature. The contents of the autoclaves were formed by a white suspension, with the final product being recovered by vacuum filtration, washed with copious amounts of distilled water, and air-dried.

Elemental composition (in %): C 11.23, H 3.58, N 2.62. Found: C 9.25, H 3.23, N 2.25.

Thermogravimetric analysis (TGA) data (weight losses in %) and derivative thermogravimetric peaks (DTG; in italics inside the parentheses): 25-155 °C -6.3% (107 °C), 155-275 °C -4.5% (205 °C), 275-580 °C -16.7% (355 °C), 580-800°C -15.5% (645 °C).

CHAPTER 7

Concluding Remarks

Following the initial objective to synthesize low dimensional coordination polymers or metal-organic frameworks, two different organic ligands were used: the triphosphonic acid H_6nmp and the tetraphosphonic acid H_8htp . Using different experimental conditions and methods, it was possible to obtain several new materials with interesting architectures.

The self assembly of H_6nmp with lanthanides allowed the preparation of four different materials: the 1D $[La_2(H_3nmp)_2(H_2O)_4] \cdot 4.5H_2O$ (**1**) and the 2D $[Gd(H_4nmp)(H_2O)_2]Cl \cdot 2H_2O$ (**2**), $[Gd_2(H_3nmp)_2] \cdot xH_2O$ (**3**) and $[Ln_2(H_4nmp)_2(H_2O)_3(SO_4)] \cdot 8H_2O$ (**4**). Compounds **1-3** could be readily isolated as pure-phases using hydrothermal, microwave-assisted or one-pot conditions. **1** is isolated preferentially at milder conditions, while **2** and **3** are obtained at longer reaction times and/or at higher temperatures. In all cases the microwave-assisted approach allowed a drastic reduction in reaction time, from several hours/days to only a few minutes (from 1 to 30 min) for all materials. Compound **4**, on the other hand, is only isolated under microwave-assisted conditions using sulfuric acid..

$[La_2(H_3nmp)_2(H_2O)_4] \cdot 4.5H_2O$ (**1**) can be further used as a precursor in the preparation of two different compounds, previously reported in our research group. **1** can be converted into a mixture of $[La(H_3nmp)] \cdot 1.5H_2O$ and $[La(H_3nmp)]$, under hydrothermal conditions or fully converted into pure $[La(H_3nmp)] \cdot 1.5H_2O$ under one-pot conditions. This “transformation” in solution is possible due to the crystallographic similarities of **1** and $[La(H_3nmp)] \cdot 1.5H_2O$ and $[La(H_3nmp)]$. However, in terms of properties they show significant differences.

1 exhibits very high catalytic activity and excellent regioselectivity in the ring opening of styrene oxide reaction, giving the corresponding β -alkoxy alcohol products with 100% selectivity and 99% yield at 30 min (for 2-methoxy-2-phenylethanol) and 3 h (for 2-ethoxy-2-phenylethanol). The catalyst **1** maintains its structural integrity even after being reused in three consecutive runs, with similar conversions: 99% in consecutive 2 h batch runs, with 2-methoxy-2-phenylethanol selectivity being always 100%. If one compare the catalytic activity of **1** and $[La(H_3nmp)]$ in the methanolysis of styrene oxide, **1** show 99% conversion after 30 min, while $[La(H_3nmp)]$ shows the same conversion only after 72 hours. The low dimensionality of **1** (1D) seem to have a particular effect, since a higher number of phosphonic acid groups are available for the catalytic reaction.

This change in properties of MOFs is also observed on $[Gd(H_4nmp)(H_2O)_2]Cl \cdot 2H_2O$ (**2**) and $[Gd_2(H_3nmp)_2] \cdot xH_2O$ (**3**). **2** and **3** have similar

structural features, being both layered 2D materials. **2** can be further converted into **3** by a SC-SC transformation at high temperature and RH. **2**, on one hand, show remarkable catalytic activity in four different organic reactions: alcoholysis of styrene oxide, with conversions similar to **1** in the methanolysis of styrene oxide (97% conversion after 30 min); acetalisation of benzaldehyde, with conversions of 92% after 1h; ketalisation of cyclohexanone, with 93% conversion reached after only 15 min; and, tested for the first time, in the acetalisation reaction of cyclohexanaldehyde, with 93% conversion after 1 h. The similar results obtained for **2** (a 2D layered material) in comparison to **1** (a 1D chain material) is associated to the electron-withdrawing chloride ions located in the interlamellar space. On the other hand, **3** show a complete different property. Although **3** show some catalytic activity in the methanolysis of styrene oxide, with 97% conversion after 72 h (data not presented in this thesis), it falls far behind the catalytic activity of **2**. However **3** show potential application for proton conduction, with conductivities of 0.51 S cm⁻¹ at 94 °C and 98% RH. The difference of properties between **2** and **3** can be easily explained: in terms of catalytic activity, the higher conversion can be is associated to the electron-withdrawing chloride ions present in **2**; in terms of proton conductivity the increased distances between layers in **3** allows the transport of a higher amount of protons and because all coordination water molecules are removed, the 2D layers of **3** are maintained by weak hydrogen interactions with the remaining crystallization water molecules, which allows fast proton transfer between neighboring phosphonate groups and water molecules. This system is the perfect example of how small changes in the overall structure can affect the properties of the materials.

H₆nmp was also assembled with lanthanum cations to produce a new family of CPs/MOFs exhibiting dynamic breathing effect. The crystalline 2D layered material obtained, [La₂(H₄nmp)₂(H₂O)₃(SO₄)]·8H₂O (**4**), shows several dynamic and reversible Single-Crystal to Single-Crystal (SC-SC) transformations. The transformation process is triggered by simple filtration of **4**, originating a new material, [La₂(H₄nmp)₂(H₂O)₃(SO₄)]·6H₂O (**5**). This is attributed to the high number of disordered water molecules present in the channels, with a small amount being released after filtration. The remaining water molecules are maintained by weak hydrogen interactions, and are gradually released over a period of one and three months, followed by two new structural transformations into [La₂(H₄nmp)₂(H₂O)₃(SO₄)]·2H₂O (**6**) and [La₂(H₄nmp)₂(H₂O)(SO₄)]·H₂O (**7**). The process can be faster just by employing temperature overnight: 50 °C for **6** and 120 °C for **7**. All materials have, nonetheless, similar structural features, as one can see by the empirical formulae of the compounds. The main difference is in distance of the ∞^2 [La₂(H₄nmp)₂(H₂O)_x(SO₄)] (x=3 or 1) layers, which decrease with the release of water molecules. This decrease in distance is responsible to the coordination of the sulfate ion to two La³⁺ centers of adjacent layers, forming the 3D structure of **5**, and in **7** it allows a new connectivity of the organic linker to form the final 3D network, which in turn is responsible for the unusual 2D-3D-2D-3D transformation.

Regarding the H₈htp organic linker, the self assembly with lanthanum or europium ions proved to be more demanding than H₆nmp, mainly due to the higher degree of

freedom of, not only the phosphonic acid groups, but also the backbone of the organic linker. By mixing the ligand solution with the metal one led to the immediate precipitation of either a gel or an amorphous material. The introduction of different acids (*e.g.* hydrochloric acid) proved to be inefficient for the synthesis of these materials, with either no precipitation after reaction or the same amorphous materials. Sulfuric acid on the other hand allowed the preparation of a series of new materials with high crystallinity. $[\text{Eu}_2(\text{SO}_4)_2(\text{H}_6\text{htp})(\text{H}_2\text{O})_4] \cdot 10\text{H}_2\text{O}$ (**8**) and $[\text{La}_2(\text{SO}_4)_2(\text{H}_6\text{htp})(\text{H}_2\text{O})_6] \cdot 6\text{H}_2\text{O}$ (**9**) were obtained by simple microwave synthesis, using water as the sole solvent, with the addition of small quantities of sulfuric acid. On the other hand $[\text{La}_2(\text{SO}_4)_2(\text{H}_6\text{htp})(\text{H}_2\text{O})_4] \cdot 2\text{H}_2\text{O}$ (**10**) was obtained by the conventional hydrothermal conditions, using similar reaction mixtures as for **8** and **9**, at 120 °C for a period of three days.

The three compounds share similar structural features, composed of a 3D networks with several hexagonal-like tube cavities filled with crystallization water molecules. The removal of the crystallization water molecules of the pores of the structures leads to a reversible structural transformation in all compounds. The structural transformation of the dried **8** and **9** compounds was not followed by single-crystal X-ray diffraction due to the poor crystal quality. Nonetheless, the removal of the water molecules is accompanied by a shift in the reflections to higher 2θ , suggesting a decrease in pore size and the formation of a much more compact structure with a decrease in distance of the 2D metallic layers. This process can be seen in the transformation of **10** after the removal of the crystallization water molecules, where the dried material show almost identical structural features to the parent compound **10**, with the main difference in the slight distortion of the hexagonal-like tube formed by the metal centers.

Another transformation was also visible when **9** is introduced in an aqueous basic solution. At these conditions, water molecules are released (both coordinated and of crystallization), followed by a decrease in distance of the metallic 2D layers. This allows the formation of a new connection between the sulfate ion and the adjacent symmetry-related metal center, originating the known compound **10**.

The results presented in this thesis were promising and, in some cases, showed the complete difference in properties of structural similar compounds. A next stage of this work should be focused in a more detailed study in the catalytic activity and proton conduction of different materials, which are already reported, using the two organic linkers used in this work, in order to better understand the role of dimensionality in these areas, ultimately leading to better design of new materials with enhance performance.

Bibliography

- [1] D.J. Cram, R.H. Bauer, *Journal of the American Chemical Society*, 81 (**1959**) 5971-5977.
- [2] B. Dietrich, J.M. Lehn, J.P. Sauvage, *Tetrahedron Letters*, 10 (**1969**) 2885-2888.
- [3] K. Ariga, T. Kunitake, *Supramolecular Chemistry – Fundamentals and Applications*, Springer-Verlag Heidelberg, **2006**.
- [4] C.R. Groom, I.J. Bruno, M.P. Lightfoot, S.C. Ward, *Acta Crystallographica Section B-Structural Science Crystal Engineering and Materials*, 72 (**2016**) 171-179.
- [5] G. Ferey, *Chemical Society Reviews*, 37 (**2008**) 191-214.
- [6] N.A. Khan, Z. Hasan, S.H. Jhung, *Journal of Hazardous Materials*, 244 (**2013**) 444-456.
- [7] L.R. MacGillivray, *Metal-Organic Framework: Design and Applications*, Willey **2010**.
- [8] O.M. Yaghi, H. Li, *Journal of the American Chemical Society*, 117 (**1995**) 10401-10402.
- [9] E.A. Tomic, *Journal of Applied Polymer Science*, 9 (**1965**) 3745-3752.
- [10] S. Qiu, G. Zhu, *Coordination Chemistry Reviews*, 253 (**2009**) 2891-2911.
- [11] K. Biradha, A. Ramanan, J.J. Vittal, *Crystal Growth & Design*, 9 (**2009**) 2969-2970.
- [12] J.L.C. Rowsell, O.M. Yaghi, *Microporous and Mesoporous Materials*, 73 (**2004**) 3-14.
- [13] R. Batten Stuart, R. Champness Neil, X.-M. Chen, J. Garcia-Martinez, S. Kitagawa, L. Öhrström, M. O’Keeffe, M. Paik Suh, J. Reedijk, *Terminology of metal–organic frameworks and coordination polymers (IUPAC Recommendations 2013)*, *Pure and Applied Chemistry*, 2013, pp. 1715.
- [14] ISI Web of Knowledge, <http://apps.webofknowledge.com>, (**2017**).
- [15] A.U. Czaja, N. Trukhan, U. Müller, *Chemical Society Reviews*, 38 (**2009**) 1284-1293.
- [16] B. Yilmaz, N. Trukhan, U. Müller, *Chinese Journal of Catalysis*, 33 (**2012**) 3-10.
- [17] P. Silva, S.M.F. Vilela, J.P.C. Tomé, F.A. Almeida Paz, *Chemical Society Reviews*, 44 (**2015**) 6774-6803.
- [18] M. Eddaoudi, D.F. Sava, J.F. Eubank, K. Adil, V. Guillerme, *Chemical Society Reviews*, 44 (**2015**) 228-249.
- [19] M.J. Zaworotko, *Nature*, 451 (**2008**) 410-411.

- [20] Y.B. He, W. Zhou, G.D. Qian, B.L. Chen, *Chemical Society Reviews*, 43 (2014) 5657-5678.
- [21] R.F. Mendes, M.M. Antunes, P. Silva, P. Barbosa, F. Figueiredo, A. Linden, J. Rocha, A.A. Valente, F.A.A. Paz, *Chemistry-A European Journal*, 22 (2016) 13136-13146.
- [22] A.H. Chughtai, N. Ahmad, H.A. Younus, A. Laypkov, F. Verpoort, *Chemical Society Reviews*, 44 (2015) 6804-6849.
- [23] R.F. Mendes, P. Silva, M.M. Antunes, A.A. Valente, F.A. Almeida Paz, *Chemical Communications*, 51 (2015) 10807-10810.
- [24] A.D.G. Firmino, R.F. Mendes, D. Ananias, S.M.F. Vilela, L.D. Carlos, J.P.C. Tomé, J. Rocha, F.A. Almeida Paz, *Inorganica Chimica Acta*, 455 (2016) 584-594.
- [25] K.C. Stylianou, R. Heck, S.Y. Chong, J. Bacsá, J.T.A. Jones, Y.Z. Khimyak, D. Bradshaw, M.J. Rosseinsky, *Journal of the American Chemical Society*, 132 (2010) 4119-4130.
- [26] J. Zhang, B. Zheng, T.T. Zhao, G.H. Li, Q.S. Huo, Y.L. Liu, *Crystal Growth & Design*, 14 (2014) 2394-2400.
- [27] J. Della Rocca, D.M. Liu, W.B. Lin, *Accounts of Chemical Research*, 44 (2011) 957-968.
- [28] P. Horcajada, R. Gref, T. Baati, P.K. Allan, G. Maurin, P. Couvreur, G. Férey, R.E. Morris, C. Serre, *Chemical Reviews*, 112 (2012) 1232-1268.
- [29] D. Bradshaw, A. Garai, J. Huo, *Chemical Society Reviews*, 41 (2012) 2344-2381.
- [30] P.O. Adelani, A.G. Oliver, T.E. Albrecht-Schmitt, *Crystal Growth & Design*, 11 (2011) 3072-3080.
- [31] V.N. Dokorou, C.J. Milios, A.C. Tsipis, M. Haukka, P.G. Weidler, A.K. Powell, G.E. Kostakis, *Dalton Transactions*, 41 (2012) 12501-12513.
- [32] J. Weber, G. Grossmann, K.D. Demadis, N. Daskalakis, E. Brendler, M. Mangstl, J. Schmedt auf der Günne, *Inorganic Chemistry*, 51 (2012) 11466-11477.
- [33] L. Wan, C.F. Pi, L. Zhang, W.J. Zheng, L.H. Weng, Z.X. Chen, Y. Zhang, *Chemical Communications*, DOI 10.1039/b800222c(2008) 2266-2268.
- [34] W.L. Queen, E.D. Bloch, C.M. Brown, M.R. Hudson, J.A. Mason, L.J. Murray, A.J. Ramirez-Cuesta, V.K. Peterson, J.R. Long, *Dalton Transactions*, 41 (2012) 4180-4187.
- [35] W. Li, M.-X. Li, J.-J. Yang, M. Shao, H.-J. Liu, *Journal of Coordination Chemistry*, 61 (2008) 2715-2724.

- [36] K.K. Bisht, E. Suresh, *Inorganic Chemistry*, 51 (2012) 9577-9579.
- [37] S. Natarajan, P. Mahata, *Current Opinion in Solid State and Materials Science*, 13 (2009) 46-53.
- [38] W.-Q. Kan, J.-F. Ma, B. Liu, J. Yang, *CrystEngComm*, 14 (2012) 286-299.
- [39] J. Cepeda, R. Balda, G. Beobide, O. Castillo, J. Fernández, A. Luque, S. Pérez-Yáñez, P. Román, D. Vallejo-Sánchez, *Inorganic Chemistry*, 50 (2011) 8437-8451.
- [40] L. Sun, Y. Li, Z. Liang, J. Yu, R. Xu, *Dalton Transactions*, 41 (2012) 12790-12796.
- [41] Y. He, S. Xiang, Z. Zhang, S. Xiong, F.R. Fronczek, R. Krishna, M. O'Keeffe, B. Chen, *Chemical Communications*, 48 (2012) 10856-10858.
- [42] H. Wang, F. Cheng, C. Zou, Q. Li, Y. Hua, J. Duan, W. Jin, *CrystEngComm*, 18 (2016) 5639-5646.
- [43] M. Bazaga-García, G.K. Angeli, K.E. Papathanasiou, I.R. Salcedo, P. Olivera-Pastor, E.R. Losilla, D. Choquesillo-Lazarte, G.B. Hix, A. Cabeza, K.D. Demadis, *Inorganic Chemistry*, 55 (2016) 7414-7424.
- [44] M. Lammert, M.T. Wharmby, S. Smolders, B. Bueken, A. Lieb, K.A. Lomachenko, D.D. Vos, N. Stock, *Chemical Communications*, 51 (2015) 12578-12581.
- [45] L. Zhai, W.-W. Zhang, X.-M. Ren, J.-L. Zuo, *Dalton Transactions*, 44 (2015) 5746-5754.
- [46] Y.F. Zhou, M. Hong, X.T. Wu, *Chemical Communications*, DOI 10.1039/b509458p(2006) 135-143.
- [47] S.M.F. Vilela, R.F. Mendes, P. Silva, J.A. Fernandes, J.P.C. Tome, F.A.A. Paz, *Crystal Growth & Design*, 13 (2013) 543-560.
- [48] M. Yamada, S.-y. Yonekura, *The Journal of Physical Chemistry C*, 113 (2009) 21531-21537.
- [49] F.A.A. Paz, S.M.F. Vilela, J.P.C. Tomé, *Crystal Growth & Design*, 14 (2014) 4873-4877.
- [50] Y. Cai, A.R. Kulkarni, Y.G. Huang, D.S. Sholl, K.S. Walton, *Crystal Growth & Design*, 14 (2014) 6122-6128.
- [51] M. Eddaoudi, J. Kim, N. Rosi, D. Vodak, J. Wachter, M. O'Keeffe, O.M. Yaghi, *Science*, 295 (2002) 469-472.
- [52] Y.F. Han, X.H. Zhou, Y.X. Zheng, Z. Shen, Y. Song, X.Z. You, *CrystEngComm*, 10 (2008) 1237-1242.

- [53] C. Ordonez, M. Fonari, J. Lindline, Q. Wei, T. Timofeeva, *Crystal Growth & Design*, 14 (2014) 5452-5465.
- [54] N. Pawlak, G. Oczko, P. Starynowicz, *Polyhedron*, 101 (2015) 152-159.
- [55] N.L. Rosi, J. Eckert, M. Eddaoudi, D.T. Vodak, J. Kim, M. O'Keeffe, O.M. Yaghi, *Science*, 300 (2003) 1127-1129.
- [56] N. Scales, Y.J. Zhang, M. Bhadbhade, I. Karatchevtseva, L.G. Kong, G.R. Lumpkin, F. Li, *Polyhedron*, 102 (2015) 130-136.
- [57] Y. Shen, X.F. Yang, H.B. Zhu, Y. Zhao, W.S. Li, *Dalton Transactions*, 44 (2015) 14741-14746.
- [58] P. Wollmann, M. Leistner, U. Stoeck, R. Grunker, K. Gedrich, N. Klein, O. Throl, W. Grahler, I. Senkovska, F. Dreisbach, S. Kaskel, *Chemical Communications*, 47 (2011) 5151-5153.
- [59] D.I. Arnold, X. Ouyang, A. Clearfield, *Chemistry of Materials*, 14 (2002) 2020-2027.
- [60] R.B. Fu, X.T. Wu, S.M. Hu, J.J. Zhang, Z.Y. Fu, W.X. Du, *Polyhedron*, 22 (2003) 2739-2744.
- [61] L. Jimenez-Garcia, A. Kaltbeitzel, V. Enkelmann, J.S. Gutmann, M. Klapper, K. Mullen, *Advanced Functional Materials*, 21 (2011) 2216-2224.
- [62] M. Taddei, F. Costantino, R. Vivani, *Inorganic Chemistry*, 49 (2010) 9664-9670.
- [63] R. Vaidhyanathan, A.H. Mahmoudkhani, G.K.H. Shimizu, *Canadian Journal of Chemistry-Revue Canadienne De Chimie*, 87 (2009) 247-253.
- [64] M.T. Wharmby, J.P.S. Mowat, S.P. Thompson, P.A. Wright, *Journal of the American Chemical Society*, 133 (2011) 1266-1269.
- [65] S.M.F. Vilela, J.A. Fernandes, D. Ananias, L.D. Carlos, J. Rocha, J.P.C. Tomé, F.A. Almeida Paz, *CrystEngComm*, 16 (2014) 344-358.
- [66] T.A. Makal, X. Wang, H.C. Zhou, *Crystal Growth & Design*, 13 (2013) 4760-4768.
- [67] H. Li, M. Eddaoudi, M. O'Keeffe, O.M. Yaghi, *Nature*, 402 (1999) 276-279.
- [68] H. Furukawa, N. Ko, Y.B. Go, N. Aratani, S.B. Choi, E. Choi, A.O. Yazaydin, R.Q. Snurr, M. O'Keeffe, J. Kim, O.M. Yaghi, *Science*, 329 (2010) 424-428.
- [69] H. Furukawa, K.E. Cordova, M. O'Keeffe, O.M. Yaghi, *Science*, 341 (2013) 974-+.
- [70] H.X. Deng, S. Grunder, K.E. Cordova, C. Valente, H. Furukawa, M. Hmadeh, F. Gandara, A.C. Whalley, Z. Liu, S. Asahina, H. Kazumori, M. O'Keeffe, O. Terasaki, J.F. Stoddart, O.M. Yaghi, *Science*, 336 (2012) 1018-1023.

- [71] H. Li, M. Eddaoudi, T.L. Groy, O.M. Yaghi, *Journal of the American Chemical Society*, 120 (1998) 8571-8572.
- [72] H.L. Li, C.E. Davis, T.L. Groy, D.G. Kelley, O.M. Yaghi, *Journal of the American Chemical Society*, 120 (1998) 2186-2187.
- [73] B. Gil-Hernandez, J.K. Maclaren, H.A. Hoppe, J. Pasan, J. Sanchiz, C. Janiak, *CrystEngComm*, 14 (2012) 2635-2644.
- [74] A.Y. Robin, K.M. Fromm, *Coordination Chemistry Reviews*, 250 (2006) 2127-2157.
- [75] S.S.Y. Chui, S.M.F. Lo, J.P.H. Charmant, A.G. Orpen, I.D. Williams, *Science*, 283 (1999) 1148-1150.
- [76] C.O. Kappe, *Chemical Society Reviews*, 37 (2008) 1127-1139.
- [77] J. Klinowski, F.A. Almeida Paz, P. Silva, J. Rocha, *Dalton Transactions*, 40 (2011) 321-330.
- [78] S.H. Jhung, J.H. Lee, J.S. Chang, *Bulletin of the Korean Chemical Society*, 26 (2005) 880-881.
- [79] G. Ferey, C. Serre, C. Mellot-Draznieks, F. Millange, S. Surble, J. Dutour, I. Margiolaki, *Angewandte Chemie-International Edition*, 43 (2004) 6296-6301.
- [80] R. Sabouni, H. Kazemian, S. Rohani, *Chemical Engineering & Technology*, 35 (2012) 1085-1092.
- [81] S.T. Meek, J.A. Greathouse, M.D. Allendorf, *Advanced Materials*, 23 (2011) 249-267.
- [82] V. Safarifard, A. Morsali, *Coordination Chemistry Reviews*, 292 (2015) 1-14.
- [83] S. Fordham, X. Wang, M. Bosch, H.C. Zhou, *Lanthanide Metal-Organic Frameworks: Syntheses, Properties, and Potential Applications*, in: P. Cheng (Ed.) *Lanthanide Metal-Organic Frameworks*, Springer-Verlag Berlin, Berlin, 2015, pp. 1-27.
- [84] A. Martinez Joaristi, J. Juan-Alcañiz, P. Serra-Crespo, F. Kapteijn, J. Gascon, *Crystal Growth & Design*, 12 (2012) 3489-3498.
- [85] Y.B. Dong, Y.Y. Jiang, J. Li, J.P. Ma, F.L. Liu, B. Tang, R.Q. Huang, S.R. Batten, *Journal of the American Chemical Society*, 129 (2007) 4520-+.
- [86] G. Ferey, C. Mellot-Draznieks, C. Serre, F. Millange, J. Dutour, S. Surble, I. Margiolaki, *Science*, 309 (2005) 2040-2042.
- [87] C. Serre, F. Millange, C. Thouvenot, M. Nogues, G. Marsolier, D. Louer, G. Ferey, *Journal of the American Chemical Society*, 124 (2002) 13519-13526.

- [88] S.M.F. Vilela, A.D.G. Firmino, R.F. Mendes, J.A. Fernandes, D. Ananias, A.A. Valente, H. Ott, L.D. Carlos, J. Rocha, J.P.C. Tome, F.A. Almeida Paz, *Chemical Communications*, 49 (**2013**) 6400-6402.
- [89] S. Bauer, T. Bein, N. Stock, *Inorganic Chemistry*, 44 (**2005**) 5882-5889.
- [90] C.-H. Zhan, F. Wang, Y. Kang, J. Zhang, *Inorganic Chemistry*, 51 (**2011**) 523-530.
- [91] M. Schubert, U. Muller, M. Tonigold, R. Ruetz, Patent WO2007023134 A1.
- [92] M. Schubert, U. Muller, H. Mattenheimer, M. Tonigold, Patent WO2007/023119.
- [93] S.H. Jhung, J.-S. Chang, Patent KR 0627634.
- [94] S.H. Jhung, J.-S. Chang, Patent JP 4610531.
- [95] J.-S. Chang, Y.K. Hwang, S.H. Jhung, J.-S. Hwang, Y.-K. Seo, Patent KR 0803945.
- [96] Q.M. Wang, D.M. Shen, M. Bulow, M.L. Lau, S.G. Deng, F.R. Fitch, N.O. Lemcoff, J. Semanscin, *Microporous and Mesoporous Materials*, 55 (**2002**) 217-230.
- [97] U. Mueller, M. Schubert, F. Teich, H. Puetter, K. Schierle-Arndt, J. Pastre, *Journal of Materials Chemistry*, 16 (**2006**) 626-636.
- [98] Heading To Market With MOFs, *Chemical & Engineering News*, American Chemical Society, (**2008**), pp. 13-16.
- [99] S.Q. Ma, H.C. Zhou, *Chemical Communications*, 46 (**2010**) 44-53.
- [100] Y. Belmabkhout, V. Guillerm, M. Eddaoudi, *Chemical Engineering Journal*, 296 (**2016**) 386-397.
- [101] B. Li, B.L. Chen, *Porous Lanthanide Metal-Organic Frameworks for Gas Storage and Separation*, in: P. Cheng (Ed.) *Lanthanide Metal-Organic Frameworks*, Springer-Verlag Berlin, Berlin, 2015, pp. 75-107.
- [102] B. Li, H.M. Wen, W. Zhou, J.Q. Xu, B.L. Chen, *Chem*, 1 (**2016**) 557-580.
- [103] Z.X. Zhao, X.M. Li, S.S. Huang, Q.B. Xia, Z. Li, *Industrial & Engineering Chemistry Research*, 50 (**2011**) 2254-2261.
- [104] D. Saha, Z.B. Bao, F. Jia, S.G. Deng, *Environmental Science & Technology*, 44 (**2010**) 1820-1826.
- [105] L. Hamon, C. Serre, T. Devic, T. Loiseau, F. Millange, G. Ferey, G. De Weireld, *Journal of the American Chemical Society*, 131 (**2009**) 8775-+.
- [106] C. Petit, T.J. Bandoz, *Advanced Functional Materials*, 20 (**2010**) 111-118.
- [107] A.R. Millward, O.M. Yaghi, *Journal of the American Chemical Society*, 127 (**2005**) 17998-17999.

- [108] L. Hamon, H. Leclerc, A. Ghoufi, L. Oliviero, A. Travert, J.C. Lavalley, T. Devic, C. Serre, G. Ferey, G. De Weireld, A. Vimont, G. Maurin, *Journal of Physical Chemistry C*, 115 (2011) 2047-2056.
- [109] J. Liu, P.K. Thallapally, B.P. McGrail, D.R. Brown, *Chemical Society Reviews*, 41 (2012) 2308-2322.
- [110] C. Petit, B. Levasseur, B. Mendoza, T.J. Bandosz, *Microporous and Mesoporous Materials*, 154 (2012) 107-112.
- [111] B.J. Zhu, X.Y. Yu, Y. Jia, F.M. Peng, B. Sun, M.Y. Zhang, T. Luo, J.H. Liu, X.J. Huang, *Journal of Physical Chemistry C*, 116 (2012) 8601-8607.
- [112] F. Ke, L.G. Qiu, Y.P. Yuan, F.M. Peng, X. Jiang, A.J. Xie, Y.H. Shen, J.F. Zhu, *Journal of Hazardous Materials*, 196 (2011) 36-43.
- [113] M. Fujita, Y.J. Kwon, S. Washizu, K. Ogura, *Journal of the American Chemical Society*, 116 (1994) 1151-1152.
- [114] D.Y. Hong, Y.K. Hwang, C. Serre, G. Ferey, J.S. Chang, *Advanced Functional Materials*, 19 (2009) 1537-1552.
- [115] Y.K. Hwang, D.Y. Hong, J.S. Chang, S.H. Jhung, Y.K. Seo, J. Kim, A. Vimont, M. Daturi, C. Serre, G. Ferey, *Angewandte Chemie-International Edition*, 47 (2008) 4144-4148.
- [116] N.B. Pathan, A.M. Rahatgaonkar, M.S. Chorghade, *Catalysis Communications*, 12 (2011) 1170-1174.
- [117] G.Q. Kong, S. Ou, C. Zou, C.D. Wu, *Journal of the American Chemical Society*, 134 (2012) 19851-19857.
- [118] M. Pourkhosravani, S. Dehghanpour, F. Farzaneh, *Catalysis Letters*, 146 (2016) 499-508.
- [119] D. Britt, C. Lee, F.J. Uribe-Romo, H. Furukawa, O.M. Yaghi, *Inorganic Chemistry*, 49 (2010) 6387-6389.
- [120] A. Corma, H. Garcia, F. Xamena, *Chemical Reviews*, 110 (2010) 4606-4655.
- [121] A. Dhakshinamoorthy, M. Alvaro, H. Garcia, *Chemistry-A European Journal*, 16 (2010) 8530-8536.
- [122] X. Tan, L. Li, J.Y. Zhang, X.R. Han, L. Jiang, F.W. Li, C.Y. Su, *Chemistry of Materials*, 24 (2012) 480-485.
- [123] K.K. Tanabe, S.M. Cohen, *Inorganic Chemistry*, 49 (2010) 6766-6774.

- [124] K.K. Gangu, S. Maddila, S.B. Mukkamala, S.B. Jonnalagadda, *Inorganica Chimica Acta*, 446 (2016) 61-74.
- [125] J.W. Liu, L.F. Chen, H. Cui, J.Y. Zhang, L. Zhang, C.Y. Su, *Chemical Society Reviews*, 43 (2014) 6011-6061.
- [126] A. Schneemann, V. Bon, I. Schwedler, I. Senkovska, S. Kaskel, R.A. Fischer, *Chemical Society Reviews*, 43 (2014) 6062-6096.
- [127] P. Horcajada, C. Serre, M. Vallet-Regi, M. Sebban, F. Taulelle, G. Ferey, *Angewandte Chemie-International Edition*, 45 (2006) 5974-5978.
- [128] P. Horcajada, C. Serre, G. Maurin, N.A. Ramsahye, F. Balas, M. Vallet-Regi, M. Sebban, F. Taulelle, G. Ferey, *Journal of the American Chemical Society*, 130 (2008) 6774-6780.
- [129] B. Singco, L.H. Liu, Y.T. Chen, Y.H. Shih, H.Y. Huang, C.H. Lin, *Microporous and Mesoporous Materials*, 223 (2016) 254-260.
- [130] A.R. Chowdhuri, D. Bhattacharya, S.K. Sahu, *Dalton Transactions*, 45 (2016) 2963-2973.
- [131] J. Della Rocca, W.B. Lin, *European Journal of Inorganic Chemistry*, DOI 10.1002/ejic.201000496(2010) 3725-3734.
- [132] W.J. Rieter, K.M.L. Taylor, H.Y. An, W.L. Lin, W.B. Lin, *Journal of the American Chemical Society*, 128 (2006) 9024-9025.
- [133] K.M.L. Taylor, A. Jin, W.B. Lin, *Angewandte Chemie-International Edition*, 47 (2008) 7722-7725.
- [134] K.M.L. Taylor, W.J. Rieter, W.B. Lin, *Journal of the American Chemical Society*, 130 (2008) 14358-+.
- [135] T. Baati, L. Njim, F. Neffati, A. Kerkeni, M. Bouttemi, R. Gref, M.F. Najjar, A. Zakhama, P. Couvreur, C. Serre, P. Horcajada, *Chemical Science*, 4 (2013) 1597-1607.
- [136] M. Sajid, *Environmental Science and Pollution Research*, 23 (2016) 14805-14807.
- [137] S. Horike, D. Umeyama, S. Kitagawa, *Accounts of Chemical Research*, 46 (2013) 2376-2384.
- [138] P. Ramaswamy, N.E. Wong, G.K.H. Shimizu, *Chemical Society Reviews*, 43 (2014) 5913-5932.
- [139] G.K.H. Shimizu, J.M. Taylor, S. Kim, *Science*, 341 (2013) 354-355.

- [140] M. Yoon, K. Suh, S. Natarajan, K. Kim, *Angewandte Chemie-International Edition*, 52 (2013) 2688-2700.
- [141] G.K.H. Shimizu, J.M. Taylor, K.W. Dawson, Metal Organophosphonate Proton Conductors, in *Metal Phosphonate Chemistry: From Synthesis to Applications*, The Royal Society of Chemistry(2012), pp. 493-524.
- [142] H.-Y. Liu, H. Wu, J. Yang, Y.-Y. Liu, B. Liu, Y.-Y. Liu, J.-F. Ma, *Crystal Growth & Design*, 11 (2011) 2920-2927.
- [143] S.M. Mobin, A.K. Srivastava, P. Mathur, G.K. Lahiri, *Dalton Transactions*, 39 (2010) 8698-8705.
- [144] M. Gustafsson, J. Su, H. Yue, Q. Yao, X. Zou, *Crystal Growth & Design*, 12 (2012) 3243-3249.
- [145] P. Díaz-Gallifa, O. Fabelo, L. Cañadillas-Delgado, J. Pasán, A. Labrador, F. Lloret, M. Julve, C. Ruiz-Pérez, *Crystal Growth & Design*, 13 (2013) 4735-4745.
- [146] Q. Chen, Z. Chang, W.-C. Song, H. Song, H.-B. Song, T.-L. Hu, X.-H. Bu, *Angewandte Chemie-International Edition*, 52 (2013) 11550-11553.
- [147] M.J. Manos, E.J. Kyprianidou, G.S. Papaefstathiou, A.J. Tasiopoulos, *Inorganic Chemistry*, 51 (2012) 6308-6314.
- [148] J. Tian, L.V. Saraf, B. Schwenzer, S.M. Taylor, E.K. Brechin, J. Liu, S.J. Dalgarno, P.K. Thallapally, *Journal of the American Chemical Society*, 134 (2012) 9581-9584.
- [149] Z. Zhang, L. Wojtas, M. Eddaoudi, M.J. Zaworotko, *Journal of the American Chemical Society*, 135 (2013) 5982-5985.
- [150] K. Davies, S.A. Bourne, C.L. Oliver, *Crystal Growth & Design*, 12 (2012) 1999-2003.
- [151] R. Medishetty, L.L. Koh, G.K. Kole, J.J. Vittal, *Angewandte Chemie-International Edition*, 50 (2011) 10949-10952.
- [152] B.-C. Tzeng, S.-L. Wei, T.-Y. Chang, *Chemistry - A European Journal*, 18 (2012) 16443-16449.
- [153] M. Mazaj, G. Mali, M. Rangus, E. Žunkovič, V. Kaučič, N. Zabukovec Logar, *Journal of Physical Chemistry C*, 117 (2013) 7552-7564.
- [154] J.P. Zhang, P.Q. Liao, H.L. Zhou, R.B. Lin, X.M. Chen, *Chemical Society Reviews*, 43 (2014) 5789-5814.
- [155] J.J. Vittal, *Coordination Chemistry Reviews*, 251 (2007) 1781-1795.

- [156] Z.Q. Wang, S.M. Cohen, *Chemical Society Reviews*, 38 (2009) 1315-1329.
- [157] J.D. Evans, C.J. Sumby, C.J. Doonan, *Chemical Society Reviews*, 43 (2014) 5933-5951.
- [158] S. Gao, R.Q. Fan, X.M. Wang, L.G. Wei, Y. Song, X. Du, K. Xing, P. Wang, Y.L. Yang, *Physical Chemistry Chemical Physics*, 18 (2016) 19001-19010.
- [159] P. Jiang, F. Peng, Y.M. Chen, *Rsc Advances*, 6 (2016) 89192-89197.
- [160] H.F. Zhou, T. He, K.F. Yue, Y.L. Liu, C.S. Zhou, N. Yan, Y.Y. Wang, *Crystal Growth & Design*, 16 (2016) 3961-3968.
- [161] L. Aboutorabi, A. Morsali, *Coordination Chemistry Reviews*, 310 (2016) 116-130.
- [162] A. Kondo, T. Nakagawa, H. Kajiro, A. Chinen, Y. Hattori, F. Okino, T. Ohba, K. Kaneko, H. Kanoh, *Inorganic Chemistry*, 49 (2010) 9247-9252.
- [163] S. Ganguly, S. Mukherjee, P. Dastidar, *Crystal Growth & Design*, 16 (2016) 5247-5259.
- [164] H.-C. Fang, J.-Q. Zhu, L.-J. Zhou, H.-Y. Jia, S.-S. Li, X. Gong, S.-B. Li, Y.-P. Cai, P.K. Thallapally, J. Liu, G.J. Exarhos, *Crystal Growth & Design*, 10 (2010) 3277-3284.
- [165] C.K. Brozek, M. Dinca, *Chemical Society Reviews*, 43 (2014) 5456-5467.
- [166] K.S. Asha, R. Bhattacharjee, S. Mandal, *Angewandte Chemie-International Edition*, 55 (2016) 11528-11532.
- [167] E. Coronado, M. Giménez-Marqués, G. Mínguez Espallargas, *Inorganic Chemistry*, 51 (2012) 4403-4410.
- [168] P. Mahata, C.-M. Draznieks, P. Roy, S. Natarajan, *Crystal Growth & Design*, 13 (2012) 155-168.
- [169] H.-L. Jiang, Y. Tatsu, Z.-H. Lu, Q. Xu, *Journal of the American Chemical Society*, 132 (2010) 5586-5587.
- [170] E. Jeong, W.R. Lee, D.W. Ryu, Y. Kim, W.J. Phang, E.K. Koh, C.S. Hong, *Chemical Communications*, 49 (2013) 2329-2331.
- [171] F. Zhai, Q. Zheng, Z. Chen, Y. Ling, X. Liu, L. Weng, Y. Zhou, *CrystEngComm*, 15 (2013) 2040-2043.
- [172] L. Wen, P. Cheng, W. Lin, *Chemical Communications*, 48 (2012) 2846-2848.
- [173] A. Husain, M. Ellwart, S.A. Bourne, L. Öhrström, C.L. Oliver, *Crystal Growth & Design*, 13 (2013) 1526-1534.

- [174] M. Dincă, J.R. Long, *Journal of the American Chemical Society*, 129 (**2007**) 11172-11176.
- [175] H.-L. Sun, D.-D. Yin, Q. Chen, Z. Wang, *Inorganic Chemistry*, 52 (**2013**) 3582-3584.
- [176] Y.-Q. Lan, H.-L. Jiang, S.-L. Li, Q. Xu, *Inorganic Chemistry*, 51 (**2012**) 7484-7491.
- [177] C.-C. Wang, C.-C. Yang, C.-T. Yeh, K.-Y. Cheng, P.-C. Chang, M.-L. Ho, G.-H. Lee, W.-J. Shih, H.-S. Sheu, *Inorganic Chemistry*, 50 (**2010**) 597-603.
- [178] A. Aslani, A. Morsali, *Chemical Communications*, DOI 10.1039/b800126j(**2008**) 3402-3404.
- [179] T. Yamada, G. Maruta, S. Takeda, *Chemical Communications*, 47 (**2011**) 653-655.
- [180] P. Smart, C.A. Mason, J.R. Loader, A.J.H.M. Meijer, A.J. Florence, K. Shankland, A.J. Fletcher, S.P. Thompson, M. Brunelli, A.H. Hill, L. Brammer, *Chemistry - A European Journal*, 19 (**2013**) 3552-3557.
- [181] Y.-C. He, J. Yang, G.-C. Yang, W.-Q. Kan, J.-F. Ma, *Chemical Communications*, 48 (**2012**) 7859-7861.
- [182] S.K. Ghosh, J.-P. Zhang, S. Kitagawa, *Angewandte Chemie-International Edition*, 46 (**2007**) 7965-7968.
- [183] Y.-J. Zhang, T. Liu, S. Kanegawa, O. Sato, *Journal of the American Chemical Society*, 131 (**2009**) 7942-7943.
- [184] R. Bhure, T.M. Abdel-Fattah, C. Bonner, J.C. Hall, A. Mahapatro, *Journal of Biomedical Nanotechnology*, 6 (**2010**) 117-128.
- [185] S.Y. Kim, J.S. Park, *Journal of Applied Polymer Science*, 131 (**2014**).
- [186] C. Lorenz, A. Hoffmann, G. Gross, H. Windhagen, P. Dellinger, K. Mohwald, W. Dempwolf, H. Menzel, *Macromolecular Bioscience*, 11 (**2011**) 234-244.
- [187] C. Pfaffenroth, A. Winkel, W. Dempwolf, L.J. Gamble, D.G. Castner, M. Stiesch, H. Menzel, *Macromolecular Bioscience*, 11 (**2011**) 1515-1525.
- [188] C. Tudisco, F. Bertani, M.T. Cambria, F. Sinatra, E. Fantechi, C. Innocenti, C. Sangregorio, E. Dalcanale, G.G. Condorelli, *Nanoscale*, 5 (**2013**) 11438-11446.
- [189] M. Bishop, S.G. Bott, A.R. Barron, *Chemistry of Materials*, 15 (**2003**) 3074-3088.
- [190] A. Cabeza, S. Bruque, A. Guagliardi, M.A.G. Aranda, *Journal of Solid State Chemistry*, 160 (**2001**) 278-286.

- [191] K.D. Demadis, S.D. Katarachia, R.G. Raptis, H. Zhao, P. Baran, *Crystal Growth & Design*, 6 (2006) 836-838.
- [192] V. Georgantas, N. Kotsakis, C.P. Raptopoulou, A. Terzis, L. Iordanidis, M. Zervou, T. Jakusch, T. Kiss, A. Salifoglou, *Journal of Inorganic Biochemistry*, 103 (2009) 1530-1541.
- [193] H.D. Li, L.R. Zhang, G.H. Li, Y. Yu, Q.S. Huo, Y.L. Liu, *Microporous and Mesoporous Materials*, 131 (2010) 186-191.
- [194] J.G. Mao, Z.K. Wang, A. Clearfield, *New Journal of Chemistry*, 26 (2002) 1010-1014.
- [195] J. Weber, G. Grossmann, K.D. Demadis, N. Daskalakis, E. Brendler, M. Mangstl, J. Gunne, *Inorganic Chemistry*, 51 (2012) 11466-11477.
- [196] S.M.F. Vilela, D. Ananias, A.C. Gomes, A.A. Valente, L.D. Carlos, J.A.S. Cavaleiro, J. Rocha, J.P.C. Tome, F.A.A. Paz, *Journal of Materials Chemistry*, 22 (2012) 18354-18371.
- [197] P. Silva, F. Vieira, A.C. Gomes, D. Ananias, J.A. Fernandes, S.M. Bruno, R. Soares, A.A. Valente, J. Rocha, F.A.A. Paz, *Journal of the American Chemical Society*, 133 (2011) 15120-15138.
- [198] L. Cunha-Silva, L. Mafra, D. Ananias, L.D. Carlos, J. Rocha, F.A. Almeida Paz, *Chemistry of Materials*, 19 (2007) 3527-3538.
- [199] G. Socrates, *Infrared Characteristic Group Frequencies - Tables and Charts*, 2nd ed., John Wiley & Sons Ltd, Baffins Lane, Chichester, 1994.
- [200] J.G. Smith, *Synthesis-Stuttgart*, DOI (1984) 629-656.
- [201] C. Wiles, P. Watts, S.J. Haswell, *Tetrahedron*, 61 (2005) 5209-5217.
- [202] T.W. Greene, P.G.M. Wuts, *Protection for the Carbonyl Group, Protective Groups in Organic Synthesis*, John Wiley & Sons, Inc., Kalamazao, Michigan, 1999, pp. 293-368.
- [203] D. Martin, *J. Prakt. Chem.*, 337 (1995) 164-165.
- [204] D.M. Jiang, A. Urakawa, M. Yulikov, T. Mallat, G. Jeschke, A. Baiker, *Chemistry-A European Journal*, 15 (2009) 12255-12262.
- [205] L.H. Wee, M.R. Lohe, N. Janssens, S. Kaskel, J.A. Martens, *Journal of Materials Chemistry*, 22 (2012) 13742-13746.

- [206] M.N. Timofeeva, V.N. Panchenko, J.W. Jun, Z. Hasan, M.M. Matrosova, S.H. Jung, *Applied Catalysis A: General*, 471 **(2014)** 91-97.
- [207] P. Silva, D. Ananias, S.M. Bruno, A.A. Valente, L.D. Carlos, J. Rocha, F.A. Almeida Paz, *European Journal of Inorganic Chemistry*, 2013 **(2013)** 5576-5591.
- [208] G. Fan, F. Li, D.G. Evans, X. Duan, *Chemical Society Reviews*, 43 **(2014)** 7040-7066.
- [209] T.W. Greene, P.G.M. Wuts, *Protective Groups in Organic Synthesis*, 3rd ed., John Wiley & Sons, Inc., New York, USA, 1999.
- [210] S. Ajaikumar, A. Pandurangan, *Journal of Molecular Catalysis A: Chemical*, 290 **(2008)** 35-43.
- [211] M.J. Climent, A. Velty, A. Corma, *Green Chemistry*, 4 **(2002)** 565-569.
- [212] K. Bauer, D. Garbe, H. Surburg, *Common Fragrances and Flavour Materials: Preparation and Uses*, Fourth, Completely Revised Edition, 2nd ed., Wiley-VCH Verlag GmbH, New York, USA, 2001.
- [213] B. Thomas, S. Prathapan, S. Sugunan, *Microporous and Mesoporous Materials*, 80 **(2005)** 65-72.
- [214] S. Wu, W. Dai, S. Yin, W. Li, C.-T. Au, *Catalysis Letters*, 124 **(2008)** 127-132.
- [215] K. Bruns, J. Conrad, A. Steigel, *Tetrahedron*, 35 **(1979)** 2523-2530.
- [216] A.J. Elliot, *1,3-Dioxalane Polymers in Comprehensive Heterocyclic Polymers*, Pergamon Press, Oxford, U. K., 1984.
- [217] D.M. Clode, *Chemical Reviews*, 79 **(1979)** 491-513.
- [218] B.M. Smith, T.M. Kubczyk, A.E. Graham, *Rsc Advances*, 2 **(2012)** 2702-2706.
- [219] D.B.G. Williams, M.C. Lawton, *Green Chemistry*, 10 **(2008)** 914-917.
- [220] D.-J. Tao, Z.-M. Li, Z. Cheng, N. Hu, X.-S. Chen, *Industrial & Engineering Chemistry Research*, 51 **(2012)** 16263-16269.
- [221] F. Vermoortele, M. Vandichel, B. Van de Voorde, R. Ameloot, M. Waroquier, V. Van Speybroeck, D.E. De Vos, *Angewandte Chemie-International Edition*, 51 **(2012)** 4887-4890.
- [222] F. Vermoortele, B. Bueken, G. Le Bars, B. Van de Voorde, M. Vandichel, K. Houthoofd, A. Vimont, M. Daturi, M. Waroquier, V. Van Speybroeck, C. Kirschhock, D.E. De Vos, *Journal of the American Chemical Society*, 135 **(2013)** 11465-11468.

- [223] L.H. Wee, F. Bonino, C. Lamberti, S. Bordiga, J.A. Martens, *Green Chemistry*, 16 (2014) 1351-1357.
- [224] A. Herbst, A. Khutia, C. Janiak, *Inorganic Chemistry*, 53 (2014) 7319-7333.
- [225] A. Dhakshinamoorthy, M. Alvaro, H. Garcia, *Advanced Synthesis & Catalysis*, 352 (2010) 3022-3030.
- [226] A. Dhakshinamoorthy, M. Alvaro, P. Horcajada, E. Gibson, M. Vishnuvarthan, A. Vimont, J.-M. Grenèche, C. Serre, M. Daturi, H. Garcia, *ACS Catalysis*, 2 (2012) 2060-2065.
- [227] U.S.F. Arrozi, H.W. Wijaya, A. Patah, Y. Permana, *Applied Catalysis A: General*, 506 (2015) 77-84.
- [228] L. Bromberg, T.A. Hatton, *Applied Materials & Interfaces*, 3 (2011) 4756-4764.
- [229] B. Thomas, S. Sugunan, *Journal of Porous Materials*, 13 (2006) 99-106.
- [230] B. Thomas, S. Sugunan, *Indian Journal Chemistry, Sect A*, 44 (2005) 1345-1354.
- [231] B. Thomas, V.G. Ramu, S. Gopinath, J. George, M. Kurian, G. Laurent, G.L. Drisko, S. Sugunan, *Applied Clay Science*, 53 (2011) 227-235.
- [232] Y. Guan, D. Zhang, Y. Wang, *Catalysis Letters*, 142 (2012) 1225-1233.
- [233] J.-Y. Liu, J.-G. Wang, N. Li, H. Zhao, H.-J. Zhou, P.-C. Sun, T.-H. Chen, *Langmuir*, 28 (2012) 8600-8607.
- [234] B. Rabindran Jermy, A. Pandurangan, *Journal of Molecular Catalysis A: Chemical*, 256 (2006) 184-192.
- [235] B. Thomas, S. Prathapan, S. Sugunan, *Applied Catalysis A: General*, 277 (2004) 247-252.
- [236] M. Iwamoto, Y. Tanaka, N. Sawamura, S. Namba, *Journal of the American Chemical Society*, 125 (2003) 13032-13033.
- [237] C.-H. Lin, S. Lin, Y.-H. Yang, T.-P. Lin, *Catalysis Letters*, 73 (2001) 121-125.
- [238] A. Clerici, N. Pastori, O. Porta, *Tetrahedron*, 54 (1998) 15679-15690.
- [239] Y.-W. Ren, J.-X. Liang, J.-X. Lu, B.-W. Cai, D.-B. Shi, C.-R. Qi, H.-F. Jiang, J. Chen, D. Zheng, *European Journal of Inorganic Chemistry*, DOI 10.1002/ejic.201100523 (2011) 4369-4376.
- [240] A. Dikhtiarenko, S.A. Khainakov, I. de Pedro, J.A. Blanco, J.R. García, J. Gimeno, *Inorganic Chemistry*, 52 (2013) 3933-3941.

- [241] R.F. Mendes, F.A.A. Paz, *Inorganic Chemistry Frontiers*, 2 **(2015)** 495-509.
- [242] W.J. Phang, H. Jo, W.R. Lee, J.H. Song, K. Yoo, B. Kim, C.S. Hong, *Angewandte Chemie-International Edition*, 54 **(2015)** 5142-5146.
- [243] M. Sadakiyo, T. Yamada, H. Kitagawa, *Chempluschem*, 81 **(2016)** 691-701.
- [244] R. Yadav, P.S. Fedkiw, *Journal of the Electrochemical Society*, 159 **(2012)** B340-B346.
- [245] N.C. Rosero-Navarro, E.M. Domingues, N. Sousa, P. Ferreira, F.M.L. Figueiredo, *Solid State Ionics*, 262 **(2014)** 324-327.
- [246] S.S. Nagarkar, S.M. Unni, A. Sharma, S. Kurungot, S.K. Ghosh, *Angewandte Chemie-International Edition*, 53 **(2014)** 2638-2642.
- [247] V.G. Ponomareva, K.A. Kovalenko, A.P. Chupakhin, D.N. Dybtsev, E.S. Shutova, V.P. Fedin, *Journal of the American Chemical Society*, 134 **(2012)** 15640-15643.
- [248] K.D. Kreuer, S.J. Paddison, E. Spohr, M. Schuster, *Chemical Reviews*, 104 **(2004)** 4637-4678.
- [249] P. Barbosa, N.C. Rosero-Navarro, F.N. Shi, F.M.L. Figueiredo, *Electrochimica Acta*, 153 **(2015)** 19-27.
- [250] X. Meng, S.Y. Song, X.Z. Song, M. Zhu, S.N. Zhao, L.L. Wu, H.J. Zhang, *Chemical Communications*, 51 **(2015)** 8150-8152.
- [251] M. Sadakiyo, H. Kasai, K. Kato, M. Takata, M. Yamauchi, *Journal of the American Chemical Society*, 136 **(2014)** 1702-1705.
- [252] M. Sadakiyo, T. Yamada, H. Kitagawa, *Journal of the American Chemical Society*, 131 **(2009)** 9906-+.
- [253] E.V. Alexandrov, V.A. Blatov, A.V. Kochetkov, D.M. Proserpio, *CrystEngComm*, 13 **(2011)** 3947-3958.
- [254] V.A. Blatov, A.P. Shevchenko, V.N. Serezhkin, *Journal of Applied Crystallography*, 33 **(2000)** 1193.
- [255] R.F. Mendes, M.M. Antunes, P. Silva, P. Barbosa, F. Figueiredo, A. Linden, J. Rocha, A.A. Valente, F.A.A. Paz, *Chemistry - A European Journal*, 22 **(2016)** 13136-13146.
- [256] R.M.P. Colodrero, P. Olivera-Pastor, E.R. Losilla, M.A.G. Aranda, L. Leon-Reina, M. Papadaki, A.C. McKinlay, R.E. Morris, K.D. Demadis, A. Cabeza, *Dalton Transactions*, 41 **(2012)** 4045-4051.

- [257] E. Barouda, K.D. Demadis, S.R. Freeman, F. Jones, M.I. Ogden, *Crystal Growth & Design*, 7 (**2007**) 321-327.
- [258] R.M.P. Colodrero, A. Cabeza, P. Olivera-Pastor, A. Infantes-Molina, E. Barouda, K.D. Demadis, M.A.G. Aranda, *Chemistry-A European Journal*, 15 (**2009**) 6612-6618.
- [259] F. Costantino, T. Bataille, N. Audebrand, E. Le Fur, C. Sangregorio, *Crystal Growth & Design*, 7 (**2007**) 1881-1888.
- [260] K.D. Demadis, E. Barouda, R.G. Raptis, H. Zhao, *Inorganic Chemistry*, 48 (**2009**) 819-821.
- [261] K.D. Demadis, C. Mantzaridis, R.G. Raptis, G. Mezel, *Inorganic Chemistry*, 44 (**2005**) 4469-4471.
- [262] M. Taddei, F. Costantino, A. Ienco, A. Comotti, P.V. Dau, S.M. Cohen, *Chemical Communications*, 49 (**2013**) 1315-1317.
- [263] F.A.A. Paz, S.M.F. Vilela, J.P.C. Tome, *Crystal Growth & Design*, 14 (**2014**) 4873-4877.
- [264] M.W. Zhang, Y.P. Chen, M. Bosch, T. Gentle, K.C. Wang, D.W. Feng, Z.Y.U. Wang, H.C. Zhou, *Angewandte Chemie-International Edition*, 53 (**2014**) 815-818.
- [265] T. Kottke, D. Stalke, *Journal of Applied Crystallography*, 26 (**1993**) 615-619.
- [266] *APEX2 Data Collection Software Version 2.1-RC13*, Bruker AXS, Delft, The Netherlands, **2006**.
- [267] G.M. Sheldrick, *SHELXL Version 2014*, Program for Crystal Structure Refinement, University of Göttingen, **2014**.
- [268] G.M. Sheldrick, *Acta Cryst. A*, 64 (**2008**) 112-122.
- [269] R.F. Mendes, F.A. Almeida Paz, *Inorganica Chimica Acta*, 460 99-107.